# SUPERHALOGENS & SUPERALKALIS: EXPLORATION OF STRUCTURE, PROPERTIES AND APPLICATIONS

EDITED BY: Ambrish Kumar Srivastava, Iwona Anusiewicz, Suzana Velickovic, Wei-Ming Sun and Gennady L. Gutsev

PUBLISHED IN: Frontiers in Chemistry and Frontiers in Physics

frontiers Research Topics

ISSN 1664-8714
ISBN 978-2-83250-893-0
DOI 10.3389/978-2-83250-893-0

## About Frontiers

Frontiers is more than just an open-access publisher of scholarly articles: it is a pioneering approach to the world of academia, radically improving the way scholarly research is managed. The grand vision of Frontiers is a world where all people have an equal opportunity to seek, share and generate knowledge. Frontiers provides immediate and permanent online open access to all its publications, but this alone is not enough to realize our grand goals.

## Frontiers Journal Series

The Frontiers Journal Series is a multi-tier and interdisciplinary set of open-access, online journals, promising a paradigm shift from the current review, selection and dissemination processes in academic publishing. All Frontiers journals are driven by researchers for researchers; therefore, they constitute a service to the scholarly community. At the same time, the Frontiers Journal Series operates on a revolutionary invention, the tiered publishing system, initially addressing specific communities of scholars, and gradually climbing up to broader public understanding, thus serving the interests of the lay society, too.

## Dedication to Quality

Each Frontiers article is a landmark of the highest quality, thanks to genuinely collaborative interactions between authors and review editors, who include some of the world's best academicians. Research must be certified by peers before entering a stream of knowledge that may eventually reach the public - and shape society; therefore, Frontiers only applies the most rigorous and unbiased reviews.
Frontiers revolutionizes research publishing by freely delivering the most outstanding research, evaluated with no bias from both the academic and social point of view. By applying the most advanced information technologies, Frontiers is catapulting scholarly publishing into a new generation.

## What are Frontiers Research Topics?

Frontiers Research Topics are very popular trademarks of the Frontiers Journals Series: they are collections of at least ten articles, all centered on a particular subject. With their unique mix of varied contributions from Original Research to Review Articles, Frontiers Research Topics unify the most influential researchers, the latest key findings and historical advances in a hot research area! Find out more on how to host your own Frontiers Research Topic or contribute to one as an author by contacting the Frontiers Editorial Office: frontiersin.org/about/contact

# SUPERHALOGENS & SUPERALKALIS: EXPLORATION OF STRUCTURE, PROPERTIES AND APPLICATIONS

Topic Editors:
**Ambrish Kumar Srivastava,** Deen Dayal Upadhyay Gorakhpur University, India
**Iwona Anusiewicz,** University of Gdansk, Poland
**Suzana Velickovic,** University of Belgrade, Serbia
**Wei-Ming Sun,** Fujian Medical University, China
**Gennady L. Gutsev,** Florida Agricultural and Mechanical University, United States

**Citation:** Srivastava, A. K., Anusiewicz, I., Velickovic, S., Sun, W.-M., Gutsev, G. L., eds. (2022). Superhalogens & Superalkalis: Exploration of Structure, Properties and Applications. Lausanne: Frontiers Media SA. doi: 10.3389/978-2-83250-893-0

# Table of Contents

frontiers | Frontiers in Chemistry

TYPE Editorial
PUBLISHED 15 November 2022
DOI 10.3389/fchem.2022.1075487



OPEN ACCESS

EDITED AND REVIEWED BY
Malgorzata Biczysko,
Shanghai University, China

*CORRESPONDENCE
Ambrish Kumar Srivastava,
ambrishphysics@gmail.com,
aks.ddugu@gmail.com

SPECIALTY SECTION
This article was submitted to Physical Chemistry and Chemical Physics, a section of the journal Frontiers in Chemistry

RECEIVED 20 October 2022
ACCEPTED 07 November 2022
PUBLISHED 15 November 2022

CITATION
Srivastava AK, Anusiewicz I, Velickovic S, Sun W-M and Gutsev GL (2022), Editorial: Superhalogens & superalkalis: Exploration of structure, properties and applications.
*Front. Chem.* 10:1075487.
doi: 10.3389/fchem.2022.1075487



# Editorial: Superhalogens & superalkalis: Exploration of structure, properties and applications

Ambrish Kumar Srivastava[1]*, Iwona Anusiewicz[2], Suzana Velickovic[3], Wei-Ming Sun[4] and Gennady L. Gutsev[5]

[1]Department of Physics, Deen Dayal Upadhyaya Gorakhpur University, Gorakhpur, India, [2]Department of Chemistry, University of Gdansk, Gdansk, Poland, [3]Department of Physical Chemistry, Vinča Institute of Nuclear Science, University of Belgrade, Belgrade, Serbia, [4]Department of Basic Chemistry, School of Pharmacy, Fujian Medical University, Fuzhou, China, [5]Department of Physics, Florida Agricultural and Mechanical University, Tallahassee, FL, United States

KEYWORDS

**atomic clusters, superalkali, theory, superatoms, superhalogen**

Editorial on the Research Topic
Superhalogens & superalkalis: Exploration of structure, properties and applications

Atomic clusters (Srivastava et al., 2021), containing a few to a hundred of atoms, are intermediates between a molecule and bulk materials. Superatoms are a special class of atomic clusters, mimicking the properties of atom. Superhalogens are superalkalis are two examples of superatoms, which possess higher electron affinity than halogen and lower ionization energy than alkali atoms, respectively. The Research Topic "*Superhalogens & Superalkalis: Exploration of Structure, Properties and Applications*" provides a compendium of the recent research and development in this field. This Research Topic concludes two review articles and seven research articles.

Srivastava and Srivastava reviewed the application of superalkalis in the activation of carbon dioxide. Owing to low ionization energy, superalkalis become reducers and can easily transfer an electron to $CO_2$, which possesses no positive electron affinity. They have discussed the $CO_2$ reduction by various types of superalkalis such as typical superalkalis, binuclear superalkalis, special superalkalis, non-metallic superalkalis. These superalkalis differ in design based on different electron-counting rules. The authors also included the successive activation of six $CO_2$ molecules using hexalithiobenzene ($C_6Li_6$), a closed-shell molecule with low ionization energy. Superalkalis have been substantially explored over the past couple of decades. In the review of Pandey et al., the recent developments in the theoretical design and characterization of a variety of superalkali-based compounds and their potential applications have been enumerated. They unveiled the potential applications of some novel superalkalis for capturing and storing $CO_2/N_2$ and also analyzed the first-order hyperpolarizability-based nonlinear optical (NLO) responses

features of fullerene-like superalkali-doped $B_{12}N_{12}$ and $B_{12}P_{12}$ nanoclusters with good ultraviolet (UV) transparency and superalkali-based $CaN_3Ca$ system, a high sensitivity alkali-earth-based aromatic multi-state NLO molecular switch, and so on. They have also highlighted the interactions of superalkalis in gas and liquid phases in this review. The authors expected that their review will provide new insights on the possibility of expanding both the experimental synthesis and the practical use of superalkalis and related species.

Ye et al. designed the X@$3^6$adz complexes by embedding X (=H, B, C, N, O, F, and Si) into the $3^6$adamanzane ($3^6$adz) complexant. It is interesting to find the low adiabatic ionization energies (AIEs), 0.78–5.28 eV of these complexes. Although the IEs of X atoms are high, the AIEs of X@$3^6$adz (X = H, B, C, N, and Si) are even lower than the IE of the Cs atom (3.89 eV), which identifies their non-metallic superalkali characteristics. Furthermore, the presence of diffuse excess electron in B@$3^6$adz enables it not only to possess a fairly low AIE of 2.16 eV but also significantly high first hyperpolarizability ($\beta_0$) of $1.35 \times 10^6$ au. This may suggest its potential to be a bifunctional molecule with both strong reducibility and larger NLO response.

Cyraniak et al. adopted the electronic transmutation concept for designing novel series of polynuclear superhalogen anions. They investigated the stability of $(BF_3(BN)_nF_{4n+1})^-$ anions for $n$ = 1–10, 13, 18–20 having alternate boron and nitrogen central atoms in the form of the $(BN)_n$ "core", $4n$+1 fluorine as well as one $BF_3$ ligand using density functional theory (DFT) and outer valence Green function (OVGF) methods with flexible atomic orbital basis sets. The newly proposed anions are reflecting the structures of chain-like $C_nH_{2n+2}$ molecules in which the $(BN)_n$ cores are supposed to resemble the bonding features of the $C_{2n}$ chain, which advocates the existence of $4n$+2 substituents similar to those in typical saturated hydrocarbons. The authors confirmed that the equilibrium configurations of these anions are completely extended chains with each B and N core atom having four peripheral substituents organized in a tetrahedral pattern. Consequently, these anions mimic the universally stable completely extended conformational changes of higher n-alkanes. Moreover, the calculations revealed that the vertical electron detachment energies (VDEs) of the $(BF_3(BN)_nF_{4n+1})^-$ anions were observed to be greater than 8 eV and to rise steadily with the increase in $n$. Additionally, the authors predicted that the upper limit of VDE which could be achieved for such polynuclear superhalogen anions is about 10.7 eV.

Guo et al. reported a quantum chemical study on a binary $B_5O_6^-$ cluster and found a global-minimum planar $C_{2v}$ ($^1A_1$) structure having a $B_3O_3$ hexagonal ring in its center. They noticed that two boronyl (BO) groups and one $O^-$ ligand terminates three unsaturated B sites and therefore, formulated this cluster as $B_3O_3(BO)_2O^-$ unlike its predecessors, $C_s$ $B_5O_5^-$ and $T_d$ $B_5O_4^-$, containing a tetrahedral B at the center. According to them, the $B_5O_n^-$ series undergoes a significant structural change after oxidation, showing an interesting rivalry among tetrahedral *versus* heterocyclic structures. Their investigations reveal that the $B_5O_6^-$ cluster has a weak $6\pi$ aromaticity, making it a boronyl counterpart of the phenolate anion ($C_6H_5O^-$) or boronyl boroxine. The authors estimated that the $B_5O_6^-$ cluster has a VDE of 5.26 eV at PBE0 method, which is much higher than the electron affinities of typical halogens, limited to 3.61 eV for Cl, and consequently, declared it as a superhalogen anion.

Zhu et al. studied the structural evolution, bonding, stability, charge transfer, and nonlinear optical characteristics of $AuMg_n$ ($n$ = 2–12) nanoclusters using the DFT method. They unraveled a planar structure of the $AuMg_3$ and the symmetrically perfect cage-like structure of the $AuMg_9$. They analyzed the charge transfer from the Mg to Au atoms and identified the covalent Mg-Mg bonds in nanoclusters larger than that of $AuMg_3$. Their polarizability and hyperpolarizability estimations predict the strong NLO behavior of the $AuMg_9$ nanocluster. Based on their theoretical results, the authors also suggested that these nanoclusters are identifiable by spectroscopic experiments.

Tkachenko et al. examined ionization potentials (IPs) for a series of clusters of various cryptand such as [bpy.bpy.bpy] cryptand (bpy = bi-pyridine), [2.2.2]cryptand, and spherical cryptand with Na, K, $NH_4$, and $H_3O$ with by using the DFT as well as *ab initio* methods. They noticed that the encapsulation of Rydberg molecules ($NH_4$ and $H_3O$) inside an organic cage leads to a decrease in their IPs, reaching the values of ~1.5 eV and an even lower value of 1.3 eV. They also showed that the Rydberg molecules coated with the "organic skin" can increase their thermodynamic stability. Therefore, they suggested that these findings provide an opportunity to obtain such strong reducing agents in the experiment. This work was contributed by the research group of Prof. Alexander Boldyrev, one of the pioneers in the field of superatoms.

He et al. investigated and studied the substituent effect in M@$Al_{12}N_{11}$ and M@$Al_{11}N_{12}$ (M = Be, Mg, and Ca) nanocages through the replacement of one Al or N atom of aluminum nitride nanocage ($Al_{12}N_{12}$) with an alkaline-earth metal atom by DFT methods. Their calculations reveal that these nanocages are highly stable and have excess electron systems. They, further, suggested that these substituted nanocages exhibit larger first hyperpolarizabilities ($\beta_0$) than that of pure $Al_{12}N_{12}$ nanocages due to the presence of diffuse excess electrons. According to them, these modified cages possess the transparency to infrared light (IR) (>1,800 nm) as well as ultraviolet light (UV) (250 nm). The authors concluded that their studied highly stable excess electron compounds might be suitable candidates for novel UV and IR NLO systems.

Yang et al. proposed and systematically investigated a new group of hetero-binuclear superhalogen anion matching the $MM'X_4^-$ (M = Li, Na; M′ = Be, Mg, Ca; X = Cl, Br) formula

by using second-order Moller-Plesset perturbation theory (MP2) and OVGF methods and 6–311+G (3df) basis set. The calculations revealed that all of the studied anions possess vertical electron detachment energies (VDEs) larger than 5.4 eV and thus confirmed their superhalogen nature. Moreover, the authors also noticed the dependence of the VDE of the $MM'X_4^-$ anions on the M and M′ atomic radius, and electronegativity of the ligand used. In particular, the inclusion of a smaller alkali metal atom M, a bigger alkaline earth metal atom M′, and a greater electronegative ligand atom X might result in larger VDE values for these heteronuclear superhalogen anions. Therefore, one isomer of $LiCaCl_4^-$ was found to possess the largest VDE value (6.799 eV). In addition, the analysis of charge distribution of all studied anions shows that the isomers exhibit considerably greater electrical stability when the excess of electrons charge is shared across all of the ligand atoms as well as with the three bridging ligand atoms.

Thus, the Research Topic not only covers the articles based on the exploration of structures, properties and applications of superatoms but also includes a few articles on atomic clusters as well. We are of the strong opinion that the contents of this Research Topic offer readers an overview of the recent progress of this constantly expanding field.

## Reference

Srivastava, A. K., Anusiewicz, I., Velickovic, S., Sun, W-M., and Misra, N. (2021). Editorial: Atomic clusters: Theory & experiments. *Front. Chem.* 9, 795113. doi:10.3389/fchem.2021.795113

## Author contributions

All authors listed have made a substantial, direct, and intellectual contribution to the work and approved it for publication.

## Conflict of interest

The authors declare that the research was conducted in the absence of any commercial or financial relationships that could be construed as a potential conflict of interest.

## Publisher's note

frontiers in Chemistry

ORIGINAL RESEARCH
published: 14 March 2022
doi: 10.3389/fchem.2022.853160

# Designing Special Nonmetallic Superalkalis Based on a Cage-like Adamanzane Complexant

*Ya-Ling Ye*[1], *Kai-Yun Pan*[1], *Bi-Lian Ni*[1] *and Wei-Ming Sun*[1,2]*

[1]*Fujian Key Laboratory of Drug Target Discovery and Structural and Functional Research, The School of Pharmacy, Fujian Medical University, Fuzhou, China,* [2]*School of Chemistry and Materials Science, University of Science and Technology of China, Hefei, China*

In this study, to examine the possibility of using cage-like complexants to design nonmetallic superalkalis, a series of X@$3^6$adz (X = H, B, C, N, O, F, and Si) complexes have been constructed and investigated by embedding nonmetallic atoms into the $3^6$adamanzane ($3^6$adz) complexant. Although X atoms possess very high ionization energies, these resulting X@$3^6$adz complexes possess low adiabatic ionization energies (AIEs) of 0.78–5.28 eV. In particular, the adiabatic ionization energies (AIEs) of X@$3^6$adz (X = H, B, C, N, and Si) are even lower than the ionization energy (3.89 eV) of Cs atoms, and thus, can be classified as novel nonmetallic superalkalis. Moreover, due to the existence of diffuse excess electrons in B@$3^6$adz, this complex not only possesses pretty low AIE of 2.16 eV but also exhibits a remarkably large first hyperpolarizability ($\beta_0$) of $1.35 \times 10^6$ au, indicating that it can also be considered as a new kind of nonlinear optical molecule. As a result, this study provides an effective approach to achieve new metal-free species with an excellent reducing capability by utilizing the cage-like organic complexants as building blocks.

**Keywords: superalkali, adamanzane, superatom, nonlinear optics, reducing matters**

OPEN ACCESS

***Edited by:***
*Sugata Chowdhury, National Institute of Standards and Technology (NIST), United States*

***Reviewed by:***
*Gourhari Jana, University of California, Irvine, United States*
*Santanab Giri, Haldia Institute of Technology, India*

***Correspondence:**
*Wei-Ming Sun*
*sunwm@fjmu.edu.cn*

***Specialty section:***
*This article was submitted to Physical Chemistry and Chemical Physics, a section of the journal Frontiers in Chemistry*

***Received:*** *12 January 2022*
***Accepted:*** *25 February 2022*
***Published:*** *14 March 2022*

***Citation:***
*Ye Y-L, Pan K-Y, Ni B-L and Sun W-M (2022) Designing Special Nonmetallic Superalkalis Based on a Cage-like Adamanzane Complexant. Front. Chem. 10:853160. doi: 10.3389/fchem.2022.853160*

## INTRODUCTION

Reducing agents with low ionization energies (IEs) play a crucial role in chemical synthesis. As is well-known, alkali metal atoms possess the lowest ionization energies (5.39–3.89 eV) (Lide, 2003) among all the elements in the periodic table. However, it is reported that a class of extraordinary compounds possesses even lower IEs than those of alkali metal atoms. Such species were termed "superalkalis" by Gutsev and Boldyrev (1982). Initially, superalkalis were designed by decorating an electronegative central atom with alkali-metal ligands, such as $FLi_2$, $OLi_3$, and $NLi_4$ following the formula $ML_{k+1}$ (L is an alkali-metal atom and M is an electronegative atom of valency $k$). In $ML_{k+1}$, one more alkali metal atom will bring an extra valence electron for the electronic shell of M according to the octet rule. Consequently, such an $ML_{k+1}$ complex has a great tendency to lose the extra valence electron and thus possess strong reducibility (Sun and Wu, 2019).

Owing to their excellent reducing ability, superalkalis can be used to synthesize unusual charge-transfer salts (Zintl and Morawietz, 1938; Jansen, 1976) with the counterpart possessing relatively low electron affinity and activate stable $CO_2$ and $N_2$ molecules (Park and Meloni, 2017; Zhao et al., 2017; Park and Meloni, 2018; Sun et al., 2019; Sikorska and Gaston, 2020) to produce high-value products (Zhang et al., 2021a; Zhang et al., 2021b). In particular, as a special subset of superatom (Reveles et al., 2009; Luo and Castleman, 2014), superalkalis can behave as alkali metal atoms and

maintain their structural and electronic integrities when assembled into extended nanostructures (Reber et al., 2007). Hence, they offer an exciting prospect of serving as building blocks for nanomaterials with highly tunable properties (Jena and Sun 2018), such as supersalts (Giri et al., 2014), hydrogen storage materials (Merino et al., 2012), noble-gas-trapping agents (Pan et al., 2013), superbases (Srivastava and Misra, 2015), and nonlinear optical materials (Sun et al., 2014a; Sun et al., 2014b; Sun et al., 2016b; Sun et al., 2016c; Sun et al., 2018a).

In view of the great importance of superalkalis in chemistry, various superalkalis have been theoretically (Tong et al., 2009; Tong et al., 2011, Tong et al., 2012a,Tong et al., 2012b; Hou et al., 2013; Liu et al., 2014; Sun et al., 2013; Sun et al., 2016a; Giri et al., 2016; Zhao et al., 2017; Sun et al., 2018b; Sun et al., 2019; Park and Meloni, 2018; Sun and Wu, 2019; Tkachenko et al., 2019; Sikorska and Gaston, 2020) and experimentally (Lievens et al., 1999; Yokoyama et al., 2000, 2001; Hou and Wang, 2020) characterized in the past decades. To date, conventional mononuclear $ML_{k+1}$ superalkalis have been expanded to dinuclear (Tong et al., 2009; Tong et al., 2011) and polynuclear (Tong et al., 2012a; Tong et al., 2012b; Liu et al., 2014) superalkalis, aromatic superalkalis (Sun et al., 2013), Zintl-ion-based superalkalis (Giri et al., 2016; Sun et al., 2018b), hyperalkalis (Sun et al., 2016a), alkali-metal complexes (Tkachenko et al., 2019), and so on. More importantly, some alkali-metal-free superalkalis (Hou et al., 2014; Liu et al., 2016), particularly nonmetallic superalkalis (Hou et al., 2013; Srivastava, 2019a; Srivastava, 2019b), have been proposed in recent years. For example, Hou et al. (2013) designed a class of $M_2H_{2n+1}^+$ (M = F, O, N, C for $n$ = 1, 2, 3, 4, respectively) superalkali cations by using hydrogen atoms as ligands. Following a similar rule, the other two series of nonmetallic superalkali cations, namely, $F_nH_{n+1}^+$ ($n$ = 1–10) and $C_xH_{4x+1}^+$ ($x$ = 1–5), have been proposed by Srivastava (2019a, 2019b). These achievements demonstrate that the potential of designing superalkalis of new type is limitless and thereby motivate us to create more diverse superalkali species by using different rules and ligands to further enrich the superalkali family.

More recently, Tkachenko et al. (2019) reported the record low ionization potentials (1.70–1.52 eV) of alkali metal complexes with crown ethers and cryptands and defined them as superalkali species. In fact, such alkali metal complexes were previously named as electrides, a special kind of ionic solids with trapped electrons serving as anions (Dye, 2009). Hence, this work first built a bridge between superalkalis and electrides. However, it is known that crown ethers and cryptands are prone to be cleaved at the C-O bonds (Redko et al., 2002). Fortunately, analogous complexants, such as adamanzane (adz) (Redko et al., 2002) and aza-cage (aza222) (Kim et al., 1999) with only C-N linkages and no amine hydrogens are considerably stable to synthesize the crystalline salts, including alkalides (Kim et al., 1999; Redko et al., 2002) and electrides (Redko et al., 2005) at room temperature. Hence, it is highly expected that such complexants could also be used as excellent building blocks to design and synthesize new superalkalis.

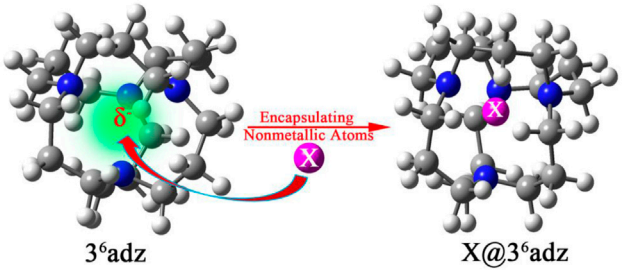


**FIGURE 1 |** The schematic design strategy of X@$3^6$adz (X = H, B, C, N, O, F, and Si) based on the cage-like $3^6$adz complexant.

To verify this hypothesis, the $3^6$adamanzane ($3^6$adz) has been chosen as a representative to design a series of X@$3^6$adz (X = H, B, C, N, O, F, and Si) by encapsulating nonmetallic atoms into the cavity of this cage-like complexant in this work (see **Figure 1**). The $3^6$adz complexant is composed of tricyclic tetra-amines with aliphatic chains (Springborg, 2003), which has been used to synthesize a stable alkalide $[H@3^6adz]^+Na^-$ (Redko et al., 2002). In this complexant, all the lone pairs of 4 N atoms direct toward the center of the cage (see **Supplementary Figure S1**). Under the repulsion of the lone pairs of N atoms, the outmost valence electrons of X are destabilized to different degrees, leading to the obvious rise of HOMO level of X@$3^6$adz as compared with the isolated $3^6$adz complexant. As a result, these proposed complexes exhibit extraordinarily low AIE values of 0.78–5.28 eV although X atoms possess very high ionization energies (IEs) of 8.15–17.42 eV (Lide, 2003). In particular, the B@$3^6$adz complex also has the potential to serve as new nonlinear optical (NLO) molecule with a remarkably large first hyperppolarizability of $1.35 \times 10^6$ au because the valence electron of boron atom is pushed out of cage to form diffuse excess electrons. We hope that this work will not only provide new nonmetallic members for the superatom family, but will also open the door to design strong reducing matters by embedding nonmetallic atoms into the various cage-like complexants.

## COMPUTATIONAL DETAILS

In this work, all the calculations were carried out by using the coulomb-attenuated hybrid exchange-correlation functional (CAM-B3LYP) (Tawada et al., 2004; Yanai et al., 2004), which has been reported to be capable of providing not only the molecular geometries close to the experimentally observed structures but also the (hyper)polarizabilities close to those of the coupled cluster calculations (Limacher et al., 2009). Hence, this method has been widely used to calculate the (hyper)polarizabilities of NLO molecules in the previous works (Sun et al., 2014a; Sun et al., 2014b, Sun et al., 2016c). Also, a method test has also been carried out by sampling B@$3^6$adz (see **Supplementary Table S1**) to verify the reliability of this method in calculating the properties of such systems.

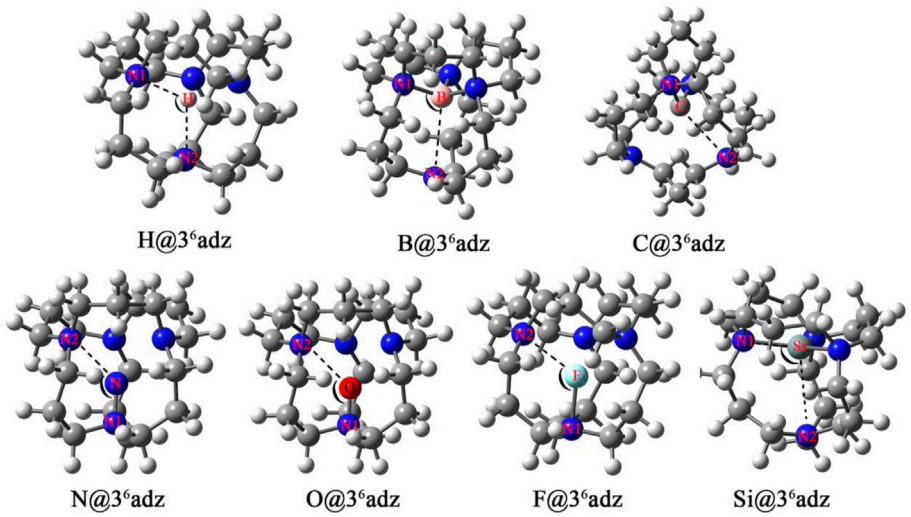


**FIGURE 2 |** Optimized geometric structures of X@$3^6$adz (X = H, B, C, N, O, F, and Si) compounds.

From **Supplementary Table S1**, it is found that CAM-B3LYP gives approximately equal VIE and $\beta_0$ to those obtained by several other functionals, which indicates that this method is reliable for these studied systems. Hence, all the optimized geometric structures of the studied species with real frequencies were obtained under the CAM-B3LYP/6-31+G(d) level. Based on the optimized structures, the single-point energies, nature population analysis (NPA) charges, and static electric properties were calculated at the CAM-B3LYP/6-311++G (d, p) level.

In this work, the vertical ionization energies (VIEs) of X@$3^6$adz (X = H, B, C, N, O, F, and Si) were calculated as the energy difference between the optimized neutral complex and the cation in the geometry of the neutral complex, while their adiabatic ionization energies (AIEs) are defined as the energy difference between the neutral and cationic complex at their respective optimized structures. In addition, the TD-M06-2X calculations were performed to obtain the transition energies and oscillator strengths of the crucial excited states as well as the difference of the dipole moments between the ground state and crucial excited state of X@$3^6$adz by using the 6-311++G (d, p) basis set. Herein, the dipole moments ($\mu_0$), polarizabilities ($\alpha_0$), and first hyperpolarizabilities ($\beta_0$) are defined as follows,

$$\mu_0 = \left(\mu_x^2 + \mu_y^2 + \mu_z^2\right)^{1/2} \quad (1)$$

$$\alpha_0 = \frac{1}{3}\left(\alpha_{xx} + \alpha_{yy} + \alpha_{zz}\right) \quad (2)$$

$$\beta_0 = \left(\beta_x^2 + \beta_y^2 + \beta_z^2\right)^{1/2} \quad (3)$$

where $\beta_i = \frac{1}{3}\sum(\beta_{ijj} + \beta_{jji} + \beta_{jij})$, $i, j = \{x, y, z\}$.

All the above calculations were performed by using the GAUSSIAN 16 program package (Frisch et al., 2016). The dimensional plots of the molecular structures were generated with the GaussView program (Dennington et al., 2016).

**TABLE 1 |** Symmetry point group, the lowest vibrational frequencies $\nu_1$ (in $cm^{-1}$), the bond lengths of X-N1 and X-N2 bonds ($d_{X\text{-}N1}$ and $d_{X\text{-}N2}$, in Å), ∠N1-X-N2 angle (in deg) of X@$3^6$adz (X = H, B, C, N, O, F, and Si) compounds.

| Species | Symmetry | $\nu_1$ | $d_{X\text{-}N1}$ | $d_{X\text{-}N2}$ | ∠N1-X-N2 |
|---|---|---|---|---|---|
| H@$3^6$adz | $S_4$ | 69 | 2.11 | 2.11 | 113.5 |
| B@$3^6$adz | $C_1$ | 91 | 1.66 | 3.02 | 105.9 |
| C@$3^6$adz | $C_2$ | 102 | 1.52 | 2.97 | 108.4 |
| N@$3^6$adz | $C_1$ | 48 | 1.41 | 2.58 | 120.3 |
| O@$3^6$adz | $C_1$ | 72 | 1.34 | 2.59 | 125.1 |
| F@$3^6$adz | $C_1$ | 61 | 1.87 | 2.41 | 123.7 |
| Si@$3^6$adz | $C_1$ | 76 | 2.06 | 3.22 | 102.0 |

## RESULTS AND DISCUSSION

Initially, seven X@$3^6$adz (X = H, B, C, N, O, F, and Si) compounds have been constructed by encapsulating one X atom into a $3^6$adz cage. After optimization, the geometric structures of X@$3^6$adz are illustrated in **Figure 2**, while the corresponding cations are plotted in **Supplementary Figure S2**. Moreover, selected structural parameters of these resulting X@$3^6$adz compounds are summarized in **Table 1**.

As shown in **Figure 1**, $3^6$adz is a cage-like complexant with $S_4$ symmetry. From **Figure 2**, it is observed that the geometric integrity of $3^6$adz cage is well-preserved in these X@$3^6$adz compounds. However, the geometric symmetries of these compounds are lowered to $C_1$ and $C_2$, except for H@$3^6$adz, which maintains the $S_4$ symmetry of $3^6$adz. To be specific, the encapsulated hydrogen atom located at the central position of $3^6$adz in H@$3^6$adz, yields the newly formed N-H bonds of 2.11 Å and ∠N1-H-N2 of 113.5°. As for B@$3^6$adz, the boron atom tends to bind with 3 N atoms of the complexant, forming 3 N-B bonds of 1.63 Å ~ 1.66 Å, while the distance between the uncombined N and B atoms is as long as 3.02 Å. The C@$3^6$adz complex possesses a $C_2$-symmetric structure, where the introduced

**TABLE 2 |** Adiabatic ionization energies (AIEs, in eV), vertical ionization energies (VIEs, in eV), HOMO and LUMO energy levels (in eV), and the HOMO–LUMO gaps of $3^6$adz and X@$3^6$adz (X = H, B, C, N, O, F, and Si) compounds.

| Species | AIE | VIE | HOMO | LUMO | Gap(eV) |
|---|---|---|---|---|---|
| $3^6$adz | 6.56 | 6.80 | −6.49 | −0.38 | 6.12 |
| H@$3^6$adz | 0.78 | 3.83 | −3.49 | 0.36 | 3.86 |
| B@$3^6$adz | 2.16 | 2.18 | −1.81 | −0.01 | 1.80 |
| C@$3^6$adz | 2.72 | 3.01 | −3.08 | 0.10 | 3.18 |
| N@$3^6$adz | 3.15 | 5.72 | −4.48 | 0.19 | 4.67 |
| O@$3^6$adz | 5.28 | 5.86 | −5.65 | 0.18 | 5.83 |
| F@$3^6$adz | 4.92 | 6.38 | −5.87 | −0.13 | 5.73 |
| Si@$3^6$adz | 1.79 | 2.73 | −2.61 | 0.26 | 2.87 |

carbon atom prefers to bind with 2 N atoms of $3^6$adz by forming two N-C bonds of 1.52 Å. Differently, the more electronegative N, O, and F atoms are linked to only 1 N atom of the cage complexant *via* N-N, N-O, and N-F bonds of 1.41, 1.34, and 1.87 Å, respectively, generating the very similar structures of X@$3^6$adz (X = N, O, and F). Similar to B@$3^6$adz, the introduced silicon atom tends to bind with 3 N atoms of complexant *via* 3 N-Si bonds of 2.06–2.35 Å in Si@$3^6$adz.

By turning to the cations of X@$3^6$adz, it is found that only the optimized structure of $[B@3^6adz]^+$ cation almost coincides with the geometry of the corresponding neutral one (see **Supplementary Figure S2**). For instance, the critical geometric parameters of $d_{B\text{-}N1}$, $d_{B\text{-}N2}$, and ∠N1-B-N2 are hardly changed after one electron is lost from B@$3^6$adz. However, for the rest of X@$3^6$adz (X = H, C, N, O, F, and Si), quite different geometries of cationic and neutral complexes were found. For instance, the $H^+$ is attached to 1 N atom of the complexant in the resulting $[H@3^6adz]^+$, while the doped N atom turns to combine with 2 N atoms of $3^6$adz in $[N@3^6adz]^+$ and Si atom almost moves to the center of the cage in $[Si@3^6adz]^+$. The geometry of C@$3^6$adz is distorted from $C_2$ symmetry to $C_1$ with the changes of 0.29 Å for the C-N2 bond and 7.3° for ∠N1-C-N2. As for $[F@3^6adz]^+$, the N-F bond is shortened from 1.87 Å to 1.38 Å because the introduced F atom further loses 0.333*e* (see **Supplementary Table S1**) and thus tends to bind more tightly with the N atom of the complexant. Also, as shown in **Table 2**, the difference in the geometry can also be reflected by the difference of 0.29–3.06 eV between the vertical ionization energies (VIEs) and adiabatic ionization energies (AIEs) of these X@$3^6$adz (X = H, C, N, O, F, and Si) species.

More interestingly, as shown in **Table 2**, extraordinarily low AIE values of 0.78–5.28 eV were found for all the studied X@$3^6$adz (X = H, B, C, N, O, F, and Si) complexes, although X atoms possess very high ionization energies (IEs) of 8.15–17.42 eV (Lide, 2003). Such low AIE values of X@$3^6$adz are not only lower than that of 6.56 eV for the $3^6$adz complexant but also significantly lower than that of 5.39 eV (Lide, 2003) for lithium atom. In particular, the AIE values of H@$3^6$adz (0.78 eV), B@$3^6$adz (2.16 eV), C@$3^6$adz (2.72 eV), N@$3^6$adz (3.15 eV), and Si@$3^6$adz (1.79 eV) are even lower than the IE of 3.89 eV (Lide, 2003) for Cs atoms. Hence, these compounds should be classified as novel nonmetallic superalkalis.

How to understand the low IE values of such X@$3^6$adz complexes? We can find some clues from the frontier molecular orbital analysis. From **Figure 3**, a clear inverse correlation between the VIE values and HOMO levels of these studied compounds can be observed, that is, the higher the HOMO level is, the lower the VIE is. This is reasonable considering the fact that the valence electrons on the higher HOMOs are easier to be ionized. To be specific, all the HOMO energies (−1.81 ~ −5.87 eV) of X@$3^6$adz are much higher than that of −6.49 eV for $3^6$adz, because of the repulsion between the lone pairs of N atoms and the outmost valence electrons of X, resulting in the lower VIEs (2.18–6.38 eV) than that (6.80 eV) of $3^6$adz. In particular, B@$3^6$adz exhibits the highest HOMO level of −1.81 eV, and thus possesses the lowest VIE of 2.18 eV among these X@$3^6$adz complexes. This is because that the valence electron of embedded boron atom is pushed out of the cage by the lone pairs of N atoms of the complexant, forming a electride-like molecule $[B^+@3^6adz](e^-)$ with obvious diffuse electrons in the HOMO of B@$3^6$adz (see **Supplementary Figure S3**). Thus, the existence of diffuse excess electrons in its high-lying HOMO level results in the high reducibility of this B@$3^6$adz complex.

Differently, as shown in **Supplementary Figure S3**, the valence electrons are accommodated into the HOMOs mainly composed of the 1*s* atomic orbital of embedded hydrogen atom in H@$3^6$adz, and the *np* orbitals of C and Si atoms in X@$3^6$adz (X = C and Si), which show obvious antibonding character with respect to the central atom-complexant interaction. Such antibonding HOMOs destabilize the neutral structures of X@$3^6$adz (X = H, C, and Si) and result in their low VIE values (Gutsev and Boldyrev, 1987; Tkachenko et al., 2019). Hence, these 3 species also have quite low VIE values of 2.73–3.83 eV. However, it should be mentioned that the VIEs of 5.72–6.38 eV for X@$3^6$adz (X = N, O, and F) are larger than that of 5.39 eV for Li atom, although their HOMOs also possess obvious

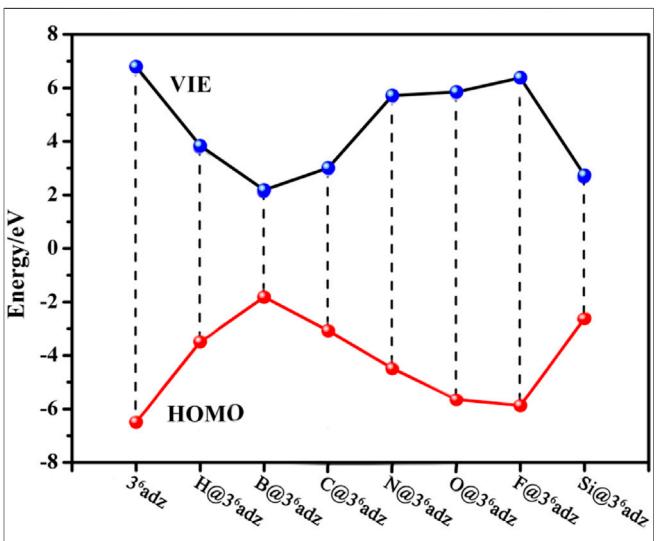


**FIGURE 3 |** The relationship between the VIE values and HOMO levels of X@$3^6$adz (X = H, B, C, N, O, F, and Si) compounds.

**TABLE 3 |** Calculated dipole moments ($\mu_0$, in au), polarizabilities ($\alpha_0$, in au), first hyperpolarizabilities ($\beta_0$, in au), transition energies ($\Delta E$, in eV), oscillator strength ($f_0$), and the difference in the dipole moments ($\Delta\mu$, in Debye) between the ground and crucial excited states of $3^6$adz and X@$3^6$adz (X = H, B, C, N, O, F, and Si) compounds.

| Species | $\mu_0$ | $\alpha_0$ | $\beta_0$ | $\Delta E$ | $f_0$ | $\Delta\mu$ |
|---|---|---|---|---|---|---|
| $3^6$adz | 0.000 | 240 | 0 | 5.64 | 0.100 | 1.113 |
| H@$3^6$adz | 0.000 | 253 | 0 | 5.03 | 0.044 | 0.001 |
| B@$3^6$adz | 3.326 | 1,599 | $1.35 \times 10^6$ | 0.40 | 0.121 | 6.428 |
| C@$3^6$adz | 2.074 | 278 | $4.05 \times 10^3$ | 2.25 | 0.064 | 2.854 |
| N@$3^6$adz | 1.471 | 257 | $2.84 \times 10^2$ | 4.67 | 0.033 | 0.495 |
| O@$3^6$adz | 1.558 | 249 | $6.84 \times 10^2$ | 5.40 | 0.059 | 1.801 |
| F@$3^6$adz | 1.142 | 255 | $2.43 \times 10^2$ | 3.52 | 0.093 | 0.544 |
| Si@$3^6$adz | 0.773 | 354 | $1.95 \times 10^4$ | 1.84 | 0.040 | 5.663 |

antibonding character. This is attributed to the larger elertonegativities of N, O, and F atoms than H, C, and Si atoms, which hinders the ionization of the valence electrons on their *np* orbitals in the HOMOs of X@$3^6$adz (X = N, O, and F).

On the other hand, the difference between the VIE and AIE values are also related to the different electron distribution in the HOMOs of X@$3^6$adz. To be specific, the geometric structure of B@$3^6$adz is hardly changed after its diffuse excess electron of HOMO is lost, resulting in its nearly equal VIE (2.18 eV) and AIE (2.16 eV) values. However, the destabilization of antibonding HOMOs for the neutral X@$3^6$adz (X = H, C, and Si) complexes drives the embedded X atom to lose nearly one valence electron ($0.667\,e \sim 0.867\,e$, as shown in **Supplementary Table S1**), forming relatively stable [X@$3^6$adz]$^+$ cations. After losing one electron, the formed $X^+$ ion changes its interaction mode with the cage complexant, which leads to the large structural distortion and considerable difference between the VIE and AIE values of X@$3^6$adz (X = H, C, and Si). Note that the AIE of H@$3^6$adz is as low as 0.78 eV because the formed [H@$3^6$adz]$^+$ is very stable and has been identified in various synthesized ionic compounds, such as [H@$3^6$adz]$^+X^-$ (X = Cl, Br, I, and Na) (Kim et al., 1994; Springborg et al., 1996; Redko et al., 2002).

Finally, considering the diffuse excess electron in the HOMO of B@$3^6$adz, it is highly expected that this superalkali also exhibits considerable nonlinear optical (NLO) response. Thus, the static electric properties of these studied X@$3^6$adz compounds and $3^6$adz complexant were calculated and listed in **Table 3**. It is observed that B@$3^6$adz has the largest dipole moment (3.326 au) and polarizability (1,599 au) among these X@$3^6$adz complexes because of the existence of diffuse electrons in the HOMO of this superalkali. In particular, the first hyperpolarizability ($\beta_0$) of B@$3^6$adz is as large as $1.35 \times 10^6$ au, which is significantly larger than those of the reported superalkalis and superalkali-based NLO materials, such as the aromatic organometallic superalkali $Au_3(Py)_3$ ($3.74 \times 10^4$ au) (Parida et al., 2018), superalkali-based alkalide $Li_3O^+$(calix [4] pyrrole)$M^-$ (M = Li, Na, and K) ($1.18 \times 10^4$–$3.33 \times 10^4$ au) (Sun et al., 2014a), and superalkali-based electride $Li_3O@Al_{12}N_{12}$ ($8.73 \times 10^5$ au) (Sun et al., 2016b), indicating that this proposed superalkali species can indeed be considered as a new kind of NLO molecule of high performance.

To understand the eminently large $\beta_0$ value of B@$3^6$adz, we focus our attention on the simple two-level model (Oudar, 1977; Oudar and Chemla, 1977),

$$\beta_0 \propto \frac{\Delta\mu \cdot f_0}{\Delta E^3} \tag{4}$$

where $\Delta E$, $f_0$, and $\Delta\mu$ are the transition energy, oscillator strength, and the difference in the dipole moment between the ground state and crucial excited state, respectively. According to this two-level expression, $\beta_0$ is proportional to $f_0$ and $\Delta\mu$, while is inversely proportional to the cube of $\Delta E$, and therefore, the transition energy is considered to be the decisive factor in the first hyperpolarizability (Sun et al., 2014a,b, 2016b,c). Hence, the $\Delta E$, $f_0$, and $\Delta\mu$ values of the crucial excited states with the largest oscillator strength of $3^6$adz and X@$3^6$adz are summarized in **Table 3**. It is noted that B@$3^6$adz possesses extremely smaller $\Delta E$ and much larger $f_0$ and $\Delta\mu$ values than those of other X@$3^6$adz (X = H, C, N, O, F, and Si) compounds, which rationalizes its largest $\beta_0$ value among these studied X@$3^6$adz species. In addition, the proposed C@$3^6$adz and Si@$3^6$adz superalkalis also show considerable $\beta_0$ values of $4.05 \times 10^3$ au and $1.95 \times 10^4$ au, respectively, because of their relatively smaller $\Delta E$ values and larger $\Delta\mu$ values.

## CONCLUSION

By using $3^6$adamanzane ($3^6$adz) as a complexant, a series of X@$3^6$adz (X = H, B, C, N, O, F, and Si) compounds were constructed and studied based on the density functional theory. It is interesting to find that the X@$3^6$adz (X = H, B, C, N, and Si) complexes possess lower AIE values than the IE of Cs atoms though the X atoms and $3^6$adz possess very high IE values. Thereby, they can be regarded as a new kind of nonmetallic superalkalis. In particular, different from other complexes, the low IE of B@$3^6$adz is derived from the diffuse excess electron formed by the repulsion between the valence electron of the embedded boron atom and lone pairs of N atoms of the complexant. Due to the existence of diffuse electrons, this superalkali also possesses a remarkably large $\beta_0$ of $1.35 \times 10^6$ au, which can serve as a new kind of NLO molecule. Hence, it is highly hoped that the theoretical design and characterization of these nonmetallic superalkali species could provide meaningful references to further design novel reducing matters or NLO materials by using such cage-like molecules as complexants.

## DATA AVAILABILITY STATEMENT

The original contributions presented in the study are included in the article/**Supplementary Material**, further inquiries can be directed to the corresponding author.

## AUTHOR CONTRIBUTIONS

All authors listed have made a substantial, direct and intellectual contribution to the work and approved it for publication.

## FUNDING

This work was supported by the Natural Science Foundation of Fujian Province (2021J01682) and the National Natural Science Foundation of China (21603032).

## ACKNOWLEDGMENTS

We thank the National Supercomputing Center in Shenzhen for providing computational resources.

## SUPPLEMENTARY MATERIAL

The Supplementary Material for this article can be found online at: https://www.frontiersin.org/articles/10.3389/fchem.2022.853160/full#supplementary-material

## REFERENCES


Dennington, R. D., Keith, T. A., and Millam, J. M. (2016). *GaussView, Version 6*. Shawnee Mission, KS: Semichem Inc.

D. R. Lide (Editor) (2003). *CRC Handbook of Chemistry and Physics* (Boca Raton, Florida: CRC Press).

Dye, J. L. (2009). Electrides: Early Examples of Quantum Confinementfinement. *Acc. Chem. Res.* 42, 1564–1572. doi:10.1021/ar9000857

Frisch, M. J., Trucks, G. W., Schlegel, H. B., Scuseria, G. E., Robb, M. A., Cheeseman, J. R., et al. (2016). *Gaussian 16, Revision A.03*. Wallingford CT, USA: Gaussian, Inc.

Giri, S., Behera, S., and Jena, P. (2014). Superalkalis and Superhalogens as Building Blocks of Supersalts. *J. Phys. Chem. A.* 118 (3), 638–645. doi:10.1021/jp4115095

Giri, S., Reddy, G. N., and Jena, P. (2016). Organo-Zintl Clusters [P7R4]: A New Class of Superalkalis. *J. Phys. Chem. Lett.* 7, 800–805. doi:10.1021/acs.jpclett.5b02892

Gutsev, G. L., and Boldyrev, A. I. (1982). DVM Xα Calculations on the Electronic Structure of "superalkali" Cations. *Chem. Phys. Lett.* 92, 262–266. doi:10.1016/0009-2614(82)80272-8

Gutsev, G. L., and Boldyrev, A. I. (1987). The Electronic Structure of Superhalogens and Superalkalies. *Russ. Chem. Rev.* 56 (6), 519–531. doi:10.1070/rc1987v056n06abeh003287

Hou, G.-L., and Wang, X.-B. (2020). Potassium Iodide Cluster Based Superhalogens and Superalkalis: Theoretical Calculations and Experimental Confirmation. *Chem. Phys. Lett.* 741, 137094. doi:10.1016/j.cplett.2020.137094

Hou, N., Li, Y., Wu, D., and Li, Z.-R. (2013). Do Nonmetallic Superalkali Cations Exist? *Chem. Phys. Lett.* 575, 32–35. doi:10.1016/j.cplett.2013.05.014

Hou, N., Wu, D., Li, Y., and Li, Z.-R. (2014). Lower the Electron Affinity by Halogenation: an Unusual Strategy to Design Superalkali Cations. *J. Am. Chem. Soc.* 136 (7), 2921–2927. doi:10.1021/ja411755t

Jansen, M. (1976). $Na^3NO_3$-kein Orthonitrit. *Angew. Chem. Int. Ed.* 88, 411. doi:10.1002/ange.19760881205

Jena, P., and Sun, Q. (2018). Super Atomic Clusters: Design Rules and Potential for Building Blocks of Materials. *Chem. Rev.* 118 (11), 5755–5870. doi:10.1021/acs.chemrev.7b00524

Kim, J., Ichimura, A. S., Huang, R. H., Redko, M., Phillips, R. C., and Jackson, J. E. (1999). Crystalline Salts of Na and K (Alkalides) that Are Stable at Room Temperature. *J. Am. Chem. Soc.* 121, 10666–10667. doi:10.1021/ja992667v

Kim, R. D. H., Wilson, M., and Haseltine, H. (1994). Simple Preparations of Tricyclic Orthoamides and Macrocyclic Triamines. *Synth. Commun.* 24 (21), 3109–3114. doi:10.1080/00397919408011324

Lievens, P., Thoen, P., Bouckaert, S., Bouwen, W., Vanhoutte, F., Weidele, H., et al. (1999). Ionization Potentials of $Li_nO$ ($2 \le n \le 70$) Clusters: Experiment and Theory. *J. Chem. Phys.* 110 (21), 10316. doi:10.1063/1.478965

Limacher, P. A., Mikkelsen, K. V., and Lüthi, H. P. (2009). On the Accurate Calculation of Polarizabilities and Second Hyperpolarizabilities of Polyacetylene Oligomer Chains Using the CAM-B3lyp Density Functional. *J. Chem. Phys.* 130 (19), 194114. doi:10.1063/1.3139023

Liu, J. Y., Wu, D., Sun, W. M., Li, Y., and Li, Z. R. (2014). Trivalent Acid Radical-Centered $YLi_4^+$ (Y = $PO_4$, $AsO_4$, $VO_4$) Cations: New Polynuclear Species Designed to Enrich the Superalkali Family. *Dalton Trans.* 43 (48), 18066–18073. doi:10.1039/c4dt02347a

Liu, J. Y., Xi, Y. J., Li, Y., Li, S. Y., Wu, D., and Li, Z. R. (2016). Does Alkaline-Earth-Metal-Based Superalkali Exist? *J. Phys. Chem. A.* 120 (51), 10281–10288. doi:10.1021/acs.jpca.6b10555

Luo, Z., and Castleman, A. W. (2014). Special and General Superatoms. *Acc. Chem. Res.* 47 (10), 2931–2940. doi:10.1021/ar5001583

Merino, G., Chattaraj, P. M., and Pan, S. (2012). Hydrogen Trapping Potential of Some Li-Doped Star-like Clusters and Super-alkali Systems. *Phys. Chem. Chem. Phys.* 14, 10345–10350. doi:10.1039/c2cp40794a

Oudar, J. L., and Chemla, D. S. (1977). Hyperpolarizabilities of the Nitroanilines and Their Relations to the Excited State Dipole Moment. *J. Chem. Phys.* 66 (6), 2664. doi:10.1063/1.434213

Oudar, J. L. (1977). Optical Nonlinearities of Conjugated Molecules. Stilbene Derivatives and Highly Polar Aromatic Compounds. *J. Chem. Phys.* 67 (2), 446. doi:10.1063/1.434888

Pan, S., Contreras, M., Romero, J., Reyes, A., Chattaraj, P. K., and Merino, G. (2013). $C_5Li_7^+$ and $O_2Li_5^+$ as Noble-Gas-Trapping Agents. *Chem. Eur. J.* 19 (7), 2322–2329. doi:10.1002/chem.201203245

Parida, R., Reddy, G. N., Ganguly, A., Roymahapatra, G., Chakraborty, A., and Giri, S. (2018). On the Making of Aromatic Organometallic Superalkali Complexes. *Chem. Commun.* 54 (31), 3903–3906. doi:10.1039/c8cc01170b

Park, H., and Meloni, G. (2018). Activation of Dinitrogen with a Superalkali Species, $Li_3F_2$. *ChemPhysChem* 19 (3), 256–260. doi:10.1002/cphc.201701232

Park, H., and Meloni, G. (2017). Reduction of Carbon Dioxide with a Superalkali. *Dalton Trans.* 46 (35), 11942–11949. doi:10.1039/c7dt02331f

Reber, A. C., Khanna, S. N., and Castleman, A. W. (2007). Superatom Compounds, Clusters, and Assemblies: Ultra Alkali Motifs and Architectures. *J. Am. Chem. Soc.* 129, 10189–10194. doi:10.1021/ja071647n

Redko, M. Y., Jackson, J. E., Huang, R. H., and Dye, J. L. (2005). Design and Synthesis of a Thermally Stable Organic Electride. *J. Am. Chem. Soc.* 127, 12416–12422. doi:10.1021/ja053216f

Redko, M. Y., Vlassa, M., Jackson, J. E., Misiolek, A. W., Huang, R. H., and Dye, J. L. (2002). Inverse Sodium Hydride": A Crystalline Salt that Contains H and Na-. *J. Am. Chem. Soc.* 124, 5928–5929. doi:10.1021/ja025655+

Reveles, J. U., Clayborne, P. A., Reber, A. C., Khanna, S. N., Pradhan, K., Sen, P., et al. (2009). Designer Magnetic Superatoms. *Nat. Chem.* 1 (4), 310–315. doi:10.1038/nchem.249

Sikorska, C., and Gaston, N. (2020). $N_4Mg_6M$ (M = Li, Na, K) Superalkalis for $CO_2$ Activation. *J. Chem. Phys.* 153, 144301. doi:10.1063/5.0025545

Springborg, J. (2003). Adamanzanes–Bi- and Tricyclic Tetraamines and Their Coordination Compounds. *Dalton Trans.* (9), 1653–1665. doi:10.1039/b300510k

Springborg, J., Pretzmann, U., and Olsen, C. E. (1996). An Inert Proton Coordinated inside the Tetrahedral Cage [$3^6$]Adamanzane. Synthesis of the inside Monoprotonated Amine 1,5,9,13-Tetraazatricyclo[7.7.3.$3^{5,13}$] docosane. *Acta Chem. Scand. A.* 50, 294–298. doi:10.3891/acta.chem.scand.50-0294

Srivastava, A. K. (2019a). Ab Initio investigations on Non-metallic Chain-Shaped $F_nH_{n+1}^+$ Series of Superalkali Cations. *Chem. Phys. Lett.* 721, 7–11. doi:10.1016/j.cplett.2019.02.021

Srivastava, A. K. (2019b). $C_xH_{4x+1}^+$ ($X$ = 1–5): a Unique Series of Organic Superalkali Cations. *Mol. Phys.*, 1–7.

Srivastava, A. K., and Misra, N. (2015). Superalkali-hydroxides as Strong Bases and Superbases. *New J. Chem.* 39 (9), 6787–6790. doi:10.1039/c5nj01259g

Sun, W.-M., Li, C.-Y., Kang, J., Wu, D., Li, Y., Ni, B.-L., et al. (2018a). Superatom Compounds under Oriented External Electric Fields: Simultaneously Enhanced Bond Energies and Nonlinear Optical Responses. *J. Phys. Chem. C* 122 (14), 7867–7876. doi:10.1021/acs.jpcc.8b01896

Sun, W.-M., Li, X.-H., Li, Y., Liu, J.-Y., Wu, D., Li, C.-Y., et al. (2016a). On the Feasibility of Designing Hyperalkali Cations Using Superalkali Clusters as Ligands. *J. Chem. Phys.* 145 (19), 194303. doi:10.1063/1.4967461

Sun, W.-M., Li, X.-H., Wu, D., Li, Y., He, H.-M., Li, Z.-R., et al. (2016b). A Theoretical Study on Superalkali-Doped Nanocages: Unique Inorganic Electrides with High Stability, Deep-Ultraviolet Transparency, and Considerable Nonlinear Optical Response. *Dalton Trans.* 45 (17), 7500–7509. doi:10.1039/c6dt00342g

Sun, W.-M., Li, Y., Wu, D., and Li, Z.-R. (2013). Designing Aromatic Superatoms. *J. Phys. Chem. C* 117 (46), 24618–24624. doi:10.1021/jp408810e

Sun, W.-M., Wu, D., Kang, J., Li, C.-Y., Chen, J.-H., Li, Y., et al. (2018b). Decorating Zintl Polyanions with Alkali Metal Cations: A Novel Strategy to Design Superatom Cations with Low Electron Affinity. *J. Alloys Compd.* 740 (5), 400–405. doi:10.1016/j.jallcom.2017.12.075

Sun, W.-M., Zhang, X.-L., Pan, K.-Y., Chen, J.-H., Wu, D., Li, C.-Y., et al. (2019). On the Possibility of Using the Jellium Model as a Guide to Design Bimetallic Superalkali Cations. *Chem. Eur. J.* 25 (17), 4358–4366. doi:10.1002/chem.201806194

Sun, W. M., Fan, L. T., Li, Y., Liu, J. Y., Wu, D., and Li, Z. R. (2014a). On the Potential Application of Superalkali Clusters in Designing Novel Alkalides with Large Nonlinear Optical Properties. *Inorg. Chem.* 53 (12), 6170–6178. doi:10.1021/ic500655s

Sun, W. M., Li, Y., Li, X. H., Wu, D., He, H. M., Li, C. Y., et al. (2016c). Stability and Nonlinear Optical Response of Alkalides that Contain a Completely Encapsulated Superalkali Cluster. *Chemphyschem* 17 (17), 2672–2678. doi:10.1002/cphc.201600389

Sun, W. M., Wu, D., Li, Y., and Li, Z. R. (2014b). Theoretical Study on Superalkali ($Li_3$) in Ammonia: Novel Alkalides with Considerably Large First Hyperpolarizabilities. *Dalton Trans.* 43 (2), 486–494. doi:10.1039/c3dt51559a

Sun, W. M., and Wu, D. (2019). Recent Progress on the Design, Characterization, and Application of Superalkalis. *Chem. Eur. J.* 25 (41), 9568–9579. doi:10.1002/chem.201901460

Tawada, Y., Tsuneda, T., Yanagisawa, S., Yanai, T., and Hirao, K. (2004). A Long-Range-Corrected Time-dependent Density Functional Theory. *J. Chem. Phys.* 120, 8425–8433. doi:10.1063/1.1688752

Tkachenko, N. V., Sun, Z. M., and Boldyrev, A. I. (2019). Record Low Ionization Potentials of Alkali Metal Complexes with Crown Ethers and Cryptands. *Chemphyschem* 20 (16), 2060–2062. doi:10.1002/cphc.201900422

Tong, J., Li, Y., Wu, D., Li, Z.-R., and Huang, X.-R. (2011). Ab Initio Investigation on a New Class of Binuclear Superalkali Cations $M_2Li_{2k+1}^+$ ($F_2Li_3^+$, $O_2Li_5^+$, $N_2Li_7^+$, and $C_2Li_9^+$). *J. Phys. Chem. A.* 115 (10), 2041–2046. doi:10.1021/jp110417z

Tong, J., Li, Y., Wu, D., Li, Z. R., and Huang, X. R. (2009). Low Ionization Potentials of Binuclear Superalkali $B_2Li_{11}$. *J. Chem. Phys.* 131 (16), 164307. doi:10.1063/1.3254835

Tong, J., Li, Y., Wu, D., and Wu, Z.-J. (2012a). Theoretical Study on Polynuclear Superalkali Cations with Various Functional Groups as the Central Core. *Inorg. Chem.* 51 (11), 6081–6088. doi:10.1021/ic202675j

Tong, J., Wu, Z., Li, Y., and Wu, D. (2012b). Prediction and Characterization of Novel Polynuclear Superalkali Cations. *Dalton Trans.* 42, 577–584. doi:10.1039/c2dt31429k

Yanai, T., Tew, D. P., and Handy, N. C. (2004). A New Hybrid Exchange–Correlation Functional Using the Coulomb-Attenuating Method (CAM-B3lyp). *Chem. Phys. Lett.* 393 (1-3), 51–57. doi:10.1016/j.cplett.2004.06.011

Yokoyama, K., Haketa, N., Tanaka, H., Furukawa, K., and Kudo, H. (2000). Ionization Energies of Hyperlithiated $Li_2F$ Molecule and $Li_nF_{n-1}$ ($N$= 3, 4) Clusters. *Chem. Phys. Lett.* 330, 339–346. doi:10.1016/s0009-2614(00)01109-x

Yokoyama, K., Tanaka, H., and Kudo, H. (2001). Structure of Hyperlithiated $Li_3O$ and Evidence for Electronomers. *J. Phys. Chem. A.* 105, 4312–4315. doi:10.1021/jp0037450

Zhang, X.-L., Ye, Y.-L., Zhang, L., Li, X.-H., Yu, D., Chen, J.-H., et al. (2021a). Designing an Alkali-metal-like Superatom $Ca_3B$ for Ambient Nitrogen Reduction to Ammonia. *Phys. Chem. Chem. Phys.* 23 (34), 18908–18915. doi:10.1039/d1cp01533h

Zhang, X.-L., Zhang, L., Ye, Y.-L., Li, X.-H., Ni, B.-L., Li, Y., et al. (2021b). On the Role of Alkali-metal-like Superatom $Al_{12}P$ in Reduction and Conversion of Carbon Dioxide. *Chem. Eur. J.* 27 (3), 1039–1045. doi:10.1002/chem.202003733

Zhao, T., Wang, Q., and Jena, P. (2017). Rational Design of Super-alkalis and Their Role in $CO_2$ Activation. *Nanoscale* 9 (15), 4891–4897. doi:10.1039/c7nr00227k

Zintl, E., and Morawietz, W. (1938). Orthosalze von Sauerstoffsäuren. *Z. Anorg. Allg. Chem.* 236, 372–410. doi:10.1002/zaac.19382360134

**Conflict of Interest:** The authors declare that the research was conducted in the absence of any commercial or financial relationships that could be construed as a potential conflict of interest.

**Publisher's Note:** All claims expressed in this article are solely those of the authors and do not necessarily represent those of their affiliated organizations, or those of the publisher, the editors, and the reviewers. Any product that may be evaluated in this article, or claim that may be made by its manufacturer, is not guaranteed or endorsed by the publisher.

frontiers in Chemistry

ORIGINAL RESEARCH
published: 29 March 2022
doi: 10.3389/fchem.2022.870985

# Computational Exploration on the Structural and Optical Properties of Gold-Doped Alkaline-Earth Magnesium $AuMg_n$ ($n$ = 2–12) Nanoclusters: DFT Study

*Ben-Chao Zhu*, Ping-Ji Deng, Jia Guo and Wen-Bin Kang**

*School of Public Health, Hubei University of Medicine, Shiyan, China*

Using CALYPSO crystal search software, the structural growth mechanism, relative stability, charge transfer, chemical bonding and optical properties of $AuMg_n$ ($n$ = 2–12) nanoclusters were extensively investigated based on DFT. The shape development uncovers two interesting properties of $AuMg_n$ nanoclusters contrasted with other doped Mg-based clusters, in particular, the planar design of $AuMg_3$ and the highly symmetrical cage-like of $AuMg_9$. The relative stability study shows that $AuMg_{10}$ has the robust local stability, followed by $AuMg_9$. In all nanoclusters, the charge is transferred from the Mg atoms to the Au atoms. Chemical bonding properties were confirmed by ELF analysis that Mg-Mg formed covalent bonds in nanoclusters larger than $AuMg_3$. Static polarizability and hyperpolarizability calculations strongly suggest that $AuMg_9$ nanocluster possesses interesting nonlinear optical properties. Boltzmann distribution weighted average IR and Raman spectroscopy studies at room temperature verify that these nanoclusters are identifiable by spectroscopic experiments. Finally, the average bond distance and average nearest neighbor distance were fully investigated.

**Keywords: calypso, DFT, AuMgn nanoclusters, optical properties, structural property**

OPEN ACCESS

***Edited by:***
*Ambrish Kumar Srivastava, Deen Dayal Upadhyay Gorakhpur University, India*

***Reviewed by:***
*Ruby Srivastava, Centre for Cellular and Molecular Biology (CCMB), India*
*Shamoon Ahmad Siddiqui, Najran University, Saudi Arabia*

****Correspondence:***
*Ben-Chao Zhu*
*benchao_zhu@126.com*
*Wen-Bin Kang*
*wbkang@hbmu.edu.cn*

***Specialty section:***
*This article was submitted to Physical Chemistry and Chemical Physics, a section of the journal Frontiers in Chemistry*

***Received:*** *07 February 2022*
***Accepted:*** *04 March 2022*
***Published:*** *29 March 2022*

***Citation:***
*Zhu B-C, Deng P-J, Guo J and Kang W-B (2022) Computational Exploration on the Structural and Optical Properties of Gold-Doped Alkaline-Earth Magnesium $AuMg_n$ (n = 2–12) Nanoclusters: DFT Study. Front. Chem. 10:870985. doi: 10.3389/fchem.2022.870985*

## INTRODUCTION

Metal nanoclusters have attracted increasing interest from academics in recent years due to their appealing micro patterns and interesting features (Jin et al., 2016; Peng et al., 2018; Tew et al., 2018). For example, $Au_n$ clusters tend to exhibit 2-dimensional structures at small sizes, while medium sizes ($n$ < 15) will transition to 3-dimension (Idrobo et al., 2007; Assadollahzadeh and Schwerdtfeger, 2009; Huang and Wang, 2009). For larger size, the study of $Au_{144}$ cluster is highly worth explaining. It was first reported in 1997 as a critical size for the transformation of Au nanoclusters into nanocrystals and worthy of being researched, but its structure could not be determined at that time (Alvarez et al., 1997), then in 2009 it was precisely predicted by theoretical studies to have a multishell structure (Qian and Jin, 2009), and finally, in 2018 it was experimentally confirmed to have a three-layer metallic core of $Au_{12}$-$Au_{42}$-$Au_{60}$ from the inside out (Yan et al., 2018). Researchers have been so persistent in studying them because the physical size of these clusters is comparable to the electron Fermi wavelength and therefore tends to show interesting electronic (Yau et al., 2013), optical properties (Ramakrishna et al., 2008; Jin, 2015) and have important application prospects in the field of medicine and biology (Shang et al., 2011). Because the physical and chemical characteristics of

nanoclusters alter with size throughout the transition to nanocrystals or nanoparticles, nanocluster research will anticipate, at least theoretically, a slew of new materials for the field of nanomaterials science.

A lot of studies on alkaline Earth metal magnesium clusters have been reported, in addition to usual studies of metal nanoclusters like gold, silver, and copper (Köhn et al., 2001; Xia et al., 2016; Zhang et al., 2020; Zhao et al., 2021). This is partly because magnesium-based nanomaterials have an exceptional hydrogen storage capacity compared to ordinary materials (Shao et al., 2012), and therefore, various kinds of Mg-based nanocluster materials, such as $CoMg_n$ (Trivedi and Bandyopadhyay, 2015), $RhMg_n$ (Trivedi and Bandyopadhyay, 2016), ScMg nanocluster (Chen et al., 2020; Lyon, 2021), are worthy of systematic study. Most of these studies were carried out theoretically and gave interesting results by predicting the hydrogen storage properties of nanocluster materials based on Mg. For example, it is shown that $MgScH_{13}$ and $MgScH_{15}$ nanoclusters have, theoretically, ultra-high hydrogen storage capacities of 15.9 wt% (Lyon, 2021) and 17.8 wt% (Chen et al., 2020), respectively. On the other hand, the optical properties of Mg and Mg-based nanoclusters are also very attractive (Belyaev et al., 2016; Shinde, 2016; Shinde and Shukla, 2017). The IR spectra of $Mg_n$ ($n$ = 2–31) nanoclusters were studied using DFT, and the results showed that their most intense peaks were distributed in the low-frequency band of 40–270 $cm^{-1}$ (Belyaev et al., 2016). The linear absorption spectroscopy studies of very small size $Mg_n$ ($n$ = 2–5) nanoclusters confirm that their low-lying structures, although small, can be experimentally distinguished, while the optical excitation spectra are confirmed to be of plasmonic collective type (Shinde, 2016).

In short, nanocluster materials, like Au and Mg, are a field of materials science full of unknown "surprises" where many interesting optical and electronic excitation properties can be "discovered". However, surprisingly, the study of gold-doped Mg nanoclusters has not been reported so far. This work aims to perform a systematic theoretical computational study of the structural and optical properties of gold-doped small-size magnesium nanoclusters. Specifically, the geometric growth mechanism, relative stability, charge transfer properties, chemical bonding properties, nonlinear optical properties, and theoretical calculations of infrared and Raman-weighted average spectra of $AuMg_n$ ($n$ = 2–12) nanoclusters will be investigated. These studies will not only enrich the research data on $AuMg_n$ nanoclusters, but also provide the opportunity to gain insight into potential nanomaterials with interesting optical properties.

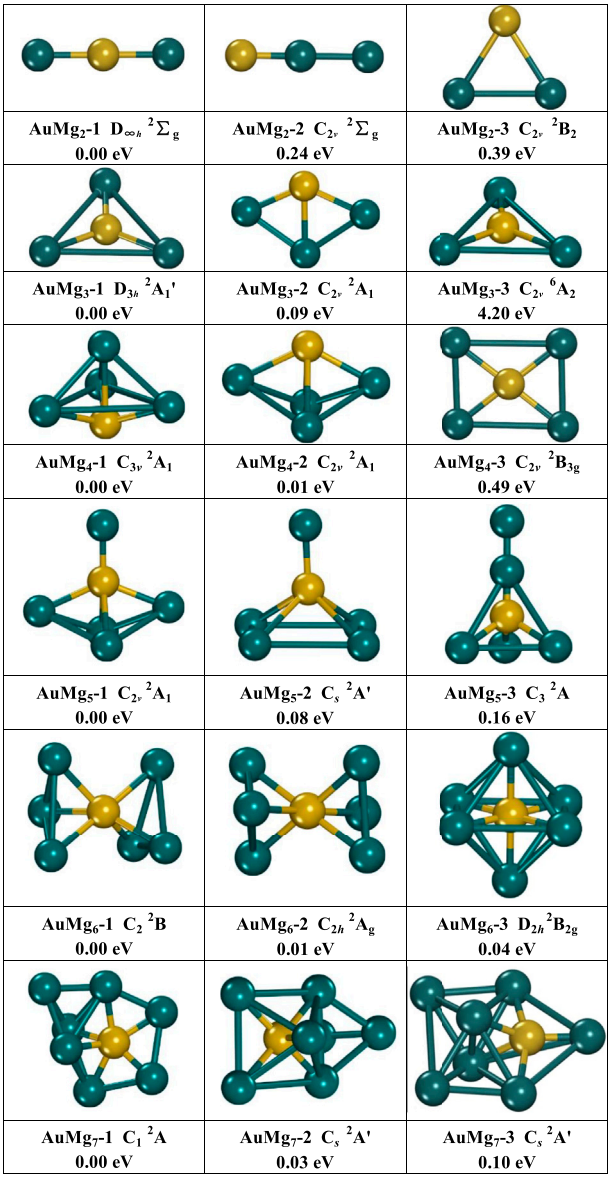


**FIGURE 1 |** The geometry of the three lowest energy isomers of $AuMg_n$ ($n$ = 2–7) nanoclusters, energy difference in eV from the lowest energy isomer at the same size.

## COMPUTATIONAL METHOD DETAILS

CALYPSO software (Wang et al., 2010, 2012) was utilized to search the initial geometries of $AuMg_n$ ($n$ = 2–12) nanoclusters. CALYPSO can perform predictions of the energetically low-lying isomers structures at given chemical compositions and pressure for nanoclusters (Lv et al., 2012; Zhao et al., 2019; Lu et al., 2020) in gas-phase and crystals (Lu and Chen, 2020a, 2020b, 2021; Sun et al., 2020; Chen et al., 2021) *via* particle swarm optimization (PSO) algorithm. To search for as many low-lying energy isomers of $AuMg_n$ ($n$ = 2–12) nanoclusters as possible, the following strategy will be employed. First, each size of AuMgn nanocluster will be searched for 50 generations, where each generation contains 20 structures. Further, 80% of these 1,000 heterogeneous structures are generated by the PSO algorithm for the initial structure, and the rest are generated randomly. These structures are then interfaced *via* CALYPSO to Gaussian 09 software (Frisch et al., 2016) for low-level HF energy calculations, and finally ranked by energy level. It is necessary to explain that many of the 1,000 isomers obtained have the same or extremely close energies, and their geometrical structures do

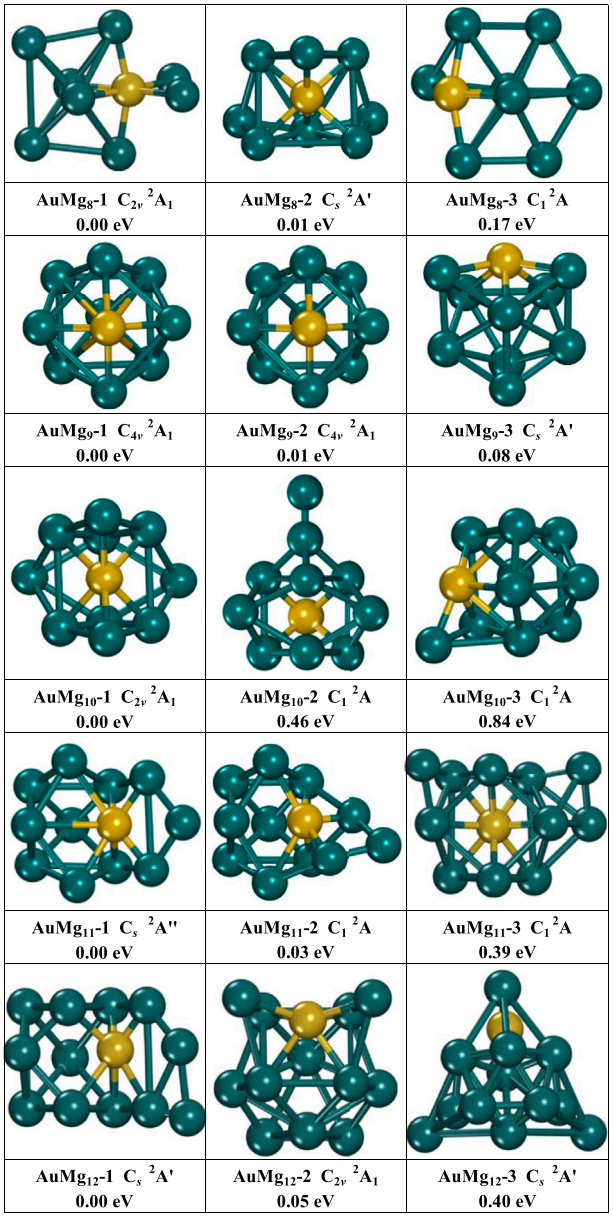


**FIGURE 2 |** The geometry of the three lowest energy isomers of $AuMg_n$ ($n$ = 8–12) nanoclusters, energy difference in eV from the lowest energy isomer at the same size.

not differ much and therefore need to be removed. Finally, isomers with significantly different energies and structures were again subjected to high-level DFT for structural optimization and frequency calculations by Gaussian 09 software. The structure optimization calculation employs the classical B3LYP functional, where the mixed basis set is considered due to the presence of Au atom. Concretely, 6–311 g (d) is applied to Mg atoms, while the pseudopotential basis set lanl2dz is used for Au atoms. The adoption of such functional and basis set is based on the following two aspects, firstly, the existing studies have shown that $Mg_n$ nanoclusters do not have any metallic properties at the size of $n < 20$ (Köhn et al., 2001; Jellinek and Acioli, 2003; Xia et al., 2016), and secondly, all-electron basis set and lanl2dz basis set have been proved to be reliable for Mg and Au nanoclusters by numerous studies (Xia et al., 2016; Zeng et al., 2020; Zhu et al., 2021). To ensure a more comprehensive structural optimization, each isomer was calculated under 2, 4, 6, and 8 spin multiplicities, respectively. In addition, to verify that the isomer is not a transition or excited state, imaginary frequencies must be excluded from any result. Once the imaginary frequency appears in the calculation result, they need to be optimized again until all frequencies are positive.

Charge transfer property of the lowest energy $AuMg_n$ ($n$ = 2–12) nanoclusters was analyzed by natural bond orbital (NBO) calculation (Reed et al., 1988). Chemical bonding properties were computed through the electron localization function (ELF) (Becke and Edgecombe, 1990). The nonlinear optical properties of the ground state $AuMg_n$ nanoclusters were investigated at the aug-cc-pVTZ level. Infrared and Raman spectra are the results of vibration frequency calculations. In particular, Multiwfn software (Lu and Chen, 2012) is a powerful tool to draw 2D map of ELF, spherical plots of static and super-static polarizabilities, Boltzmann distribution probabilities of different isomers and weighted average IR and Raman spectral data.

# RESULTS

## The Geometrical Growth Mechanism of $AuMg_n$ Nanoclusters

The growth mechanism of nanoclusters can be studied by their geometric structures. Three low-lying energy isomers of each size $AuMg_n$ ($n$ = 2–12) nanoclusters are presented in **Figure 1** and **Figure 2**. Under each structure, the "i" in $AuMg_n$-i is their energy order, with "1" indicating the lowest and "2" the second-lowest ones. The energy difference (eV) between the AuMgn-i and $AuMg_n$-1 at each size can also be found. In addition to the symmetry, and the electronic structure information is also shown in **Figures 1**, **2**. All information about the lowest energy state of $AuMg_n$ ($n$ = 2–12) nanoclusters is summarized in **Table 1**, where the results of the frequency calculations show the lowest and highest vibrational frequencies satisfying the requirements that the results of the frequency calculations cannot contain any imaginary frequency. As can be seen from **Figure 1**, isomers $AuMg_2$-1 ($D_{\infty h}$ symmetry with $^2\Sigma_g$ electronic state) and $AuMg_2$-2 ($C_{2v}$ symmetry with $^2\Sigma_g$ electronic state) have a similar linear structure, the difference being that the Au atom is in the center of the former and on the side of the latter. Isomers $AuMg_2$-3 ($C_{2v}$ symmetry with $^2B_2$ electronic state) show a 2D planar isosceles triangle structure. Relative to the lowest energy state $AuMg_2$-1 isomer energy, $AuMg_2$-2 and $AuMg_2$-3 isomers have 0.24 and 0.39 eV higher energy than it, respectively. The isomer $AuMg_3$-1 ($D_{3h}$ symmetry with $^2A'_1$ electronic state) has an equilateral triangular geometry, while the isomer $AuMg_3$-3 ($C_{2v}$ symmetry with $^6A_2$ electronic state) has an isosceles triangular structure, and interestingly the Au atoms are located at the center of their triangular structures, respectively. The structure of the isomer

**TABLE 1 |** State, symmetry, Eb, $\Delta_2$E, Egap for α- and β-electrons, frequency and NCP on Au atom in the ground state of $AuMg_n$ (*n* = 2–12) nanoclusters.

| Clusters | State | Symmetry | $E_b$(eV) | $\Delta_2$E(eV) | $E_{gap}\alpha$(eV) | $E_{gap}\beta$(eV) | Frequency ($cm^{-1}$) | | NCP on Au (e) |
|---|---|---|---|---|---|---|---|---|---|
| | | | | | | | Highest | Lowest | |
| $AuMg_2$ | $D_{\infty h}$ | $^2\sum_g$ | 1.72 | — | 2.76 | 2.53 | 220 | 14 | –0.74 |
| $AuMg_3$ | $D_{3h}$ | $^2A_1'$ | 1.78 | –0.15 | 2.28 | 2.22 | 197 | 25 | –1.35 |
| $AuMg_4$ | $C_{3v}$ | $^2A_1$ | 1.84 | 0.29 | 2.19 | 2.15 | 212 | 23 | –1.68 |
| $AuMg_5$ | $C_{2v}$ | $^2A_1$ | 1.83 | –0.03 | 2.28 | 1.29 | 232 | 13 | –2.17 |
| $AuMg_6$ | $C_2$ | $^2B$ | 1.83 | –0.04 | 2.21 | 1.14 | 225 | 9 | –2.99 |
| $AuMg_7$ | $C_1$ | $^2A$ | 1.84 | –0.05 | 1.74 | 1.65 | 207 | 10 | –2.44 |
| $AuMg_8$ | $C_{2v}$ | $^2A_1$ | 1.85 | –0.32 | 1.55 | 1.58 | 203 | 20 | –3.05 |
| $AuMg_9$ | $C_{4v}$ | $^2A_1$ | 1.89 | 0.24 | 1.63 | 1.75 | 236 | 53 | –1.00 |
| $AuMg_{10}$ | $C_{2v}$ | $^2A_1$ | 1.90 | 0.28 | 1.14 | 1.85 | 224 | 21 | –2.49 |
| $AuMg_{11}$ | $C_s$ | $^2A''$ | 1.89 | –0.12 | 1.70 | 1.39 | 232 | 27 | –2.39 |
| $AuMg_{12}$ | $C_s$ | $^2A'$ | 1.88 | — | 1.15 | 1.88 | 243 | 13 | –2.47 |

$AuMg_3$-2 ($C_{2v}$ symmetry with $^2A_1$ electronic state) is a planar combination of Au-Mg-Mg isosceles triangle and Mg-Mg-Mg isosceles triangle. Calculations show nanoclusters of 2 Mg atoms doped with one Au atom, where the second and third lowest isomers are 0.03 and 4.20 eV higher than the lowest energy isomer, respectively. The structures of the isomers $AuMg_4$-1 ($C_{3v}$ symmetry with $^2A_1$ electronic state) and $AuMg_4$-2 ($C_{2v}$ symmetry with $^2A_1$ electronic state) can be considered as formed based on the tetrahedral (pyramid-like) structure of Au-Mg-Mg-Mg adsorbing an Mg atom in different directions. The isomer $AuMg_4$-3 ($C_{2v}$ symmetry with $^2B_{3g}$ electronic state) shows a rectangular structure in which the 4 Mg atoms are at the vertices while Au atom is at the geometric center. For the isomer $AuMg_4$-1, $AuMg_4$-2 and $AuMg_4$-3 are higher in energy by 0.01 and 0.49 eV, respectively. The structure of the isomer $AuMg_5$-1 ($C_{2v}$ symmetry with $^2A_1$ electronic state) is based on the formation of $AuMg_4$-2 by adsorbing an Mg atom on its top. The isomers $AuMg_4$-3 and $AuMg_4$-1 form the isomers $AuMg_5$-2 ($C_s$ symmetry with $^2A'$ electronic state) and $AuMg_5$-3 ($C_3$ symmetry with $^2A$ electronic state) after pulling up the Au atom into the interior of the polyhedral while adsorbing an Mg atom on their tops. The second- and third-lowest energy isomers of the $AuMg_5$ nanocluster are 0.08 and 0.16 eV higher than that of the lowest-energy isomer. The isomers $AuMg_6$-1 ($C_2$ symmetry with $^2B$ electronic state) and $AuMg_6$-2 ($C_{2h}$ symmetry with $^2A_g$ electronic state) have extremely close energies and structures, which exhibit rotational symmetry with Au atom. The isomer $AuMg_6$-3 ($^2B_{2g}$ electronic state), which is higher 0.04 eV in energy than $AuMg_6$-1, possesses a high symmetry ($D_{2h}$) octahedron in which the Au atom is located at its center. The structures of the isomers $AuMg_7$-1 ($C_1$ symmetry with $^2A$ electronic state), $AuMg_7$-2 ($C_s$ symmetry with $^2A'$ electronic state) and $AuMg_7$-3 ($C_s$ symmetry with $^2A'$ electronic state) are all grown based on the diversity of Au-Mg-Mg-Mg tetrahedra-like geometries. In addition, the energy shift of the isomers $AuMg_7$-2 and $AuMg_7$-3 relative to the lowest energy state are 0.03 and 0.10 eV, respectively.

As **Figure 2** displayed, the medium-sized $AuMg_n$ (8–12) nanoclusters exhibit a diversity of structures. The structures of the isomers $AuMg_8$-1 ($C_{2v}$ symmetry with $^2A_1$ electronic state) and $AuMg_8$-3 ($C_1$ symmetry with $^2A$ electronic state) are generated based on the deformation of $AuMg_7$-3 after adsorption of an Mg atom, while the structure of the isomer $AuMg_8$-2 ($C_s$ symmetry with $^2A'$ electronic state) can be obtained from the deformation of $AuMg_7$-2 by adsorption of an Mg atom. The second and third lowest energy isomers of $AuMg_8$ nanoclusters are higher in energy than the ground state by 0.01 and 0.17 eV. The isomers $AuMg_9$-1 and $AuMg_9$-2 have the same symmetry ($C_{4v}$), electronic structure ($^2A_1$), energy and "fascinating cage-like" structures. The isomer $AuMg_9$-3 ($^2A'$ electronic state), which is 0.08 eV higher in energy than $AuMg_9$-1, has a cage-like structure with $C_s$ symmetry. The structures of the isomers $AuMg_{10}$-1 ($C_{2v}$ symmetry with $^2A_1$ electronic state), $AuMg_{10}$-2 ($C_1$ symmetry with $^2A$ electronic state) and $AuMg_{10}$-3 ($C_1$ symmetry with $^2A$ electronic state) are generated based on the deformation of $AuMg_9$-1 by adsorption of Mg atoms in different directions. The second and third lowest energy isomers of $AuMg_{10}$ nanoclusters are higher in energy than the first lowest energy by 0.46 and 0.84 eV, respectively. Interestingly, the isomers $AuMg_{11}$-1 ($C_s$ symmetry with $^2A'$ electronic state) and $AuMg_{11}$-2 ($C_1$ symmetry with $^2A$ electronic state) are easily obtained by the deformation of $AuMg_{10}$-2 by adsorption of an Mg atom. On the other hand, $AuMg_{11}$-3 ($C_1$ symmetry with $^2A$ electronic state) is formed by the deformation of AuMg10-1 after the adsorption of an Mg atom. $AuMg_{11}$-2 and $AuMg_{11}$-3 have higher energies than $AuMg_{11}$-1 at 0.03 and 0.39 eV. The isomer $AuMg_{12}$-1 ($C_s$ symmetry with $^2A'$ electronic state) is generated by the adsorption of an Mg atom by $AuMg_{11}$-1. The isomer $AuMg_{12}$-2 ($C_{2v}$ symmetry with $^2A_1$ electronic state), on the other hand, exhibits a deformed tubular-like structure, while the isomer $AuMg_{12}$-3 ($C_s$ symmetry with $^2A'$ electronic state) has a pyramid-like structure. Furthermore, compared to the energy of $AuMg_{12}$-1, $AuMg_{12}$-2 and $AuMg_{12}$-3 are 0.05 and 0.40 eV higher, respectively. Because the lowest energy state isomers of nanoclusters often require more comprehensive studies to explore their various physical and chemical properties, the atomic coordinates of the $AuMg_n$-1 (*n* = 2–20) nanoclusters are shown in **Supplementary Table S1** in the Supplemental Material.

In conclusion, based on the small size of $AuMg_{n-1}$ or smaller, $AuMg_n$ (*n* = 2–12) nanoclusters can usually be formed by

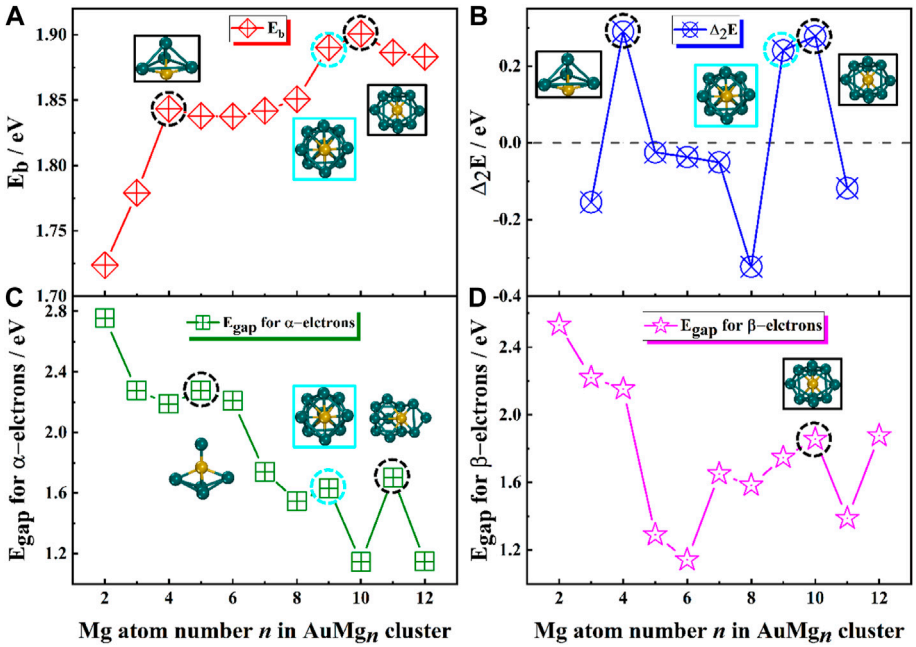


**FIGURE 3 | (A)** Average binding energy $E_b$, **(B)** The second order difference energy $\Delta_2E$, **(C)** The HOMO-LUMO energy gap $E_{gap}$ for α-electrons, **(D)** The HOMO-LUMO energy gap $E_{gap}$ for β-electrons in the ground state of $AuMg_n$ (*n* = 2–12) nanoclusters.

adsorption of Mg atoms in different directions, and the interesting point is that the direction of adsorption does not have a fixed pattern. Such result is consistent with many existed Mg-based nanoclusters reported (Li et al., 2017; Zeng et al., 2020, 2021; Zhu et al., 2020). However, despite the many similarities, the structures of gold-doped Mg nanoclusters have unique properties compared to other Mg-based nanoclusters studies. For example, the structure of $AuMg_3$ nanoclusters is 2D planar, while the lowest energy heterostructures of Be (Zeng et al., 2020), Si (Zhu et al., 2020), C, Ge, Sn (Zeng et al., 2021), Zn-doped (Li et al., 2017) Mg nanoclusters of corresponding sizes are all ortho-tetrahedral in shape. Interestingly, although the ground-state structures of $AuMg_9$ and $BeMg_9$ (Zeng et al., 2020) look similar, the significant difference between them is that the Au atom locates on the surface of $AuMg_9$ while the Be atom is absorbed into the inside of $BeMg_9$.

## The Relative Stabilities

Since clusters exhibit different physical and chemical properties at different sizes, their relative stability is well worth studying. The relative stability of cluster can be calculated through the following three quantities, that is the binding energy per atom ($E_b$ in eV), the second-order energy difference ($\Delta_2E$ in eV) and the HOMO-LUMO energy gap ($E_{gap}$ in eV). **Equations 1–3** display the above three energies for $AuMg_n$-1 (*n* = 2–20) nanoclusters in **Figure 1**.

$$E_b(AuMg_n) = [nE(Mg) + E(Au) - E(AuMg_n)]/(n+1) \quad (1)$$

$$\Delta_2E(AuMg_n) = E(AuMg_{n+1}) + E(AuMg_{n-1}) - 2E(AuMg_n) \quad (2)$$

$$E_{gap}(AuMg_n) = E_{LUMO}(AuMg_n) - E_{HOMO}(AuMg_n) \quad (3)$$

*E* (Au) and *E* (Mg) denote the energies of free Au and Mg atoms, *E* ($AuMg_n$) means the energy of the corresponding nanocluster. The lowest unoccupied molecular orbital (LUMO) and highest occupied molecular orbital (HOMO) energies are $E_{LUMO}$ and $E_{HOMO}$.

The theoretically calculated values of these quantities for $AuMg_n$-1 (*n* = 2–20) nanoclusters are presented in **Table 1** and their curves with size are showed in **Figure 3**. As **Figure 3A** displayed, overall, the $E_b$ curve becomes larger as the size of the nanoclusters increases, implying that the atoms within the $AuMg_n$ nanoclusters bind more stably as the Au atoms are doped. Locally, the maximum value of $E_b$ appears at $AuMg_{10}$ (1.90 eV), indicating that this nanocluster has the robust stability. Secondly, a small local peak (1.84 eV) appears at $AuMg_4$, indicating that it is slightly more stable than its neighbors. **Figure 3B** shows the curve of the $\Delta_2E$, which can be detected experimentally by mass spectrometry. Interestingly, as in the case of the local peaks of the $E_b$ curve, $AuMg_4$ and $AuMg_{10}$ have local maximum $\Delta_2E$ values of 0.29 and 0.28 eV, respectively. This conclusion suggests that they are both the most stable and have a high probability of being observed in mass spectrometry experiments. The thermodynamic stability of nanoclusters can be characterized by the value of their $E_{gap}$. Since $AuMg_n$ nanoclusters are open-shell systems, they have both α and β-electrons, and the $E_{gap}$ of α and β-electrons are illustrated in **Figure 3C** and **Figure 3D**. For α-electrons $E_{gap}$ curve of $AuMg_n$ nanoclusters, the local peaks appear at *n* = 5, 9 and 11, while $AuMg_{10}$ has the largest local β-electron $E_{gap}$, indicating that the thermal stability of these clusters is relatively high.

In conclusion, $AuMg_4$ and $AuMg_{10}$ nanoclusters show the robust stability. However, it is noteworthy that the $AuMg_9$

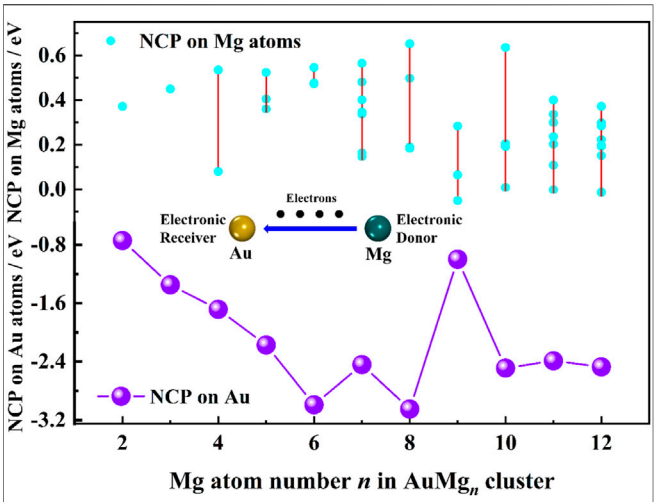


**FIGURE 4 |** NCP analysis on Au and Mg atoms in the ground state of $AuMg_n$ (*n* = 2–12) nanoclusters.

nanocluster is always the second largest value in both $E_b$ and $\Delta_2E$ curves, although they are not the maximum values. Therefore, combined with the $E_{gap}$ maximum for α-electrons, $AuMg_9$ nanocluster also has considerable robust stability and be worthy studying.

## Charge Transfer Property and Chemical Bond Analysis

The natural charge population (NCP) results from the NBO calculations can reveal the charge transfer properties in the nanoclusters. The NCP values of Au atoms in **Table 1** are in the range of [−2.99, −0.74] e, indicating that Au atoms play the role of electron receiver in all nanoclusters. The curve of NCP on Au atom with the size is ploted in **Figure 4**. The $AuMg_9$ nanocluster appears to be very special, which is probably originated from its high symmetry structure. **Supplementary Table S2** in the Supplementary Material shows the NCP values on the Mg atoms. Except for 4 Mg atoms in $AuMg_9$ with a charge of −0.05 e and 1 Mg atom in $AuMg_{12}$ with an NCP value of −0.01 e, all other Mg atoms have positive NCP values, distributed from 0.65 to 0.01 e, suggesting that they are losing electrons. In other words, Mg atoms are electron donors in the $AnMg_n$ nanoclusters. The charge transfer property depends on the electronegativity of the atom, the greater the electronegativity, the easier it is to get electrons. The electronegativity value of Mg atom is 1.31, while that of Au atom is 2.54, so the charge transfer is mostly from Mg atom to Au atom.

The ELF values of atomic bonding regions and their 2D maps are useful tools for analyzing the chemical bonding properties of nanoclusters. ELF is a value greater than 0 and less than 1, which characterizes the degree of electron localization and thus can determine the bonding properties. A region with ELF > 0.5 implies high electron localization and covalent bonding in the bonding region, while a region with ELF < 0.5 has low electron localization and non-covalent bonding in the bonding region. **Figure 5** and **Supplementary Figure S1** in the Supplementary Material display the 2D distribution of the EFL value for the ground state $AuMg_n$ (*n* = 2–12) nanoclusters. The calculations show that Mg-Mg in $AuMg_n$ nanoclusters is covalently bonded, while Au-Mg bond is non-covalent. The relatively large value of ELF around Au atom and low in bonding region indicates that the valence layer of Au atom is solidified around it, so it does not form covalent bonds with Mg. Furthermore, considering that the Au atom always gains electrons and the Mg atom around it loses electrons to be positively charged, it can be concluded that Au-Mg is ionic bonding. Another noteworthy point is that the critical size for Mg-Mg bonding is $AuMg_4$. ELF distribution map shows that Mg-Mg does not covalently bond in $AuMg_2$ and $AuMg_3$ nanoclusters.

## The Nonlinear Optical Property

Static polarizabilities α (∞) and hyperpolarizabilities β (∞) for the ground state $AuMg_n$ (*n* = 2–20) nanoclusters were calculated to analyze their nonlinear optical property. Specifically, the coupled-perturbed Kohn-Sham (CPKS) method (Jensen, 2017) was adopted for the $AuMg_n$ nanoclusters to compute the polarizabilities and hyperpolarizabilities in the zero-frequency limit (λ→∞). The results of α(∞) and β(∞) calculations are presented in **Supplementary Table S3** in the Supplementary Material and are shown in **Figure 6**. From **Figure 6A**, it can be seen that the polarization anisotropy $\alpha_{aniso}$ (∞) and isotropy $\alpha_{iso}$ (∞) of $AuMg_n$ nanoclusters do not change consistently with the size. The $\alpha_{iso}$ (∞) shows an overall upward trend, except for $AuMg_9$, while the $\alpha_{aniso}$ (∞) oscillates with increasing size. In addition, $\alpha_{xx}$ (∞), $\alpha_{yy}$ (∞), $\alpha_{zz}$ (∞) of each nanocluster are also shown in **Figure 6A**. Due to the diversity of the nanoclusters structures, these quantities display irregular oscillations in different directions. However, $AuMg_9$ nanocluster with high structural symmetry exhibits synchronous local minimum anisotropic and isotropic polarization, suggesting that it has special nonlinear optical properties compared to other nanoclusters. In order to study the polarization of $AuMg_9$ more intuitively, the unit sphere representation of its polarization tensor is plotted in **Figure 6C**. One can find the anisotropic polarization of $AuMg_9$, more specifically, the small polarization rate in the x-y plane and the maximum polarization rate in the z-direction (i.e., the direction of the line connecting the leftmost Au and the rightmost Mg in the figure).

**Figure 6B** exhibits the static hyperpolarizability β (∞) of the $AuMg_n$ nanoclusters and their projection values in the dipole moment direction $\beta_{prj}$ (∞). Since $\beta_{prj}$ (∞) can be measured by the electric field-induced second harmonic generation experiment (EFISH), it serves as a guide for experiments. Specifically, β increases from $AuMg_2$ to a maximum value of $AuMg_5$, then gradually decreases to a minimum value of $AuMg_9$, and increases again afterward. Interestingly, the β and $\beta_{prj}$ of $AuMg_9$ and the nanoclusters smaller than it are exactly equal, indicating that its β is isotropic with the dipole moment. However, starting from $AuMg_{10}$ nanocluster, the two curves are reversed, forming a mirror-symmetric trend. **Figure 6D** shows the unit sphere representation of static

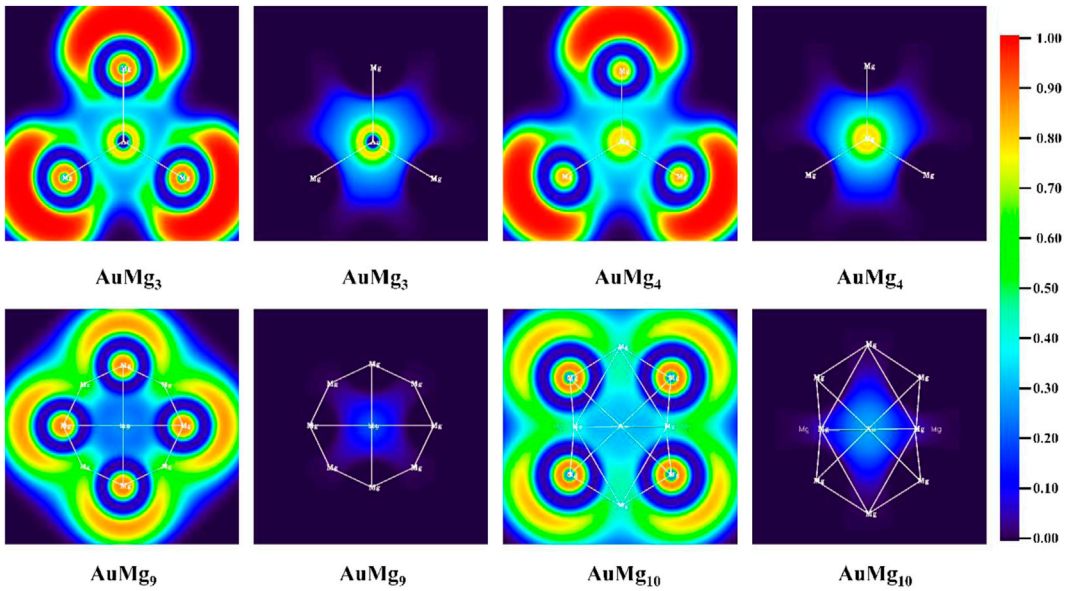


**FIGURE 5 |** The ELF analysis for Mg-Mg and Au-Mg chemical bonds for $AuMg_n$ (*n* = 3, 4, 9, 10) nanoclusters.

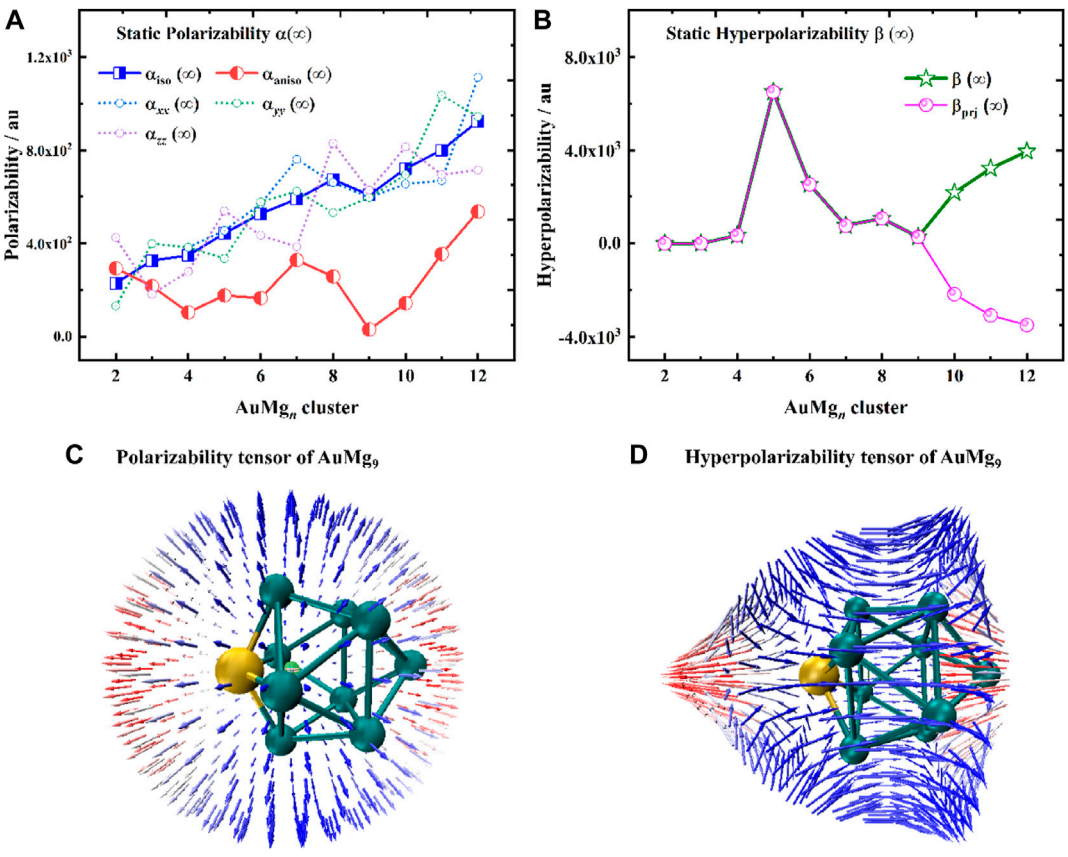


**FIGURE 6 | (A)** Static polarizabilities α(∞), **(B)** Static hyperpolarizabilities β(∞) for the ground state of $AuMg_n$ (*n* = 2–12) nanoclusters, **(C)** The unit sphere representation of static polarizability tensor α, **(D)** The unit sphere representation of static hyperpolarizability tensor β of $AuMg_9$ nanocluster.

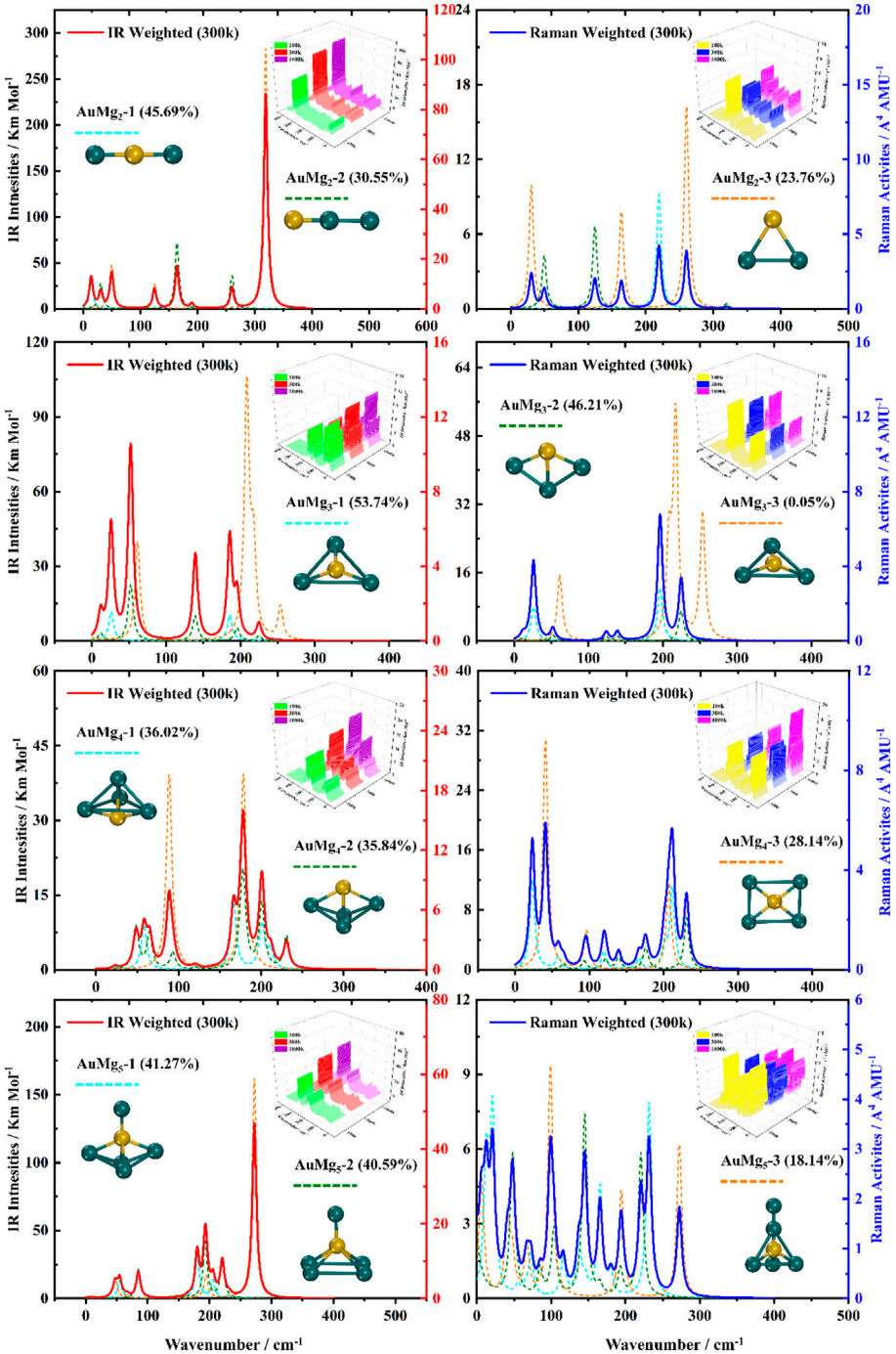


**FIGURE 7 |** Boltzmann distribution weighted average spectra of the three lowest energy isomers of $AuMg_n$ (*n* = 2–5) nanoclusters at room temperature (IR on the left side, Raman on the right side).

hyperpolarizability tensor β of $AuMg_9$, it is found that β is also anisotropic, with a maximum in the z-direction, and changes in the x-y plane as the Mg atoms surround it. In conclusion, relative to other nanoclusters, AuMg9 exhibits distinctive nonlinear optical properties.

## Boltzmann Distribution Weighted Average Spectra of IR and Raman

For the ground state $AuMg_n$ nanoclusters, the infrared and Raman spectra with weighted average of the Boltzmann distribution were calculated for guidance experiments. The

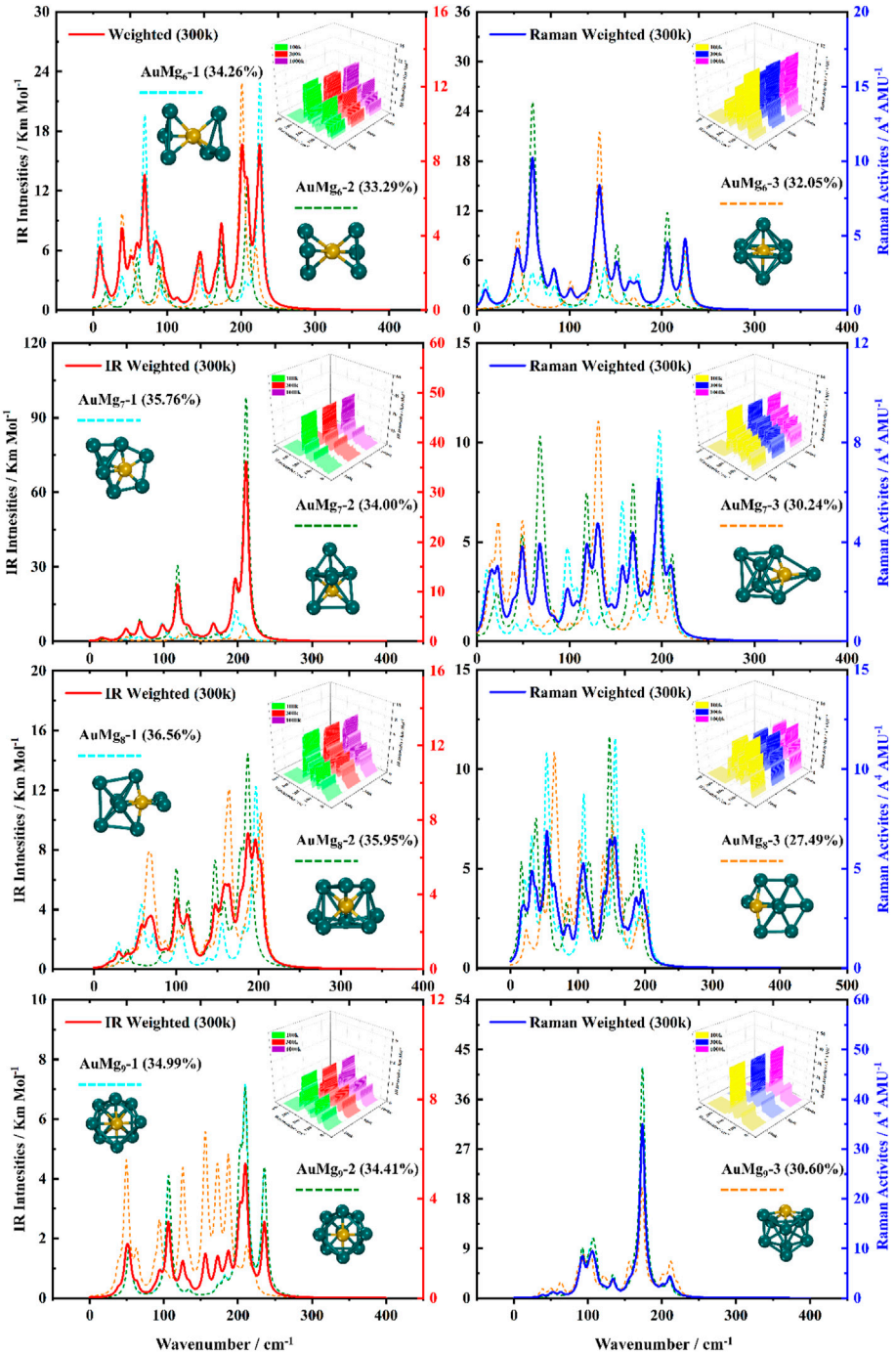


**FIGURE 8 |** Boltzmann distribution weighted average spectra of the three lowest energy isomers of $AuMg_n$ (*n* = 6–9) nanoclusters at room temperature (IR on the left side, Raman on the right side).

motivation for considering the Boltzmann distribution is due to the difficulty of observing only the ground state nanoclusters in experiments, especially in the gas-phase nanoclusters. **Figure 7** display the IR and Raman spectra of the weighted average of the Boltzmann distribution at room temperature. The Boltzmann distribution probabilities of each isomer at different temperatures were also calculated by the relevant equations in the Supplementary Material. The small 3D plots in each map are the corresponding weighted average spectra at 100 k, 300 k and 1000 k temperatures. As shown in **Figures 7–9**, the strongest absorption peaks of IR spectra are distributed in the 40–350 $cm^{-1}$ frequency band, while the strongest peaks of Raman spectra are

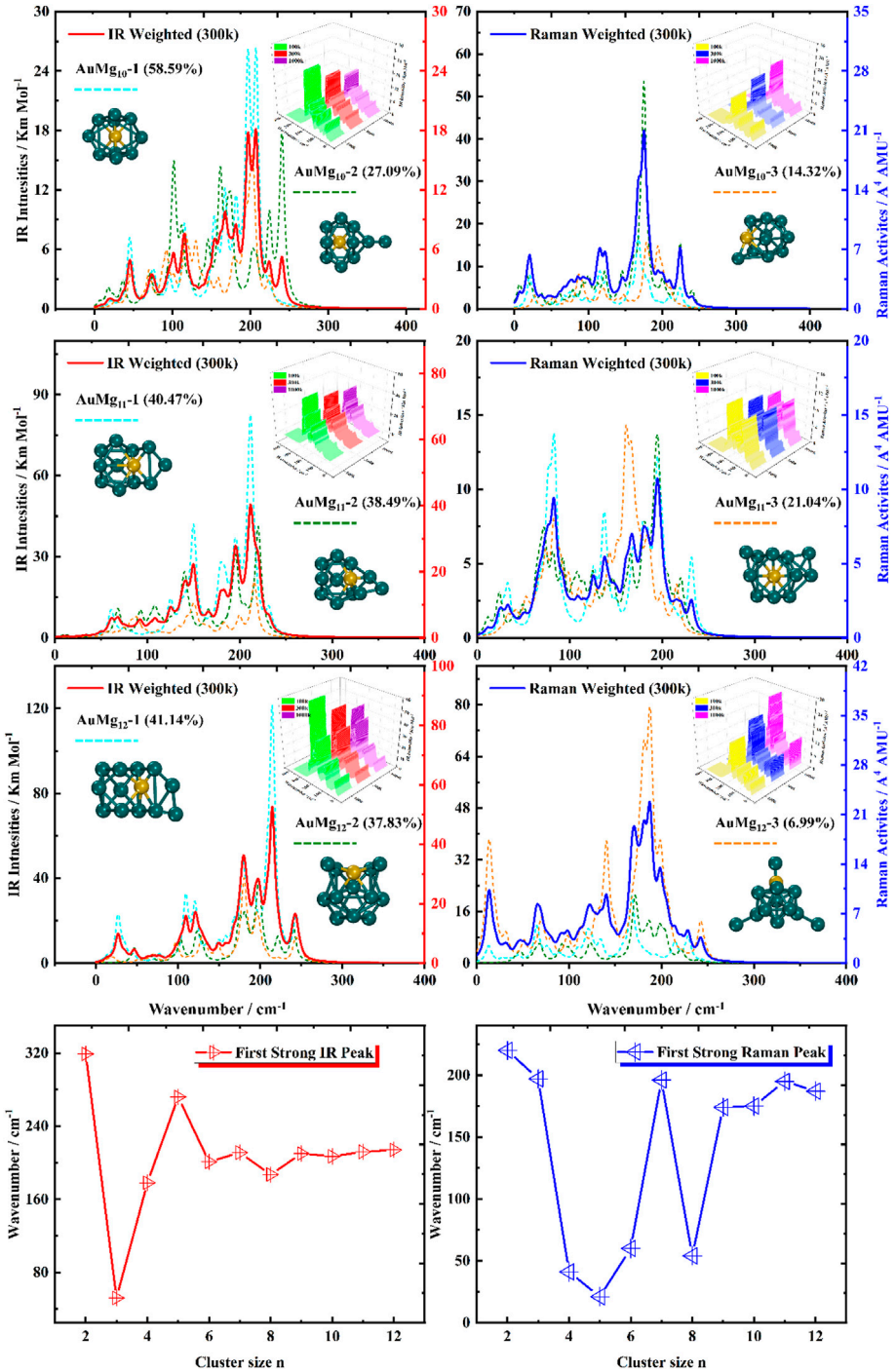


**FIGURE 9 |** Boltzmann distribution weighted average spectra of the three lowest energy isomers of $AuMg_n$ (*n* = 10–12) nanoclusters at room temperature (IR on the left side, Raman on the right side), and the first strong IR and Raman peaks in $AuMg_n$ (*n* = 2–12) nanoclusters.

distributed in a narrower band of 20–220 $cm^{-1}$. However, the most intense peaks of both IR and Raman weighted average spectra appear around 200 $cm^{-1}$ as the size increases. In addition, as can be seen from the small 3D plots in each figure and **Supplementary Figure S2** in the Supplementary Material, the location of the most intense peak of the weighted average spectrum does not shift as the temperature increases, but the intensity changes.

Specifically, for the weighted average IR spectra at room temperature, the nanoclusters of $AuMg_n$ (*n* = 4–12) are easily distinguished as separate strong bands in the 200 $cm^{-1}$ regions of the spectra, except for the $AuMg_2$ and $AuMg_3$ nanoclusters. This

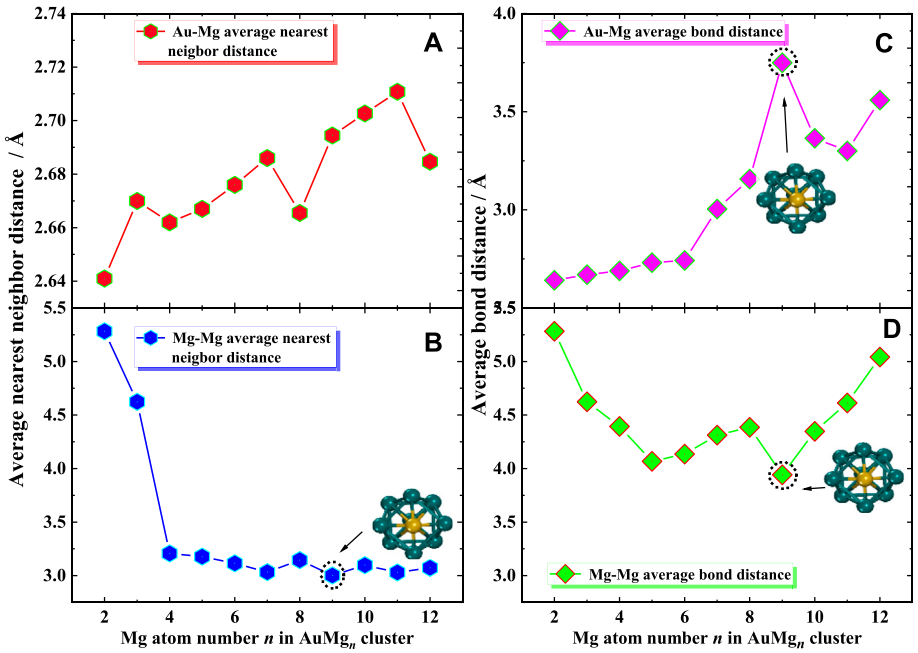


**FIGURE 10 | (A,B)** Average nearest neighbor distance for Au-Mg and Mg-Mg, **(C,D)** Average bond distance for Au-Mg and Mg-Mg.

result is in good agreement with the results of infrared spectroscopy of pure Mg nanoclusters studied by Belyaev et al. (Belyaev et al., 2016). For the Raman weighted average spectrum at room temperature, although the strongest Raman activity peaks of $AuMg_4$, $AuMg_5$ and $AuMg_6$ nanoclusters appear in the low-frequency band (20–50 $cm^{-1}$), they still have many strong peaks in the 200 $cm^{-1}$ regions. Therefore, for all the Raman spectra of the $AuMg_n$ ($n$ = 2–12) nanoclusters, the 200 $cm^{-1}$ regions can be more easily distinguished as individual strong bands. In conclusion, it was computationally shown that the formation of $AuMg_n$ ($n$ = 2–12) nanoclusters at room temperature is possible to identify these nanoclusters by IR and Raman spectroscopy.

## The Average Bond Distance and Average Nearest Neighbor Distance

In order to provide more data support for future possible experiments, the average bond distance and average nearest neighbor distance were calculated. As shown in **Figure 10**, the average nearest neighbor distance and bond distance for Au-Mg and Mg-Mg in the ground state of $AuMg_n$ ($n$ = 2–12) clusters display some interesting conclusions. **Figures 10A,B** show that, overall, the nearest neighbor distance for Au-Mg becomes larger as the cluster size increases (except for $n$ = 8 and 12), while Mg-Mg is overall decreasing. The average nearest neighbor distance of Au-Mg is 2.68 Å, and that of Mg-Mg is 3.44 Å. **Figure 10C** gives the average bond distance of Au-Mg with cluster size dependence similar to the nearest neighbor distance of Au-Mg, i.e., increasing overall. However, **Figure 10D** demonstrates that the average Mg-Mg bond distance decreases and then increases with cluster size. Another interesting conclusion is that the local turning points of the average bond and nearest-neighbor distances for Mg-Mg and the average bond distance curves for Au-Mg occur at $AuMg_9$, suggesting that they influence the local stability of the clusters.

## CONCLUSION

In this work, the structure of Au-doped $Mg_n$ ($n$ = 2–12) nanoclusters was investigated by CALYPSO crystal search software. It is shown that the geometric growth mechanism of this nanocluster has similarities to other atom-doped $Mg_n$ clusters but also has unique features, such as the planar structure of $AuMg_3$ and the high symmetry cage-like structure of $AuMg_9$. Stability calculations show that $AuMg_4$ and $AuMg_{10}$ have high local stability, while $AuMg_9$ nanoclusters are the second most stable nanoclusters. The charge transfer study reveals that Au atoms are electron receivers and Mg atoms are electron donors in $AuMg_n$ nanoclusters. ELF analysis showed that Mg-Mg formed a covalent chemical bond while Au-Mg was an ionic bond, and the critical size for the appearance of the Mg-Mg covalent bond was found to be $AuMg_3$. The nonlinear optical properties of $AuMg_n$ nanoclusters were probed by calculating the static polarizability and hyperpolarizability, and the results indicate that $AuMg_9$ is a special one of interest. Boltzmann distribution weighted average IR and Raman spectroscopy studies at room temperature confirm that these nanoclusters can be identified by spectroscopic experiments. Finally, the average bond distance and average nearest neighbor distance were fully investigated.

## DATA AVAILABILITY STATEMENT

The original contributions presented in the study are included in the article/**Supplementary Material**, further inquiries can be directed to the corresponding authors.

## AUTHOR CONTRIBUTIONS

B-CZ: Software, Investigation, Writing Original draft preparation. P-JD: Methodology, Investigation, Data curation, Visualization. JG: Data curation, Visualization. W-BK: Conceptualization, Methodology, Formal analysis, Investigation, Writing review and editing.

## FUNDING

This work is supported partly by National Natural Science Foundation of China (No. 11947006), and partly by the Cultivating Project for Young Scholar at Hubei University of Medicine (No. 2019QDJZR12).

## SUPPLEMENTARY MATERIAL

The Supplementary Material for this article can be found online at: https://www.frontiersin.org/articles/10.3389/fchem.2022.870985/full#supplementary-material

## REFERENCES

Alvarez, M. M., Khoury, J. T., Schaaff, T. G., Shafigullin, M., Vezmar, I., and Whetten, R. L. (1997). Critical Sizes in the Growth of Au Clusters. *Chem. Phys. Lett.* 266, 91–98. doi:10.1016/S0009-2614(96)01535-7

Assadollahzadeh, B., and Schwerdtfeger, P. (2009). A Systematic Search for Minimum Structures of Small Gold Clusters Au[sub N] (N=2-20) and Their Electronic Properties. *J. Chem. Phys.* 131, 064306. doi:10.1063/1.3204488

Becke, A. D., and Edgecombe, K. E. (1990). A Simple Measure of Electron Localization in Atomic and Molecular Systems. *J. Chem. Phys.* 92, 5397–5403. doi:10.1063/1.458517

Belyaev, S. N., Panteleev, S. V., Ignatov, S. K., and Razuvaev, A. G. (2016). Structural, Electronic, Thermodynamic and Spectral Properties of Mgn (N=2-31) Clusters. A DFT Study. *Comput. Theor. Chem.* 1079, 34–46. doi:10.1016/j.comptc.2016.01.011

Chen, B., Conway, L. J., Sun, W., Kuang, X., Lu, C., and Hermann, A. (2021). Phase Stability and Superconductivity of lead Hydrides at High Pressure. *Phys. Rev. B* 103, 035131. doi:10.1103/PhysRevB.103.035131

Chen, H., Liang, H., Dai, W., Lu, C., Ding, K., Bi, J., et al. (2020). MgScH15: A Highly Stable Cluster for Hydrogen Storage. *Int. J. Hydrogen Energ.* 45, 32260–32268. doi:10.1016/j.ijhydene.2020.08.229

Frisch, M. J., Trucks, G. W., Schlegel, H. B., Scuseria, G. E., Robb, M. A., Cheeseman, J. R., et al. (2016). *Gaussian 09, Revision A.02*. Wallingford, CT: Gaussian, Inc. Available at: https://gaussian.com/g09citation/.

Huang, W., and Wang, L.-S. (2009). Probing the 2D to 3D Structural Transition in Gold Cluster Anions Using Argon Tagging. *Phys. Rev. Lett.* 102, 153401. doi:10.1103/PhysRevLett.102.153401

Idrobo, J. C., Walkosz, W., Yip, S. F., Öğüt, S., Wang, J., and Jellinek, J. (2007). Static Polarizabilities and Optical Absorption Spectra of Gold Clusters (Aun,n=2-14and 20) from First Principles. *Phys. Rev. B* 76, 205422. doi:10.1103/PhysRevB.76.205422

Jellinek, J., and Acioli, P. H. (2003). Magnesium Clusters: Structural and Electronic Properties and the Size-Induced Nonmetal-To-Metal Transition. *J. Phys. Chem. A.* 107, 1670. doi:10.1021/jp0301655

Jensen, F. (2017). *Introduction to Computational Chemistry*. West Sussex: John Wiley & Sons. Available at: https://xs.dailyheadlines.cc/books/about/Introduction_to_Computational_Chemistry.html?hl=zh-CN&id=UZOVDQAAQBAJ (Accessed October 14, 2021).

Jin, R. (2015). Atomically Precise Metal Nanoclusters: Stable Sizes and Optical Properties. *Nanoscale* 7, 1549–1565. doi:10.1039/C4NR05794E

Jin, R., Zeng, C., Zhou, M., and Chen, Y. (2016). Atomically Precise Colloidal Metal Nanoclusters and Nanoparticles: Fundamentals and Opportunities. *Chem. Rev.* 116, 10346–10413. doi:10.1021/acs.chemrev.5b00703

Köhn, A., Weigend, F., and Ahlrichs, R. (2001). Theoretical Study on Clusters of Magnesium. *Phys. Chem. Chem. Phys.* 3, 711–719. doi:10.1039/B007869G

Li, Z., Zhao, Z., Zhou, Z., Wang, H., and Li, S. (2017). First-principles Calculations on Small MgnZn and Mgn-1Zn2 Clusters: Structures, Stability, Electronic Properties. *Mater. Chem. Phys.* 199, 585–590. doi:10.1016/j.matchemphys.2017.07.049

Lu, C., and Chen, C. (2021). Indentation Strengths of Zirconium Diboride: Intrinsic versus Extrinsic Mechanisms. *J. Phys. Chem. Lett.* 12, 2848–2853. doi:10.1021/acs.jpclett.1c00434

Lu, C., and Chen, C. (2020a). Indentation-strain Stiffening in Tungsten Nitrides: Mechanisms and Implications. *Phys. Rev. Mater.* 4, 043402. doi:10.1103/PhysRevMaterials.4.043402

Lu, C., and Chen, C. (2020b). Structure-strength Relations of Distinct Mon Phases from First-Principles Calculations. *Phys. Rev. Mater.* 4, 044002. doi:10.1103/PhysRevMaterials.4.044002

Lu, C., Gong, W., Li, Q., and Chen, C. (2020). Elucidating Stress-Strain Relations of ZrB12 from First-Principles Studies. *J. Phys. Chem. Lett.* 11, 9165–9170. doi:10.1021/acs.jpclett.0c02656

Lu, T., and Chen, F. (2012). Multiwfn: A Multifunctional Wavefunction Analyzer. *J. Comput. Chem.* 33, 580–592. doi:10.1002/jcc.22885

Lv, J., Wang, Y., Zhu, L., and Ma, Y. (2012). Particle-swarm Structure Prediction on Clusters. *J. Chem. Phys.* 137, 084104. doi:10.1063/1.4746757

Lyon, J. T. (2021). Hydrogen Binding and Dissociation in MgScH Clusters (N ≤ 20). *Int. J. Hydrogen Energ.* 46, 36872–36877. doi:10.1016/j.ijhydene.2021.08.228

Peng, Y., Wang, P., Luo, L., Liu, L., and Wang, F. (2018). Green Synthesis of Fluorescent Palladium Nanoclusters. *Materials* 11, 191. doi:10.3390/ma11020191

Qian, H., and Jin, R. (2009). Controlling Nanoparticles with Atomic Precision: The Case of Au144(SCH2CH2Ph)60. *Nano Lett.* 9, 4083–4087. doi:10.1021/nl902300y

Ramakrishna, G., Varnavski, O., Kim, J., Lee, D., and Goodson, T. (2008). Quantum-Sized Gold Clusters as Efficient Two-Photon Absorbers. *J. Am. Chem. Soc.* 130, 5032–5033. doi:10.1021/ja800341v

Reed, A. E., Curtiss, L. A., and Weinhold, F. (1988). Intermolecular Interactions from a Natural Bond Orbital, Donor-Acceptor Viewpoint. *Chem. Rev.* 88, 899–926. doi:10.1021/cr00088a005

Shang, L., Dong, S., and Nienhaus, G. U. (2011). Ultra-small Fluorescent Metal Nanoclusters: Synthesis and Biological Applications. *Nano Today* 6, 401–418. doi:10.1016/j.nantod.2011.06.004

Shao, H., Xin, G., Zheng, J., Li, X., and Akiba, E. (2012). Nanotechnology in Mg-Based Materials for Hydrogen Storage. *Nano Energy* 1, 590–601. doi:10.1016/j.nanoen.2012.05.005

Shinde, R. (2016). Ab Initio Calculations of Optical Properties of Clusters. ArXiv160706928 Phys Available at: http://arxiv.org/abs/1607.06928 (Accessed October 11, 2021).

Shinde, R., and Shukla, A. (2017). First Principles Electron-Correlated Calculations of Optical Absorption in Magnesium Clusters. *Eur. Phys. J. D* 71, 301. doi:10.1140/epjd/e2017-80356-6

Sun, W., Kuang, X., Keen, H. D. J., Lu, C., and Hermann, A. (2020). Second Group of High-Pressure High-Temperature Lanthanide Polyhydride Superconductors. *Phys. Rev. B* 102, 144524. doi:10.1103/PhysRevB.102.144524

Tew, L., Cai, M.-T., Lo, L.-W., Khung, Y., and Chen, N.-T. (2018). Pollen-Structured Gold Nanoclusters for X-ray Induced Photodynamic Therapy. *Materials* 11, 1170. doi:10.3390/ma11071170

Trivedi, R., and Bandyopadhyay, D. (2015). Hydrogen Storage in Small Size MgnCo Clusters: A Density Functional Study. *Int. J. Hydrogen Energ.* 40, 12727–12735. doi:10.1016/j.ijhydene.2015.07.122

Trivedi, R., and Bandyopadhyay, D. (2016). Study of Adsorption and Dissociation Pathway of H 2 Molecule on Mg N Rh (N = 1-10) Clusters: A First Principle Investigation. *Int. J. Hydrogen Energ.* 41, 20113–20121. doi:10.1016/j.ijhydene.2016.09.007

Wang, Y., Lv, J., Zhu, L., and Ma, Y. (2012). CALYPSO: A Method for crystal Structure Prediction. *Comput. Phys. Commun.* 183, 2063–2070. doi:10.1016/j.cpc.2012.05.008

Wang, Y., Lv, J., Zhu, L., and Ma, Y. (2010). Crystal Structure Prediction via Particle-Swarm Optimization. *Phys. Rev. B* 82, 094116. doi:10.1103/PhysRevB.82.094116

Xia, X., Kuang, X., Lu, C., Jin, Y., Xing, X., Merino, G., et al. (2016). Deciphering the Structural Evolution and Electronic Properties of Magnesium Clusters: An Aromatic Homonuclear Metal Mg17 Cluster. *J. Phys. Chem. A.* 120, 7947–7954. doi:10.1021/acs.jpca.6b07322

Yan, N., Xia, N., Liao, L., Zhu, M., Jin, F., Jin, R., et al. (2018). Unraveling the Long-Pursued Au 144 Structure by X-ray Crystallography. *Sci. Adv.* 4, eaat7259. doi:10.1126/sciadv.aat7259

Yau, S. H., Varnavski, O., and Goodson, T. (2013). An Ultrafast Look at Au Nanoclusters. *Acc. Chem. Res.* 46, 1506–1516. doi:10.1021/ar300280w

Zeng, L., Liang, M.-K., Wei, X.-F., Guo, J., Dai, W., and Zhu, B.-C. (2021). New Potential Stable Structures of XMg N (X = Ge, C, Sn; N = 2-12) Clusters: XMg8 with High Stability. *J. Phys. Condens. Matter* 33, 065302. doi:10.1088/1361-648X/abc401

Zeng, L., Wei, X.-F., Liang, M.-K., Deng, P.-J., Bi, J., and Zhu, B.-C. (2020). BeMg9: A tower-like Type Doped Magnesium Clusters with High Stability. *Comput. Mater. Sci.* 182, 109795. doi:10.1016/j.commatsci.2020.109795

Zhang, F., Zhang, H., Xin, W., Chen, P., Hu, Y., Zhang, X., et al. (2020). Probing the Structural Evolution and Electronic Properties of Divalent Metal Be2Mgn Clusters from Small to Medium-Size. *Sci. Rep.* 10, 6052. doi:10.1038/s41598-020-63237-8

Zhao, Y. R., Bai, T. T., Jia, L. N., Xin, W., Hu, Y. F., Zheng, X. S., et al. (2019). Probing the Structural and Electronic Properties of Neutral and Anionic Lanthanum-Doped Silicon Clusters. *J. Phys. Chem. C* 123, 28561–28568. doi:10.1021/acs.jpcc.9b07184

Zhao, Y., Xu, Y., Chen, P., Yuan, Y., Qian, Y., and Li, Q. (2021). Structural and Electronic Properties of Medium-Sized Beryllium Doped Magnesium BeMg Clusters and Their Anions. *Results Phys.* 26, 104341. doi:10.1016/j.rinp.2021.104341

Zhu, B.-C., Deng, P.-J., Xiong, S.-Y., Dai, W., Zeng, L., and Guo, J. (2021). Au5Br: A New Member of Highly Stable 2D-type Doped Gold Nanomaterial. *Comput. Mater. Sci.* 194, 110446. doi:10.1016/j.commatsci.2021.110446

Zhu, B. C., Zhang, S., and Zeng, L. (2020). The Effect of Silicon Doping on the Geometrical Structures, Stability, and Electronic and Spectral Properties of Magnesium Clusters: DFT Study of SiMg N ( N = 1-12) Clusters. *Int. J. Quan. Chem.* 120, e26143. doi:10.1002/qua.26143

**Conflict of Interest:** The authors declare that the research was conducted in the absence of any commercial or financial relationships that could be construed as a potential conflict of interest.

**Publisher's Note:** All claims expressed in this article are solely those of the authors and do not necessarily represent those of their affiliated organizations, or those of the publisher, the editors and the reviewers. Any product that may be evaluated in this article, or claim that may be made by its manufacturer, is not guaranteed or endorsed by the publisher.

frontiers | Frontiers in Physics

REVIEW
published: 05 April 2022
doi: 10.3389/fphy.2022.870205

# Superalkalis for the Activation of Carbon Dioxide: A Review

*Harshita Srivastava and Ambrish Kumar Srivastava**

*Department of Physics, Deen Dayal Upadhyaya Gorakhpur University, Gorakhpur, India*

The activation of carbon dioxide is essential not only for global carbon balance but also for its conversion into fuel. As $CO_2$ is highly stable, it is quite challenging to activate or reduce $CO_2$. Recently, the ability of superalkalis to easily transfer an electron to $CO_2$ has been proposed in several studies. The superalkalis are species possessing lower ionization energy than alkali atoms. These are hypervalent species, having an excess of electrons. Owing to this, they possess strong reducing power and cause the linear structure of $CO_2$ to bend by transferring an electron to it. Herein, we present a comprehensive account of the single-electron reduction and activation of $CO_2$ by various kinds of superalkalis. This review also includes a novel strategy for the capture and storage of $CO_2$ by superalkali.

**Keywords: $CO_2$ activation, $CO_2$ reduction, charge transfer, superalkalis, theoretical studies**

OPEN ACCESS

***Edited by:***
*Moyuan Cao,*
*Tianjin University, China*

***Reviewed by:***
*Jin-Chang Guo,*
*Shanxi University, China*
*Di Qiu,*
*Tianjin Normal University, China*

****Correspondence:***
*Ambrish Kumar Srivastava*
*ambrishphysics@gmail.com*

***Specialty section:***
*This article was submitted to Physical Chemistry and Chemical Physics, a section of the journal Frontiers in Physics*

***Received:*** *06 February 2022*
***Accepted:*** *08 March 2022*
***Published:*** *05 April 2022*

***Citation:***
*Srivastava H and Srivastava AK (2022) Superalkalis for the Activation of Carbon Dioxide: A Review. Front. Phys. 10:870205. doi: 10.3389/fphy.2022.870205*

## INTRODUCTION

Carbon dioxide ($CO_2$) is a colorless and odorless gas with the property of trapping greenhouse gases, which are produced due to human activities as well as natural processes. Recently, the sharp decline in $CO_2$ levels has been noticed at the expense of the COVID-19 pandemic, which has caused a severe health emergency in the world and is not sustainable. The fueling of $CO_2$ in our environment is mainly through the $CO_2$ emissions from power plants and other industrial facilities, primarily waste products, and the developed economies are the leading contributors. As mentioned, it traps greenhouse gases which generally cause a change in the behavior of climate since it is a major contributor to global warming. In order to reduce its contribution to global warming, it is necessary to convert $CO_2$ into value-added products. The best way to back-pedal climate change without using expensive methods is extricating $CO_2$ from the air and then converting it into a useful product like fuel. These important issues were addressed by numerous techniques, which can be employed to reduce and capture $CO_2$ by other molecules [1–7]. As $CO_2$ is an extremely stable molecule [8, 9], it is quite challenging to convert it into usable fuel. To convert $CO_2$ into fuel, it is needed to activate $CO_2$ by some means or chemically reduce it by catalysts. $CO_2$ can be reduced either electrochemically (electrical energy) or photoelectrochemically (incident light) into CO. Single-electron reduction of $CO_2$ to $CO_2^-$ was experimentally not viable due to the large energy of reorganization between linear $CO_2$ and bent $CO_2^-$ anion. Notably, the electron affinity of $CO_2$ is negative so that $CO_2^-$ is metastable. $CO_2^-$ anion is stable in the $^2A_1$ state [10] which can be treated as an activated $CO_2$ moiety with the weaker C-O bond. The potential energy surface of the $CO_2^-$ anion suggests three vibronically coupled bound states [11].

It is difficult to extract an electron from carbon dioxide because of its high ionization energy (13 eV) [12]. However, it has been revealed that there is a possibility of oxidation of $CO_2$ using superhalogens [13], whose electron affinity overrides the halogen atoms [14]. The counterparts of superhalogens are superalkalis which bear lower ionization energy than alkali atoms [15]. Due to the stronger reducibility of superalkalis over alkali atoms, they might activate stable $CO_2$. To investigate this, a few studies have been performed recently. In this review, we will provide an

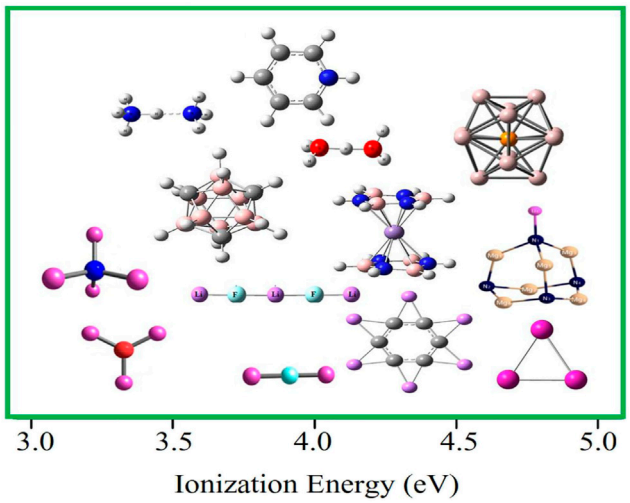


**FIGURE 1 |** Ionization energy scale of various superalkalis is considered here. The values are taken from Refs. 17–22, 25, and 35.

overview of how superalkalis play a significant role in the activation or reduction of $CO_2$, which is the initial step to convert $CO_2$ into fuel. Exploration of chemical processes used in the reduction of $CO_2$ is of tremendous importance in various fields, like biological, environmental, and industrial processes [16]. Before we go further, let us first have a look at superalkalis.

## What Are Superalkalis?

Alkali atoms possess the lowest ionization energy (IE), ranging from 5.39 to 3.89 eV, among all the elements in the periodic table. However, superalkalis are clusters whose ionization energies are even lower than this range. These clusters were originally introduced by Gutsev and Boldyrev in 1982 using *sp*-block elements [15]. They proposed species like $Li_2F$, $Li_3O$, and $Li_4N$ as superalkalis. In the form of a superatom, these clusters impersonate the behavior of alkali atoms. There have been several studies on the design of various kinds of superalkalis [17–24]. For instance, the binuclear superalkalis including $F_2Li_3$, have been widely studied [17]. Hou et al. [18] described non-metallic binuclear cations such as $F_2H_3^+$ and $O_2H_5^+$. Zhao et al. [19] proposed some special superalkalis like $N_4Mg_6Li$, $Al_3$, $Mn(B_3N_3H_6)_2$, $B_9C_3H_{12}$, $Al_{12}P$, and $C_5NH_6$, which were designed by using different schemes like jellium rule, 18-electron rule, Wade–Mingos rule, and Huckle's rule, respectively. $Al_{12}P$ was reported to be an alkali–metal-like superatom [20, 21]. Recently, Sikorska and Gaston [22] reported the superalkali behavior of polynuclear $N_4Mg_6M$ for M = Li, Na, and K. Srivastava [25] noticed that the IE of $C_6Li_6$, being lower than that of Li, makes it a closed-shell superalkali. The IE scale of these superalkalis is depicted in **Figure 1**.

Superalkalis find applications in the design of supersalts [26–28], superbases [29–31], alkaloids [32–34], and so forth. Due to their low IE, superalkalis play an important role in chemical industries as reducing agents. Here, we provide an account of how superalkalis are exploited to activate the $CO_2$ molecule.

## ACTIVATION OF $CO_2$ BY SUPERALKALIS

$CO_2$ is known to be a highly stable molecule due to its very high IE [12], as mentioned earlier, and no positive electron affinity [36, 37]. However, the low IE of superalkalis enables them to transfer an electron to $CO_2$, reducing it to $CO_2^-$ anion and thus activating it. In **Figure 2**, we show the structures of $CO_2$ and its anion, along with the charge distribution. One can see that the $CO_2^-$ anion is bent, in which the bond length is increased as compared to neutral $CO_2$ due to the negative charge.

Thus, the activation of $CO_2$ requires the following conditions to be satisfied:

1) The negative charge on $CO_2$ moiety is close to unity.
2) The structure of the $CO_2$ moiety is bent.
3) The bond length of $CO_2$ moiety is increased.

It has been reported earlier [38] that $CO_2$ would assume a bent structure when an electron is transferred to it or due to its interaction with the electrons of the metal atom. One would expect that the stable geometry of the M-$CO_2$ complex depends upon the IE of the metal atom, M. This may lead us to infer that an atom with a smaller IE should be able to transfer an electron to $CO_2$ more easily than one with a large IE. Later, we will discuss the interaction of $CO_2$ with various superalkalis described earlier.

### Interaction With Typical Superalkalis ($FLi_2$, $OLi_3$, and $NLi_4$)

Srivastava [35] studied the interaction of $CO_2$ with $FLi_2$, $OLi_3$, and $NLi_4$ superalkalis using the second-order Møller–Plesset perturbative (MP2) method [39] and the 6–311+G(d) basis set in the Gaussian 09 program [40]. Such interaction leads to the formation of complexes, as shown in **Figure 3**, and corresponding parameters can be found in **Table 1**. It is evident that the minimum energy of these complexes corresponds to the structure in which the interaction between $CO_2$, and superalkalis is mediated by both the O atoms of $CO_2$. The bond length of Li-O lies between 1.865 and 1.892 Å. The low-lying isomers of $FLi_2$-$CO_2$ and $OLi_3$-$CO_2$ are of higher energy in which $CO_2$ interacts *via* a single atom, whereas in the case of $NLi_4$-$CO_2$, there are no competing isomers obtained.

The binding energy (BE) of superalkali–$CO_2$ complexes is calculated and listed in **Table 1**. The BE of these complexes monotonically decreases with the increase in the size of superalkalis. This can be explained on the basis of a more delocalized electron cloud that is generally associated with the larger superalkalis. The natural population analysis (NPA) [45] charges ($\Delta q$) on $CO_2$ have also been listed. The most stable structure of superalkali–$CO_2$ complexes takes the values of $\Delta q$ as −0.90e for $FLi_2$, −0.88e for $OLi_3$, and −0.85e for $NLi_4$.

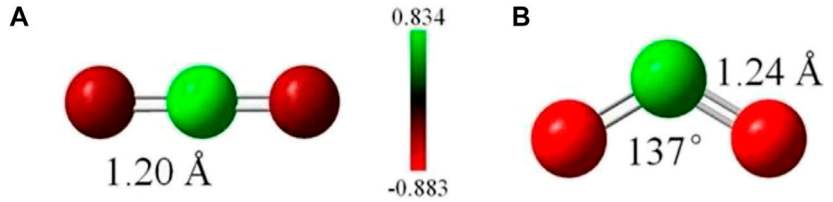


**FIGURE 2 |** Structure and NPA charge distribution in **(A)** neutral $CO_2$ and **(B)** $CO_2^-$anion, Ref. 19 with the permission of the Royal Society of Chemistry.

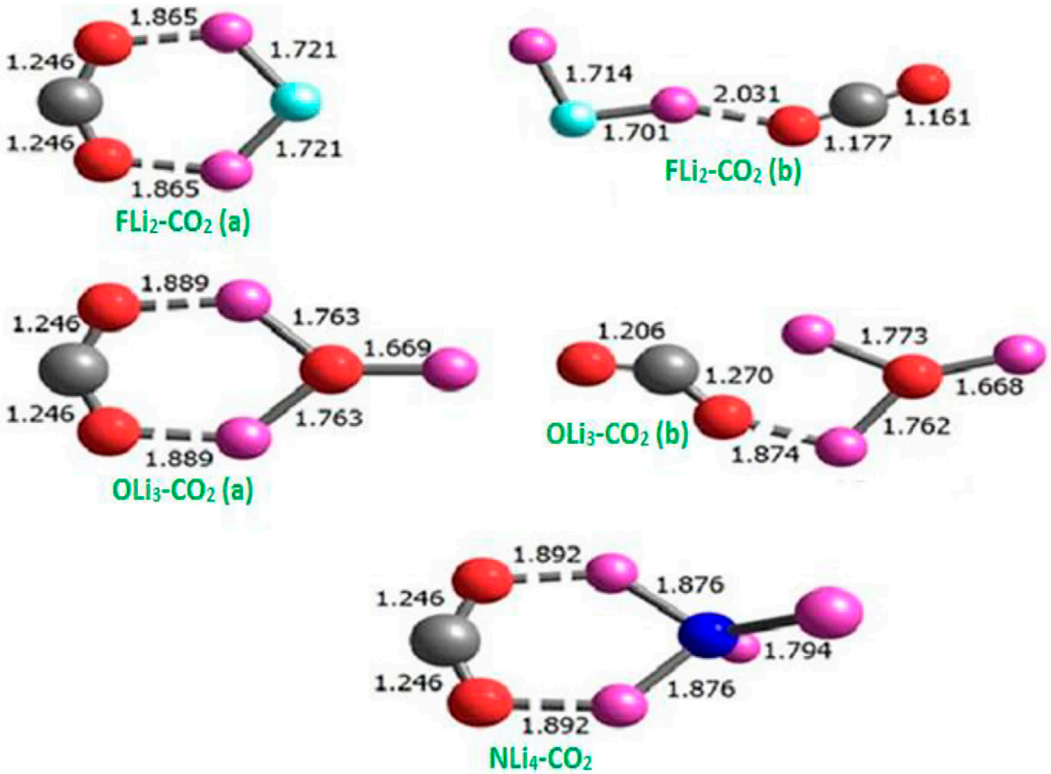


**FIGURE 3 |** Equilibrium structures of $CO_2$ complexes with typical superalkalis, with bond lengths in Å from Ref. 35 with the permission of Wiley.

In isomer (b) of $FLi_2$-$CO_2$, $\Delta q$ has a very small magnitude (−0.17e), which is consistent with an almost linear $CO_2$ moiety just as in a neutral $CO_2$ molecule. On the contrary, the $\Delta q$ in isomer (b) of $OLi_3$-$CO_2$ is, albeit smaller than that in its lowest energy structure (a), large enough to bend the $CO_2$ moiety. It should be noted that the size of the superalkalis is a more important factor than their IE in $CO_2$ activation. As per calculated binding energy and charge transfer, $FLi_2$ is more effective for $CO_2$ reduction. In these complexes, the $CO_2$ moiety is bent by 133° and the bond length C-O becomes 1.246 Å which is comparable to the bond lengths of 1.237 Å and bond angle 137° in the $CO_2^-$ anion, obtained at the MP2/6-311+G(d) level. This study suggests simple and catalyst-free single-electron reduction of $CO_2$ by using typical superalkalis such as $FLi_2$, $OLi_3$, and $NLi_4$.

## Interaction With Binuclear Superalkali ($Li_3F_2$)

Park and Meloni [41] reported the interaction of $CO_2$ and superalkali species $Li_3F_2$ using the CBS-OB3 composite model [46] through the Gaussian 09 program. They obtained three isomers, two planar (a) and (b), as well as one non-planar (c), of the $Li_3F_2$-$CO_2$ complex, as shown in **Figure 4**. There was no appreciable change in bond lengths between Li and F on interaction with $CO_2$. Despite some structural changes in the superalkalis, the structure of $CO_2$ changes from linear to bending. Therefore, it is clear that the strongly bound $CO_2$ is activated upon interaction with the superalkali. From **Table 1**, the BE of $Li_3F_2$-$CO_2$ isomers is found to be in the range of 1.06–1.63 eV (106–163 kJ/mol). The lowest BE was obtained for the isomer (c) in which one oxygen interacts with both the terminal Li atoms

**TABLE 1 |** Relative energy, binding energy (BE), NPA charge ($\Delta q$), bond length (C-O), and bond angle (O-C-O) of the complexes of $CO_2$ with various superalkalis.

| System | Isomers | Relative energy (eV) | BE (eV) | $\Delta q$ (e) | C-O (Å) | O-C-O (Deg) |
|---|---|---|---|---|---|---|
| $FLi_2$-$CO_2$[1] | (a) | 0 | 2.41 | −0.90 | 1.25 | 133 |
| | (b) | 1.07 | 1.34 | −0.17 | | |
| $OLi_3$-$CO_2$[1] | (a) | 0 | 1.23 | −0.88 | 1.24 | 133 |
| | (b) | 0.40 | 0.83 | −0.82 | | |
| $NLi_4$-$CO_2$[1] | — | — | 1.17 | −0.85 | 1.25 | 133 |
| $Li_3F_2$-$CO_2$[2] | (a) | 0 | 1.63 | −0.78 | 1.24 | 137 |
| | (b) | 0.05 | 1.58 | −0.63 | 1.23 | 133 |
| | (c) | 0.57 | 1.06 | −0.88 | 1.25 | 131 |
| $Al_3$-$CO_2$[3] | — | — | — | −1.26 | 1.29 | 126 |
| | | | | | 1.51 | |
| $Mn(B_3N_3H_6)_2$-$CO_2$[3] | — | — | — | −0.90 | 1.25 | 133 |
| $B_9C_3H_{12}$-$CO_2$[3] | — | — | — | −0.91 | 1.28 | 131 |
| | | | | | 1.29 | |
| $C_5NH_6$-$CO_2$[3] | — | — | — | −0.63 | 1.35 | 129 |
| $O_2H_5$-$CO_2$[4] | (a) | 0 | 1.30 | −0.75 | 1.26 | 126 |
| | (b) | 0.02 | 1.28 | −0.72 | 1.25 | 138 |
| $N_2H_7$-$CO_2$[4] | (a) | 0 | −0.03 | −0.77 | 1.23 | 139 |
| | (b) | 0.79 | −0.82 | −0.38 | 1.27 | 140 |
| $Al_{12}P$-$CO_2$[5] | (a) | 0 | — | −0.71 | 1.24 | 130 |
| | (b) | 0.11 | — | — | 1.97 | 125 |
| | (c) | 0.20 | — | — | 1.26 | 132 |
| $N_4Mg_6Li$-$CO_2$[6] | (a) | 0 | 1.57 | −0.79 | 1.28 | 125 |
| | (b) | 0.04 | 1.53 | −0.79 | | 126 |
| | (c) | 0.11 | 1.46 | −0.87 | | 123 |
| $Li_3F_2$-$CO_2$@$C_{60}$[7] | — | — | 1.84 | — | 1.20 | 132 |

[1]*Calculated at MP2/6-311+G (d) level in Ref. 35.*
[2]*Calculated at CBS-QB3 composite model in Ref. 41.*
[3]*Calculated at MP2/6-311+G (d) level in Ref. 19.*
[4]*Calculated at MP2/6-311+G (d,p) level in Ref. 42.*
[5]*Calculated at M06-2X/6-311+G (d) level in Ref. 43.*
[6]*Calculated at CCSD (T)/6-311+G (3df)//MP2/6-311+G (d) level in Ref. 22.*
[7]*Calculated at B3LYP/6-31G (d) level in Ref.44.*

and the other oxygen with the central Li atom. The isomer (a) possesses greater BE and therefore stronger intermolecular interaction than isomer (b) because the electron density is more localized between the two terminal Li atoms and two oxygen atoms.

The BE of $Li_3F_2$-$CO_2$ complexes is comparable to or smaller than the BE of superalkali ($FLi_2$, $OLi_3$, $NLi_4$)-$CO_2$ complexes reported by Srivastava [35]. The charge transfer to $CO_2$ in $Li_3F_2$-$CO_2$ isomers ranges from −0.63e to −0.88e (see **Table 1**). Thus, the charge on the $CO_2$ moiety along with its structure suggests that $CO_2$ is reduced to a $CO_2^-$ anion.

## Interaction With Special Superalkalis [$Al_3$, $Mn(B_3N_3H_6)_2$, $B_9C_3H_{12}$, $C_5NH_6$]

Zhao et al. [19] presented the rational design of superalkalis and studied the activation of $CO_2$ by these special superalkalis using MP2/6-311+G(d) level in the Gaussian 09 program. They analyzed the interaction of $CO_2$ with special superalkalis like $Al_3$, Mn $(B_3N_3H_6)_2$, $B_9C_3H_{12}$, and $C_5NH_6$, which leads to the complexes shown in **Figure 5**. The distance between the $CO_2$ moiety and superalkali clusters has been calculated as 1.950 Å, 1.730 Å, 2.320 Å, and 1.040 Å for $Al_3$, Mn $(B_3N_3H_6)_2$, $B_9C_3H_{12}$, and $C_5NH_6$, respectively. In the case of $Al_3$, O-C bonds extend to 1.290 and 1.510 Å, about 4.4–22% longer than those in the $CO_2^-$anion, whereas in $B_9C_3H_{12}$, the O-C bonds are extended to 1.290 and 1.280 Å, about 3.3–4.4% longer than those in $CO_2^-$. The bond extension in Mn $(B_3N_3H_6)_2$ and $C_5NH_6$ is observed to be 1.250 Å which is slightly longer than that of 1.240 Å in $CO_2^-$ and 1.35 Å which is about 9.3% longer than that in $CO_2^-$, respectively. The bond angle of O-C-O in $Al_3CO_2$, Mn $(B_3N_3H_6)_2CO_2$, $B_9C_3H_{12}CO_2$, and $C_5NH_6CO_2$ is 126°, 133°, 131°, and 129° making the bond bend by 8°, 3, 4, and 7% more than the corresponding value in $CO_2^-$. Thus, both the stretching of the O-C bonds and the bending of the O-C-O angle weaken the O-C bonds of $CO_2$, making it easy to activate.

The NPA charge has been listed in **Table 1** to show how much charge is transferred to $CO_2$. This transfer of charge results in the bending of $CO_2$ and weakens the $CO_2$ bond, and therefore making it easier to break. The amount of charge transferred from $Al_3$, Mn $(B_3N_3H_6)_2$, $B_9C_3H_{12}$, and $C_5NH_6$ to $CO_2$ are −1.26e, −0.90e, −0.91e, and −0.63e, respectively. Note that this amount of charge transferred from $Al_3$, Mn $(B_3N_3H_6)_2$, $B_9C_3H_{12}$ are greater than that of noble gas (0.77e) [47] being very close to unity, whereas in the case of $C_5NH_6$, the amount of charge transferred is less. From this analysis, one may note that although the IE of $Al_3$ is not the lowest among these four superalkalis (see **Figure 1**), the charge transferred is the most

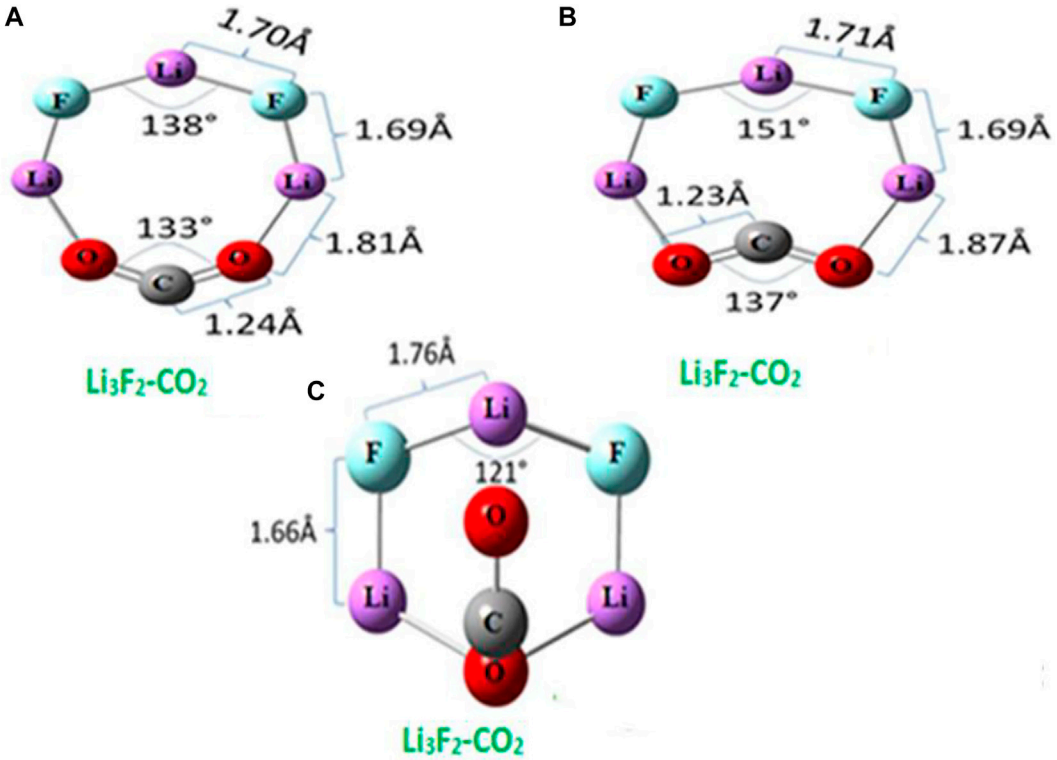


**FIGURE 4 |** Equilibrium structures of $CO_2$ complex with binuclear superalkali with bond lengths from Ref. 41 with the permission of the Royal Society of Chemistry.

and it is capable of bending the $CO_2$ molecule the most. This indicates that the quantitative nature of the activation of $CO_2$ depends on the electronic structure and size of the superalkalis, as seen in an earlier section.

## Interaction With Non-Metallic Superalkalis ($O_2H_5$, $N_2H_7$)

Kumar et al. [42] explored the scope of non-metallic superalkalis in the activation of $CO_2$. They studied the interaction of $CO_2$ with non-metallic superalkalis such as $O_2H_5$ and $N_2H_7$, employing the MP2/6-311++G (d,p) level *via* the Gaussian 09 program. The equilibrium structures of $O_2H_5$-$CO_2$ and $N_2H_7$-$CO_2$ are shown in **Figure 6**, and related parameters are listed in **Table 1**. It was noticed that in $O_2H_5$-$CO_2$ complexes, O atoms of $CO_2$ interact with the H-atom of superalkali, unlike in $N_2H_7$-$CO_2$, in which the C-atom of $CO_2$ interacts with the H-atom. This may be due to the repulsion between excess electrons of N and O atoms.

The (b) isomers of $O_2H_5$-$CO_2$ and $N_2H_7$-$CO_2$ are 0.24 and 0.78 eV, higher in energy in which $CO_2$ interacts through the O-atom as well as the C-atom in the $N_2H_7$-$CO_2$ isomer. The relative stability of isomers can be explained on the basis of H-bond interactions. For instance, the bond lengths of O-H and C-H are 2.060 Å and 3.710 Å, respectively. The BE of these complexes provides relative strength through the interaction of $CO_2$ with non-metallic superalkalis. From **Table 1**, the BE suggests that $O_2H_5$-$CO_2$ isomers are stable, whereas $N_2H_7$-$CO_2$ is slightly destabilized due to the negative value of BE.

From **Table 1**, the value of NPA charges of $CO_2$ is calculated to be −0.75e for $O_2H_5$-$CO_2$ and −0.77e for $N_2H_7$-$CO_2$ lowest energy structures (a). Thus, the NPA charge values are very close to each other. In isomer (b) of $O_2H_5$-$CO_2$ and $N_2H_7$-$CO_2$, the $CO_2$ moiety is bent, similar to that in its lowest energy structure. Therefore, the activation and the consequential reduction of $CO_2$ can also be possible by non-metallic superalkalis such as $O_2H_5$, if not by $N_2H_7$.

## Interaction With Polynuclear Species ($Al_{12}P$, $N_4Mg_6M$)

The compact (quasi) icosahedral $Al_{12}X$ (X = Be, Al, C, and P) clusters have been employed to analyze the dissociation and absorption of small gas molecules [48–54]. Zhang et al. [43] studied the interaction of $Al_{12}P$ superalkali with $CO_2$ using Minnesota density functional (M06-2X) [55] and 6-311+G(d) basis set in the Gaussian 09 program. They obtained three isomers of the $Al_{12}P$-$CO_2$ complex as shown in **Figure 7**. The lowest energy corresponds to the isomer (a) in which the interaction is mediated by both O atoms. The isomers (b) and (c) are found to have a high energy of 0.11 eV (2.64 kcal/mol) and 0.20 eV (4.52 kcal/mol), respectively. Obviously, the chemisorbed $CO_2$ molecule undergoes structural changes from linear to bending in each $Al_{12}P$-$CO_2$ isomer.

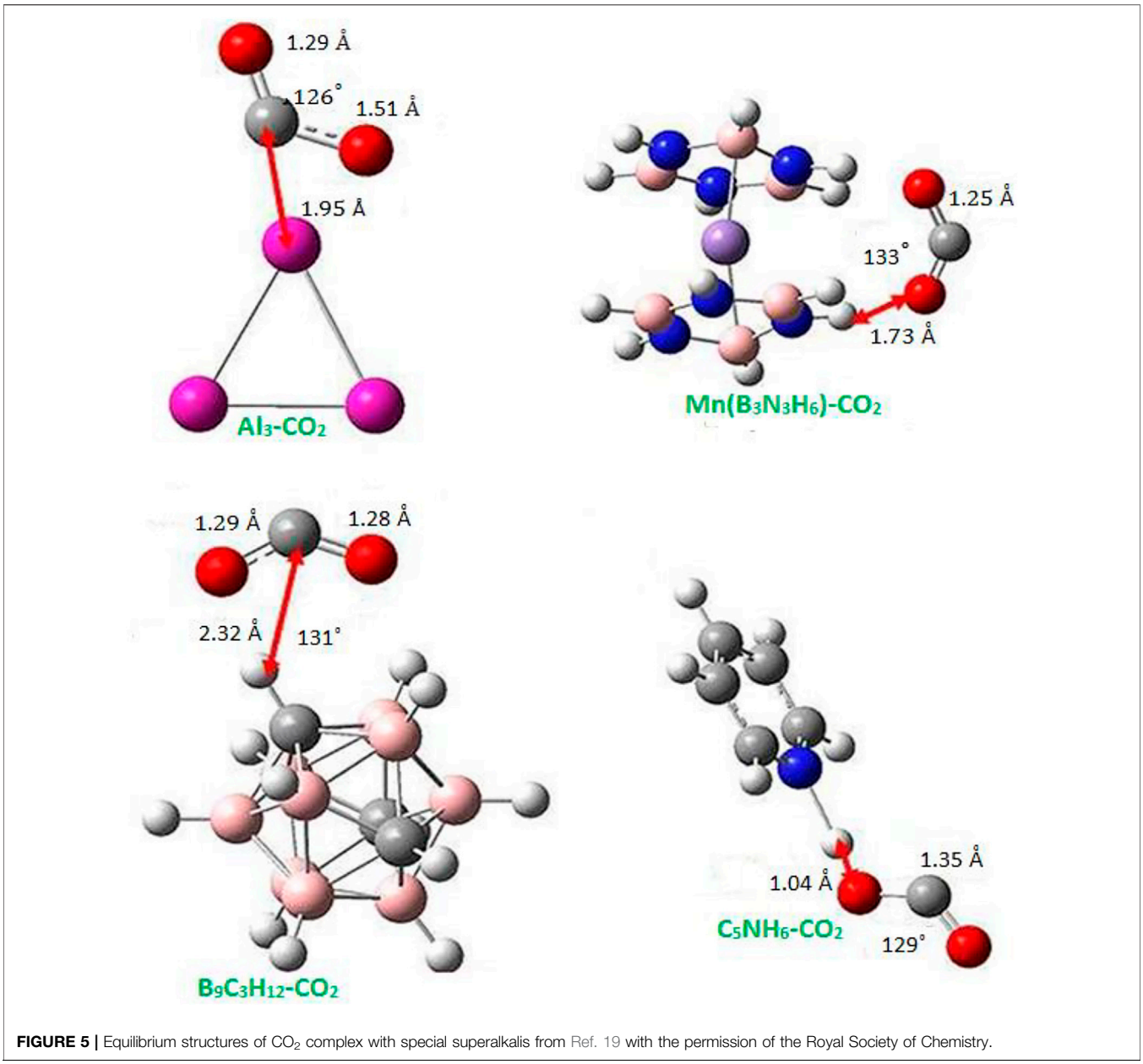


**FIGURE 5 |** Equilibrium structures of $CO_2$ complex with special superalkalis from Ref. 19 with the permission of the Royal Society of Chemistry.

They confined their analyses to the global minimum structure, that is, isomer (a). The bond distance of C-O in isomer (a) is 1.24 Å, which is found to be 7.6% larger than free $CO_2$ (1.15 Å), consequently, weakening the C-O bond. Moreover, the variation of the C-O-C angle from 180° to 130.4° in isomer (a) advocates the change in hybridization of carbon in $CO_2$ from *sp* to quasi-$sp^2$ after activation by $Al_{12}P$. Furthermore, the C-O bond is marginally larger (1.23 Å) as compared to isolated $CO_2^-$, whereas bond bending is also larger, about 4.7%, than that in isolated $CO_2^-$, which clearly supports the activation of $CO_2$ assimilated on the $Al_{12}P$ cluster. The computed total NPA charge on the $CO_2$ subunit is −0.707e, which shows the transfer of almost one electron charge from $Al_{12}P$ to $CO_2$ in the complex. Thus, $CO_2$ is successfully reduced to $CO_2^-$ anion. The low IE of $Al_{12}P$ superatom is the main source of $CO_2$ reduction as it facilitates the transfer of charge to $CO_2$, which ultimately results in the contraction of the O-C-O angle and the weakening of the C-O bond of the $CO_2$ moiety. The small activation barrier of 23 kcal/mol is calculated for the chemisorption of $CO_2$ on $Al_{12}P$ to form the $Al_{12}P$-$CO_2$ complex (a), which further suggests the application of $Al_{12}P$ as a potential catalyst for $CO_2$ conversion. It has been found that the $Al_{12}P$ complex shows high adsorption intensities in the visible region and, hence, promotes photocatalysis or photothermal catalysis of $CO_2$ and its transformation by absorbing sunlight.

Recently, Sikorska and Gaston [22] explored new superalkali species, $N_4Mg_6M$ (M = Li, Na, K) by performing the MP2/6-311+G(d) and single-point CCSD(T)/6-311+G (3df) calculations

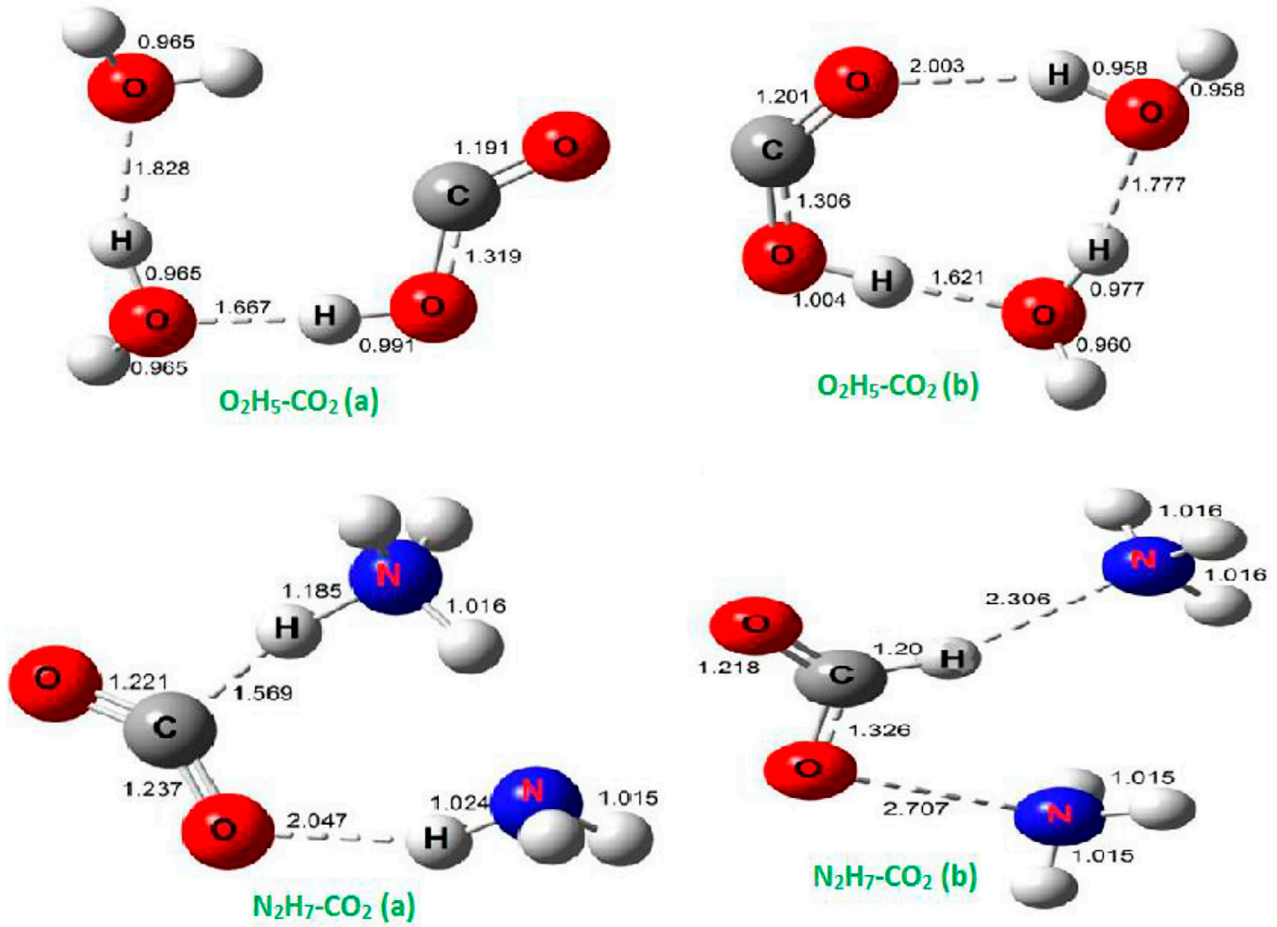


**FIGURE 6 |** Equilibrium structures of $CO_2$ complexes with non-metallic superalkalis from Ref. 42 with the permission of the Taylor & Francis.

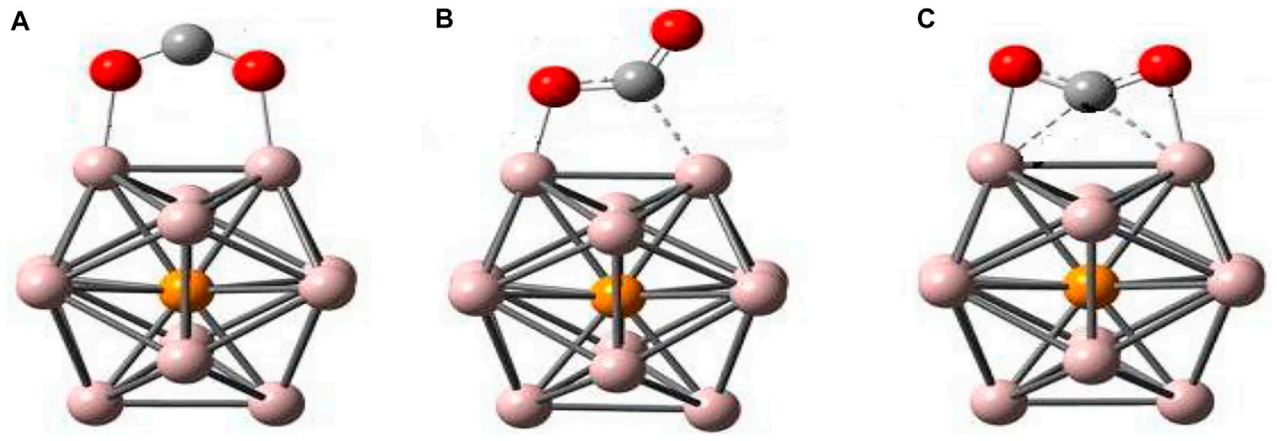


**FIGURE 7 |** Equilibrium structures of $CO_2$ complex with $Al_{12}P$ from Ref. 43 with the permission of Wiley.

Ref. 56 in the Gaussian 09 program. They studied the catalytic behavior of $N_4Mg_6Li$, $N_4Mg_6Na$, and $N_4Mg_6K$ for $CO_2$ activation. For the sake of brevity, we will discuss the interaction of $CO_2$ with $N_4Mg_6Li$ superalkali. $CO_2$ interacts with $N_4Mg_6M$ and the resultant $N_4Mg_6M$-$CO_2$ complexes are displayed in **Figure 8** for M = Li. In all isomers, the interaction between $CO_2$ and

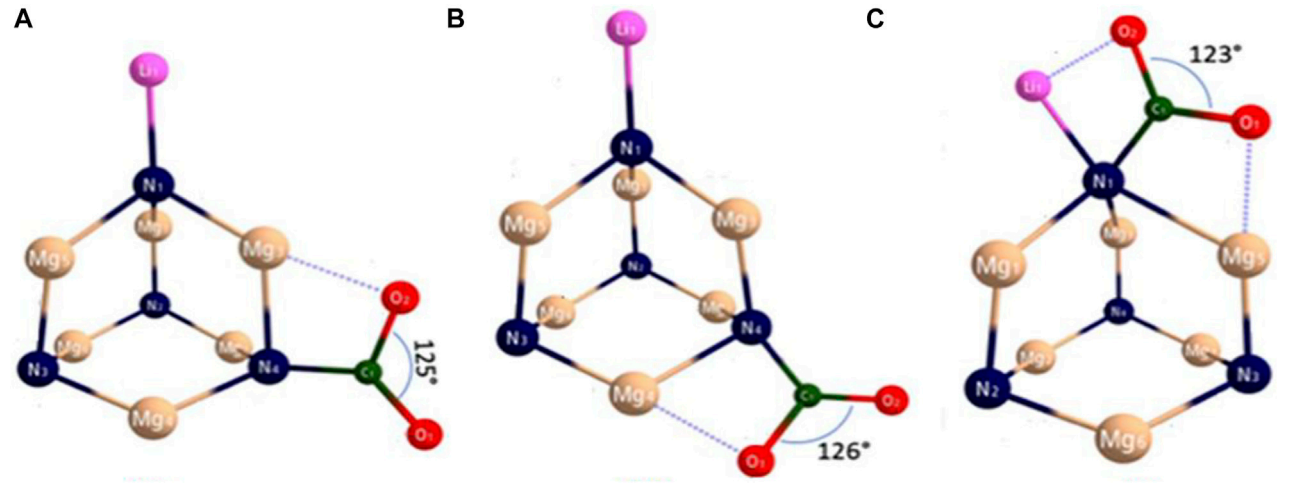


**FIGURE 8 |** Equilibrium structures of $CO_2$ complex with $N_4Mg_6Li$ from Ref. 22 with the permission of the American Institute of Physics.

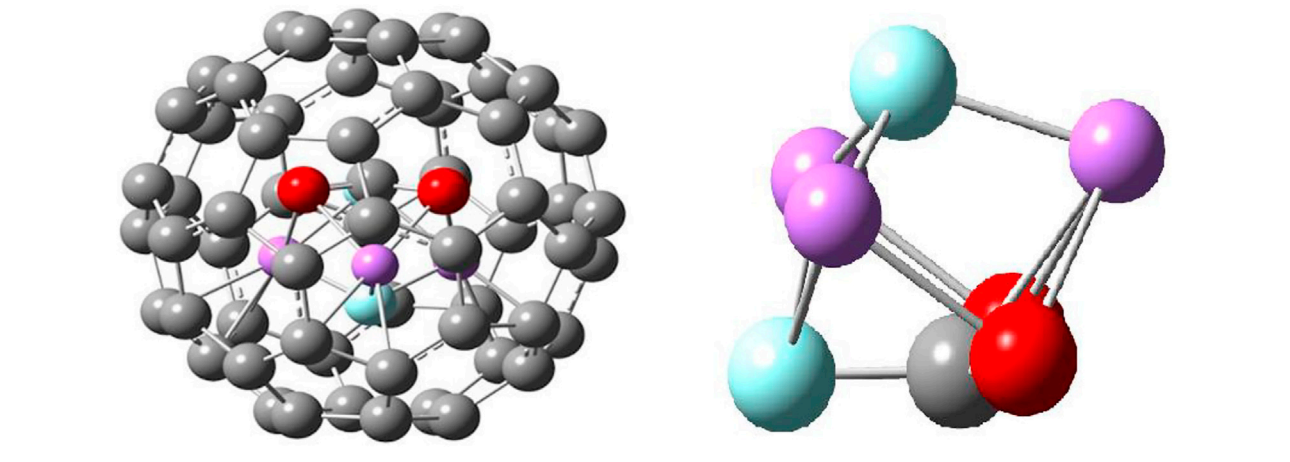

**FIGURE 9 |** Equilibrium structures of $[Li_3F_2\text{-}CO_2]@C_{60}$ endofullerene and $Li_3F_2\text{-}CO_2$ inside $C_{60}$ from Ref. 44.

$N_4Mg_6M$ takes place via the C-N bond of 1.452–1.454 Å, which supports the evolution of a single bond between carbon and nitrogen.

The isomers (b) and (c) are found to be 0.04 eV (0.97 kcal/mol) and 0.11 eV (2.48 kcal/mol) higher in energy than the lowest energy isomer (a) in the case of $N_4Mg_6Li\text{-}CO_2$. The binding energy of these isomers lies in the range of 1.46–1.57 eV (see **Table 1**). The C-O bond lengths, being in the range of 1.223–1.224 Å and 1.335–1.336 Å are indeed 8% larger than that of the $CO_2$ anion. Furthermore, the bending of the angle O-C-O, 123–126°, was 9% more than the angle of isolated $CO_2^-$. The NPA charge transferred from $N_4Mg_6M$ superalkalis to $CO_2$ varies from −0.799e to −0.806e. Ionization energy plays a major role in the activation process of $CO_2$, as the amount of transferred charge increases with the decrease in ionization energy because it is effortless to transfer charge from species with low ionization energy. Therefore, the extension of the bond distance of C-O along with the bending of angle O-C-O results in the weakening of C-O bonds of $CO_2$. Thus, the newly designed $N_4Mg_6M$ superalkalis could be used as a catalyst for $CO_2$ activation.

## Interaction With $Li_3F_2$ Superalkali Inside Buckminsterfullerene ($C_{60}$)

The interaction of $CO_2$ with the binuclear $Li_3F_2$ superalkali was reported by Park and Meloni as discussed in an earlier section. Recently, Meloni et al. [44] investigated the interaction of $CO_2$ with $Li_3F_2$ inside fullerene ($C_{60}$) by using B3LYP [57, 58] with the 6-31G (d) basis set in the Gaussian 09 program. They noticed two important features. When $CO_2$ is encapsulated within $C_{60}$, it gets destabilized as its binding energy is −147 kJ/mol. The $Li_3F_2$ inside $C_{60}$ assumes trigonal bipyramidal ($D_{3h}$) geometry with a binding energy of 119 kJ/mol, unlike the free

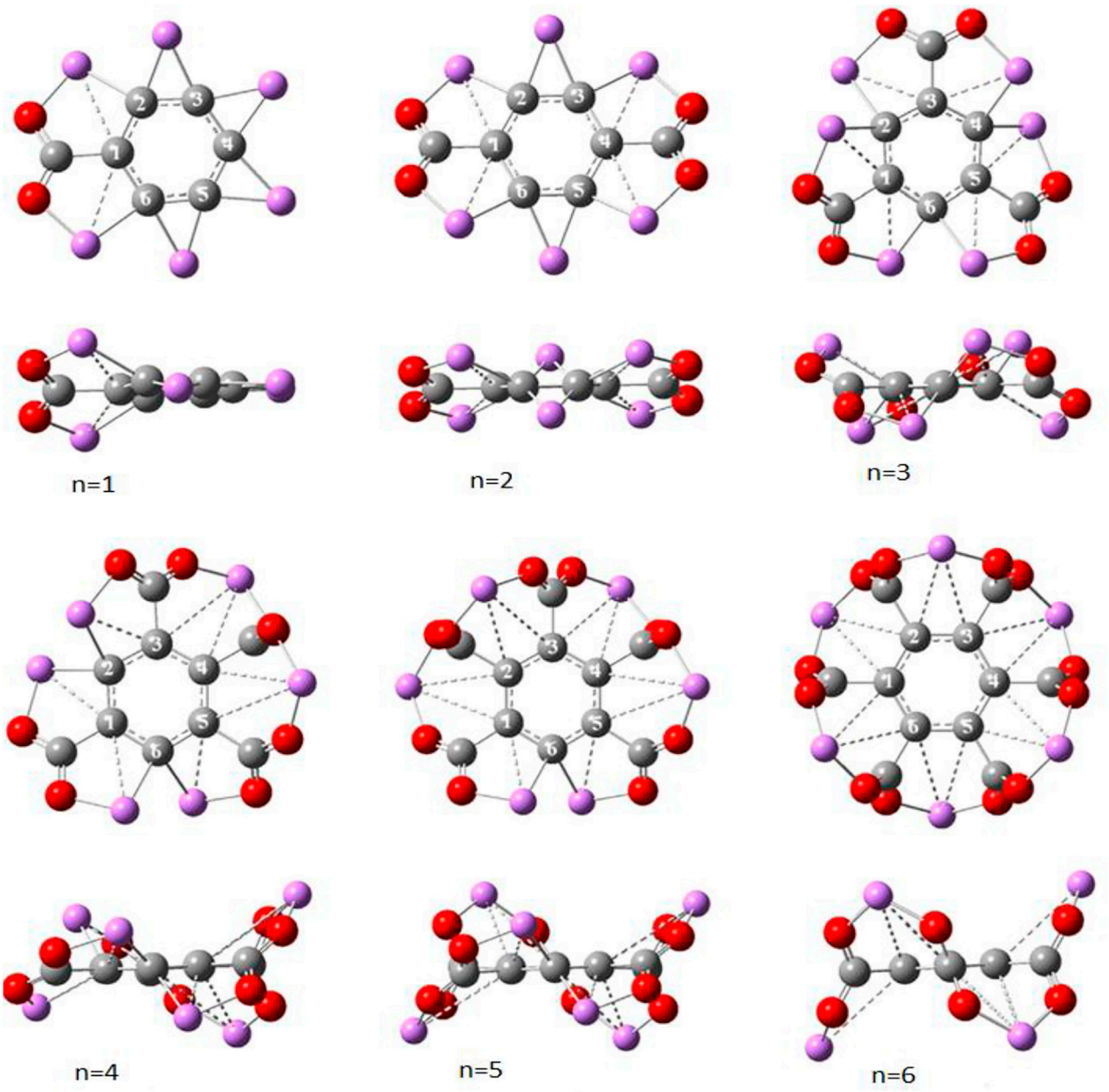


**FIGURE 10 |** Optimized structure of $C_6Li_6$-$nCO_2$ complexes (front and side views) for $n$ = 1–6 from Ref. 63 with the permission of Wiley.

$Li_3F_2$ linear cluster (see **Figure 1**). Thus, $C_{60}$ strongly interacts with $Li_3F_2$ and there is no reduction of $C_{60}$.

The unforeseen result has been noticed on insertion of $CO_2$ inside $Li_3F_2(D_3h)@C_{60}$ endofullerene, as displayed in **Figure 9**. On the inspection of the geometry inside the $C_{60}$, it was found that $CO_2$ has been activated by making a ∠OCO 132° and that the bond length of C-O has been increased to 1.20 Å. The activation of $CO_2$ has been attained by the transfer of F atom from $Li_3F_2$ to $CO_2$, due to the F-C interaction with the bond distance of 1.38 Å. Thus, the endo-reaction simulates a non-planar (trigonal pyramidal) $FCO_2$ interacting with the $FLi_3$-like species (also shown in **Figure 9**). There have been several studies [59, 60] in which the structures and interactions between species are greatly modified by encapsulation within $C_{60}$.

## Interaction With $C_6Li_6$: Capture and Storage of $CO_2$

Thus, the strong reducing power enables superalkalis to reduce $CO_2$ as well as several other molecules [61, 62], So far, it has been found that the superalkalis are restricted to activate one $CO_2$

**TABLE 2 |** ωB97xD/6-311+G (d) calculated NBO charge on $CO_2$ ($\Delta q$), adsorption energy per $CO_2$ ($E_{ad}$), and consecutive adsorption energy ($\Delta E_{ad}$) for $C_6Li_6$-$nCO_2$ complexes taken from Ref. 63.

| System | $\Delta q$ (e) | $E_{ad}$ (eV) | $\Delta E_{ad}$ (eV) |
|---|---|---|---|
| $C_6Li_6$-$CO_2$ | −0.829 | 3.18 | 3.18 |
| $C_6Li_6$-$2CO_2$ | −0.827 | 3.16 | 3.11 |
| $C_6Li_6$-$3CO_2$ | −0.826 | 3.31 | 3.63 |
| $C_6Li_6$-$4CO_2$ | −0.807 | 3.07 | 2.33 |
| $C_6Li_6$-$5CO_2$ | −0.790 | 2.91 | 2.27 |
| $C_6Li_6$-$6CO_2$ | −0.770 | 2.79 | 2.21 |

molecule per unit, that is, only one $CO_2$ molecule is reduced by a superalkali. This may limit the capture and storage of superalkalis for practical applications. Srivastava [63] reported that a single molecule of hexalithiobenzene ($C_6Li_6$) is not only capable of reducing but also capturing up to six $CO_2$ molecules sequentially using the ωB97xD functional [64] and 6-311+G(d) basis set in the Gaussian 09 program. The planar $C_6Li_6$ molecule has equal ring bond lengths of 1.418 Å, whose IE is reported to be lower than that of Li, thereby characterizing it as a superalkali molecule [25]. Note that planar star-like $C_6Li_6$ has been previously studied by several groups [65–67]. The sequential interaction of $CO_2$ molecules with $C_6Li_6$ results in the $C_6Li_6$-$nCO_2$ complexes as displayed in **Figure 10**.

The interaction between $CO_2$ and $C_6Li_6$ is mediated by one C-C and two Li-O bonds in these complexes. The $C_6Li_6$ ring moiety in $C_6Li_6$-$nCO_2$is deviated from planarity due to the out-of-plane displacement of Li atoms because of the Coulomb-repulsion between neighboring Li-atoms for $n$ = 1, 2, 4, and 5. However, both $C_6Li_6$-$3CO_2$ and $C_6Li_6$-$6CO_2$ possess the perfect planar ring moiety, having equal bond lengths of 1.42 Å and 1.40 Å, respectively. The $CO_2$ moiety in $C_6Li_6$-$CO_2$ has a bond length and an angle of 1.26 Å and 122.5°, respectively. With an increase in the number of $CO_2$, the average bond length and the average bond angle of $CO_2$ decrease and increase continuously up to 1.25 Å and 125.2°, respectively, for $C_6Li_6$-$6CO_2$.

The activation of $CO_2$ leads to an increase in the bond length and a decrease in the bond angle by bending. **Table 2** lists the NBO charge ($\Delta q$) located at $CO_2$ moieties, adsorption (binding) energy ($E_{ad}$) per $CO_2$ molecule, and consecutive adsorption energy ($\Delta E_{ad}$). It is clear that the $\Delta q$ of $C_6Li_6$-$nCO_2$ becomes −0.83e, −0.81e, −0.79e, and −0.77e for $n$ = 1–3, $n$ = 4, $n$ = 5, and $n$ = 6, respectively. This suggests that $C_6Li_6$ can be employed in the activation of all $CO_2$ molecules and, consequently, their adsorption. One can note that the $E_{ad}$ values are fairly large, ranging from 3.18 to 2.79 eV per $CO_2$, which predicts the stability of these $C_6Li_6$-$nCO_2$ complexes. It is to be noticed that the adsorption of molecules is not feasible with negative $\Delta E_{ad}$ values, whereas sequential adsorption becomes feasible with positive $\Delta E_{ad}$ values. Thus, the study suggests that $C_6Li_6$ is not only capable of activation but also effective in the sequential adsorption of six $CO_2$ molecules.

## CONCLUSION AND PERSPECTIVE

In summary, we have discussed the activation of $CO_2$ using various superalkalis. $CO_2$ is said to be activated when the charge is transferred to $CO_2$ from superalkali clusters, which ultimately results in the transformation of the linear structure of $CO_2$ to the bent structure of $CO_2^-$. Based on quantum chemical methods, $CO_2$ is successfully reduced to $CO_2^-$ by using typical superalkalis ($FLi_2$, $OLi_3$, and $NLi_4$), binuclear superalkali ($Li_3F_2$), special superalkalis ($Al_3$, $Mn(B_3N_3H_6)_2$, $B_9C_3H_{12}$, $C_5NH_6$), polynuclear superalkalis ($Al_{12}P$, $N_4Mg_6M$), and non-metallic superalkalis ($O_2H_5$ and $N_2H_7$). It was noticed that the amount of charge transfer depends on the electronic structure, size, and ionization energy of superalkalis. The activation of $CO_2$ by $Li_3F_2$ inside $C_{60}$ fullerene has also been discussed. It was also revealed that the $C_6Li_6$ molecule is not only capable of activating $CO_2$ but also capturing up to six $CO_2$ molecules. These results suggest that the superalkalis might be used as efficient catalysts for $CO_2$ activation. Thus, this activated $CO_2$ ion can be converted into fuel, such as methanol [68] *via* hydrogenation reaction.

## AUTHOR CONTRIBUTIONS

HS: literature survey, data collection, writing draft. AKS: conceptualization, supervision, editing, and finalizing the draft.

## REFERENCES


1. Mirzaei S, Shamiri A, Aroua MK. Simulation of Aqueous Blend of Monoethanolamine and Glycerol for Carbon Dioxide Capture from Flue Gas. *Energy Fuels* (2016) 30(11):9540–53. doi:10.1021/acs.energyfuels.6b01230
2. Andreoni W, Pietrucci F. CO2 Capture in Amine Solutions: Modelling and Simulations with Non-empirical Methods. *J Phys Condens Matter* (2016) 28(50):503003. doi:10.1088/0953-8984/28/50/503003
3. Yeh JT, Resnik KP, Rygle K, Pennline HW. Semi-batch Absorption and Regeneration Studies for CO2 Capture by Aqueous Ammonia. *Fuel Process Tech* (2005) 86(14-15):1533–46. doi:10.1016/j.fuproc.2005.01.015
4. Kim HR, Yoon T-U, Kim S-I, An J, Bae Y-S, Lee CY. Beyond Pristine MOFs: Carbon Dioxide Capture by Metal-Organic Frameworks (MOFs)-Derived Porous Carbon Materials. *RSC Adv* (2017) 7:1266–70. doi:10.1039/c6ra26824b
5. Jiang J-X, Su F, Trewin A, Wood CD, Campbell NL, Niu H, et al. Conjugated Microporous Poly(aryleneethynylene) Networks. *Angew Chem Int Ed* (2008) 47(7):1167. doi:10.1002/anie.200890021
6. Plaza MG, García S, Rubiera F, Pis JJ, Pevida C. Post-combustion CO2 Capture with a Commercial Activated Carbon: Comparison of Different Regeneration Strategies. *Chem Eng J* (2010) 163(1-2):41–7. doi:10.1016/j.cej.2010.07.030
7. Wang L, Zhao J, Zhou Z, Zhang SB, Chen Z. First-principles Study of Molecular Hydrogen Dissociation on Doped Al12X (X = B, Al, C, Si, P, Mg, and Ca) Clusters. *J Comput Chem* (2009) 30(15):2509–14. doi:10.1002/jcc.21239
8. Centi G, Perathoner S. Opportunities and Prospects in the Chemical Recycling of Carbon Dioxide to Fuels. *Catal Today* (2009) 148(3-4):191–205. doi:10.1016/j.cattod.2009.07.075
9. Qiao J, Liu Y, Hong F, Zhang J. A Review of Catalysts for the Electroreduction of Carbon Dioxide to Produce Low-Carbon Fuels. *Chem Soc Rev* (2014) 43(2):631–75. doi:10.1039/c3cs60323g

10. Schröder D, Schalley CA, Harvey JN, Schwarz H. On the Formation of the Carbon Dioxide Anion Radical $CO_2^{-\cdot}$ in the Gas Phase. *Int J Mass Spectrom* (1999) 185-187:25–35. doi:10.1016/s1387-3806(98)14042-3
11. Sommerfeld T, Meyer H-D, Cederbaum LS. Potential Energy Surface of the CO2? Anion. *Phys Chem Chem Phys* (2004) 6(1):42. doi:10.1039/b312005h
12. Wang L-S, Reutt JE, Lee YT, Shirley DA. High Resolution UV Photoelectron Spectroscopy of CO+2, COS+ and CS+2 Using Supersonic Molecular Beams. *J Electron Spectrosc Relat Phenomena* (1988) 47:167–86. doi:10.1016/0368-2048(88)85010-2
13. Czapla M, Skurski P. Oxidizing CO2 with Superhalogens. *Phys Chem Chem Phys* (2017) 19(7):5435–40. doi:10.1039/c6cp08043j
14. Gutsev GL, Boldyrev AI. DVM-xα Calculations on the Ionization Potentials of MXk+1− Complex Anions and the Electron Affinities of MXk+1 "superhalogens". *Chem Phys* (1981) 56(3):277–83. doi:10.1016/0301-0104(81)80150-4
15. Gutsev GL, Boldyrev AI. DVM Xα Calculations on the Electronic Structure of "superalkali" Cations. *Chem Phys Lett* (1982) 92:262–6. doi:10.1016/0009-2614(82)80272-8
16. Weber JM. The Interaction of Negative Charge with Carbon Dioxide - Insight into Solvation, Speciation and Reductive Activation from Cluster Studies. *Int Rev Phys Chem* (2014) 33(4):489–519. doi:10.1080/0144235x.2014.969554
17. Tong J, Li Y, Wu D, Li Z-R, Huang X-R. Ab Initio Investigation on a New Class of Binuclear Superalkali Cations M2Li2k+1+ (F2Li3+, O2Li5+, N2Li7+, and C2Li9+). *J Phys Chem A* (2011) 115(10):2041–6. doi:10.1021/jp110417z
18. Hou N, Li Y, Wu D, Li Z-R. Do nonmetallic Superalkali Cations Exist? *Chem Phys Lett* (2013) 575:32–5. doi:10.1016/j.cplett.2013.05.014
19. Zhao T, Wang Q, Jena P. Rational Design of Super-alkalis and Their Role in CO2activation. *Nanoscale* (2017) 9:4891–7. doi:10.1039/c7nr00227k
20. Molina B, Soto JR, Castro JJ. Stability and Nonadiabatic Effects of the Endohedral Clusters X@Al12 (X = B, C, N, Al, Si, P) with 39, 40, and 41 Valence Electrons. *J Phys Chem C* (2012) 116(16):9290–9. doi:10.1021/jp3004135
21. Akutsu M, Koyasu K, Atobe J, Hosoya N, Miyajima K, Mitsui M, et al. Experimental and Theoretical Characterization of Aluminum-Based Binary Superatoms of Al12X and Their Cluster Salts. *J Phys Chem A* (2006) 110(44):12073–6. doi:10.1021/jp065161p
22. Sikorska C, Gaston N. N4Mg6M (M = Li, Na, K) Superalkalis for CO2 Activation. *J Chem Phys* (2020) 153(14):144301. doi:10.1063/5.0025545
23. Sun W-M, Li Y, Wu D, Li Z-R. Designing Aromatic Superatoms. *J Phys Chem C* (2013) 117(46):24618–24. doi:10.1021/jp408810e
24. Giri S, Reddy GN, Jena P. Organo-Zintl Clusters [P7R4]: A New Class of Superalkalis. *J Phys Chem Lett* (2016) 7(5):800–5. doi:10.1021/acs.jpclett.5b02892
25. Srivastava AK. Organic Superalkalis with Closed-Shell Structure and Aromaticity. *Mol Phys* (2018) 116(12):1642–9. doi:10.1080/00268976.2018.1438678
26. Yang H, Li Y, Wu D, Li Z-R. Structural Properties and Nonlinear Optical Responses of Superatom Compounds BF4 -M (M = Li, FLi2 , OLi3 , NLi4 ). *Int J Quan Chem.* (2012) 112:770–8. doi:10.1002/qua.23053
27. Li Y, Wu D, Li Z-R. Compounds of Superatom Clusters: Preferred Structures and Significant Nonlinear Optical Properties of the BLi6-X (X = F, LiF2, BeF3, BF4) Motifs. *Inorg Chem* (2008) 47(21):9773–8. doi:10.1021/ic800184z
28. Giri S, Behera S, Jena P. Superalkalis and Superhalogens as Building Blocks of Supersalts. *J Phys Chem A* (2014) 118(3):638–45. doi:10.1021/jp4115095
29. Srivastava AK, Misra N. Superalkali-hydroxides as strong Bases and Superbases. *New J Chem* (2015) 39(9):6787–90. doi:10.1039/c5nj01259g
30. Srivastava AK, Misra N. OLi3O− Anion: Designing the Strongest Base to Date Using OLi3 Superalkali. *Chem Phys Lett* (2016) 648:152–5. doi:10.1016/j.cplett.2016.02.010
31. Winfough M, Meloni G. Ab Initio analysis on Potential Superbases of Several Hyperlithiated Species: Li3F2O and Li3F2OHn (N = 1, 2). *Dalton Trans* (2017) 47(1):159–68. doi:10.1039/c7dt03579a
32. Chen W, Li Z-R, Wu D, Li Y, Li R-Y, Sun C-C. Inverse Sodium Hydride: Density Functional Theory Study of the Large Nonlinear Optical Properties. *J Phys Chem A* (2005) 109(12):2920–4. doi:10.1021/jp044541c
33. Sun W-M, Fan L-T, Li Y, Liu J-Y, Wu D, Li Z-R. On the Potential Application of Superalkali Clusters in Designing Novel Alkalides with Large Nonlinear Optical Properties. *Inorg Chem* (2014) 53(12):6170–8. doi:10.1021/ic500655s
34. Srivastava AK, Misra N. Competition between Alkalide Characteristics and Nonlinear Optical Properties in OLi3MLi3O (M = Li, Na, and K) Complexes. *Int J Quan Chem.* (2017) 117(3):208–12. doi:10.1021/ic500655s10.1002/qua.25313
35. Srivastava AK. Single- and Double-Electron Reductions of CO2 by Using Superalkalis: An Ab Initio Study. *Int J Quan Chem.* (2018) 118:e25598. doi:10.1002/qua.25598
36. Compton RN, Reinhardt PW, Cooper CD. Collisional Ionization of Na, K, and Cs by CO2, COS, and CS2: Molecular Electron Affinities. *J Chem Phys* (1975) 63(9):3821. doi:10.1063/1.431875
37. Knapp M, Echt O, Kreisle D, Märk TD, Recknagel E. Formation of long-lived $CO_2^-$, $N_2O^-$, and their dimer anions, by electron attachment to van der waals clusters. *Chem Phys Lett* (1986) 126(3):225–31. doi:10.1016/s0009-2614(86)80074-4
38. Gutsev GL, Bartlett RJ, Compton RN. Electron Affinities of CO2, OCS, and CS2. *J Chem Phys* (1998) 108:6756–62. doi:10.1063/1.476091
39. Møller C, Plesset MS. Note on an Approximation Treatment for Many-Electron Systems. *Phys Rev* (1934) 46(7):618–22. doi:10.1103/physrev.46.618
40. Frisch MJ, Trucks GW, Schlegel HB, Scuseria GE, Robb MA, Cheeseman JR, et al. *Gaussian 09,* Revision C02. Wallingford, CT: Gaussian, Inc. (2009).
41. Park H, Meloni G. Reduction of Carbon Dioxide with a Superalkali. *Dalton Trans* (2017) 46:11942–9. doi:10.1039/c7dt02331f
42. Kumar R, Kumar A, Srivastava AK, Misra N. Ab Initio investigations on the Interaction of CO2 and Non-metallic Superalkalis: Structure, Stability and Electronic Properties. *Mol Phys* (2021) 119(6):e1841311. doi:10.1080/00268976.2020.1841311
43. Zhang XL, Zhang L, Ye YL, Li XH, Ni BL, Li Y, et al. On the Role of Alkali-Metal-Like Superatom Al 12 P in Reduction and Conversion of Carbon Dioxide. *Chem Eur J* (2020) 27(3):1039–45. doi:10.1002/chem.202003733
44. Meloni G, Giustini A, Park H. CO2 Activation within a Superalkali-Doped Fullerene. *Front Chem* (2021) 9:712960. doi:10.3389/fchem.2021.712960
45. Reed AE, Weinstock RB, Weinhold F. Natural Population Analysis. *J Chem Phys* (1985) 83(2):735–46. doi:10.1063/1.449486
46. Montgomery JA, Frisch MJ, Ochterski JW, Petersson GA. A Complete Basis Set Model Chemistry. VI. Use of Density Functional Geometries and Frequencies. *J Chem Phys* (1999) 110(6):2822–7. doi:10.1063/1.477924
47. Zhang X, Liu G, Meiwes-Broer KH, Ganteför G, Bowen K. CO 2 Activation and Hydrogenation by PtH N − Cluster Anions. *Angew Chem Int Ed* (2016) 55(33):9644–7. doi:10.1002/ange.20160430810.1002/anie.201604308
48. Wang Y, LeVan MD. Adsorption Equilibrium of Carbon Dioxide and Water Vapor on Zeolites 5A and 13X and Silica Gel: Pure Components. *J Chem Eng Data* (2009) 54(10):2839–44. doi:10.1021/je800900a
49. Henry DJ, Yarovsky I. Dissociative Adsorption of Hydrogen Molecule on Aluminum Clusters: Effect of Charge and Doping. *J Phys Chem A* (2009) 113:2565–71. doi:10.1021/jp809619q
50. Lu QL, Chen LL, Wan JG, Wang GH. First Principles Studies on the Interaction of O2 with X@Al12 (X = Al−, P+, C, Si) Clusters. *J Comput Chem* (2010) 31(15):2804–9. doi:10.1002/jcc.21573
51. Zhao J-Y, Zhao F-Q, Xu S-Y, Ju X-H. DFT Studies on Doping Effect of Al12X: Adsorption and Dissociation of H2O on Al12X Clusters. *J Phys Chem A* (2013) 117(10):2213–22. doi:10.1021/jp309422p
52. Zhao J-Y, Zhang Y, Zhao F-Q, Ju X-H. Adsorption of Carbon Dioxide on Al12X Clusters Studied by Density Functional Theory: Effect of Charge and Doping. *J Phys Chem A* (2013) 117:12519–28. doi:10.1021/jp405934w
53. Zhao J-Y, Zhao F-Q, Xu S-Y, Ju X-H. Theoretical Study of the Geometries and Decomposition Energies of CO2 on Al12X: Doping Effect of Al12X. *J Mol Graphics Model* (2014) 48:9–17. doi:10.1016/j.jmgm.2013.11.002
54. Chakraborty D, Chattaraj PK. Reactions Involving Some Gas Molecules through Sequestration on Al12 Be Cluster: An Electron Density Based Study. *J Comput Chem* (2017) 39(10):535–45. doi:10.1002/jcc.25092
55. Zhao Y, Truhlar DG. The M06 Suite of Density Functionals for Main Group Thermochemistry, Thermochemical Kinetics, Noncovalent Interactions, Excited States, and Transition Elements: Two New Functionals and Systematic Testing of Four M06-Class Functionals and 12 Other

Functionals. *Theor Chem Account* (2008) 120(1-3):215–41. doi:10.1007/s00214-007-0310-x
56. Watts JD, Gauss J, Bartlett RJ. Coupled-cluster Methods with Noniterative Triple Excitations for Restricted Open-shell Hartree-Fock and Other General Single Determinant Reference Functions. Energies and Analytical Gradients. *J Chem Phys* (1993) 98(11):8718–33. doi:10.1063/1.464480
57. Becke AD. Density-functional Exchange-Energy Approximation with Correct Asymptotic Behavior. *Phys Rev A* (1988) 38:3098–100. doi:10.1103/physreva.38.30910.1103/physreva.38.3098
58. Lee C, Yang W, Parr RG. Development of the Colle-Salvetti Correlation-Energy Formula into a Functional of the Electron Density. *Phys Rev B* (1988) 37:785–9. doi:10.1103/physrevb.37.785
59. Ramachandran CN, Sathyamurthy N. Water Clusters in a Confined Nonpolar Environment. *Chem Phys Lett* (2005) 410(4-6):348–51. doi:10.1016/j.cplett.2005.04.113
60. Srivastava AK, Pandey SK, Misra N. (CH3Br···NH3)@C60: The Effect of Nanoconfinement on Halogen Bonding. *Chem Phys Lett* (2016) 662:240–3. doi:10.1016/j.cplett.2016.09.036
61. Srivastava AK. Reduction of Nitrogen Oxides (NO ) by Superalkalis. *Chem Phys Lett* (2018) 695:205–10. doi:10.1016/j.cplett.2018.02.029
62. Srivastava AK. DFT and QTAIM Studies on the Reduction of Carbon Monoxide by Superalkalis. *J Mol Graphics Model* (2021) 102:107765. doi:10.1016/j.jmgm.2020.107765
63. Srivastava AK. CO 2 -activation and Enhanced Capture by C 6 Li 6 : A Density Functional Approach. *Int J Quan Chem.* (2019) 119:e25904. doi:10.1002/qua.25904
64. Chai J-D, Head-Gordon M. Long-range Corrected Hybrid Density Functionals with Damped Atom-Atom Dispersion Corrections. *Phys Chem Chem Phys* (2008) 10(44):6615–20. doi:10.1039/b810189b
65. Xie Y, Schaefer HF, III. Hexalithiobenzene: a $D_6$h Equilibrium Geometry with Six Lithium Atoms in Bridging Positions. *Chem Phys Lett* (1991) 179(5-6):563–7. doi:10.1016/0009-2614(91)87104-j
66. Smith BJ. Hexalithiobenzene: beauty Is in the Eye of the Beholder. *Chem Phys Lett* (1993) 207(4-6):403–6. doi:10.1016/0009-2614(93)89021-9
67. Bachrach SM, Miller JV. Structures and Relative Energies of Polylithiated Benzenes. *J Org Chem* (2002) 67(21):7389–98. doi:10.1021/jo02592010.1021/jo025920
68. Liu X, Song Y, Geng W, Li H, Xiao L, Wu W. Cu-Mo2C/MCM-41: An Efficient Catalyst for the Selective Synthesis of Methanol from CO2. *Catalysts* (2016) 6(5):75. doi:10.3390/catal6050075

**Conflict of Interest:** The authors declare that the research was conducted in the absence of any commercial or financial relationships that could be construed as a potential conflict of interest.

**Publisher's Note:** All claims expressed in this article are solely those of the authors and do not necessarily represent those of their affiliated organizations, or those of the publisher, the editors, and the reviewers. Any product that may be evaluated in this article, or any claim that may be made by its manufacturer, is not guaranteed or endorsed by the publisher.

frontiers | Frontiers in Chemistry

ORIGINAL RESEARCH
published: 08 April 2022
doi: 10.3389/fchem.2022.868782

# Boron Oxide $B_5O_6^-$ Cluster as a Boronyl-Based Inorganic Analog of Phenolate Anion

*Shu-Juan Gao*[1,2], *Jin-Chang Guo*[1]* and *Hua-Jin Zhai*[1]*

[1]Nanocluster Laboratory, Institute of Molecular Science, Shanxi University, Taiyuan, China, [2]Department of Chemistry and Chemical Engineering, Lvliang University, Lvliang, China

Boron oxide clusters have structural richness and exotic chemical bonding. We report a quantum chemical study on the binary $B_5O_6^-$ cluster, which is relatively oxygen-rich. A global structural search reveals planar $C_{2v}$ ($^1A_1$) geometry as the global minimum structure, featuring a heteroatomic hexagonal $B_3O_3$ ring as its core. The three unsaturated B sites are terminated by two boronyl (BO) groups and an $O^-$ ligand. The $B_5O_6^-$ cluster can be faithfully formulated as $B_3O_3(BO)_2O^-$. This structure is in stark contrast to that of its predecessors, $C_s$ $B_5O_5^-$ and $T_d$ $B_5O_4^-$, both of which have a tetrahedral B center. Thus, there exists a major structural transformation in $B_5O_n^-$ series upon oxidation, indicating intriguing competition between tetrahedral and heterocyclic structures. The chemical bonding analyses show weak 6π aromaticity in the $B_5O_6^-$ cluster, rendering it a boronyl analog of phenolate anion ($C_6H_5O^-$) or boronyl boroxine. The calculated vertical detachment energy of $B_5O_6^-$ cluster is 5.26 eV at PBE0, which greatly surpasses the electron affinities of halogens (Cl: 3.61 eV), suggesting that the cluster belongs to superhalogen anions.

**Keywords: boron oxide clusters, boronyl, heteroatomic hexagonal $B_3O_3$ ring, chemical bonding, superhalogen anions**

OPEN ACCESS

***Edited by:***
*Ambrish Kumar Srivastava, Deen Dayal Upadhyay Gorakhpur University, India*

***Reviewed by:***
*Piotr Skurski, University of Gdansk, Poland*
*Celina Sikorska, The University of Auckland, New Zealand*

***Correspondence:**
*Jin-Chang Guo*
*guojc@sxu.edu.cn*
*Hua-Jin Zhai*
*hj.zhai@sxu.edu.cn*

***Specialty section:***
*This article was submitted to Physical Chemistry and Chemical Physics, a section of the journal Frontiers in Chemistry*

***Received:*** *03 February 2022*
***Accepted:*** *04 March 2022*
***Published:*** *08 April 2022*

***Citation:***
*Gao S-J, Guo J-C and Zhai H-J (2022) Boron Oxide $B_5O_6^-$ Cluster as a Boronyl-Based Inorganic Analog of Phenolate Anion. Front. Chem. 10:868782. doi: 10.3389/fchem.2022.868782*

## INTRODUCTION

Boron is an electron-deficient element with the capacity to build strong covalent bonds with other elements. Owing to boron's high affinity to oxygen, boron oxide clusters readily form, exhibiting usual structures and exotic chemical bonding (Doyle, 1988; Peiris et al., 1997; Zhai et al., 2007a; Zhai et al., 2007b; Drummond et al., 2007; Li et al., 2008; Shao et al., 2009; Tai and Nguyen, 2009; Yao et al., 2009; Braunschweig et al., 2010; Tai et al., 2010; Zhai et al., 2011; Guo et al., 2013; Li et al., 2013; Miao et al., 2013; Zhai et al., 2014a; Chen et al., 2014; Tian et al., 2015a; Tian et al., 2015b; Zhao et al., 2016; Li et al., 2018; Feng et al., 2019; Li et al., 2019). Elemental boron clusters are intrinsically electron-deficient themselves (Zhai et al., 2003; Alexandrova et al., 2006), and therefore boron oxide clusters are anticipated to be even more electron-deficient. In boron-rich oxide clusters, the boronyl (BO) group has recently emerged as an interesting inorganic ligand (Zhai et al., 2014a), which features a robust B≡O triple bond. In fact, the diatomic BO and $BO^-$ species are isoelectronic to CN and $CN^-$/CO, respectively. In addition, boronyl is a monovalent σ radical, thus leading to isolobal analogy between the BO and H ligands. As the oxidation proceeds, direct B–B bonding gradually diminishes. Consequently, heteroatomic B–O rings start to appear, which serve as the structural core of boron oxide clusters. Such a heteroatomic ring can be rhombic, pentagonal, hexagonal, or polycyclic, giving rise to a diversity

of boron oxide cluster structures that mimic aromatic hydrocarbons (including polycyclic aromatic hydrocarbons, PAHs). Among these is the heterocyclic hexagonal $B_3O_3$ ring, whose relevant clusters are classified as inorganic benzenes. Typical examples are boroxine ($B_3O_3H_3$) and, more recently, the boronyl boroxine $B_3O_3(BO)_3$ cluster (Li et al., 2013).

It is interesting and invaluable to follow the oxidation process of a specific bare boron cluster, step by step. The effort should help precisely identify a variety of cluster structures and structural transformations. Along this line, the $B_5O_n^-$ clusters are an intriguing and informative system, which have been extensively studied in the past years (Yao et al., 2009; Zhai et al., 2011; Tian et al., 2015b), (Chen et al., 2012; Chen et al., 2013), (Zhai et al., 2002), including a number of gas-phase spectroscopic works. The $B_5^-$ cluster assumes double-chain ribbon geometry with a "W" shape (Zhai et al., 2002), while the $B_5^+$ cluster is pentagonal (Alexandrova et al., 2006). The $B_5O_n^-$ ($n$ = 1–3) clusters are entirely dictated by boronyl groups, whose number increases steadily from 1 to 3, reducing the size of boron core from rhombic $B_4$ to triangular $B_3$ and then to dimer $B_2$ (Zhai et al., 2011; Chen et al., 2012; Chen et al., 2013). The first one or two boronyl ligands are terminally attached to the boron core, whereas the third one occupies a bridging position. The coordination pattern is similar to a hydrogen ligand in boranes, demonstrating the BO/H isolobal analogy. It is noted that all $B_5O_n^-$ ($n$ = 0–3) clusters are perfectly planar. In the $B_5O_4^-$ cluster (Yao et al., 2009), a tetrahedral geometry occurs, which is still governed by boronyl ligands, except that their number increases to four. It can be formulated as $B(BO)_4^-$, being isovalent to $BH_4^-$ or $CH_4$. The $B_5O_5^-$ cluster inherits the tetrahedral geometry of $B_5O_4^-$ upon substitution of one boronyl terminal by a linear OBO unit (Tian et al., 2015b). What is next in the sequential oxidation process of bare $B_5$ cluster? Would the tetrahedral geometry persist? What new type of structure would appear? These remain to be open questions in the field.

In the present work, we are motivated to address the abovementioned issues. We report on the structural, electronic, and chemical bonding properties of boron oxide $B_5O_6^-$ cluster *via* computer global searches and quantum chemical calculations. It turns out that the global minimum (GM) structure of $B_5O_6^-$ cluster features a heterocyclic $B_3O_3$ core, whose three unsaturated B sites are decorated by two BO ligands and one $O^-$ unit. Herein, the abbreviation "GM" refers to a structure that is lowest in energy on the potential energy surface of a specific molecular system, which is routinely used in physical chemistry or cluster literature. The hexagonal $B_3O_3$ core is stabilized by a moderately delocalized 6π system, thus rendering the $B_5O_6^-$ cluster a boronyl-based analog of benzene, akin to boroxine or boronyl boroxine (Li et al., 2013). In terms of the overall chemical bonding pattern, it is proposed that the $B_5O_6^-$ cluster closely mimics phenolate anion ($C_6H_5O^-$). The relatively localized extra charge ($O^-$) in $B_5O_6^-$ cluster gives rise to high vertical detachment energy (VDE) beyond 5 eV, indicating that the cluster is a superhalogen anion (Gutsev and Boldyrev, 1984; Srivastava, 2022; Kandalam et al., 2015; A Technical Note).

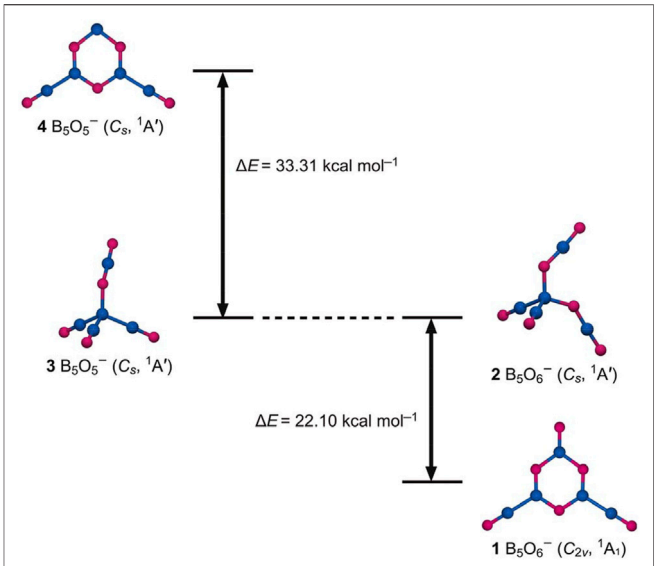


**FIGURE 1 |** Global minimum (GM) structure of $B_5O_6^-$ (1, $C_{2v}$, $^1A_1$) cluster and a representative 2 ($C_s$, $^1A'$) isomer. They feature a heterocyclic hexagonal $B_3O_3$ ring and a tetrahedral B center, respectively. Relevant structures 3/4 of $B_5O_5^-$ cluster (left panels) show a distinctly reversed energy order. The relative energies are shown in kcal mol$^{-1}$ at the PBE0/6-311+G(d) level.

## METHODS

The GM structural searches for $B_5O_6^-$ cluster were carried out at the PBE0/3-21G level using the coalescence kick (CK) algorithm (Saunders, 2004; Sergeeva et al., 2011). A total of 8000 stationary points were probed on its potential energy surface (4000 for singlet and triplet states each). The identified low-lying isomers were then fully reoptimized at the PBE0/6-311+G(d) level and their relative energies evaluated, including zero-point energy (ZPE) corrections. The vibrational frequencies were calculated at the same level to ensure that the reported structures are true minima on the potential energy surface.

Our further effort to assess the energetics for top candidate structures is as follows. First, the PBE0-D3/6-311+G(d) calculations were carried out to take into account dispersion correction. Second, comparative B3LYP-D3/6-311+G(d) calculations were carried out to check for consistency of density functionals; the PBE0 and B3LYP functionals have been widely considered to be complementary with each other. Third, single-point CCSD(T)/6-311+G(d) calculations (Purvis and Bartlett, 1982) were carried out on the basis of optimized PBE0-D3/6-311+G(d) geometries, which shall serve as a benchmark of the energetics data. All four sets of energetics data are highly consistent.

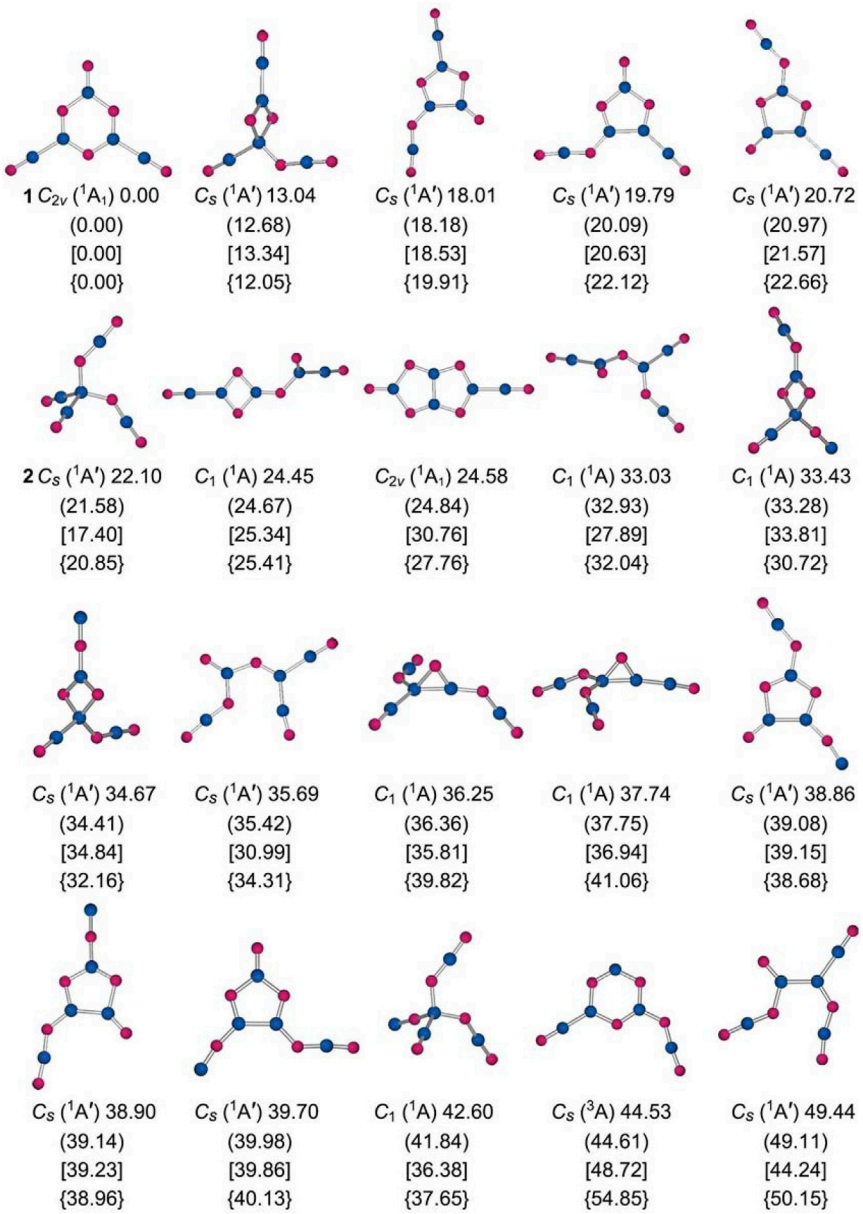


**FIGURE 2 |** Alternative optimized low-lying isomeric structures of $B_5O_6^-$ cluster at the PBE0/6-311+G(d) level along with their relative energies (in kcal $mol^{-1}$), including zero-point energy (ZPE) corrections. The energetics data are also presented at the PBE0-D3/6-311+G(d) (in brackets, with ZPE corrections) and B3LYP-D3/6-311+G(d) (in square brackets, with ZPE corrections) levels, as well as at single-point CCSD(T)/6-311+G(d) level based on their PBE0-D3/6-311+G(d) geometries (in curly brackets).

The NBO 6.0 program (Glendening et al., 2013) was used for the natural bond orbital (NBO) (Reed et al., 1988) analysis, which offers Wiberg bond indices (WBIs) and natural atomic charges. Chemical bonding was elucidated v*ia* canonical molecular orbital (CMO) analysis, adaptive natural density partitioning (AdNDP) (Zubarev and Boldyrev, 2008), and electron local functions (ELFs) (Silvi and Savin, 1994). To assess π aromaticity, nucleus-independent chemical shifts (NICSs) were also calculated (Schleyer et al., 1996), which were supplemented by the isochemical shielded surface (ICSS) analysis (Guo et al., 2020). The latter was performed using the Multiwfn program (Lu and Chen, 2012). The VDEs were calculated using the time-dependent PBE0 (TD-PBE0) (Bauernschmitt and Ahlrichs, 1996; Casida et al., 1998) and outer valence Green's function (OVGF) (von Niessen et al., 1984; Zakrzewski and von Niessen, 1993; Zakrzewski and Ortiz, 1995) methods and at the single-point CCSD(T) level. All the electronic structure calculations were carried out using the Gaussian 09 package (Frisch, 2009).

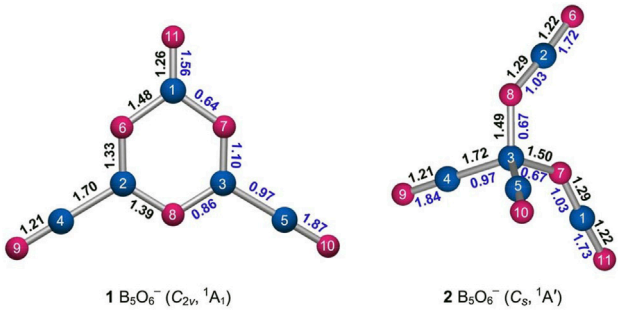


**FIGURE 3 |** Optimized bond distances (in Å; black color) of GM structure 1 and isomer 2 of the $B_5O_6^-$ cluster at the PBE0/6-311+G(d) level. Also shown are their Wiberg bond indices (WBIs; blue color) from the natural bond orbital (NBO) analysis. The B atoms are illustrated in blue and O in red.

# RESULTS

## Global Minimum Structure and Alternative Low-Lying Isomers

Our computational structural searches lead to the GM structure 1 ($C_{2v}$, $^1A_1$) for anion $B_5O_6^-$ cluster; see **Figure 1**. Alternative low-lying isomeric structures are presented in **Figure 2** along with their relative energies at four levels of theory: PBE0/6-311+G(d), PBE0-D3/6-311+G(d), and B3LYP-D3/6-311+G(d) levels, as well as the single-point CCSD(T)/6-311+G(d) level on the basis of PBE0-D3/6-311+G(d) geometries. The four sets of independent energetics data are highly consistent (**Figure 2**), firmly establishing cluster 1 as the GM structure. It is relatively well-defined on the potential energy surface, being at least 12 kcal $mol^{-1}$ more stable than any alternative geometry. It is noted that the PBE0 functional has been widely tested for boron clusters (Zhai et al., 2014b; Fagiani et al., 2017; Guo et al., 2017), which is a popular and reliable choice for boron-based systems.

Cluster 1 is closed-shell. The lowest-energy triplet structure is 54.85 kcal $mol^{-1}$ higher in energy at the single-point CCSD(T) level (**Figure 2**). Among the low-lying isomers is a tetrahedral 2 ($C_s$, $^1A'$) structure, which is 22.10 kcal $mol^{-1}$ above GM cluster 1 at PBE0 [20.85 kcal $mol^{-1}$ at single-point CCSD(T)]. Its geometry can be traced back to the GM structure 3 ($C_s$, $^1A'$) of anion $B_5O_5^-$ cluster (**Figure 1**) (Tian et al., 2015b), upon substitution of one terminal boronyl by an OBO unit. For the latter cluster, hexagonal isomer 4 ($C_s$, $^1A'$) is substantially higher in energy than GM cluster 3, by as much as 33.31 kcal $mol^{-1}$ at PBE0. Structures 1–4 have an intriguing energetics relationship; see **Figure 1**. A clear structural transition occurs from $B_5O_5^-$ to $B_5O_6^-$. The optimized Cartesian coordinates of structures 1 and 2 are presented in **Supplementary Table S1 (ESI†)**.

## Bond Distances, Wiberg Bond Indices, and Natural Atomic Charges

As shown in **Figure 3**, the perfectly planar GM $B_5O_6^-$ (1, $C_{2v}$, $^1A_1$) cluster contains a heteroatomic hexagonal $B_3O_3$ ring, two-terminal BO ligands, and one terminal O unit. The BO or O units are attached to three B sites on the periphery. The structure is relatively straightforward to elucidate based on interatomic distances. Typical triple B≡O, double B=O, single B–O, and single B–B bonds are around 1.21, 1.28, 1.37, and 1.66 Å, respectively (Yao et al., 2009; Zhai et al., 2014a; Tian et al., 2015b; Pyykkö and Atsumi, 2009). The bond distances for BO links in hexagonal ring of cluster 1 are slightly uneven (1.33–1.48 Å; **Figure 3**, left panel) due to asymmetric coordination of B sites. Their average value is in line with single B–O bonds. The terminal BO groups (1.21 Å) are assigned as boronyls with triple B≡O bonds. In contrast, the upper BO unit (1.26 Å) is close to a double B=O bond.

The calculated WBIs generally confirm the abovementioned assignments (**Figure 3**, left panel). The inner BO links have WBI values of 0.64–1.10, in line with (uneven) single bonds. The boronyl groups have WBIs of 1.87 owing to their polar nature (Zhai et al., 2014a). The upper BO unit has a smaller WBI value of 1.56, in line with a double bond. The calculated natural atomic charges for cluster 1 are shown in **Figure 4**. There are moderate intramolecular B–O charge transfers within the $B_3O_3$ core, within boronyl groups, and in between the core and terminals. The charge transfers are relatively local processes, suggesting polar and yet covalent BO chemical bonding.

Likewise, the isomeric tetrahedral $B_5O_6^-$ (2, $C_s$, $^1A'$) structure can be easily understood (**Figures 3**, **4**). It consists of a central B site, two BO groups, and two OBO groups. The components are held together in a tetrahedral fashion. Approximately, in anion cluster, the B center forms four B–B or B–O single bonds with terminal ligands, whose B–B (1.72 Å) and B–O (1.49–1.50 Å) links are somewhat elongated with respect to the abovementioned reference values for single bonds. However, their WBIs are 0.97 and 0.67, respectively, and even the latter seems reasonable (for a polar bond). Such a bonding situation around the B center is less than ideal, which is partly the reason why this structure is a higher-energy isomer (*vide infra*). For the terminal ligands, two BO groups (1.21 Å) are boronyls with WBIs of 1.84. The two OBO units are asymmetric in terms of B–O distances: 1.22 versus 1.29 Å. Their average is close to a double B=O bond. The calculated natural atomic charges of cluster 2 are presented in **Figure 4**. The central B site is practically neutral (+0.12 |e|) despite the fact that other B atoms each carry a larger positive charge (+0.85 and +1.21 |e|). This situation again hints that the central B site struggles severely in order to maintain four-fold bonding.

To aid the understanding of GM $C_{2v}$ $B_5O_6^-$ (1) and isomeric $C_s$ $B_5O_6^-$ (2) clusters, three prior species (Yao et al., 2009; Tian et al., 2015b) are also analyzed: tetrahedral GM $C_s$ $B_5O_5^-$ (3), hexagonal isomeric $C_s$ $B_5O_5^-$ (4), and tetrahedral GM $T_d$ $B_5O_4^-$ (5). Their calculated bond distances and WBIs (**Supplementary Figure S1, ESI†**) and natural atomic charges (**Figure 4**) are well behaved, providing support to our assessment with regard to clusters 1 and 2 (as described above).

## Superhalogen Anion

The electronic properties of GM $B_5O_6^-$ (1) cluster are predicted here to aid its future experimental characterization in the gas phase. The calculated ground-state VDE of $B_5O_6^-$ (1) cluster and those of a few relevant species are presented in **Supplementary Table S2 (ESI†)** at

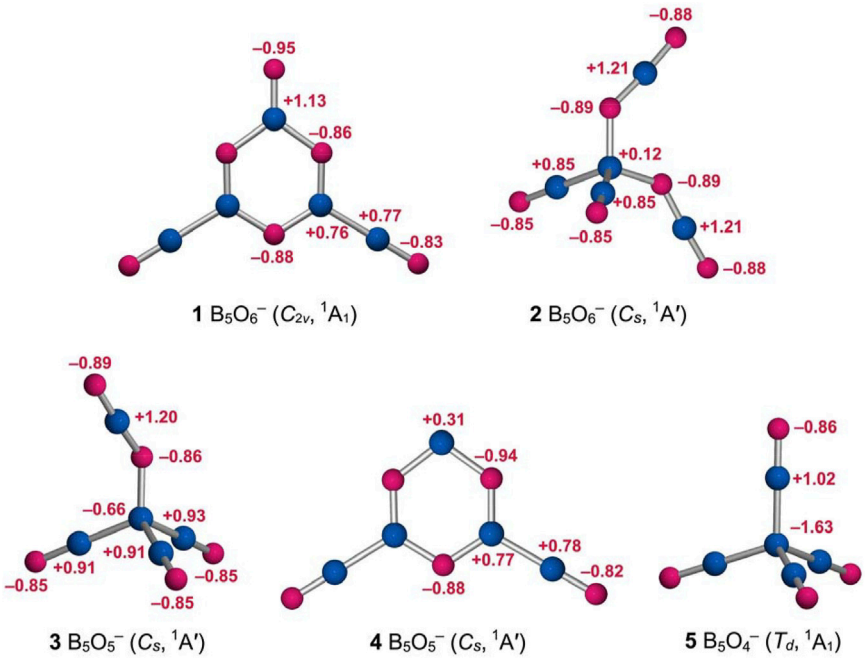


**FIGURE 4 |** Calculated natural atomic charges (in |e|) for structures 1 and 2 of the $B_5O_6^-$ cluster from the NBO analysis at PBE0/6-311+G(d), as compared to those of $B_5O_5^-$ (3, $C_s$, $^1A'$), $B_5O_5^-$ (4, $C_s$, $^1A'$), and $B_5O_4^-$ (5, $T_d$, $^1A_1$) clusters. The B atoms are shown in blue and O in red.

three levels of theory: PBE0, single-point CCSD(T), and OVGF. Using the experimentally known $B_4O_3^-$ cluster (Zhai et al., 2007a) as a calibration, it is shown that the PBE0 and single-point CCSD(T) data are superior to those of OVGF; see a note in **Supplementary Table S2 (ESI†)**. The VDE of GM $B_5O_6^-$ (1) cluster amounts to 5.26 eV at PBE0 and 5.14 eV at CCSD(T), which is quite high, markedly surpassing the electron affinities of halogens (Cl: 3.61 eV). The ground-state VDEs of the whole $B_5O_n^-$ ($n$ = 1–6) series at PBE0/6-311+G(d) are plotted in **Figure 5**, which show an abrupt increase between $n$ = 3 and 4. All the $B_5O_n^-$ ($n$ = 4–6) species have high VDEs. Based on this observation, the GM $B_5O_6^-$ (1) cluster clearly belongs to the class of species called superhalogen anions. (Gutsev and Boldyrev, 1984; Srivastava, 2022; Kandalam et al., 2015; A Technical Note)

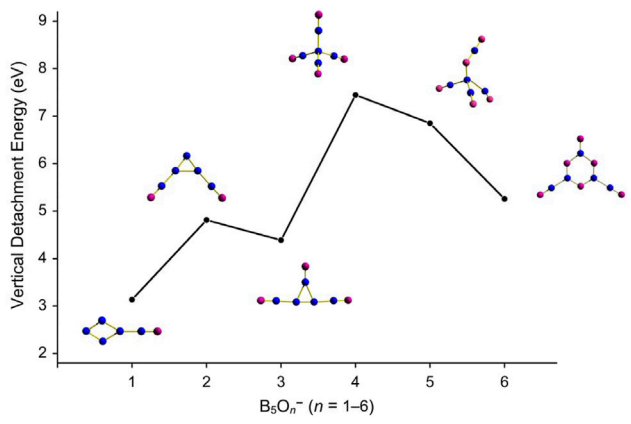


**FIGURE 5 |** Evolution of ground-state vertical detachment energies (VDEs) of $B_5O_n^-$ ($n$ = 1–6) series calculated at the PBE0/6-311+G(d) level.

The simulated photoelectron spectrum of GM $B_5O_6^-$ (1) cluster is presented in **Figure 6**, according to the TD-PBE0 calculation, which has three well-separated bands in the 5–7 eV binding energy regime. For comparison, the simulation is also carried out for isomeric structure 2 with a higher ground-state band (**Figure 6B**). A nature implication is that for their corresponding neutral species, the hexagonal structure has an even greater advantage in terms of energetics (over tetrahedral structure). Indeed, our PBE0 calculations show that the hexagonal neutral $B_5O_6$ cluster is 54.59 kcal mol$^{-1}$ below its tetrahedral counterpart, as compared to a relative energy of 22.10 kcal mol$^{-1}$ between anionic 1/2 structures at the same level (**Figure 1**). The two neutral structures are analyzed in **Supplementary Figures S2, S3 (ESI†)**. For the hexagonal anion/neutral system, the extra charge goes primarily to the upper O terminal (by as much as 0.66 |e|), which further justifies the assessment of an $O^-$ terminal for GM $B_5O_6^-$ (1) cluster, as well as its exact analogy to phenolate anion (*vide infra*). In contrast, the extra charge in the tetrahedral system smears over the entire cluster (with the central B site gaining 0.34 |e| only), thus leading to an even higher ground-state VDE.

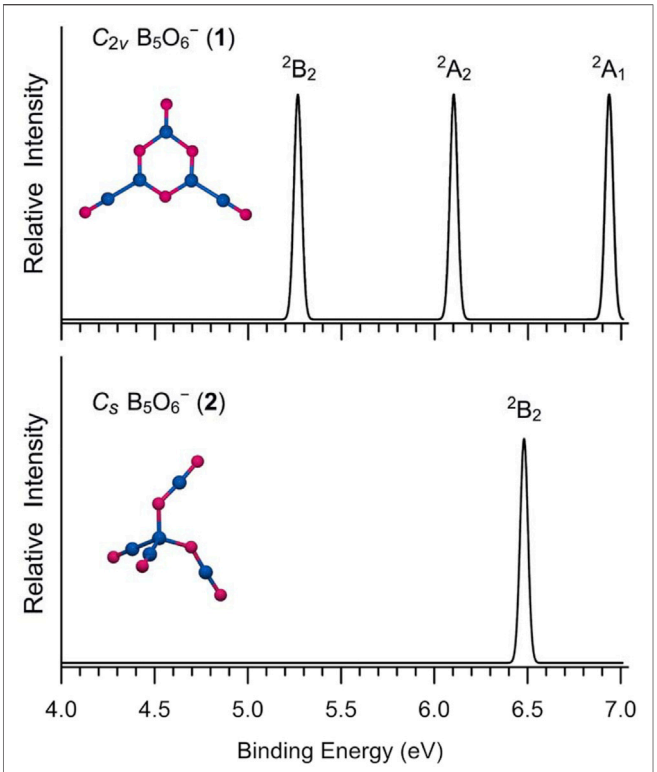


**FIGURE 6 |** Simulated photoelectron spectra of anionic $B_5O_6^-$ (1) and $B_5O_6^-$ (2) clusters at the time-dependent PBE0/6-311+G(d) (TD-PBE0) level.

## DISCUSSION

### Heterocyclic Hexagonal Global-Minimum $C_{2v}$ $B_5O_6^-$ Cluster: A Boronyl-Based Inorganic Analog of Phenolate Anion

The GM $C_{2v}$ $B_5O_6^-$ (1) cluster marks the exact onset of a heteroatomic hexagonal $B_3O_3$ ring along the whole $B_5O_n^-$ ($n$ = 0–6) series (Zhai et al., 2002; Yao et al., 2009; Zhai et al., 2011; Chen et al., 2012; Chen et al., 2013; Tian et al., 2015b). A simple valence electron counting suggests that the available number of electrons for direct B–B bonding diminishes gradually from 16 electrons in $B_5^-$ down to 4 in $B_5O_6^-$, two electrons for each additional O atom. Indeed, both GM $B_5O_6^-$ cluster 1 and isomeric structure 2 have four electrons for direct B–B bonding, that is, two B–B single bonds (see **Figure 1**).

To fully understand GM $B_5O_6^-$ (1) cluster, it is essential to conduct an in-depth analysis of chemical bonding. We choose to focus on the CMO analysis, which is fundamental for a molecular system. Cluster 1 is a closed-shell structure with 52 valence electrons. The 26 occupied CMOs are presented in **Figure 7**, which are sorted into five subsets according to their components of atomic orbitals (AOs). The seven CMOs in subset (a) are classified as O lone-pairs. Among them, HOMO–21/HOMO–24/HOMO–25 are typical bonding/nonbonding/antibonding combination of O 2s AOs from three O sites in the hexagonal ring owing to pseudo-three-fold symmetry of the cluster. According to the CMO building principles, they are readily recombined as three O 2s lone pairs. HOMO–20 is an O 2s lone-pair on the upper O site, whereas HOMO–22/HOMO–23 recombine as two O 2s lone-pairs on terminal boronyls. The HOMO approximately represents an O 2p lone-pair on the upper O site with 88% contribution from tangential O 2p AO. Thus, the upper O site has two lone pairs, and the remaining O sites each have one lone pair.

In subset (b), nine B–O σ single bonds are presented. Specifically, HOMO–3 is a σ bond for terminal B–O unit at the top. HOMO–13/HOMO–14 recombine as two σ bonds on the bottom boronyl groups. These are primarily contributed by radial O 2p AOs from three terminal O sites. The next six CMOs are responsible for skeleton B–O σ bonds along the hexagonal ring, which are evenly contributed by the B/O sites: radial O 2p AOs versus tangential B 2p AOs.

The CMOs in subset (c) are two B–B σ bonds, which link hexagonal rings and two boronyl ligands. The subset (d) shows the terminal B–O π bonds, including two in-plane π bonds on boronyls. Overall, the three-terminal B–O links each have one σ bond (**Figure 7B**) and one out-of-plane π bond (**Figure 7D**). Furthermore, the boronyl groups each have one in-plane π bond. The boronyls show triple bonds, whereas the upper B–O terminal has a double bond.

All the abovementioned CMOs are Lewis-type bonding elements: seven O 2s/2p lone-pairs, six B–O σ single bonds along the hexagon, two B–B σ bonds, one B=O double bond for the upper terminal, and two B≡O triple bonds for boronyls. These Lewis elements collectively consume 23 pairs of electrons, leaving the remaining six electrons for a π framework over the hexagonal ring (**Figure 7E**). Of the three π CMOs, HOMO–4 recombines partially with HOMO–10 to get "purified," which has a B versus O ratio of roughly 1/11 in the hexagon. HOMO–6 has a ratio of 1/11 for B/O contributions. For HOMO–15, the ratio of B/O contributions in the ring boosts greatly to about 1/1. Overall, the B components in the π framework cannot be ignored, and the π sextet should be viewed as six-centered (at least formally). This π pattern is closely similar to that in boroxine and boronyl boroxine (Li et al., 2013), thus rendering GM $B_5O_6^-$ (1) cluster a new member of the "inorganic benzene" family. The 6π electron-counting conforms to the ($4n$ + 2) Hückel rule for aromaticity. The bonding picture is elegantly borne out from the AdNDP analysis (Zubarev and Boldyrev, 2008), as shown in **Figure 8**. All the occupation numbers (ONs) are close to ideal.

Based on the bonding picture, we should propose that GM $B_5O_6^-$ (1) cluster is an exact boronyl-based analog of phenolate anion. They share the same characteristic structural and bonding features. First, they both have a hexagonal core: heteroatomic $B_3O_3$ ring versus $C_6$ ring. The two kinds of rings are actually isoelectronic in terms of hexagonal bonding, once lone-pairs or terminal Lewis-type bonds are accounted for. Indeed, each ring consumes 18 electrons for chemical bonding within the ring. Second, both species possess a π sextet. Third, both species have an $O^-$ terminal, which is attached to the hexagon *via* a double bond (B=$O^-$ versus C=$O^-$). It is appropriate to state that the current finding of chemical analogy between GM $B_5O_6^-$ (1)

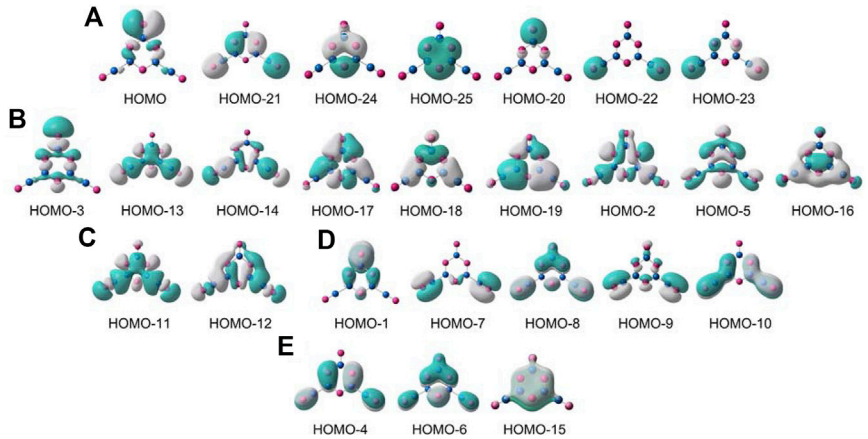


**FIGURE 7 |** Pictures of occupied canonical molecular orbitals (CMOs) of $B_5O_6^-$ (1) cluster. **(A)** Seven lone pairs for the O atoms, including two for the upper O site. **(B)** Nine σ CMOs for Lewis-type skeleton and terminal B–O σ bonds. **(C)** Two σ CMOs for Lewis-type B–B σ single bonds. **(D)** Five CMOs for both in-plane and out-of-plane π bonds relevant to terminal B–O units. **(E)** Three delocalized π CMOs over the $B_3O_3$ ring.

cluster and phenolate anion parallels that between boronyl boroxine (Li et al., 2013) and benzene.

We shall only briefly mention the tetrahedral isomeric cluster $B_5O_6^-$ (2). Its structural characters suggest a relatively classical cluster between a formal $B^-$ center and four ligands (two boronyls versus two OBO units), *via* single bonds in a tetrahedral fashion. The chemical bonding within an OBO unit is presented in **Supplementary Figure S4 (ESI†)**. Here, HOMO−16 and HOMO form a three-center, four-electron (3c-4e) π bond in the vicinity of an OBO unit, that is, "π hyperbond," which is in a bonding/nonbonding combination due to its three-center nature. The upper CMO has relatively minor bonding or antibonding effect. Thus, a 3c-4e π bond is, in effect, equivalent to a 3c-2e bond or two B–O half bonds. There is a second 3c-4e π bond (HOMO−17 and HOMO−1) on the same OBO unit, which offers two B–O half bonds in the perpendicular direction. In short, the four CMOs in **Supplementary Figure S4A (ESI†)** can be collectively viewed as two B–O single bonds, similar to the prior tetrahedral $C_s$ $B_5O_5^-$ (3) cluster (Tian et al., 2015b) (see **Supplementary Figure S4B, ESI†**). An OBO unit in cluster 2 also has two B–O σ bonds (not shown). The same ideal works for the other OBO ligand. Overall, the OBO ligands can be formulated as O=B=O, featuring double bonds.

## Weak 6π Aromaticity in $C_{2v}$ $B_5O_6^-$ Cluster: Comparison With a Series of Relevant Species

The π sextet in GM $B_5O_6^-$ (1) cluster stems primarily from three O $2p_z$ lone-pairs in the hexagonal ring, taking advantage of the empty B $2p_z$ AOs from three neighboring B sites for six-centered π delocalization. Consequently, π aromaticity in cluster 1 is expected to be moderate only, despite its ideal 6π electron-counting. To quantitatively probe π aromaticity in cluster 1, we have calculated the color-filled maps of ICSS in the z-direction, that is, $ICSS_{zz}$ (in ppm) (Guo et al., 2020), as shown in **Figure 9A** at 1.0 Å above the molecular plane. It noted that a positive $ICSS_{zz}$ value indicates aromaticity. It turns out that the shielding effect at 1.0 Å above the ring center of cluster 1 is weak and only at a larger distance (such as 1.5 or 2.0 Å) does the shielding become apparent. Specifically, the calculated $NICS_{zz}$ values for cluster 1 are +2.08 (likely due to disturbance from O lone-pairs), −3.24, and −4.02 ppm at 1.0, 1.5, and 2.0 Å, respectively, a trend in line with weak π aromaticity. For comparison, the corresponding $NICS_{zz}$ values for boronyl boroxine are −1.97, −6.07, and −5.73 ppm, respectively, indicating slightly stronger π aromaticity.

Alternatively, we can also compare the extent of π aromaticity of GM $B_5O_6^-$ (1) cluster and relevant species using the ELF data. (Silvi and Savin, 1994), (Wang et al., 2017) The π bifurcation value, $ELF_\pi$, of GM $B_5O_6^-$ (1) cluster is compared with those of boroxine $D_{3h}$ $B_3O_3H_3$, boronyl boroxine $D_{3h}$ $B_6O_6$, and benzene $D_{6h}$ $C_6H_6$ in **Supplementary Figure S5 (ESI†)**. Not surprisingly, benzene has a π bifurcation value that is close to 1.0. Boroxine and boronyl boroxine (Li et al., 2013) have smaller and yet comparable π bifurcation values (0.64 versus 0.67). The GM $B_5O_6^-$ (1) cluster has an even smaller π bifurcation value of 0.53, which is marginally π aromatic. The primary reason is that cluster 1 is asymmetrically coordinated so that its hexagonal ring has uneven B–O bond distances (**Figure 3**).

## A Plausible Mechanism for Structural Transition in the $B_5O_6^-$ Cluster: From Tetrahedral Isomer to Hexagonal Global Minimum

A possible mechanism for tetrahedral-to-hexagonal structure transition from 3/2 to 1 is illustrated in **Figure 10**. This is an oxygen diradical nucleophilic substitution mechanism. Our starting point is tetrahedral GM $B_5O_5^-$ (3) cluster, which is substantially more stable than its hexagonal isomer 4 (**Figure 1**) and inherits the geometry from GM $T_d$ $B_5O_4^-$ (5) cluster. Upon insertion of an O atom (assumed as oxygen diradical) between the $B^-$ center and one boronyl terminal, the

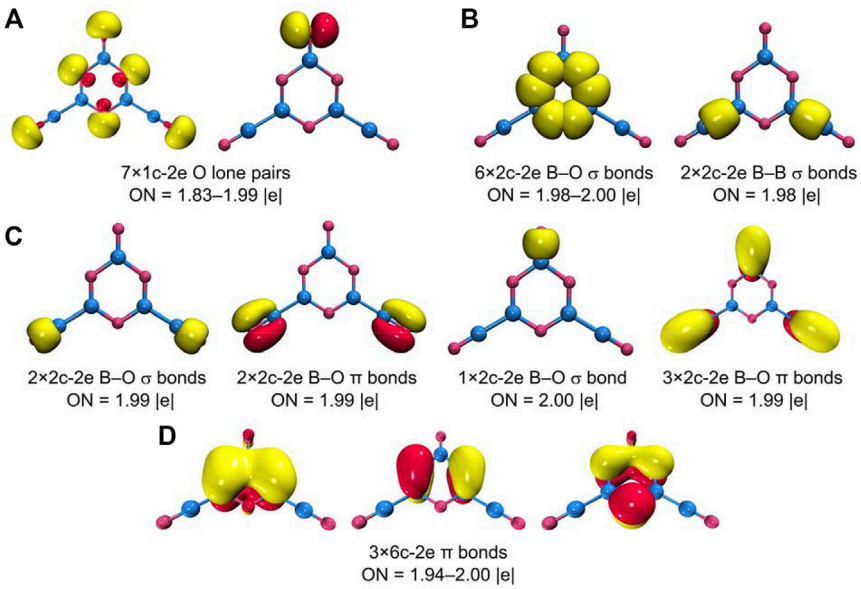


**FIGURE 8 |** Chemical bonding pattern of $B_5O_6^-$ (1) cluster according to the adaptive natural density partitioning (AdNDP) analysis. The occupation numbers (ONs) are indicated.

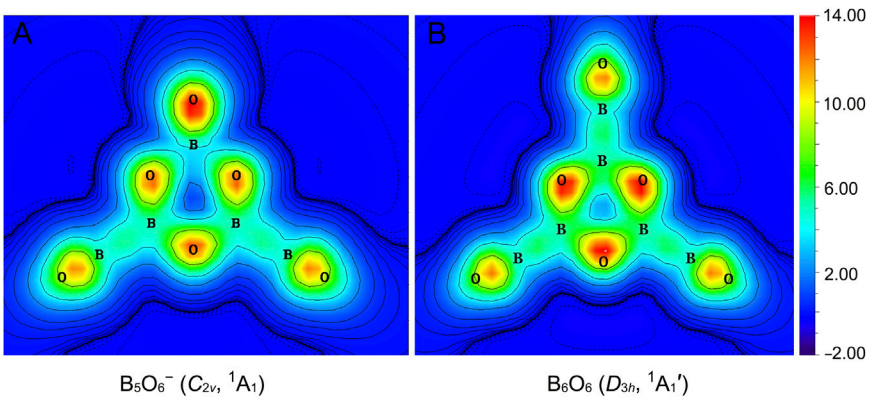


**FIGURE 9 |** Color-filled maps of iso-chemical shielding surfaces (ICSSs) in the z-direction, $ICSS_{zz}$ (in ppm), for **(A)** $B_5O_6^-$ (1) and **(B)** boronyl boroxine $D_{3h}$, $B_6O_6$ clusters. Positive $ICSS_{zz}$ values indicate aromaticity. The calculations are carried out on a plane that is 1.0 Å above the molecular plane.

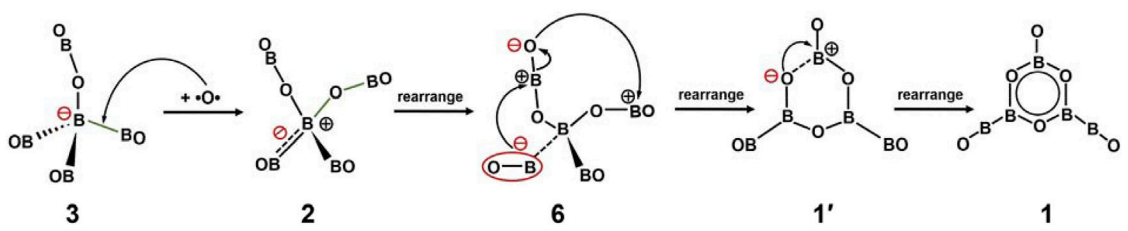


**FIGURE 10 |** Plausible mechanism for the structural evolution between tetrahedral $B_5O_5^-$ (3) and hexagonal $B_5O_6^-$ (1) clusters.

negative charge on central $B^-$ site would migrate to its surrounding, thus leading to structure 2 (step 1), which is illustrated approximately only. Next, the negatively charged BO migrates to bind a neighboring positively charged B center in the OBO ligand and the charge further migrates so that the former OBO units are ready to fuse (step 2). In other words, the electron-rich boronyl group acts as a nucleophilic reagent to attack a weaker B–O link. A key structure 6 is present here. Interestingly, structure 6 has been identified as well in our structural searches, which is the 9th isomer in **Figure 2**.

Once structure 6 is reached, the next are downhill processes. The negative terminal O center binds with the positive B center in the second OBO ligand and a heterocyclic hexagon is formed (structure 1′; step 3). The formation of π sextet from 1′ results in the final structure of cluster 1 (step 4). The abovementioned mechanism is primarily based on regioselectivity and stereoselectivity (Ren et al., 2017).

The proposed mechanism is reasonable also for a different reason, as outlined in Section *Bond Distances, Wiberg Bond Indices, and Natural Atomic Charges*. Basically, isomer $B_5O_6^-$ (2) is not an ideal system, despite its tetrahedral configuration similar to those of $B_5O_4^-$ (5) and $B_5O_5^-$ (3) (see **Figure 4**). Ideally, the central site of a tetrahedral molecular system should be valence four so that four Lewis-type single σ bonds can form, such as in $CH_4$ and $BH_4^-$. The central B site in $B_5O_4^-$ (**5**) and $B_5O_5^-$ (**3**) are in the $B^{-1.63}$ and $B^{-0.66}$ charge states, respectively (**Figure 4**). In stark contrast, the central B site in $B_5O_6^-$ (2) is practically neutral (+0.12 |e|) and inconsistent with a formal $B^-$ center. As a consequence, the tetrahedral coordination is not favorable for the $B_5O_6^-$ cluster, which is susceptible to structural transformation.

## CONCLUSION

The structural and bonding properties of a boron oxide $B_5O_6^-$ cluster has been studied using computer global structure searches and quantum chemical calculations, revealing a perfectly planar $C_{2v}$ ($^1A_1$) global minimum geometry. It has a heterocyclic $B_3O_3$ hexagon as the core, which is terminally bonded to two boronyls and one $O^-$ ligand, marking the exact onset of a hexagonal ring in the $B_5O_n^-$ ($n$ = 1–6) cluster series. The electronic structure shows a rather high vertical electron affinity of greater than 5 eV, suggesting that the species belongs to superhalogen anions. Chemically, the $B_5O_6^-$ $C_{2v}$ ($^1A_1$) cluster is a close boronyl-based analog to phenolate anion, in which a boronyl ligand is isovalent to hydrogen and a heteroatomic $B_3O_3$ ring substitutes a $C_6$ ring. The two kinds of hexagonal rings are, in effect, isoelectronic with each other in terms of the available number of electrons for bonding within the rings. The $B_5O_6^-$ $C_{2v}$ ($^1A_1$) cluster features a π sextet, similar to those in boroxine and boronyl boroxine, thus also rendering the cluster a new member of the "inorganic benzene" family. A plausible mechanism is proposed to account for the tetrahedral-to-hexagonal structure transition in the $B_5O_n^-$ ($n$ = 1–6) clusters.

## DATA AVAILABILITY STATEMENT

The original contributions presented in the study are included in the article/**Supplementary Material**; further inquiries can be directed to the corresponding authors.

## AUTHOR CONTRIBUTIONS

The topic of this study is discussed and determined by J-CG and H-JZ. S-JG performed the global minimum search; carried out the geometry optimization and frequency calculations of all the isomers; and the calculations of VDEs, molecular orbital chemical bonding analyses, and the AdNDP chemical bonding analyses. The data analyses were carried out by J-CG and H-JZ. The manuscript was written and commented by all the authors.

## FUNDING

This work was supported by the National Natural Science Foundation of China (Nos. 21873058, 21573138, and 22173053), the Natural Science Foundation of Shanxi Province (Nos. 201801D121103 and 20210302123439), the Shanxi "1331" Project, the Scientific and Technological Innovation Programs of Higher Education Institutions in Shanxi (No. STIP 2019L0965), the Key Research and Development Project in High-tech Field of the Lvliang Science and Technology Bureau (No. 2021GXYF-2-62), and the Lvliang Key Laboratory of Optical and Electronic Materials and Devices (No. 2021ZDSY-2-88).

## SUPPLEMENTARY MATERIAL

The Supplementary Material for this article can be found online at: https://www.frontiersin.org/articles/10.3389/fchem.2022.868782/full#supplementary-material

## REFERENCES

Alexandrova, A. N., Boldyrev, A. I., Zhai, H.-J., and Wang, L.-S. (2006). All-boron Aromatic Clusters as Potential New Inorganic Ligands and Building Blocks in Chemistry. *Coord. Chem. Rev.* 250, 2811–2866. doi:10.1016/j.ccr.2006.03.032

A Technical Note, Electron Affinity (EA) characterizes the energetic gain of a neutral molecular system upon attachment of an extra charge, that is, its oxidation capability. Among atoms in the periodic table, halogens have the largest EAs (3.06–3.61 eV). In particular, the Cl atom has the greatest value of 3.61 eV. Due to collective effects, certain molecules or polyatomic radicals can possess EAs that are even higher than those of halogens and such exotic systems have been called "superhalogens". Their corresponding anions are electronically robust, similar to halogen anions. These cluster or molecular anions are therefore called the "superhalogen anions".

Bauernschmitt, R., and Ahlrichs, R. (1996). Treatment of Electronic Excitations within the Adiabatic Approximation of Time Dependent Density Functional Theory. *Chem. Phys. Lett.* 256, 454–464. doi:10.1016/0009-2614(96)00440-x

Braunschweig, H., Radacki, K., and Schneider, A. (2010). Oxoboryl Complexes: Boron−Oxygen Triple Bonds Stabilized in the Coordination Sphere of Platinum. *Science* 328, 345–347. doi:10.1126/science.1186028

Casida, M. E., Jamorski, C., Casida, K. C., and Salahub, D. R. (1998). Molecular Excitation Energies to High-Lying Bound States from Time-dependent Density-Functional Response Theory: Characterization and Correction of the Time-dependent Local Density Approximation Ionization Threshold. *J. Chem. Phys.* 108, 4439–4449. doi:10.1063/1.475855

Chen, Q., Bai, H., Zhai, H.-J., Li, S.-D., and Wang, L.-S. (2013). Photoelectron Spectroscopy of boron-gold alloy Clusters and boron Boronyl Clusters: $B_3Au_n^-$ and $B_3(BO)_n^-$ ($n$ = 1, 2). *J. Chem. Phys.* 139, 044308. doi:10.1063/1.4816010

Chen, Q., Lu, H.G, Zhai, H.-J., and Li, S.-D. (2014). Chemical bonding in electron-deficient boron oxide clusters: core boronyl groups, dual 3c-4e hypervalent bonds, and rhombic 4c-4e bonds. *Phys. Chem. Chem. Phys.* 16, 7274. doi:10.1039/c4cp00406j

Chen, Q., Zhai, H.-J., Li, S.-D., and Wang, L.-S. (2012). Probing the Structures and Chemical Bonding of boron-boronyl Clusters Using Photoelectron Spectroscopy and Computational Chemistry: $B_4(BO)_n^-$ ($n$ = 1–3). *J. Chem. Phys.* 137, 044307. doi:10.1063/1.4737863

Doyle, R. J. (1988). High-molecular-weight boron Oxides in the Gas Phase. *J. Am. Chem. Soc.* 110, 4120–4126. doi:10.1021/ja00221a004

Drummond, M. L., Meunier, V., and Sumpter, B. G. (2007). Structure and Stability of Small Boron and Boron Oxide Clusters. *J. Phys. Chem. A.* 111, 6539–6551. doi:10.1021/jp0726182

Fagiani, M. R., Song, X., Petkov, P., Debnath, S., Gewinner, S., Schöllkopf, W., et al. (2017). Structure and Fluxionality of $B_{13}^+$ Probed by Infrared Photodissociation Spectroscopy. *Angew. Chem. Int. Ed.* 56, 501–504. doi:10.1002/anie.201609766

Feng, L.-Y., Li, R., and Zhai, H.-J. (2019). Boron-based Inorganic Heterocyclic Clusters: Electronic Structure, Chemical Bonding, Aromaticity, and Analogy to Hydrocarbons. *Phys. Chem. Chem. Phys.* 21, 20523–20537. doi:10.1039/c9cp03254a

Frisch, M. J., et al. (2009). *GAUSSIAN 09, Revision D.01*. Wallingford, CT: Gaussian, Inc..

Glendening, E. D., Badenhoop, J. K., Reed, A. E., Carpenter, J. E., Bohmann, J. A., Morales, C. M., et al. (2013). *NBO 6.0*. Madison: Theoretical Chemistry Institute, University of Wisconsin.

Guo, J.-C., Feng, L.-Y., Dong, C., and Zhai, H.-J. (2020). A Designer 32-electron Superatomic $CBe_8H_{12}$ Cluster: Core-Shell Geometry, Octacoordinate Carbon, and Cubic Aromaticity. *New J. Chem.* 44, 7286–7292. doi:10.1039/d0nj00778a

Guo, J.-C., Feng, L.-Y., Wang, Y.-J., Jalife, S., Vásquez-Espinal, A., Cabellos, J. L., et al. (2017). Coaxial Triple-Layered versus Helical $Be_6B_{11}$− Clusters: Dual Structural Fluxionality and Multifold Aromaticity. *Angew. Chem. Int. Ed.* 56, 10174–10177. doi:10.1002/anie.201703979

Guo, J.-C., Lu, H.-G., Zhai, H.-J., and Li, S.-D. (2013). Face-Capping $\mu^3$-BO in $B_6(BO)_7^-$: Boron Oxide Analogue of $B_6H_7^-$ with Rhombic 4c-2e Bonds. *J. Phys. Chem. A.* 117, 11587–11591. doi:10.1021/jp4089723

Gutsev, G. L., and Boldyrev, A. I. (1984). The Way to Systems with the Highest Possible Electron Affinity. *Chem. Phys. Lett.* 108, 250–254. doi:10.1016/0009-2614(84)87059-1

Kandalam, A. K., Kiran, B., Jena, P., Pietsch, S., and Ganteför, G. (2015). Superhalogens Beget Superhalogens: a Case Study of $(BO_2)n$ Oligomers. *Phys. Chem. Chem. Phys.* 17, 26589–26593. doi:10.1039/c5cp04600a

Li, D.-Z., Bai, H., Chen, Q., Lu, H., Zhai, H.-J., and Li, S.-D. (2013). Perfectly Planar Boronyl Boroxine $D_3h$ $B_6O_6$: A boron Oxide Analog of Boroxine and Benzene. *J. Chem. Phys.* 138, 244304. doi:10.1063/1.4811330

Li, D.-Z., Feng, L.-Y., Zhang, L.-J., Pei, L., Tian, W.-J., Li, P.-F., et al. (2018). Planar Tricyclic $B_8O_8$ and $B_8O_8^-$ Clusters: Boron Oxide Analogues of *s*-Indacene $C_{12}H_8$. *J. Phys. Chem. A.* 122, 2297–2306. doi:10.1021/acs.jpca.7b12479

Li, D. Z., Feng, L. Y., Pei, L., Song, M. Z., Zhang, L. J., Wang, H., et al. (2019). Structures and Bonding of $B_4O_5$ and $B_4O_5^-$ Clusters: Emergence of Boroxol Ring and Competition Between Rhombic $B_2O_2$ and Hexagonal $B_3O_3$ Cores. *Int. J. Quan. Chem.* 119, 25907. doi:10.1002/qua.25907

Li, S.-D., Zhai, H.-J., and Wang, L.-S. (2008). $B_2(BO)_2^{2-}$ Diboronyl Diborene: A Linear Molecule with a Triple Boron−Boron Bond. *J. Am. Chem. Soc.* 130, 2573–2579. doi:10.1021/ja0771080

Lu, T., and Chen, F.W. (2012). Multiwfn: A Multifunctional Wavefunction Analyzer. *J. Comput. Chem.* 33, 580–592. doi:10.1002/jcc.22885

Miao, C.-Q., Lu, H.-G., and Li, S.-D. (2013). Covalent Bonding in $Au(BO)_2^-$ and $Au(BS)_2^-$. *J. Clust. Sci.* 24, 233–241. doi:10.1007/s10876-012-0546-z

Peiris, D., Lapicki, A., Anderson, S. L., Napora, R., Linder, D., and Page, M. (1997). Boron Oxide Oligomer Collision-Induced Dissociation: Thermochemistry, Structure, and Implications for Boron Combustion. *J. Phys. Chem. A.* 101, 9935–9941. doi:10.1021/jp972157s

Purvis, G. D., and Bartlett, R. J. (1982). A Full Coupled-cluster Singles and Doubles Model: The Inclusion of Disconnected Triples. *J. Chem. Phys.* 76, 1910–1918. doi:10.1063/1.443164

Pyykkö, P., and Atsumi, M. (2009). Molecular Single-Bond Covalent Radii for Elements 1-118. *Chem. Eur. J.* 15, 12770. doi:10.1002/chem.200800987

Reed, A. E., Curtiss, L. A., and Weinhold, F. (1988). Intermolecular Interactions from a Natural Bond Orbital, Donor-Acceptor Viewpoint. *Chem. Rev.* 88, 899–926. doi:10.1021/cr00088a005

Ren, S.-C., Zhang, F.-L., Qi, J., Huang, Y.-S., Xu, A.-Q., Yan, H.-Y., et al. (2017). Radical Borylation/Cyclization Cascade of 1,6-Enynes for the Synthesis of Boron-Handled Hetero- and Carbocycles. *J. Am. Chem. Soc.* 139, 6050–6053. doi:10.1021/jacs.7b01889

Saunders, M. (2004). Stochastic Search for Isomers on a Quantum Mechanical Surface. *J. Comput. Chem.* 25, 621–626. doi:10.1002/jcc.10407

Schleyer, P. v. R., Maerker, C., Dransfeld, A., Jiao, H., and van Eikema Hommes, N. J. R. (1996). Nucleus-Independent Chemical Shifts: A Simple and Efficient Aromaticity Probe. *J. Am. Chem. Soc.* 118, 6317–6318. doi:10.1021/ja960582d

Sergeeva, A. P., Averkiev, B. B., Zhai, H.-J., Boldyrev, A. I., and Wang, L.-S. (2011). All-boron Analogues of Aromatic Hydrocarbons: $B_{17}^-$ and $B_{18}^-$. *J. Chem. Phys.* 134, 224304. doi:10.1063/1.3599452

Shao, C.-B., Jin, L., Fu, L.-J., and Ding, Y.-H. (2009). Theoretical Study of $B_3O$ Radical Isomers and Their Interconversion Pathways. *Mol. Phys.* 107, 2395–2402. doi:10.1080/00268970903317247

Silvi, B., and Savin, A. (1994). Classification of Chemical Bonds Based on Topological Analysis of Electron Localization Functions. *Nature* 371, 683–686. doi:10.1038/371683a0

Srivastava, A. K. (2022). $M(BO)_{k+1}^-$ Anions: Novel Superhalogens Based on Boronyl Ligands. *J. Phys. Chem. A.* 126, 513–520. doi:10.1021/acs.jpca.1c08773

Tai, T. B., Nguyen, M. T., and Dixon, D. A. (2010). Thermochemical Properties and Electronic Structure of Boron Oxides $B_nO_m$ ($n$ = 5–10, $m$ = 1–2) and Their Anions. *J. Phys. Chem. A.* 114, 2893–2912. doi:10.1021/jp909512m

Tai, T. B., and Nguyen, M. T. (2009). Structure and Electron Delocalization of the boron Oxide Cluster $B_3(BO)_3$ and its Anion and Dianion. *Chem. Phys. Lett.* 483, 35–42. doi:10.1016/j.cplett.2009.10.054

Tian, W.-J., You, X.-R., Li, D.-Z., Ou, T., Chen, Q., Zhai, H.-J., et al. (2015). A First-Principles Study on the $B_5O_5^{+/0}$ and $B_5O_5^-$ Clusters: The boron Oxide Analogs of $C_6H_5^{+/0}$ and $CH_3Cl$. *J. Chem. Phys.* 143, 064303. doi:10.1063/1.4928282

Tian, W.-J., Zhao, L.-J., Chen, Q., Ou, T., Xu, H.-G., Zheng, W.-J., et al. (2015). Photoelectron spectroscopy of $B_4O_4^-$: Dual 3c-4e π hyperbonds and rhombic 4c-4e *o*-bond in boron oxide clusters. *J. Chem. Phys.* 142, 134305. doi:10.1063/1.4916386

von Niessen, W., Schirmer, J., and Cederbaum, L. S. (1984). Computational Methods for the One-Particle green's Function. *Comp. Phys. Rep.* 1, 57–125. doi:10.1016/0167-7977(84)90002-9

Wang, Y.-J., Guo, J.-C., and Zhai, H.-J. (2017). Why Nanoscale Tank Treads Move? Structures, Chemical Bonding, and Molecular Dynamics of a Doped boron Cluster $B_{10}C$. *Nanoscale* 9, 9310–9316. doi:10.1039/c7nr03193a

Yao, W.-Z., Guo, J.-C., Lu, H.-G., and Li, S.-D. (2009). $T_d$ $B(BO)_4^-$: A Tetrahedral Boron Oxide Cluster Analogous to Boron Hydride $T_d$ $BH_4^-$. *J. Phys. Chem. A.* 113, 2561–2564. doi:10.1021/jp809463j

Zakrzewski, V. G., and Ortiz, J. V. (1995). Semidirect Algorithms for Third-Order Electron Propagator Calculations. *Int. J. Quan. Chem.* 53, 583–590. doi:10.1002/qua.560530602

Zakrzewski, V. G., and von Niessen, W. (1993). Vectorizable Algorithm for green Function and many-body Perturbation Methods. *J. Comput. Chem.* 14, 13–18. doi:10.1002/jcc.540140105

Zhai, H.-J., Chen, Q., Bai, H., Li, S.-D., and Wang, L.-S. (2014). Boronyl Chemistry: The BO Group as a New Ligand in Gas-phase Clusters and Synthetic Compounds. *Acc. Chem. Res.* 47, 2435–2445. doi:10.1021/ar500136j

Zhai, H.-J., Guo, J.-C., Li, S.-D., and Wang, L.-S. (2011). Bridging $\eta^2$-BO in $B_2(BO)_3^-$ and $B_3(BO)_3^-$ Clusters: Boronyl Analogs of Boranes. *ChemPhysChem* 12, 2549–2553. doi:10.1002/cphc.201100553

Zhai, H.-J., Kiran, B., Li, J., and Wang, L.-S. (2003). Hydrocarbon Analogues of boron Clusters - Planarity, Aromaticity and Antiaromaticity. *Nat. Mater* 2, 827–833. doi:10.1038/nmat1012

Zhai, H.-J., Li, S.-D., and Wang, L.-S. (2007). Boronyls as Key Structural Units in Boron Oxide Clusters: $B(BO)_2^-$ and $B(BO)_3^-$. *J. Am. Chem. Soc.* 129, 9254–9255. doi:10.1021/ja072611y

Zhai, H.-J., Wang, L.-M., Li, S.-D., and Wang, L.-S. (2007). Vibrationally Resolved Photoelectron Spectroscopy of $BO^-$ and $BO_2^-$: A Joint Experimental and Theoretical Study. *J. Phys. Chem. A.* 111, 1030–1035. doi:10.1021/jp0666939

Zhai, H.-J., Wang, L.-S., Alexandrova, A. N., and Boldyrev, A. I. (2002). Electronic Structure and Chemical Bonding of $B_5^-$ and $B_5$ by Photoelectron Spectroscopy Andab Initiocalculations. *J. Chem. Phys.* 117, 7917–7924. doi:10.1063/1.1511184

Zhai, H.-J., Zhao, Y.-F., Li, W.-L., Chen, Q., Bai, H., Hu, H.-S., et al. (2014). Observation of an All-boron Fullerene. *Nat. Chem* 6, 727–731. doi:10.1038/nchem.1999

Zhao, L.-J., Tian, W.-J., Ou, T., Xu, H.-G., Feng, G., Xu, X.-L., et al. (2016). Structures and Chemical Bonding of $B_3O_3^{-/0}$ and $B_3O_3H^{-/0}$: A Combined Photoelectron Spectroscopy and First-Principles Theory Study. *J. Chem. Phys.* 144, 124301. doi:10.1063/1.4943768

Zubarev, D. Y., and Boldyrev, A. I. (2008). Developing Paradigms of Chemical Bonding: Adaptive Natural Density Partitioning. *Phys. Chem. Chem. Phys.* 10, 5207. doi:10.1039/b804083d

**Conflict of Interest:** The authors declare that the research was conducted in the absence of any commercial or financial relationships that could be construed as a potential conflict of interest.

**Publisher's Note:** All claims expressed in this article are solely those of the authors and do not necessarily represent those of their affiliated organizations, or those of the publisher, the editors, and the reviewers. Any product that may be evaluated in this article, or claim that may be made by its manufacturer, is not guaranteed or endorsed by the publisher.

frontiers | Frontiers in Chemistry

ORIGINAL RESEARCH
published: 13 April 2022
doi: 10.3389/fchem.2022.880804

# Superalkali Coated Rydberg Molecules

*Nikolay V. Tkachenko*[1], *Pavel Rublev*[1], *Alexander I. Boldyrev*[1]* *and Jean-Marie Lehn*[2]

[1]*Department of Chemistry and Biochemistry, Utah State University, Logan, UT, United States,* [2]*Laboratoire de Chimie Supramoléculaire, Institut de Science et d'Ingénierie, Supramoléculaires Université de Strasbourg, Strasbourg, France*

A series of complexes of Na, K, $NH_4$, and $H_3O$ with [bpy.bpy.bpy]cryptand, [2.2.2] cryptand, and spherical cryptand were investigated *via* DFT and ab initio methods. We found that by coating Rydberg molecules with the "organic skin" one could further decrease their ionization potential energy, reaching the values of ~1.5 eV and a new low record of 1.3 eV. The neutral cryptand complexes in this sense possess a weakly bounded electron and may be considered as very strong reducing agents. Moreover, the presence of an organic cage increases the thermodynamic stability of Rydberg molecules making them stable toward the proton detachment.

**Keywords: cryptands, cryptatium, superalkalis, Rydberg molecules, ionization potential (IP)**

OPEN ACCESS

***Edited by:***
*Suzana Velickovic, University of Belgrade, Serbia*

***Reviewed by:***
*Cina Foroutan-Nejad, Institute of Organic Chemistry (PAN), Poland*
*Jose Luis Cabellos, Polytechnic University of Tapachula, Mexico*

***Correspondence:**
*Alexander I. Boldyrev*
*a.i.boldyrev@usu.edu*

***Specialty section:***
*This article was submitted to Physical Chemistry and Chemical Physics, a section of the journal Frontiers in Chemistry*

***Received:*** *21 February 2022*
***Accepted:*** *14 March 2022*
***Published:*** *13 April 2022*

***Citation:***
*Tkachenko NV, Rublev P, Boldyrev AI and Lehn J-M (2022) Superalkali Coated Rydberg Molecules. Front. Chem. 10:880804. doi: 10.3389/fchem.2022.880804*

## INTRODUCTION

The [2.2.2]cryptand and spherical cryptand (**Scheme 1A, B**) invented by Lehn (Lehn, 1977), have been a subject of both theoretical (Elroby et al., 2006; Elroby, 2009; Puchta et al., 2019; Isaeva et al., 2021; Ćoćić et al., 2021; Ariyarathna, 2022) and experimental (Lehn, 1977; Lehn, 1978; Lehn, 1979; Lehn, 1980; Echegoyen et al., 1991; Arnaud-Neu et al., 2002; Cram et al., 2002; Izatt et al., 2002; Miyamoto et al., 2002; Badjić et al., 2011; Chung et al., 2020) studies for decades. The discovery of those fascinating compounds opened a huge field of supramolecular chemistry. Their unique guest particle selectivity and extremely low ionization potentials of neutral alkali-metal complexes (Cram and Lein, 1985; Huang et al., 1988; Kim et al., 1999) found an application in synthetic organic and inorganic chemistry. In particular, a huge number of multiply-charged Zintl anions with unusual structures have been synthesized using the popular [K⊂[2.2.2]cryptand] complex (Sun et al., 2018; Tkachenko et al., 2020; Wang et al., 2020).

Firstly, introduced by Gutsev and Boldyrev (Gutsev and Boldyrev, 1982), the family of superalkalis has been growing significantly. Despite the initially proposed $M_{k+1}L$ family, where M is an alkali atom and L is an electronegative atom of valence k, other superalkalis have been proposed and synthesized. Along with other inorganic binuclear superalkali (Tong et al., 2009), the definition of superalkalis was extended to polynuclear species such as polynuclear aromatic superalkalis (Sun et al., 2013; Parida et al., 2018), superalkali cations (Tong et al., 2011; Tong et al., 2012a; Tong et al., 2012b; Hou et al., 2013), organo-Zintl clusters (Giri et al., 2016; Reddy and Giri, 2016). Another family of compounds with low ionization potential is Rydberg molecules. Vivid examples of Rydberg molecules are $NH_4$ and $H_3O$ neutral species, whose unpa`ired electron occupies a diffuse orbital around the molecule. It has been shown that such Rydberg molecules are not long-living particles. Although the $T_d$ structure of $NH_4$ radical is a local minimum, it is only a metastable molecule and undergoes a dissociation into $NH_3$ and H* radical species (Herzberg, 1981; Signorell et al., 1997). Similar behavior is found for $H_3O$ neutral species (Luo and Jungen, 1999; Melin et al., 2005). It has been shown before that cryptand compounds can bind both $NH_4^+$ and $H_3O^+$ cations with a great selectivity (Cram et al., 1985; Behr et al., 2002; Junk, 2008). Thus, it will be interesting to

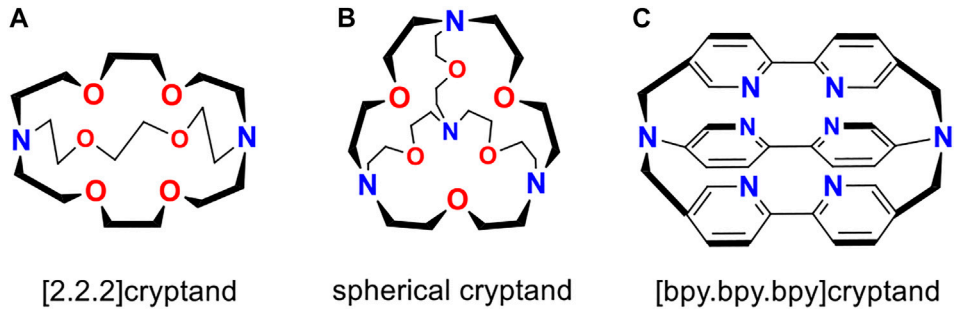


**SCHEME 1 |** The structures of organic cages considered in this work. [2.2.2]cryptand **(A)**, spherical cryptand **(B)**, and [bpy.bpy.bpy]cryptand **(C)** are shown.

investigate the electronic properties of neutral [R⊂cryptand] (R = $NH_4$, $H_3O$) complexes, since the organic coating could stabilize the Rydberg molecules and decrease their ionization potential as it was observed for alkali metal complexes (Cram and Lein, 1985; Huang et al., 1988; Kim et al., 1999). In this work, we investigate the electronic properties of coated Rydberg molecules *via* DFT and *ab initio* methods and compare their properties with alkali-metal cryptand complexes.

## COMPUTATIONAL METHODS

All structures were optimized using Perdew–Burke-Ernzerhof (PBE0) (Perdew et al., 1996) and Tao-Perdew-Staroverov-Scuseria (TPSSh) (Staroverov et al., 2003) hybrid functionals using def2-SVP basis set (Weigend and Ahlrichs, 2005). The frequency calculations were performed at the same level of theory. No imaginary frequencies were present, showing that the optimized structures are at local minima on the given PES. Ionization potentials were calculated at three different levels of theory. In particular, the single-point calculations at optimized geometry using DFT functionals (PBE0 and TPSSh) and a moderately large basis set def2-TZVPPD (Weigend and Ahlrichs, 2005) were carried out. In addition, single-point calculations using MP2 level of theory with cc-pvdz (C, N, O atoms) and aug-cc-pvdz (H, K, Na atoms) basis sets (Dunning, 1989; Kendall et al., 1992; Hill and Peterson, 2017) were performed. For convenience, we will denote this combination of basis functions as *Basis-1*. Due to the large values of spin contamination, the [bpy.bpy.bpy]cryptand complexes were calculated using ROHF-MBPT2 formalism (Lauderdale et al., 1991; Lauderdale et al., 1992). The vertical ionization potential (VIP) was calculated as the energy difference between the optimized neutral complex and the cation in the geometry of the neutral complex. The adiabatic ionization potential (AIP) was calculated as the energy differences between an optimized neutral cluster and an optimized cation. The natural charge distribution was calculated via NBO method as implemented in NBO7 software (Glendening et al., 2019). The topology analysis of electron localization function (ELF) (Silvi and Savin, 1994) was performed with the Multiwfn program (Lu and Chen, 2012). All calculations were performed with Gaussian 16 program (Frisch et al., 2016). The visualization of SOMO orbitals and geometries of the investigated species were performed using IboView software (Knizia, 2013; Knizia and Klein, 2015).

## RESULTS AND DISCUSSION

The neutral [Na⊂[bpy.bpy.bpy]cryptand] was firstly synthesized in 1991 by Lehn and coworkers (Echegoyen et al., 1991) through the electrochemical reduction of [$Na^+$⊂[bpy.bpy.bpy]cryptand] cation. This approach potentially can be used for the synthesis of superalkali cryptand complexes with Rydberg molecules. To investigate the electronic properties of such species, we chose three different organic cages ([2.2.2]cryptand, [bpy.bpy.bpy] cryptand, and spherical cryptand) that are very promising candidates for the capturing of $NH_4$ and $H_3O$ species. The structures of those cages are given in **Scheme 1**. For the comparison of ionization potentials, two alkali metal complexes were also considered. In particular [Na⊂[bpy.bpy.bpy]cryptand] was chosen as the first synthesized cryptand-superalkali species, and [K⊂[2.2.2]cryptand] was chosen as one of the most popular examples of alkali metal macrocyclic complex.

The geometries of neutral and cationic complexes were optimized with two different DFT hybrid functionals. It was shown before that PBE0 and TPSSh functionals can provide accurate geometries for macrocyclic and cryptand complexes (Tkachenko et al., 2019). The optimized geometries are consistent within two methods, showing the functional independence of the results. The geometries of neutral species are only slightly distorted from the geometries of cationic species, showing that the additional electron of neutral complexes does not participate in a significant

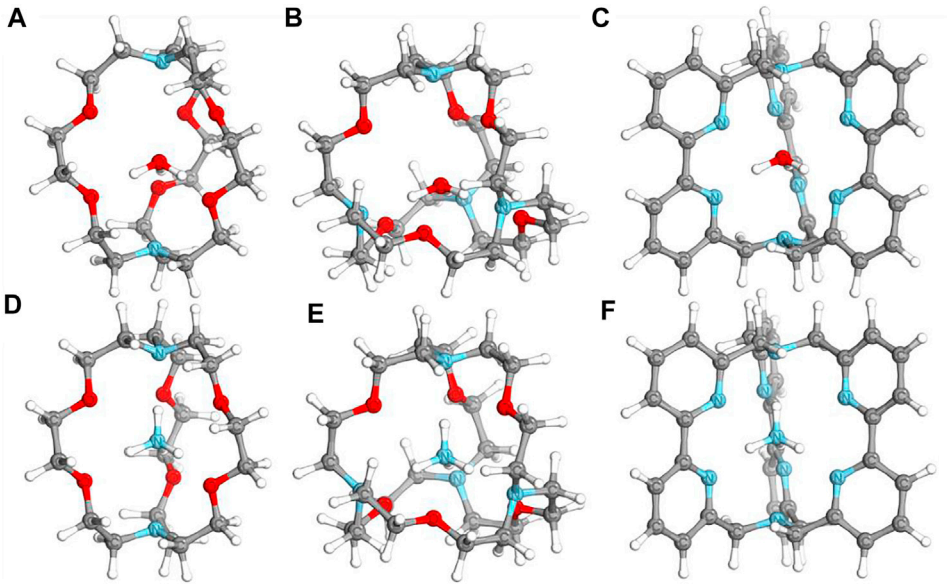


**FIGURE 1 |** Structures of optimized neutral complexes of $NH_4$ and $H_3O$. **(A)** [$H_3O$⊂[2.2.2]cryptand]; **(B)** [$H_3O$⊂spherical cryptand]; **(C)** [$H_3O$⊂[bpy.bpy.bpy] cryptand]; **(D)** [$NH_4$⊂[2.2.2]cryptand]; **(E)** [$NH_4$⊂spherical cryptand]; **(F)** [$NH_4$⊂[bpy.bpy.bpy]cryptand].

**TABLE 1 |** Free energies [kcal/mol] for the dissociation reaction of hydrogen radical from the central unit of investigated species calculated at TPSSh/def2-TZVPPD//TPSSh/def2-SVP level.

| Species | $\Delta G_r$ | Species | $\Delta G_r$ |
|---|---|---|---|
| $NH_4$ | −12.98 | $H_3O$ | −21.94 |
| [$NH_4$⊂spherical cryptand] | 24.61 | [$H_3O$⊂spherical cryptand] | −6.43 |
| [$NH_4$⊂[2.2.2]cryptand] | 17.10 | [$H_3O$⊂[2.2.2]cryptand] | −26.00 |
| [$NH_4$⊂[bpy.bpy.bpy]cryptand] | 52.98 | [$H_3O$⊂[bpy.bpy.bpy]cryptand] | 32.55 |

bonding formation process. The optimized structures of selected neutral species are given in **Figure 1**. Cartesian coordinates of all optimized structures are provided in the Supporting Information file (**Supplementary Table S1**). The natural charge distribution of neutral species showed that the negative charge is mainly distributed over the oxygen and nitrogen atoms of the organic ligand, while the central unit (either $H_3O$ or $NH_4$ species) formally possesses a +1 positive charge. In particular 0.757–0.806 and 0.794–0.876 positive natural charges on $H_3O$ and $NH_4$ molecules, respectively, were found in investigated complexes. This might be one of the key reasons for the stabilization of those Rydberg molecules, which are thermodynamically unstable toward dissociation of a proton in their naked form.

To illustrate the enhanced stability of encapsulated neutral molecules we performed calculations of dissociation energies for both naked and coated species. The reaction that was considered is a dissociation of a proton from the central unit with a formal reaction: $AH^{\bullet} \rightarrow A + H^{\bullet}$. Energies were calculated using the following expression: $\Delta G_r = \Delta G(A) + \Delta G(H^{\bullet}) - \Delta G(AH^{\bullet})$. The results are shown in **Table 1**. As we can observe, the dissociation of naked $H_3O$ and $NH_4$ occurs with a significant release of energy (21.9 and 13.0 kcal/mol, respectively). While the dissociation of the same species coated by cryptand complexes is energetically not favorable for most of the compexes (**Table 1**). Such a difference in $\Delta G_r$ values can lead us to the conclusion that [R⊂cryptand] complexes are thermodynamically more stable species, which may open the possibility of their fabrication.

Interestingly, for both $NH_4$ and $H_3O$, a significant decrease in ionization potentials was found after encapsulating the corresponding Rydberg molecules into organic cages. Particularly, the naked $NH_4$ and $H_3O$ molecules possess 4.57 and 5.55 eV VIP, respectively. Whereas the $NH_4$ and $H_3O$ encapsulated in [2.2.2]cryptand and spherical cryptand possess ionization potentials about 3–4 eV lower than the naked species (**Table 2**). Interestingly [bpy.bpy.bpy]cryptand systems show larger IPs by ~1.1 eV. A similar but not so pronounced pattern was found for alkali metals encapsulated in the [bpy.bpy.bpy]cryptand. The nature of such an increase in IPs is discussed below and related to the presence of a diffuse SOMO orbital in the system. We note, that the obtained IPs for $NH_4$ and $H_3O$ species are even lower than

**TABLE 2 |** Values of VIP and AIP [eV] obtained at MP2/*Basis-1* level of theory.

| Species | AIP | VIP | Species | AIP | VIP |
|---|---|---|---|---|---|
| Na | N/A | 4.961 | [$NH_4$⊂spherical cryptand] | 1.358 | 1.389 |
| K | N/A | 4.072 | [$NH_4$⊂[2.2.2]cryptand] | 1.308 | 1.381 |
| $NH_4$ | 4.429 | 4.566 | [$NH_4$⊂[bpy.bpy.bpy]cryptand] | 2.385 | 2.582 |
| $H_3O$ | 5.310 | 5.552 | [$H_3O$⊂spherical cryptand] | 1.379 | 1.696 |
| [Na⊂[bpy.bpy.bpy]cryptand] | 2.440 | 2.729 | [$H_3O$⊂[2.2.2]cryptand] | 1.362 | 1.676 |
| [K⊂[2.2.2]cryptand] | 1.387 | 1.612 | [$H_3O$⊂[bpy.bpy.bpy]cryptand] | 2.501 | 2.729 |

**TABLE 3 |** Values of VIP and AIP [eV] obtained using PBE0 and TPSSh functionals with def2-TZVPPD basis set.

| Species | PBE0 | | TPSSh | |
|---|---|---|---|---|
| | AIP | VIP | AIP | VIP |
| K | N/A | 4.370 | N/A | 4.233 |
| Na | N/A | 5.280 | N/A | 5.152 |
| $NH_4$ | 4.417 | 4.584 | 4.313 | 4.462 |
| $H_3O$ | 5.384 | 5.964 | 5.343 | 5.606 |
| [$NH_4$⊂spherical cryptand] | 1.440 | 1.519 | 1.400 | 1.479 |
| [$NH_4$⊂[2.2.2]cryptand] | 1.445 | 1.537 | 1.403 | 1.504 |
| [$NH_4$⊂[bpy.bpy.bpy]cryptand] | 3.060 | 3.220 | 3.214 | 3.359 |
| [$H_3O$⊂ spherical cryptand] | 1.457 | 1.780 | 1.388 | 1.704 |
| [$H_3O$⊂[2.2.2]cryptand] | 1.387 | 1.821 | 1.492 | 1.638 |
| [$H_3O$⊂[bpy.bpy.bpy]cryptand] | 3.162 | 3.323 | 3.307 | 3.452 |
| [Na⊂[bpy.bpy.bpy]cryptand] | 3.157 | 3.335 | 3.298 | 3.407 |
| [K⊂[2.2.2]cryptand] | 1.811 | 1.830 | 1.784 | 1.803 |

IPs of [K⊂[2.2.2]cryptand] which was shown before to be a superalkali with record low ionization potential (Tkachenko et al., 2019).

Similar results were obtained using PBE0 and TPSSh functionals with def2-TZVPPD basis set. Although the values of IPs are slightly higher than it was obtained for the MP2 method, the main trends preserve the same (**Table 3**).

To illustrate the diffuse nature of SOMO of investigated species, we plotted the isosurface graphs of corresponding orbitals shown in **Figure 2** (the orbitals were obtained from quasi-restricted orbitals formalism). We can see that for [2.2.2] cryptand and spherical cryptand complexes (**Figures 2A,B,D,E**), SOMO orbitals have a diffuse nature and surround the whole molecule entirely. In contrast, the unpaired electron of [bpy.bpy.bpy]cryptand complexes sit on the antibonding orbital of a π-conjugated system (**Figures 2C,F**). Isosurface plots of SOMO visualized with a different contour value can be found in the supporting information file (**Supplementary Figure S1**). Such an interesting difference in SOMO can be explained by the fact that different organic cages form different types of complexes with Rydberg molecules. Thus [2.2.2]cryptand and spherical

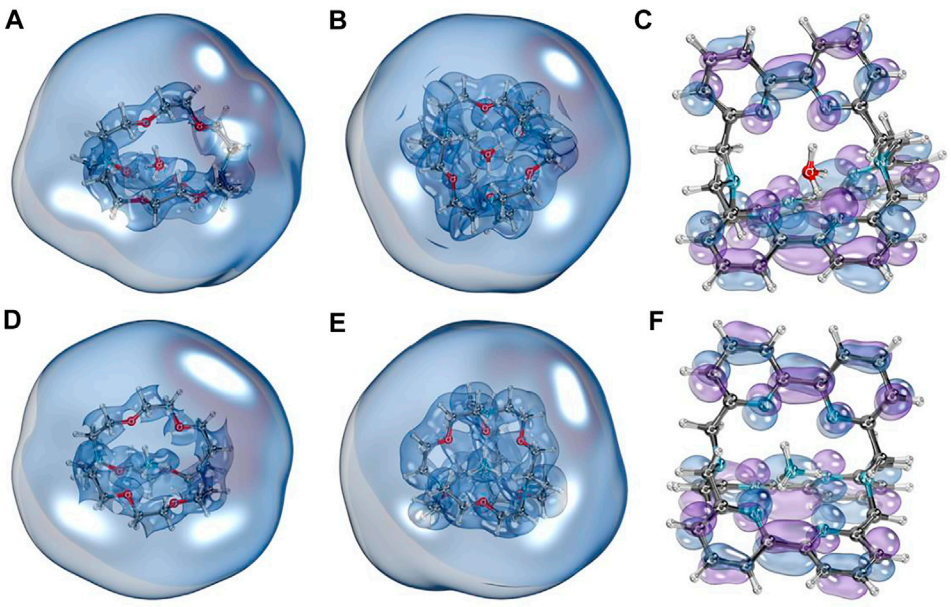


**FIGURE 2 |** Isosurface plots of singly occupied molecular orbitals of $NH_4$ and $H_3O$ complexes. **(A)** [$H_3O$⊂[2.2.2]cryptand]; **(B)** [$H_3O$⊂spherical cryptand]; **(C)** [$H_3O$⊂[bpy.bpy.bpy]cryptand]; **(D)** [$NH_4$⊂[2.2.2]cryptand]; **(E)** [$NH_4$⊂spherical cryptand]; **(F)** [$NH_4$⊂[bpy.bpy.bpy]cryptand]. A threshold of 100% was used for A, B, D, E to illustrate the diffuse nature of those orbitals. For C and F a lower 80% threshold was used for visualization.

cryptand complexes behave as electrides, possessing an electron density outside of the molecule, whereas [bpy.bpy.bpy]cryptand complexes form an ionic molecular compound bearing a negative charge entirely on the organic ligand. Such behavior can also be explained by the possibility of bipyridine molecules to form stable anionic species, that were experimentally isolated before (Bock et al., 1999; Gore-Randall et al., 2009). To further show the differences between the two types of complexes we performed an ELF basins analysis. The basins laying outside of the molecule were found for [2.2.2]cryptand and spherical cryptand complexes (**Supplementary Figure S2**). The integration of the electron density within the volume of the found ELF basins resulted in 0.3–0.6 |e| basins occupancy. In turn, no outside lying ELF basins were found for [bpy.bpy.bpy]cryptand complexes. Thus [2.2.2]cryptand and spherical cryptand complexes demonstrate an electride nature which is the reason for their lower IP values in comparison to [bpy.bpy.bpy] cryptand complexes.

## CONCLUSION

In this work we investigated the electronic properties of Rydberg molecules coated with cryptand organic cages. We showed that it is possible to significantly decrease the values of the ionization potentials by covering Rydberg molecules with an "organic skin." In particular, we found that the IP could be decreased, reaching the values of ~1.5 eV and a new low record of 1.3 eV (at MP2/*Basis-1* level). In addition, the coating ligand can increase the thermodynamic stability of a Rydberg molecule, opening an opportunity to obtain such strong reducing agents in the experiment.

## DATA AVAILABILITY STATEMENT

The additional data that support the findings of this study are available from the corresponding author on a reasonable request.

## AUTHOR CONTRIBUTIONS

All authors listed have made a substantial, direct, and intellectual contribution to the work and approved it for publication. NVT and PR performed the quantum chemical calculations and analyzed the data. AIB and JML conceived and designed the project.

## FUNDING

AIB acknowledges financial support from the R. Gaurth Hansen Professorship fund.

## ACKNOWLEDGMENTS

The support and resources from the Centre for High Performance Computing at the University of Utah are gratefully acknowledged. The authors thank the reviewer 1 for proposing a discussion on electride nature of [2.2.2]cryptand and spherical cryptand complexes.

## SUPPLEMENTARY MATERIAL

The Supplementary Material for this article can be found online at: https://www.frontiersin.org/articles/10.3389/fchem.2022.880804/full#supplementary-material

## REFERENCES

Ariyarathna, I. R. (2022). Superatomic Chelates: The Cases of Metal Aza-Crown Ethers and Cryptands. *Inorg. Chem.* 61 (1), 579–585. doi:10.1021/ACS.INORGCHEM.1C03261

Arnaud-Neu, F., Spiess, B., and Schwing-Weill, M. J. (2002). Solvent Effects in the Complexation of [2]-Cryptands and Related Monocycles with Transition- and Heavy-Metal Cations. *J. Am. Chem. Soc.* 104 (21), 5641–5645. doi:10.1021/JA00385A014

Badjić, J. D., Stojanović, S., and Ruan, Y. (2011). Kinetically and Thermodynamically Controlled Syntheses of Covalent Molecular Capsules. *Adv. Phys. Org. Chem.* 45, 1–37. doi:10.1016/B978-0-12-386047-7.00001-1

Behr, J. P., Dumas, P., and Moras, D. (2002). The Oxonium ($H_3O^+$) Cation: Molecular Structure of an Oxonium-Macrocyclic Polyether Complex. *J. Am. Chem. Soc.* 104 (17), 4540–4543. doi:10.1021/JA00381A007

Bock, H., Lehn, J. M., Pauls, J., Holl, S., Krenzel, V., Rousset, C. J., et al. (1999). Sodium Salts of the Bipyridine Dianion: Polymer $[(bpy)^{2-}\{Na^+(dme)\}_2]\infty$, Cluster $[(Na_8O)^{6+}\ Na^+{}_6(bpy)^{2-}{}_6\ (Tmeda)_6$, and Monomer $[(bpy)^{2-}\{Na^+(Pmdta)\}_2]$. *Angew. Chem. Intl Edit* 38 (7), 952–955. doi:10.1002/(sici)1521-3773(19990401)38:7<952:aid-anie952>3.0.co;2-#

Chung, A. B., Huh, D. N., Ziller, J. W., and Evans, W. J. (2020). 2.2.2-Cryptand as a Bidentate Ligand in Rare-Earth Metal Chemistry. *Inorg. Chem. Front.* 7 (22), 4445–4451. doi:10.1039/D0QI00746C

Ćoćić, D., Manaa, A., Siegl, S., Puchta, R., and Eldik, R. (2021). [3.2.1] and [4.1.1] Isomers of Lehn's [2.2.2] Cryptand: Prediction of Ion Selectivity by Quantum Chemical Calculations XV**. *Z. Anorg. Allg. Chem.* 647 (8), 915–921. doi:10.1002/ZAAC.202000452

Cram, D. J., Kaneda, T., Helgeson, R. C., Brown, S. B., Knobler, C. B., Maverick, E., et al. (1985). Host-guest Complexation. 35. Spherands, the First Completely Preorganized Ligand Systems. *J. Am. Chem. Soc.* 107 (12), 3645–3657. doi:10.1021/JA00298A040

Cram, D. J., Kaneda, T., Helgeson, R. C., and Lein, G. M. (2002). Spherands - Ligands Whose Binding of Cations Relieves Enforced Electron-Electron Repulsions. *J. Am. Chem. Soc.* 101 (22), 6752–6754. doi:10.1021/JA00516A048

Cram, D. J., and Lein, G. M. (1985). Host-guest Complexation. 36. Spherand and Lithium and Sodium Ion Complexation Rates and Equilibria. *J. Am. Chem. Soc.* 107 (12), 3657–3668. doi:10.1021/JA00298A041

Dunning, T. H. (1989). Gaussian Basis Sets for Use in Correlated Molecular Calculations. I. The Atoms boron through Neon and Hydrogen. *J. Chem. Phys.* 90 (2), 1007–1023. doi:10.1063/1.456153

Echegoyen, L., DeCian, A., Fischer, J., and Lehn, J.-M. (1991). Cryptatium: A Species of Expanded Atom/Radical Ion Pair Type from Electroreductive Crystallization of the Macrobicyclic Sodium Tris(Bipyridine) Cryptate. *Angew. Chem. Int. Ed. Engl.* 30 (7), 838–840. doi:10.1002/ANIE.199108381

Elroby, S. A. K. (2009). The Effect of Donor Atoms on the Complexation of Alkali Cations with Spherands: A Density Functional Investigation. *Int. J. Quan. Chem.* 109 (7), 1515–1521. doi:10.1002/QUA.21970

Elroby, S. A., Lee, K. H., Cho, S. J., and Hinchliffe, A. (2006). A DFT Study of Spherands Containing Five Anisyl Groups - Highly Preorganized to Bind the Alkali Metal. *Can. J. Chem.* 84 (8), 1045–1049. doi:10.1139/V06-130

Frisch, M. J., Trucks, G. W., Schlegel, H. B., Scuseria, G. E., Robb, M. A., Cheeseman, J. R., et al. (2016). *Gaussian 16, Revision B.01.* Wallingford, CT: Gaussian, Inc.

Giri, S., Reddy, G. N., and Jena, P. (2016). Organo-Zintl Clusters [$P_7R_4$]: A New Class of Superalkalis. *J. Phys. Chem. Lett.* 7 (5), 800–805. doi:10.1021/ACS.JPCLETT.5B02892/SUPPL_FILE/JZ5B02892_LIVESLIDES.MP4

Glendening, E. D., Landis, C. R., and Weinhold, F. (2019). NBO 7.0 : New Vistas in Localized and Delocalized Chemical Bonding Theory. *J. Comput. Chem.* 40 (25), 2234–2241. doi:10.1002/JCC.25873

Gore-Randall, E., Irwin, M., Denning, M. S., and Goicoechea, J. M. (2009). Synthesis and Characterization of Alkali-Metal Salts of 2,2′- and 2,4′-Bipyridyl Radicals and Dianions. *Inorg. Chem.* 48 (17), 8304–8316. doi:10.1021/IC9009459

Gutsev, G. L., and Boldyrev, A. I. (1982). DVM $X_\alpha$ Calculations on the Electronic Structure of "superalkali" Cations. *Chem. Phys. Lett.* 92 (3), 262–266. doi:10.1016/0009-2614(82)80272-8

Herzberg, G. (1981). Rydberg Spectra of Triatomic Hydrogen and of the Ammonium Radical. *Faraday Discuss. Chem. Soc.* 71 (0), 165–173. doi:10.1039/DC9817100165

Hill, J. G., and Peterson, K. A. (2017). Gaussian Basis Sets for Use in Correlated Molecular Calculations. XI. Pseudopotential-Based and All-Electron Relativistic Basis Sets for Alkali Metal (K-Fr) and Alkaline Earth (Ca-Ra) Elements. *J. Chem. Phys.* 147 (24), 244106. doi:10.1063/1.5010587

Hou, N., Li, Y., Wu, D., and Li, Z.-R. (2013). Do Nonmetallic Superalkali Cations Exist? *Chem. Phys. Lett.* 575, 32–35. doi:10.1016/J.CPLETT.2013.05.014

Huang, R. H., Faber, M. K., Moeggenborg, K. J., Ward, D. L., and Dye, J. L. (1988). Structure of $K^+$(cryptand[2.2.2]) Electride and Evidence for Trapped Electron Pairs. *Nature* 331 (6157), 599–601. doi:10.1038/331599a0

Isaeva, V. A., Gamov, G. A., and Sharnin, V. A. (2021). Quantum-Chemical Calculations and Stability Analysis of Copper(II) Complexes with Cryptand [2.2.2]. *Russ. J. Inorg. Chem.* 66 (11), 1696–1702. doi:10.1134/S0036023621110097

Izatt, R. M., Bradshaw, J. S., Nielsen, S. A., Lamb, J. D., Christensen, J. J., and Sen, D. (2002). Thermodynamic and Kinetic Data for Cation-Macrocycle Interaction. *Chem. Rev.* 85 (4), 271–339. doi:10.1021/CR00068A003

Junk, P. C. (2008). Crown Ethers as Stabilising Ligands for Oxonium Ions. *New J. Chem.* 32 (5), 762–773. doi:10.1039/B800122G

Kendall, R. A., Dunning, T. H., and Harrison, R. J. (1992). Electron Affinities of the First-row Atoms Revisited. Systematic Basis Sets and Wave Functions. *J. Chem. Phys.* 96 (9), 6796–6806. doi:10.1063/1.462569

Kim, J., Ichimura, A. S., Huang, R. H., Redko, M., Phillips, R. C., Jackson, J. E., et al. (1999). Crystalline Salts of $Na^-$ and $K^-$ (Alkalides) that Are Stable at Room Temperature. *J. Am. Chem. Soc.* 121 (45), 10666–10667. doi:10.1021/JA992667V

Knizia, G. (2013). Intrinsic Atomic Orbitals: An Unbiased Bridge between Quantum Theory and Chemical Concepts. *J. Chem. Theor. Comput.* 9 (11), 4834–4843. doi:10.1021/CT400687B

Knizia, G., and Klein, J. E. M. N. (2015). Electron Flow in Reaction Mechanisms-Revealed from First Principles. *Angew. Chem. Int. Ed.* 54 (18), 5518–5522. doi:10.1002/ANIE.201410637

Lauderdale, W. J., Stanton, J. F., Gauss, J., Watts, J. D., and Bartlett, R. J. (1991). Many-body Perturbation Theory with a Restricted Open-Shell Hartree—Fock Reference. *Chem. Phys. Lett.* 187 (1–2), 21–28. doi:10.1016/0009-2614(91)90478-R

Lauderdale, W. J., Stanton, J. F., Gauss, J., Watts, J. D., and Bartlett, R. J. (1992). Restricted Open-shell Hartree-Fock-based Many-body Perturbation Theory: Theory and Application of Energy and Gradient Calculations. *J. Chem. Phys.* 97 (9), 6606–6620. doi:10.1063/1.463664

Lehn, J.-M. (1979). Macrocyclic Receptor Molecules: Aspects of Chemical Reactivity. Investigations into Molecular Catalysis and Transport Processes. *Pure Appl. Chem.* 51 (5), 979–997. doi:10.1351/PAC197951050979

Lehn, J. M. (1980). Cryptate Inclusion Complexes, Effects on Solute-Solute and Solute-Solvent Interactions and on Ionic Reactivity. *Pure Appl. Chem.* 52 (10), 2303–2319. doi:10.1351/PAC198052102303

Lehn, J. M. (1978). Cryptates: Inclusion Complexes of Macropolycyclic Receptor Molecules. *Pure Appl. Chem.* 50 (9–10), 871–892. doi:10.1351/PAC197850090871

Lehn, J. M. (1977). Cryptates: Macropolycyclic Inclusion Complexes. *Pure Appl. Chem.* 49 (6), 857–870. doi:10.1351/PAC197749060857

Lu, T., and Chen, F. (2012). Multiwfn: A Multifunctional Wavefunction Analyzer. *J. Comput. Chem.* 33 (5), 580–592. doi:10.1002/JCC.22885

Luo, M., and Jungen, M. (1999). The $H_3O$ Rydberg Radical. *Chem. Phys.* 241 (3), 297–303. doi:10.1016/S0301-0104(98)00426-1

Melin, J., Ortiz, J. V., Martín, I., Velasco, A. M., and Lavín, C. (2005). Ground and Excited States of the Rydberg Radical $H_3O$: Electron Propagator and Quantum Defect Analysis. *J. Chem. Phys.* 122 (23), 234317. doi:10.1063/1.1926286

Miyamoto, R., Sato, H., and Sudoh, S. (2002). EPR Spectral Study of Gadolinium(III) Cryptate. *EPR in the 21st Century* 2002, 316–321. doi:10.1016/B978-044450973-4/50058-5

Parida, R., Reddy, G. N., Ganguly, A., Roymahapatra, G., Chakraborty, A., and Giri, S. (2018). On the Making of Aromatic Organometallic Superalkali Complexes. *Chem. Commun.* 54 (31), 3903–3906. doi:10.1039/C8CC01170B

Perdew, J. P., Burke, K., and Ernzerhof, M. (1996). Generalized Gradient Approximation Made Simple. *Phys. Rev. Lett.* 77 (18), 3865–3868. doi:10.1103/PHYSREVLETT.77.3865

Puchta, R., Ćoćić, D., Michel, M., and van Eldik, R. (2019). Host-guest Complexes of the Beer-Can-Cryptand: Prediction of Ion Selectivity by Quantum Chemical Calculations XI. *J. Coord. Chem.* 72 (12), 2106–2114. doi:10.1080/00958972.2019.1636975

Reddy, G. N., and Giri, S. (2016). Organic Heterocyclic Molecules Become Superalkalis. *Phys. Chem. Chem. Phys.* 18 (35), 24356–24360. doi:10.1039/C6CP04430A

Signorell, R., Palm, H., and Merkt, F. (1997). Structure of the Ammonium Radical from a Rotationally Resolved Photoelectron Spectrum. *J. Chem. Phys.* 106 (16), 6523–6533. doi:10.1063/1.473653

Silvi, B., and Savin, A. (1994). Classification of Chemical Bonds Based on Topological Analysis of Electron Localization Functions. *Nature* 371 (6499), 683–686. doi:10.1038/371683a0

Staroverov, V. N., Scuseria, G. E., Tao, J., and Perdew, J. P. (2003). Comparative Assessment of a New Nonempirical Density Functional: Molecules and Hydrogen-Bonded Complexes. *J. Chem. Phys.* 119 (23), 12129–12137. doi:10.1063/1.1626543

Sun, W.-M., Li, Y., Wu, D., and Li, Z.-R. (2013). Designing Aromatic Superatoms. *J. Phys. Chem. C* 117 (46), 24618–24624. doi:10.1021/JP408810E

Sun, W.-M., Wu, D., Kang, J., Li, C.-Y., Chen, J.-H., Li, Y., et al. (2018). Decorating Zintl Polyanions with Alkali Metal Cations: A Novel Strategy to Design Superatom Cations with Low Electron Affinity. *J. Alloys Compd.* 740, 400–405. doi:10.1016/J.JALLCOM.2017.12.075

Tkachenko, N. V., Sun, Z. M., and Boldyrev, A. I. (2019). Record Low Ionization Potentials of Alkali Metal Complexes with Crown Ethers and Cryptands. *ChemPhysChem* 20 (16), 2060–2062. doi:10.1002/CPHC.201900422

Tkachenko, N. V., Zhang, X. W., Qiao, L., Shu, C. C., Steglenko, D., Muñoz-Castro, A., et al. (2020). Spherical Aromaticity of All-Metal $[Bi@In_8Bi_{12}]^{3-/5-}$ Clusters. *Chem. Eur. J.* 26 (9), 2073–2079. doi:10.1002/CHEM.201905264

Tong, J., Li, Y., Wu, D., Li, Z.-R., and Huang, X.-R. (2011). Ab Initio Investigation on a New Class of Binuclear Superalkali Cations $M_2Li_{2k+1}^+$ ($F_2Li_3^+$, $O_2Li_5^+$, $N_2Li_7^+$, and $C_2Li_9^+$). *J. Phys. Chem. A.* 115 (10), 2041–2046. doi:10.1021/JP110417Z

Tong, J., Li, Y., Wu, D., Li, Z.-R., and Huang, X.-R. (2009). Low Ionization Potentials of Binuclear Superalkali $B_2Li_{11}$. *J. Chem. Phys.* 131 (16), 164307. doi:10.1063/1.3254835

Tong, J., Li, Y., Wu, D., and Wu, Z.-J. (2012). Theoretical Study on Polynuclear Superalkali Cations with Various Functional Groups as the Central Core. *Inorg. Chem.* 51 (11), 6081–6088. doi:10.1021/IC202675J

Tong, J., Wu, Z., Li, Y., and Wu, D. (2012). Prediction and Characterization of Novel Polynuclear Superalkali Cations. *Dalton Trans.* 42 (2), 577–584. doi:10.1039/C2DT31429K

Wang, Z.-C., Tkachenko, N. v., Qiao, L., Matito, E., Muñoz-Castro, A., Boldyrev, A. I., et al. (2020). All-metal σ-antiaromaticity in Dimeric Cluster Anion $\{[CuGe_9Mes]_2\}^{4-}$. *Chem. Commun.* 56 (48), 6583–6586. doi:10.1039/D0CC02525A

Weigend, F., and Ahlrichs, R. (2005). Balanced Basis Sets of Split Valence, Triple Zeta Valence and Quadruple Zeta Valence Quality for H to Rn: Design and Assessment of Accuracy. *Phys. Chem. Chem. Phys.* 7 (18), 3297–3305. doi:10.1039/B508541A

**Conflict of Interest:** The authors declare that the research was conducted in the absence of any commercial or financial relationships that could be construed as a potential conflict of interest.

**Publisher's Note:** All claims expressed in this article are solely those of the authors and do not necessarily represent those of their affiliated organizations or those of the publisher, the editors, and the reviewers. Any product that may be evaluated in this article, or claim that may be made by its manufacturer, is not guaranteed or endorsed by the publisher.

frontiers | Frontiers in Chemistry

ORIGINAL RESEARCH
published: 21 April 2022
doi: 10.3389/fchem.2022.863408

# Superhalogen Anions Supported by the Systems Comprising Alternately Aligned Boron and Nitrogen Central Atoms

*Adrianna Cyraniak, Dawid Faron, Sylwia Freza, Iwona Anusiewicz and Piotr Skurski**

*Laboratory of Quantum Chemistry, Faculty of Chemistry, University of Gdańsk, Gdańsk, Poland*

Using DFT/(B3LYP/wB97XD/B2PLYPD) and OVGF electronic structure methods with flexible atomic orbital basis sets, we examined the series of polynuclear superhalogen anions matching the $(BF_3(BN)_nF_{4n+1})^-$ formula (for $n$ = 1-10,13,18-20) containing alternately aligned boron and nitrogen central atoms decorated with fluorine ligands. It was found that the equilibrium structures of these anions correspond to fully extended chains (with each B and N central atom surrounded by four substituents arranged in a tetrahedral manner) and thus mimic the globally stable fully extended (all-*trans*) conformations of higher n-alkanes. The vertical electron detachment energies of the $(BF_3(BN)_nF_{4n+1})^-$ anions were found to exceed 8 eV in all cases and gradually increase with the increasing number of $n$. The approximate limiting value of vertical electron binding energy that could be achieved for such polynuclear superhalogen anions was estimated as equal to ca. 10.7 eV.

**Keywords: polynuclear superhalogens, anions, electronic transmutation, excess electron, electron binding energies**

OPEN ACCESS

***Edited by:***
*Sugata Chowdhury, National Institute of Standards and Technology (NIST), United States*

***Reviewed by:***
*Sarvesh Kumar Pandey, Indian Institute of Science (IISc), India*
*Bing Yin, Northwest University, China*
*Purusottam Jena, Virginia Commonwealth University, United States*

****Correspondence:***
*Piotr Skurski*
*piotr.skurski@ug.edu.pl*

***Specialty section:***
*This article was submitted to Physical Chemistry and Chemical Physics, a section of the journal Frontiers in Chemistry*

***Received:*** *27 January 2022*
***Accepted:*** *07 April 2022*
***Published:*** *21 April 2022*

***Citation:***
*Cyraniak A, Faron D, Freza S, Anusiewicz I and Skurski P (2022) Superhalogen Anions Supported by the Systems Comprising Alternately Aligned Boron and Nitrogen Central Atoms. Front. Chem. 10:863408. doi: 10.3389/fchem.2022.863408*

## INTRODUCTION

Superhalogens are commonly defined as the systems exhibiting the electron affinity (EA) larger than that of a chlorine atom (3.62 eV) (Hotop and Lineberger, 1985). The existence of such molecules and their corresponding anions (so-called superhalogen anions) was proposed in 1981 by Gutsev and Boldyrev who characterized (on the basis of theoretical calculations) several negatively charged compounds matching the $(MF_{k+1})^-$ formula and a few $(MO_{(k+1)/2})^-$ anions (where M is main-group central atom of maximal valence k) and confirmed their large excess electron binding energies (Gutsev and Boldyrev, 1981a). In the course of later studies, Gutsev and Boldyrev modified their formula describing superhalogens to cover various halogen atoms X that may serve as ligands in such systems (i.e., $MX_{k+1}$ for the neutral molecules and $(MX_{k+1})^-$ for the corresponding anions) (Gutsev and Boldyrev, 1981a; 1981b, 1984, 1985). On the other hand, many experimental attempts to measure the electronic stability of such anions were made, however, all determinations performed before 1999 were related to condensed phases only whereas the gas phase electron detachment energies had not been measured (Heni and Illenberger, 1985; Metz et al., 1988; Weaver et al., 1988; Compton, 1995; Huey et al., 1996; Wu et al., 1996; Taylor et al., 1998). The existence of superhalogen anions in gas phase was experimentally confirmed in 1999 by Wang and co-workers who measured gas-phase electron detachment energies of $(MX_2)^-$ (M = Li, Na; X = Cl, Br, I) systems (Wang et al., 1999). The measurements performed by the Wang group were supported by the advanced ab initio calculations executed by Boldyrev and Simons and it turned out that the vertical electron detachment

energies (VDE) elucidated from the photoelectron spectra (i.e., 5.92 ± 0.04 $(LiCl_2)^-$, 5.42 ± 0.03 $(LiBr_2)^-$, 4.88 ± 0.03 $(LiI_2)^-$, 5.86 ± 0.06 $(NaCl_2)^-$, 5.36 ± 0.06 $(NaBr_2)^-$, and 4.84 ± 0.06 eV $(NaI_2)^-$) were in excellent agreement with the values predicted by theoretical calculations (Wang et al., 1999). This joined experimental and theoretical study of selected superhalogen anions was in fact a milestone achievement which both confirmed the existence and stability of such species in gas phase and demonstrated the usefulness of certain ab initio methods to predict their structures and excess electron binding energies. Since then, many research groups turned their attention to superhalogens which resulted in proposing numerous new compounds of that type in the following years. These studies included various alternative superhalogen anions utilizing non-metal or metalloid central atoms (e.g., $(SiF_5)^-$ (VDE = 9.32 eV), $(GeF_5)^-$ (VDE = 9.74 eV), $(PF_6)^-$ (VDE = 9.43 eV)) (Sobczyk et al., 2003; Marchaj et al., 2012), as well as numerous non-halogen ligands (such as halogenoids (Smuczyńska and Skurski, 2009; Li and Yin, 2021), electrophilic groups(Anusiewicz, 2009a), acidic functional groups (Anusiewicz, 2009b), and other halogen-free fragments (Sun et al., 2016c). In addition, it was found that even superhalogens themselves may act as effective ligands in superhalogen systems (Wang et al., 2009; Götz et al., 2010; Koirala et al., 2010, 2013; Willis et al., 2010; Feng et al., 2011; Paduani and Jena, 2012, 2013; Hou et al., 2013; Li et al., 2013; Tian et al., 2014; Yang et al., 2014; Sun W.-M. et al., 2016; Paduani, 2016; Liu et al., 2017). These and other superhalogen anions have recently been described in a comprehensive review article (Skurski, 2021).

Compounds exhibiting large excess electron binding energy or small ionization potential are of special interest because a wide range of new materials (such as organic superconductors, organic metals, ionic liquids, etc.) could be designed and synthesized on their base (Awasthi et al., 2021; Pandey, 2021). Since superhalogens represent the species having larger EAs than other commonly known systems, the search for strong electron acceptors is focused primarily on these compounds. Taking into account that the electronic stability of a monoanion strongly depends on the ability of excess charge delocalization over the molecular framework, one may anticipate that superhalogens containing large number of electronegative ligands should exhibit large excess electron binding energies. However, the number of ligands bound to a single central atom cannot be increased beyond certain values (mostly due to destabilizing valence repulsion effects and steric hindrance). Hence, polynuclear superhalogen anions matching the $(M_nX_{n\times k+1})^-$ formula in which an excess electron density is expected to delocalize over $n\times k+1$ electronegative ligands have been extensively studied in recent years (Alexandrova et al., 2004; Anusiewicz and Skurski, 2007; Freza and Skurski, 2010; Sikorska and Skurski, 2012; Wileńska et al., 2014; Yin et al., 2014; Li et al., 2015a, 2015b, Li et al., 2015 M.-M.; Czapla and Skurski, 2015, 2018; Díaz-Tinoco and Ortiz, 2016a; Díaz-Tinoco and Ortiz, 2016b; Sun et al., 2016b; Ding et al., 2017; Zhao et al., 2017; Anusiewicz et al., 2018; Cyraniak et al., 2019; Shi et al., 2019). Even though the polynuclear superhalogens investigated to date contain various central atoms (e.g., Li, Na, Mg, Ca, B, Al, Ge, Sn, P, Ti, Sb, As, V, In, Ta, Fe, Au, Pt), the systems utilizing nitrogen central atoms have not been proposed thus far. The lack of polynuclear superhalogens containing N central atoms seems intriguing and inspired us to make an attempt to propose and characterize such compounds. In addition, having in mind the well-known stability of saturated hydrocarbon structures, we decided to design our systems in a way that reflects the structures of chain-like $C_nH_{2n+2}$ molecules. In order to achieve that goal, we adopted the electronic transmutation concept which was introduced a decade ago.

Electronic transmutation is a concept introduced by Olson and Boldyrev (Olson and Boldyrev, 2012) who utilized the isoelectronic principle (Gillis, 1958) by proving that an element M with atomic number Z (i.e., $_ZM$) is expected to undergo a transmutation into $_{Z+1}M$ *via* the acquisition of an extra electron. It was demonstrated (Alexandrova et al., 2003; Jemmis and Jayasree, 2003; Osorio et al., 2012; Popov and Boldyrev, 2013; Gish et al., 2015; Popov et al., 2015; Zhang et al., 2018a, 2018b; Lundell et al., 2020) that the resulting species (having Z+1 electrons) possesses the chemical bonding properties of the neighboring element $_{Z+1}M$ as if it was put in the place of the transmuted element $_ZM$. Certainly, the same line of reasoning can be used for turning the element $_ZM$ into $_{Z-1}M$ by withdrawing one electron from it. Hence, we decided to design the structures containing the alternately aligned boron and nitrogen atoms (forming the $(BN)_n$ 'core' of various length) and decorated with $4n+2$ substituents (as if the B and N atoms comprising the core were carbon atoms). Indeed, assuming that each boron atom acquires an electron from its neighboring nitrogen atom, one may view the $(BN)_n$ core as composed of alternately aligned $B^-$and $N^+$ ions, each of which is expected to mimic the bonding properties of a carbon atom (due to the presence of four valence electrons). As a result, the $(BN)_n$ core might be expected to exhibit the bonding properties of the $C_{2n}$ chain which naturally suggests the presence of $4n+2$ substituents (to mimic the saturated hydrocarbon structure). Recalling that fluorine atoms are likely the most effective ligands in superhalogen systems, we decided to decorate the $(BN)_n$ core with $4n+1$ fluorine substituents and one $BF_3$ substituent. The reason for using one $BF_3$ substituent (instead of F) was that we wanted the whole system to represent a closed-shell superhalogen monoanion $(BF_3(BN)_nF_{4n+1})^-$ rather than a closed shell neutral molecule $(BN)_nF_{4n+2}$.

Hence, in this contribution, we first describe the structures of the $(BF_3(BN)_nF_{4n+1})^-$ ($n$ = 1-10,13,18-20) systems followed by our theoretical findings concerning their thermodynamic stability and then we move on to discuss the vertical electron detachment energies these polynuclear superhalogen anions are characterized with.

## METHODS

The stationary point structures of all systems investigated were obtained by applying the Density Functional Theory (DFT) method with the B3LYP (Becke, 1988; Lee et al., 1988)

functional and the 6-311+G(d) (Krishnan et al., 1980; McLean and Chandler, 1980) basis set for all atoms. The harmonic vibrational frequencies characterizing the stationary points were evaluated (without scaling) at the same level of theory to assure that all obtained structures correspond to true minima on the potential energy surface. The vertical electron detachment energies of the $(BF_3(BN)_nF_{4n+1})^-$ ($n$ = 1-8) anions were calculated by applying the outer valence Green function OVGF method (*B* approximation) (Rowe, 1968; Simons, 1971; Cederbaum, 1975; Ortiz, 1988; Zakrzewski and Ortiz, 1994; Zakrzewski et al., 1996b) together with the 6-311+G(d) basis sets. Due to the limited computer resources available, the VDE values for larger systems (i.e., $(BF_3(BN)_nF_{4n+1})^-$ ($n$ = 9,10,13,18-20)) were estimated at the B3LYP/6-311+G(d) level of theory.

In order to verify the performance of the 6-311+G(d) basis set in predicting the VDE values of the anions studied we calculated (for $(BF_3(BN)F_5)^-$ and $(BF_3(BN)_2F_9)^-$) the vertical electron detachment energies with two additional basis sets (i.e., aug-cc-pVTZ (Dunning, 1989) and Def2TZVP (Weigend and Ahlrichs, 2005)). As it turned out, the VDEs calculated at the OVGF/aug-cc-pVTZ level differ from those obtained by employing the OVGF/6-311+G(d) treatment by less than 0.2 eV (ca. 2%) whereas the VDEs calculated at the OVGF/Def2TZVP level differ by less than 0.3 eV (ca. 4%) from the OVGF/6-311+G(d) values. Since the above mentioned differences were found to be both relatively small and nearly insignificant (0.02–0.05 eV) for the larger anion tested (i.e., $(BF_3(BN)_2F_9)^-$), we conclude that our VDEs predicted with the 6-311+G(d) basis set can be considered reliable, especially for the $(BF_3(BN)_nF_{4n+1})^-$, n > 1 anions).

As far as the performance of other DFT functionals in reproducing the preliminary estimates of the VDE values is concerned, we found (again, for $(BF_3(BN)F_5)^-$ and $(BF_3(BN)_2F_9)^-$) that 1) employing the wB97XD functional (Chai and Head-Gordon, 2008) leads to the vertical electron detachment energies whose values are smaller by 0.08–0.12 eV than those predicted at the OVGF/6-311+G(d) level and larger by 0.20–0.49 eV than the values obtained with the B3LYP functional; 2) the use of the B2PLYPD functional (Grimme, 2006; Schwabe and Grimme, 2007) leads to the VDEs whose values are smaller by 0.22–0.36 eV than those predicted at the OVGF/6-311+G(d) level and larger by 0.10–0.14 eV than the values calculated with the B3LYP functional. Therefore, we conclude that our preliminary estimations of the VDEs characterizing the $(BF_3(BN)_nF_{4n+1})^-$ anions are reliable yet the results obtained for two smallest systems considered indicate that the wB97XD functional performs best and thus it should be chosen if the VDE values were to be calculated only by DFT methods.

Due to the fact that the OVGF approximation remains valid only for outer valence ionization for which the pole strengths (PS) are greater than 0.80–0.85 (Zakrzewski et al., 1996a), we verified that the PS values obtained were sufficiently large to justify the use of the OVGF method.

The partial atomic charges were fitted to the electrostatic potential according to the Merz-Singh-Kollman scheme (Besler et al., 1990).

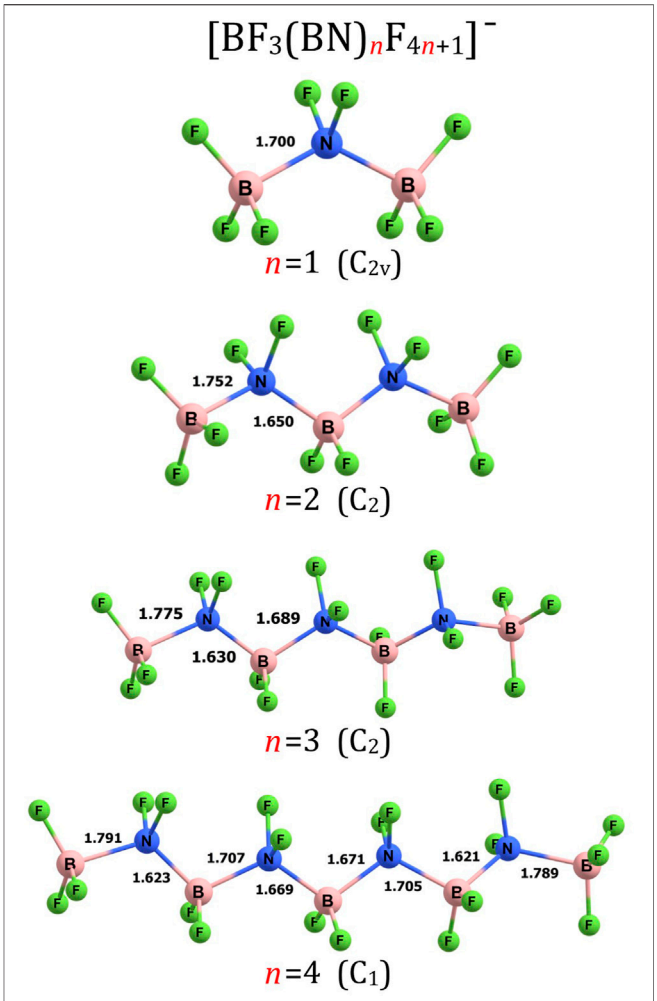


**FIGURE 1 |** Equilibrium structures of $(BF_3(BN)_nF_{4n+1})^-$ ($n$ = 1–4) anions (symmetry point group in parenthesis). Selected bond lengths are given in Å.

All calculations were carried out using the GAUSSIAN16 (Rev.B.01) package(Frisch et al., 2016).

## RESULTS

In order to study the series of $(BF_3(BN)_nF_{4n+1})^-$ anions, we decided to examine their structures for $n$ = 1-10 and a few arbitrarily selected larger structures (for $n$ = 13, 18-20). The reason was to verify whether the structures of larger $(BF_3(BN)_nF_{4n+1})^-$ systems reflect those containing shorter $(BN)_n$ core and to establish the approximate limit for the vertical electron detachment energy which could be achieved for these anions (presumably for large values of $n$).

### Equilibrium Structures and Stability of $(BF_3(BN)_nF_{4n+1})^-$ ($n$ = 1-10,13,18-20) Anions

The simplest anion matching the $(BF_3(BN)_nF_{4n+1})^-$ formula corresponds to the $(BF_3BNF_5)^-$ system (i.e., $(BF_3(BN)_nF_{4n+1})^-$

for $n$ = 1). We verified that its equilibrium structure is of $C_{2v}$-symmetry and can be viewed as two $BF_3$ groups connected to the central $NF_2$ fragment (i.e., $(BF_3\text{-}NF_2\text{-}BF_3)^-$), see **Figure 1**. The length of both B-N bonds is equal to 1.700 Å, the length of both N-F bonds is equal to 1.399 Å, whereas the B-F bond lengths span the 1.376–1.382 Å range. As depicted in **Figure 1**, the substituents around each B and N central atom are arranged in a tetrahedral manner, as if B and N atoms were carbon atoms. In consequence, the structure of the $(BF_3\text{-}NF_2\text{-}BF_3)^-$ system resembles that of propane (or perfluoropropane) which in turn indicates that one may consider the electronic transmutation of B and N atoms in $(BF_3\text{-}NF_2\text{-}BF_3)^-$ accomplished. We verified that the $(BF_3\text{-}NF_2\text{-}BF_3)^-$ is actually the only geometrically stable isomer of the $(BF_3BNF_5)^-$ system as all attempts to find the structures having different arrangement of atoms failed (i.e., the geometry optimizations of various initial structures resulted in fragmentation of the system). As far as the thermodynamic stability of $(BF_3\text{-}NF_2\text{-}BF_3)^-$ is concerned, we considered several fragmentation paths leading to various molecular fragments (such as $BF_4^-$, $F_2^-$, $F_2$, $NF_3$, $BF_3$, $NF_4^-$, etc.) and we verified that none of those paths is energetically favorable. Since we have also proven that the $(BF_3\text{-}NF_2\text{-}BF_3)^-$ anion is electronically stable (by verifying that its excess electron binding energy is positive, see the following section for details), we are confident that the $(BF_3BNF_5)^-$ system is a thermodynamically stable species.

The structure of $(BF_3(BN)_nF_{4n+1})^-$ for $n$ = 2 exhibits $C_2$-symmetry and contains alternately aligned B and N central atoms forming the B-N-B-N-B chain decorated with 12 fluorine ligands, see **Figure 1**. As it was the case for the $(BF_3\text{-}NF_2\text{-}BF_3)^-$ anion, we found only one geometrically stable structure of $(BF_3\text{-}NF_2\text{-}BF_2\text{-}NF_2\text{-}BF_3)^-$ despite the fact that we considered a large number of alternative structures having various arrangements of B, N and F atoms, including not only chain-like structures but also branched systems. Nevertheless, all these alternative initial structures turned out to be geometrically unstable. The terminal B-N bonds in $(BF_3\text{-}NF_2\text{-}BF_2\text{-}NF_2\text{-}BF_3)^-$ were found to be longer (by 0.052 Å) than the B-N bonds in $(BF_3\text{-}NF_2\text{-}BF_3)^-$ whereas the remaining B-N bonds in the former system were predicted to be shorter (by 0.050 Å) than those in the latter one. The B-F and N-F bond lengths in $(BF_3\text{-}NF_2\text{-}BF_2\text{-}NF_2\text{-}BF_3)^-$ were found to be slightly shorter than the corresponding separations in $(BF_3\text{-}NF_2\text{-}BF_3)^-$ as they span the 1.352–1.371 and 1.390–1.394 Å range, respectively. Tetrahedral arrangement of the substituents around each B and N atom causes the $(BF_3\text{-}NF_2\text{-}BF_2\text{-}NF_2\text{-}BF_3)^-$ structure to resemble that of n-pentane (as if all boron and nitrogen atoms were mimicking the bonding pattern typical for carbon atoms).

Since the $(BF_3\text{-}NF_2\text{-}BF_2\text{-}NF_2\text{-}BF_3)^-$ system (i.e., $BF_3(BN)_nF_{4n+1})^-$ for $n$ = 2) is larger than $(BF_3\text{-}NF_2\text{-}BF_3)^-$ anion (i.e., $BF_3(BN)_nF_{4n+1})^-$ for $n$ = 1) (and thus it is likely more similar to larger $(BF_3(BN)_nF_{4n+1})^-$ ($n$ > 2) systems than the latter) yet small enough to enable a comprehensive analysis of its possible fragmentation channels, we decided to choose this particular species to verify whether the more complex $(BF_3(BN)_nF_{4n+1})^-$ anions might be vulnerable to fragmentation processes. Hence, we considered the possible loss of various molecular fragments from $(BF_3(BN)_2F_9)^-$ by calculating the

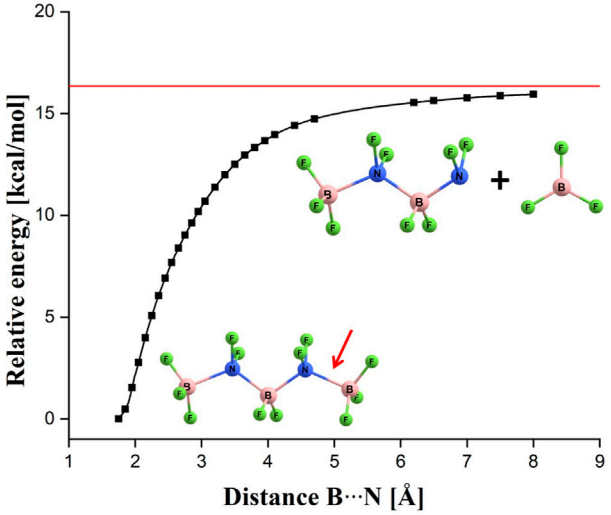


**FIGURE 2 |** Energy profile corresponding to the relaxed scan along the terminal B-N bond (indicated by a red arrow) in the $(BF_3\text{-}NF_2\text{-}BF_2\text{-}NF_2\text{-}BF_3)^-$ anion. The horizontal red line indicates the sum of the energies of the isolated $(BF_3\text{-}NF_2\text{-}BF_2\text{-}NF_2)^-$ and $BF_3$ systems.

energies of various fragmentation products and then comparing them to the energy of $(BF_3(BN)_2F_9)^-$. We found one (and only) case in which the fragments are lower in energy than the $(BF_3\text{-}NF_2\text{-}BF_2\text{-}NF_2\text{-}BF_3)^-$ anion, namely, we verified that the energy sum of $BF_3$ and a branched $(BF_3\text{-}NF(BF_3)\text{-}NF_2)^-$ system is smaller by about 24 kcal/mol than the energy of $(BF_3\text{-}NF_2\text{-}BF_2\text{-}NF_2\text{-}BF_3)^-$. From the formal point of view, this finding indicates thermodynamic instability of $(BF_3(BN)_2F_9)^-$, however, one should also consider the fragmentation path which could potentially be pursued to generate such a set of species. Obviously, the process of transformation of the $(BF_3\text{-}NF_2\text{-}BF_2\text{-}NF_2\text{-}BF_3)^-$ anion into $BF_3$ and $(BF_3\text{-}NF(BF_3)\text{-}NF_2)^-$ fragments would have to proceed according to some stepwise mechanism involving the detachment of $BF_3$ molecule from $(BF_3\text{-}NF_2\text{-}BF_2\text{-}NF_2\text{-}BF_3)^-$ followed by the substantial reorganization of the remaining $(BF_3\text{-}NF_2\text{-}BF_2\text{-}NF_2)^-$ anion (in order to produce a final branched $(BF_3\text{-}NF(BF_3)\text{-}NF_2)^-$ structure). Having this in mind, we performed a relaxed scan of the potential energy surface of $(BF_3\text{-}NF_2\text{-}BF_2\text{-}NF_2\text{-}BF_3)^-$ along the terminal N-B bond, see **Figure 2**. Our calculations revealed that a spontaneous detachment of the $BF_3$ molecule from the $(BF_3\text{-}NF_2\text{-}BF_2\text{-}NF_2\text{-}BF_3)^-$ anion would be energetically unfavorable by ca. 16 kcal/mol (as the energy profile shown in **Figure 2** affirms) and thus should be considered not likely. Therefore, we conclude that the $(BF_3(BN)_2F_9)^-$ isomer, although higher in energy than the $(BF_3\text{-}NF(BF_3)\text{-}NF_2)^-$ + $BF_3$ fragments, should remain stable. Moreover, we believe that we can extend that conclusion to cover also larger $(BF_3(BN)_nF_{4n+1})^-$ ($n$ > 2) systems by assuming that our considerations based on the $n$ = 2 case can be treated as representative for longer chain-like $(BF_3(BN)_nF_{4n+1})^-$ anions whose structures we are about to discuss. In other words, we assume that all larger

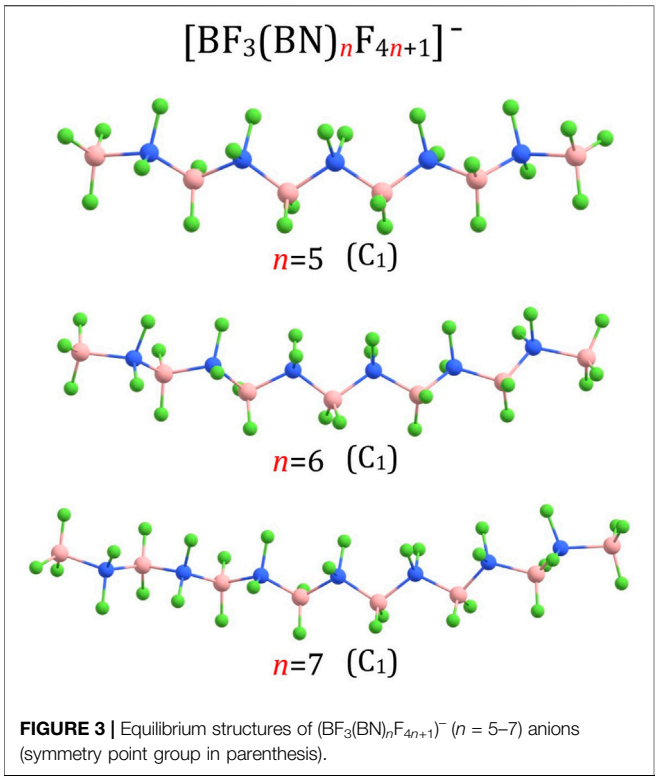


**FIGURE 3 |** Equilibrium structures of $(BF_3(BN)_nF_{4n+1})^-$ ($n$ = 5–7) anions (symmetry point group in parenthesis).

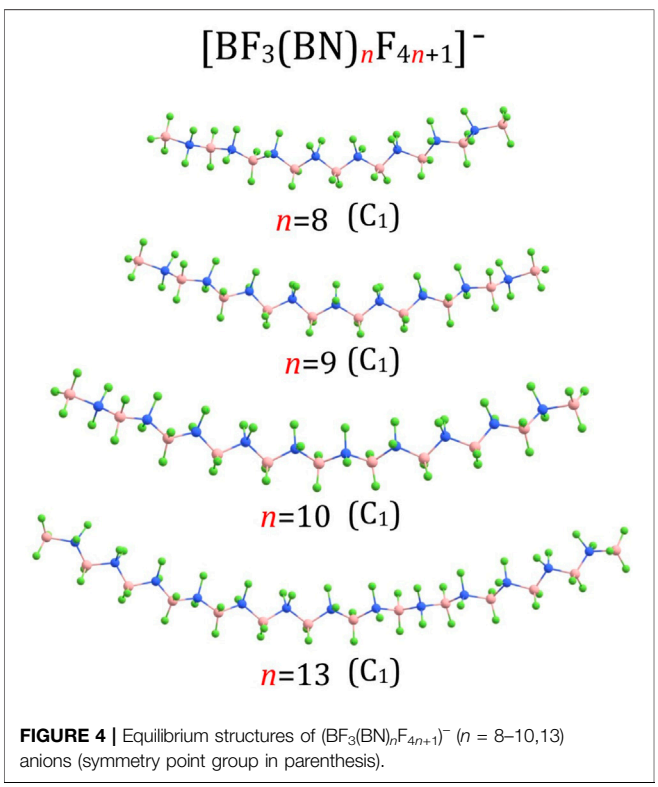


**FIGURE 4 |** Equilibrium structures of $(BF_3(BN)_nF_{4n+1})^-$ ($n$ = 8–10,13) anions (symmetry point group in parenthesis).

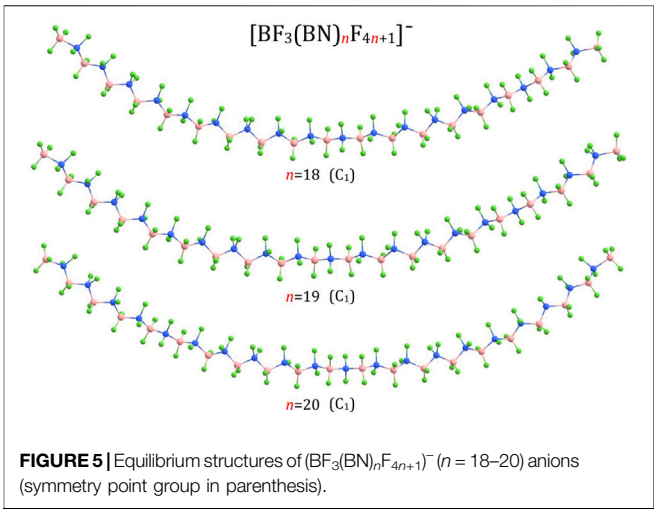


**FIGURE 5 |** Equilibrium structures of $(BF_3(BN)_nF_{4n+1})^-$ ($n$ = 18–20) anions (symmetry point group in parenthesis).

$(BF_3(BN)_nF_{4n+1})^-$ ($n$ > 2) systems we consider in this work are likely not thermodynamically stable with respect to the formation of $BF_3$ and the remaining branched anionic fragment, yet should be long lived due to the fact that the $BF_3$ loss which would have to happen to trigger such a process is energetically unfavorable.

Since the structures of larger $(BF_3(BN)_nF_{4n+1})^-$ anions (i.e., for $n$ = 3-10, 13, 18-20) resemble many similarities with one another, we describe them together in this section. The $(BF_3(BN)_nF_{4n+1})^-$ structures for $n$ = 3 and $n$ = 4 are shown in **Figure 1**, the structures for $n$ = 5-7 are presented in **Figure 3**, the structures for $n$ = 8-10 and $n$ = 13 are depicted in **Figure 4**, whereas the structures for $n$ = 18-20 are gathered in **Figure 5**.

Our calculations revealed similarities among the corresponding B-N, B-F, and N-F bond lengths in the $(BF_3(BN)_nF_{4n+1})^-$ anions considered (i.e., for $n$ = 1-10, 13, 18-20). Namely, the B-N bonds in $(BF_3(BN)_3F_{13})^-$ (1.630–1.775 Å) and $(BF_3(BN)_4F_{17})^-$ (1.621–1.791 Å) are of similar lengths to those found for $(BF_3(BN)F_5)^-$ and $(BF_3(BN)_2F_9)^-$, see the discussion in the preceding paragraphs. In addition, B-N bond lengths predicted for larger systems (1.616–1.797 Å for $n$ = 5, 1.613–1.805 Å for $n$ = 6, 1.611–1.807 Å for $n$ = 7, 1.610–1.811 Å for $n$ = 8, 1.609–1.812 Å for $n$ = 9, 1.608–1.813 Å for $n$ = 10, 1.607–1.815 Å for $n$ = 13, and 1.607–1.817 Å for $n$ = 18-20) show an analogous pattern (i.e., slightly larger separations between terminal $BF_3$ groups and the remaining molecular fragment). The N-F bonds in the $(BF_3(BN)_nF_{4n+1})^-$ ($n$ > 2) anions (1.387–1.394 Å for $n$ = 3, 1.383–1.394 Å for $n$ = 4, 1.384–1.394 Å for $n$ = 5, 1.383–1.394 Å for $n$ = 6, 1.381–1.394 Å for $n$ = 7, 1.380–1.394 Å for $n$ = 8-10 and $n$ = 13, 1.379–1.394 Å for $n$ = 18-20) are also similar to those in $(BF_3(BN)_3F_{13})^-$ and $(BF_3(BN)_4F_{17})^-$. The B-F bond lengths in the $(BF_3(BN)_nF_{4n+1})^-$ ($n$ > 2) systems span the following ranges: 1.347–1.366 Å for $n$ = 3, 1.342–1.365 Å for $n$ = 4 and $n$ = 5, 1.338–1.363 Å for $n$ = 6-9, 1.336–1.362 Å for $n$ = 10, $n$ = 13, and $n$ = 18-20. In addition to the similar lengths of the corresponding B-N, B-F, and N-F bonds, the substituents around each B and N atom in the $(BF_3(BN)_nF_{4n+1})^-$ ($n$ = 3-10, 13, 18-20) anions are arranged in a tetrahedral manner as it was the case for $(BF_3(BN)_3F_{13})^-$ and $(BF_3(BN)_4F_{17})^-$, see **Figure 1** and **Figures 3–5**.

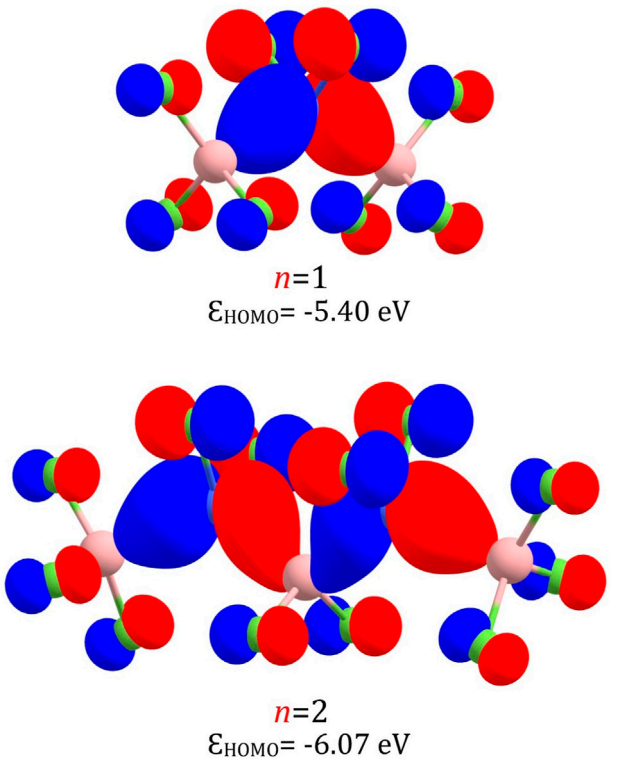


**FIGURE 6 |** HOMO orbitals of the $(BF_3(BN)F_5)^-$ and $(BF_3(BN)_2F_9)^-$ anions with their orbital energies ($\varepsilon$).

According to our predictions, the structures of $(BF_3(BN)_nF_{4n+1})^-$ anions correspond to extended conformations with a tendency to form arched chains when the number of BN units ($n$) develops. In general, the structures predicted for $(BF_3(BN)_nF_{4n+1})^-$ systems resemble the extended conformations of higher n-alkanes. Indeed, as it was established in the earlier studies (Lüttschwager et al., 2013), linear alkanes of moderate length (i.e., containing up to 17(Thomas et al., 2006) or 21 (Grimme et al., 2007) carbon atoms (depending on the research method used)) tend to adopt a fully extended (all-*trans*) conformations at low temperatures, whereas weak dispersion interactions between chain fragments come into play for larger systems by causing the *trans-gauche* isomerizations which eventually transform an extended chain into a hairpin structure (Lüttschwager et al., 2013). Therefore, we believe that the structures of the $(BF_3(BN)_nF_{4n+1})^-$ ($n$ = 1-10) anions presented in **Figures 1**, **3**, **4** likely correspond to globally stable conformations as the number of B and N atoms (each of which mimics a carbon atom due to electronic transmutation) does not exceed 21, hence it approaches the maximum number of C atoms for which the fully extended alkanes remain to be globally stable structures. As far as the $(BF_3(BN)_nF_{4n+1})^-$ ($n$ = 13,18-20) anions are concerned, the possible existence of alternative lower energy conformers should be considered likely.

## Excess Electron Binding Energies of $(BF_3(BN)_nF_{4n+1})^-$ ($n$ = 1-10,13,18-20) Anions

The population analysis performed according to the Merz-Singh-Kollman scheme revealed that the excess negative charge in all $(BF_3(BN)_nF_{4n+1})^-$ ($n$ = 1-10,13,18-20) anions is distributed among the fluorine ligands, yet not evenly. In order to simplify the discussion, we decided to describe the partial atomic charges obtained for two structurally smallest systems, $(BF_3(BN)F_5)^-$ and $(BF_3(BN)_2F_9)^-$ which can be considered representative for all $(BF_3(BN)_nF_{4n+1})^-$ anions studied in this work. In the case of $(BF_3(BN)F_5)^-$ system (i.e., $(BF_3\text{-}NF_2\text{-}BF_3)^-$), the partial charges ($q$) localized on the F atoms connected to boron atoms are equal to –0.43|e| whereas those localized on the F atoms linked to the nitrogen atom are equal to –0.11|e| (naturally, all partial charges sum up to –1|e| as the partial charges predicted for two boron atoms and for one nitrogen atom are equal to +0.92|e| and –0.02|e|, respectively). In the case of $(BF_3(BN)_2F_9)^-$ anion (i.e., $(BF_3\text{-}NF_2\text{-}BF_2\text{-}NF_2\text{-}BF_3)^-$), the $q^F$ charges determined for the F atoms connected to the terminal B atoms are equal to ca. –0.41|e|, the $q^F$ of –0.32|e| are predicted for fluorine atoms bound to the central B atom, whereas $q^F$ for the F atoms linked to N atoms are equal to –0.09|e|. Since partial atomic charges determined for larger $(BF_3(BN)_nF_{4n+1})^-$ ($n$ > 2) anions exhibit approximately the same pattern as we found for these two smallest systems (for $n$ = 1,2), one may arrive at the following generalizations: 1) the excess negative charge is delocalized among all fluorine ligands (which is reasonable taking into account the substantial electronegativity of F atoms), 2) the atomic partial charges localized on the F, N, and B atoms constituting the central part of a chain (i.e., the chain without two terminal $BF_3$ groups) sum up to approximately zero, and 3) the atomic partial charges on B and F atoms comprising each terminal $BF_3$ group sum up to ca. –0.5|e|. Therefore, we conclude that the excess negative charge in the anions considered is localized mainly on the two terminal $BF_3$ fragments.

**TABLE 1 |** Vertical electron detachment energies (in eV) of the $(BF_3(BN)_nF_{4n+1})^-$ anions ($n$ = 1-10,13,18-20) determined at the OVGF/6-311+G(d) (labeled $VDE^{OVGF}$) and B3LYP/6-311+G(d) (labeled $VDE^{B3LYP}$) level of theory. ΔVDE stands for the difference between $VDE^{OVGF}$ and $VDE^{B3LYP}$.

| System | $VDE^{OVGF}$ (eV) | $VDE^{B3LYP}$ (eV) | ΔVDE (eV) |
|---|---|---|---|
| $(BF_3(BN)F_5)^-$ | 8.10 | 7.78 | 0.32 |
| $(BF_3(BN)_2F_9)^-$ | 8.57 | 8.07 | 0.50 |
| $(BF_3(BN)_3F_{13})^-$ | 9.07 | 8.35 | 0.72 |
| $(BF_3(BN)_4F_{17})^-$ | 9.45 | 8.53 | 0.92 |
| $(BF_3(BN)_5F_{21})^-$ | 9.77 | 8.68 | 1.09 |
| $(BF_3(BN)_6F_{25})^-$ | 9.96 | 8.76 | 1.20 |
| $(BF_3(BN)_7F_{29})^-$ | 10.10 | 8.84 | 1.26 |
| $(BF_3(BN)_8F_{33})^-$ | 10.18 | 8.89 | 1.29 |
| $(BF_3(BN)_9F_{37})^-$ | ~10.33[a] | 8.92 | 1.41 |
| $(BF_3(BN)_{10}F_{41})^-$ | ~10.41[a] | 8.95 | 1.46 |
| $(BF_3(BN)_{13}F_{53})^-$ | ~10.55[a] | 9.01 | 1.54 |
| $(BF_3(BN)_{18}F_{73})^-$ | ~10.64[a] | 9.05 | 1.59 |
| $(BF_3(BN)_{19}F_{77})^-$ | ~10.65[a] | 9.06 | 1.59 |
| $(BF_3(BN)_{20}F_{81})^-$ | ~10.66[a] | 9.07 | 1.59 |

[a]*alues extrapolated on the basis of the exponential fitting function, see caption for Figure 7.*

The highest occupied molecular orbitals (HOMO) of the smallest $(BF_3(BN)_nF_{4n+1})^-$ anions (i.e., $(BF_3(BN)F_5)^-$ and $(BF_3(BN)_2F_9)^-$) exhibit the bonding pattern typical for almost all superhalogen anions described in the literature(Skurski, 2021), see **Figure 6**. Indeed, one may easily notice the absence of destabilizing antibonding ligand-central atom interactions, which is characteristic not only for $(MX_{k+1})^-$ systems containing one central atom but also for polynuclear $(M_nX_{n\times k+1})^-$ superhalogen anions. In addition, the analysis of HOMO for $(BF_3(BN)F_5)^-$ and $(BF_3(BN)_2F_9)^-$ reveals strong bonding boron-nitrogen interactions and substantial contributions from 2*p* atomic orbitals of fluorine atoms. Since the HOMOs calculated for larger $(BF_3(BN)_nF_{4n+1})^-$ anions ($n > 2$) look alike, we do not present them here (as the HOMO contour plots for $n = 1$ and $n = 2$ are representative for all systems considered).

The vertical electron detachment energies predicted for the $(BF_3(BN)_nF_{4n+1})^-$ anions ($n$ = 1-10,13,18-20) are collected in **Table 1**. In fact, we present the VDEs calculated by using the OVGF method (for $n$ = 1-8) and the B3LYP method (for $n$ = 1-10,13,18-20). Certainly, the VDE values obtained by employing the OVGF method ($VDE^{OVGF}$) are much more reliable than those determined by the use of the B3LYP method ($VDE^{B3LYP}$), however, our computer resources enabled performing the calculations of $VDE^{OVGF}$ values only for the $(BF_3(BN)_nF_{4n+1})^-$ anions up to $n = 8$. Therefore, we decided to determine the VDEs for the larger systems (i.e., for $n$ = 9,10,13,18-20) by employing a less computationally demanding B3LYP approach. In fact, we applied the B3LYP method to predict the VDEs also for those systems ($n$ = 1-8) whose vertical electron detachment energies were calculated with the OVGF method (to enable the comparison between the OVGF and B3LYP results which allowed us to assess the reliability of the $VDE^{B3LYP}$ values). Hence, we discuss the VDEs of the $(BF_3(BN)_nF_{4n+1})^-$ anions based on the $VDE^{OVGF}$ values whereas the $VDE^{B3LYP}$ results we use only to predict a likely VDE dependence on $n$ (i.e., the VDE = $f(n)$ function) and thus to estimate the approximate values of $VDE^{OVGF}$ for $n$ = 9,10,13,18-20.

We start our discussion with recalling the fact that the VDE of the $(BF_4)^-$ was earlier calculated to be 8.98 eV (Sikorska et al., 2008). We consider this result important because the $(BF_4)^-$ system matches the $(BF_3(BN)_nF_{4n+1})^-$ formula for $n = 0$. The VDE of the smallest anion investigated in this work ($(BF_3(BN)F_5)^-$, which can be treated as the $(BF_4)^-$ system having one of its ligands replaced with the $NF_2$-$BF_3$ fragment) was evaluated as equal to 8.10 eV, see **Table 1**. We believe the reason why the VDE of $(BF_3(BN)F_5)^-$ is smaller than that of $(BF_4)^-$ is that replacing one F ligand with $NF_2$-$BF_3$ fragment lowers the symmetry of the system which in turn causes the decrease of the excess electron binding energy (as it was established for various superhalogen anions (Smuczyńska and Skurski, 2008)). However, the molecular fragment $(BN)_nF_{4n+1}$ that the F atom is replaced with contains more and more electronegative fluorine ligands when $n$ develops and thus the VDE of the $(BF_3(BN)_nF_{4n+1})^-$ anion increases when $n$ increases, see **Table 1**. In particular, the VDE of 8.57 eV was calculated for $n = 2$ and the VDE of 9.07 eV was predicted for $n$ = 3. As one can notice, the VDE found for $(BF_3(BN)_3F_{13})^-$ slightly exceeds that found for the reference $(BF_4)^-$ anion, which means that the presence of electronegative ligands in the $(BN)_3F_{13}$ fragment compensates (in terms of the excess electron binding energy) the destabilizing effects related to the symmetry lowering.

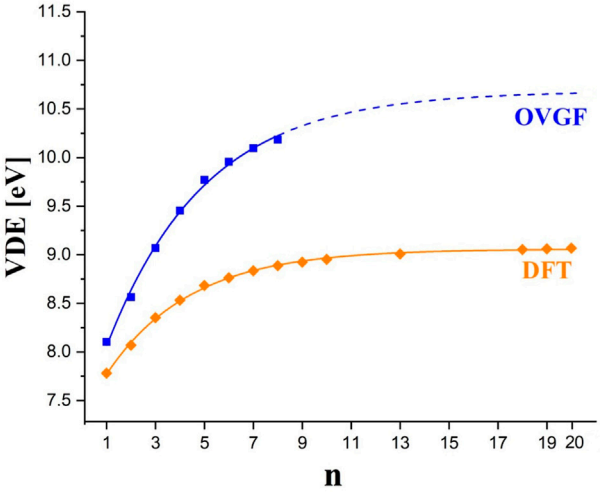


**FIGURE 7 |** The $VDE^{OVGF}$ values (blue squares) and $VDE^{B3LYP}$ values (orange diamonds) calculated for $(BF_3(BN)_nF_{4n+1})^-$ anions. The plots correspond to the fitting formula given by $VDE = A \cdot exp(-n/B) + C$ (where *A*, *B*, and *C* stand for fitting parameters). The fitted parameters $A = -3.36783 \pm 0.09853$, $B = 4.00503 \pm 0.45838$, and $C = 10.68291 \pm 0.14242$ and the coefficient of determination $r^2 = 0.99665$ were obtained for the function approximating $VDE^{OVGF}$ results (blue line) while $A = -1.72646 \pm 0.02308$, $B = 3.40804 \pm 0.08137$, and $C = 9.03863 \pm 0.00786$ and the $r^2$ of 0.99878 were obtained for that approximating $VDE^{B3LYP}$ results (orange line).

The VDE predicted for larger $(BF_3(BN)_nF_{4n+1})^-$ anions gradually increases to achieve the value of 10.18 eV for $n = 8$, see **Table 1**. Although one might anticipate the continuation of this tendency for larger $n$ values, we cannot provide the precise numeric values due to the lack of the OVGF-based results for $n >$ 8. Despite this, we made an attempt to estimate the VDEs of the larger systems considered (i.e., $(BF_3(BN)_nF_{4n+1})^-$ for $n > 8$) by finding the approximate function $VDE^{OVGF} = f(n)$ and extrapolating it to achieve the $VDE^{OVGF}$ for $n = 20$. In order to do this, we decided to choose the fitting function given by the $VDE^{OVGF} = A \cdot exp(-n/B) + C$ formula (where *A*, *B*, and *C* are the fitting parameters) because we verified that such a function properly describes the set of $VDE^{B3LYP}$ values we obtained for all $(BF_3(BN)_nF_{4n+1})^-$ anions ($n$ = 1-10,13,18-20) which the $VDE^{B3LYP} = f(n)$ plot depicted in **Figure 7** affirms. In other words, we assume that the $VDE^{B3LYP}$ values, although clearly underestimated with respect to more reliable $VDE^{OVGF}$ values (see **Table 1**), show the proper VDE trend for developing $n$. According to the fitting function obtained for the $VDE^{OVGF}$ results, the vertical electron detachment energy of the $(BF_3(BN)_{20}F_{81})^-$ anion is approximately equal to 10.7 eV. Although this value comes from the extrapolation to $n = 20$, we consider this estimate rather reliable because the $r^2$ (i.e., coefficient of determination) for that fit approaches 1.0 (0.99665, see the caption for **Figure 7**). Both the shape of the $VDE^{OVGF} = f(n)$ plot and the fact that the differences between the

consecutive $VDE^{OVGF}$ values for $n$ developing from 6 to 8 are small (ca. 0.1 eV) indicate that the extrapolated VDE of 10.7 eV for $n = 20$ may actually approach the maximal VDE which can be obtained for $(BF_3(BN)_nF_{4n+1})^-$ polynuclear superhalogen anions (even for $n > 20$).

## CONCLUSION

On the basis of the B3LYP/6-311+G(d) and OVGF/6-311+G(d) calculations (whose accuracy were verified by employing the wB97XD/6-311+G(d), B2PLYPD/6-311+G(d), OVGF/aug-cc-VTZ, and OVGF/Def2TZVP treatments) performed for the $(BF_3(BN)_nF_{4n+1})^-$ ($n$ = 1-10,13,18-20) anions we arrive at the following conclusions:

1) The electronic transmutation concept can be employed to design polynuclear superhalogen anions matching the $(BF_3(BN)_nF_{4n+1})^-$ formula and comprising alternately aligned boron and nitrogen central atoms.
2) The equilibrium structures of $(BF_3(BN)_nF_{4n+1})^-$ ($n$ = 1-10,13,18-20) anions correspond to fully extended (all-*trans*) chains with four substituents arranged in a tetrahedral manner around each B and N central atom and thus mimic the globally stable fully extended conformations of higher n-alkanes.
3) The excess negative charge in $(BF_3(BN)_nF_{4n+1})^-$ ($n$ = 1-10,13,18-20) anions is delocalized mainly among the fluorine ligands attached to two terminal boron atoms.
4) The vertical electron detachment energies predicted for $(BF_3(BN)_nF_{4n+1})^-$ ($n$ = 1-8) anions always exceed 8 eV, gradually increase with developing $n$ and approach 10.2 eV for $n = 8$.
5) The estimated VDE value for $n = 20$ (i.e., for the $(BF_3(BN)_{20}F_{81})^-$ system) is about 10.7 eV and it is anticipated to represent the upper limit of vertical electron binding energy which could be achieved for polynuclear superhalogen anions matching the $(BF_3(BN)_nF_{4n+1})^-$ formula.

## DATA AVAILABILITY STATEMENT

The original contributions presented in the study are included in the article/Supplementary Material, further inquiries can be directed to the corresponding author.

## AUTHOR CONTRIBUTIONS

Conceptualization, PS; Methodology, PS, and IA; Computations, AC, DF, SF, and IA; Validation, SF, and IA; Investigation, SF, and IA; Resources, PS; Writing—original draft preparation, PS; writing—review and editing, PS and IA; Supervision, PS, IA, and SF; Project administration, AC and DF; Funding acquisition, PS. All authors have read and agreed to the published version of the manuscript.

## FUNDING

This research was supported by the Polish Ministry of Science and Higher Education Grant No. DS 531-T110-D844-21 (to PS).

## ACKNOWLEDGMENTS

The calculations have been carried out using resources provided by Wroclaw Centre for Networking and Supercomputing (http://wcss.pl) Grant Nos. 435, 436 and 455.

## REFERENCES

Alexandrova, A. N., Birch, K. A., and Boldyrev, A. I. (2003). Flattening the B6H62- Octahedron. Ab Initio Prediction of a New Family of Planar All-Boron Aromatic Molecules. *J. Am. Chem. Soc.* 125, 10786–10787. doi:10.1021/ja0361906

Alexandrova, A. N., Boldyrev, A. I., Fu, Y.-J., Yang, X., Wang, X.-B., and Wang, L.-S. (2004). Structure of the NaxClx+1− (X=1-4) Clusters Viaab Initiogenetic Algorithm and Photoelectron Spectroscopy. *J. Chem. Phys.* 121, 5709–5719. doi:10.1063/1.1783276

Anusiewicz, I. (2009a). Electrophilic Substituents as Ligands in Superhalogen Anions. *J. Phys. Chem. A.* 113, 6511–6516. doi:10.1021/jp901910q

Anusiewicz, I., Freza, S., and Skurski, P. (2018). Stability of the TinF4n+1− and GenF4n+1− Superhalogen Anions and the Acidity of the HTi F4+1 and HGe F4+1 (N = 1-3) Superacids. *Polyhedron* 144, 125–130. doi:10.1016/j.poly.2017.12.041

Anusiewicz, I., and Skurski, P. (2007). Unusual Structures of $Mg_2F_5^-$ Superhalogen Anion. *Chem. Phys. Lett.* 440, 41–44. doi:10.1016/j.cplett.2007.04.016

Anusiewicz, I. (2009b). Superhalogen Anions Utilizing Acidic Functional Groups as Ligands. *J. Phys. Chem. A.* 113, 11429–11434. doi:10.1021/jp907246w

Awasthi, S., Gaur, J. K., Pandey, S. K., Bobji, M. S., and Srivastava, C. (2021). High-Strength, Strongly Bonded Nanocomposite Hydrogels for Cartilage Repair. *ACS Appl. Mater. Inter.* 13, 24505–24523. doi:10.1021/acsami.1c05394

Becke, A. D. (1988). Density-functional Exchange-Energy Approximation with Correct Asymptotic Behavior. *Phys. Rev. A.* 38, 3098–3100. doi:10.1103/PhysRevA.38.3098

Besler, B. H., Merz, K. M., and Kollman, P. A. (1990). Atomic Charges Derived from Semiempirical Methods. *J. Comput. Chem.* 11, 431–439. doi:10.1002/jcc.540110404

Cederbaum, L. S. (1975). One-body Green′s Function for Atoms and Molecules: Theory and Application. *J. Phys. B: Mol. Phys.* 8, 290–303. doi:10.1088/0022-3700/8/2/018

Chai, J.-D., and Head-Gordon, M. (2008). Systematic Optimization of Long-Range Corrected Hybrid Density Functionals. *J. Chem. Phys.* 128, 084106. doi:10.1063/1.2834918

Compton, R. N. (1995). *Negative Ions (Multiply Charged Negative Ions).*

Cyraniak, A., Skurski, P., and Czapla, M. (2019). The Presence of Two Different central Atoms Increases the Strength of Lewis-Brønsted Superacids. *Chem. Phys. Lett.* 717, 77–81. doi:10.1016/j.cplett.2019.01.004

Czapla, M., and Skurski, P. (2015). Strength of the Lewis-Brønsted Superacids Containing in, Sn, and Sb and the Electron Binding Energies of Their Corresponding Superhalogen Anions. *J. Phys. Chem. A.* 119, 12868–12875. doi:10.1021/acs.jpca.5b10205

Czapla, M., and Skurski, P. (2018). Toward the Preparation of the HAuF6 , HAu2 F11 , and HAu3 F16 Superacids: Theoretical Study. *Int. J. Quan. Chem.* 118, e25494. doi:10.1002/qua.25494

Díaz-Tinoco, M., and Ortiz, J. V. (2016b). Comment on "Are Polynuclear Superhalogens without Halogen Atoms Probable? A High-Level Ab Initio Case Study on Triple-Bridged Binuclear Anions with Cyanide Ligands" [J. Chem. Phys. 140, 094301 (2014)]. *The J. Chem. PhysicsJ. Chem. Phys.* 140145, 094301147101. doi:10.1063/1.4964502

Díaz-Tinoco, M., and Ortiz, J. V. (2016a). Comment on: "Probing the Properties of Polynuclear Superhalogens without Halogen Ligand *via* Ab Initio Calculations: A Case Study on Double-Bridged [Mg2(CN)5]−1Anions" by Li et al. *ChemPhysChem* 17, 2945–2946. doi:10.1002/cphc.201600519

Ding, L.-P., Shao, P., Lu, C., Zhang, F.-H., Liu, Y., and Mu, Q. (2017). Prediction of the Iron-Based Polynuclear Magnetic Superhalogens with Pseudohalogen CN as Ligands. *Inorg. Chem.* 56, 7928–7935. doi:10.1021/acs.inorgchem.7b00646

Dunning, T. H. (1989). Gaussian Basis Sets for Use in Correlated Molecular Calculations. I the Atoms boron through Neon and Hydrogen. *J. Chem. Phys.* 90, 1007–1023. doi:10.1063/1.456153

Feng, Y., Xu, H.-G., Zheng, W., Zhao, H., Kandalam, A. K., and Jena, P. (2011). Structures and Photoelectron Spectroscopy of Cun(BO2)m− (N, M = 1, 2) Clusters: Observation of Hyperhalogen Behavior. *J. Chem. Phys.* 134, 094309. doi:10.1063/1.3556818

Freza, S., and Skurski, P. (2010). Enormously Large (Approaching 14 eV!) Electron Binding Energies of [HnFn+1]- (N= 1-5, 7, 9, 12) Anions. *Chem. Phys. Lett.* 487, 19–23. doi:10.1016/j.cplett.2010.01.022

Frisch, M. J., Trucks, G. W., Schlegel, H. E., Scuseria, G. E., Robb, M. A., Cheeseman, J. R., et al. (2016). *Gaussian 16*. Wallingford CT: Gaussian, Inc.

Gillis, R. G. (1958). Isoelectronic Molecules: The Effect of Number of Outer-Shell Electrons on Structure. *J. Chem. Educ.* 35, 66. doi:10.1021/ed035p66

Gish, J. T., Popov, I. A., and Boldyrev, A. I. (2015). Homocatenation of Aluminum: Alkane-like Structures of Li2Al2H6and Li3Al3H8. *Chem. Eur. J.* 21, 5307–5310. doi:10.1002/chem.201500298

Götz, M., Willis, M., Kandalam, A. K., Ganteför, G. F., and Jena, P. (2010). Origin of the Unusual Properties of Aun(BO2) Clusters. *ChemPhysChem* 11, 853–858. doi:10.1002/cphc.200901027

Grimme, S., Antony, J., Schwabe, T., and Mück-Lichtenfeld, C. (2007). Density Functional Theory with Dispersion Corrections for Supramolecular Structures, Aggregates, and Complexes of (Bio)organic Molecules. *Org. Biomol. Chem.* 5, 741–758. doi:10.1039/B615319B

Grimme, S. (2006). Semiempirical Hybrid Density Functional with Perturbative Second-Order Correlation. *J. Chem. Phys.* 124, 034108. doi:10.1063/1.2148954

Gutsev, G. L., and Boldyrev, A. I. (1981b). DVM α Calculations on the Electronic Structure of Complex Chlorine Anions. *Chem. Phys. Lett.* 84, 352–355. doi:10.1016/0009-2614(81)80362-4

Gutsev, G. L., and Boldyrev, A. I. (1981a). DVM-xα Calculations on the Ionization Potentials of MXk+1− Complex Anions and the Electron Affinities of MXk+1 "superhalogens". *Chem. Phys.* 56, 277–283. doi:10.1016/0301-0104(81)80150-4

Gutsev, G. L., and Boldyrev, A. I. (1984). The Electronic Structure of the 3dand 4dmetal Hexafluoride Anions and the Electron Affinities of the Corresponding Neutrals. *Mol. Phys.* 53, 23–31. doi:10.1080/00268978400102111

Gutsev, G. L., and Boldyrev, A. I. (1985). The Theoretical Investigation of the Electron Affinity of Chemical Compounds. *Adv. Chem. Phys.* 61, 169–221. doi:10.1002/9780470142851.ch3

Heni, M., and Illenberger, E. (1985). The Stability of the Bifluoride Ion (HF−2) in the Gas Phase. *J. Chem. Phys.* 83, 6056–6057. doi:10.1063/1.449594

Hotop, H., and Lineberger, W. C. (1985). Binding Energies in Atomic Negative Ions: II. *J. Phys. Chem. Reference Data* 14, 731–750. doi:10.1063/1.555735

Hou, G.-L., Wu, M. M., Wen, H., Sun, Q., Wang, X.-B., and Zheng, W.-J. (2013). Photoelectron Spectroscopy and Theoretical Study of M(IO3)2− (M = H, Li, Na, K): Structural Evolution, Optical Isomers, and Hyperhalogen Behavior. *J. Chem. Phys.* 139, 044312. doi:10.1063/1.4816525

Huey, L. G., Dunlea, E. J., and Howard, C. J. (1996). Gas-Phase Acidity of CF3OH. *J. Phys. Chem.* 100, 6504–6508. doi:10.1021/jp953058m

Jemmis, E. D., and Jayasree, E. G. (2003). Analogies between Boron and Carbon. *Acc. Chem. Res.* 36, 816–824. doi:10.1021/ar0300266

Koirala, P., Pradhan, K., Kandalam, A. K., and Jena, P. (2013). Electronic and Magnetic Properties of Manganese and Iron Atoms Decorated with BO2 Superhalogens. *J. Phys. Chem. A.* 117, 1310–1318. doi:10.1021/jp307467j

Koirala, P., Willis, M., Kiran, B., Kandalam, A. K., and Jena, P. (2010). Superhalogen Properties of Fluorinated Coinage Metal Clusters. *J. Phys. Chem. C* 114, 16018–16024. doi:10.1021/jp101807s

Krishnan, R., Binkley, J. S., Seeger, R., and Pople, J. A. (1980). Self-consistent Molecular Orbital Methods. XX. A Basis Set for Correlated Wave Functions. *J. Chem. Phys.* 72, 650–654. doi:10.1063/1.438955

Lee, C., Yang, W., and Parr, R. G. (1988). Development of the Colle-Salvetti Correlation-Energy Formula into a Functional of the Electron Density. *Phys. Rev. B* 37, 785–789. doi:10.1103/PhysRevB.37.785

Li, J.-F., Li, M.-M., Bai, H., Sun, Y.-Y., Li, J.-L., and Yin, B. (2015a). Probing the Properties of Polynuclear Superhalogens without Halogen Ligand *via* Ab Initio Calculations: A Case Study on Double-Bridged [Mg2(CN)5]−1Anions. *ChemPhysChem* 16, 3652–3659. doi:10.1002/cphc.201500517

Li, J.-F., Sun, Y.-Y., Bai, H., Li, M.-M., Li, J.-L., and Yin, B. (2015b). Are Superhalogens without Halogen Ligand Capable of Transcending Traditional Halogen-Based Superhalogens? Ab Initio Case Study of Binuclear Anions Based on Pseudohalogen Ligand. *AIP Adv.* 5, 067143. doi:10.1063/1.4922958

Li, J.-F., and Yin, B. (2021). Exploring the Superhalogen Properties of Polynuclear Structures without Halogen Ligands: A Combined Ab Initio and DFT Study on Triple-Bridged [Mg2L5]−1 (L = −OCN, −SCN) Anions. *J. Phys. Chem. A.* 125, 3378–3386. doi:10.1021/acs.jpca.1c01623

Li, M.-M., Li, J.-F., Bai, H., Sun, Y.-Y., Li, J.-L., and Yin, B. (2015c). Is the Regulation of the Electronic Properties of Organic Molecules by Polynuclear Superhalogens More Effective Than that by Mononuclear Superhalogens? A High-Level Ab Initio Case Study. *Phys. Chem. Chem. Phys.* 17, 20338–20346. doi:10.1039/C5CP03155A

Li, Y., Zhang, S., Wang, Q., and Jena, P. (2013). Structure and Properties of Mn4Cl9: An Antiferromagnetic Binary Hyperhalogen. *J. Chem. Phys.* 138, 054309. doi:10.1063/1.4776217

Liu, J.-Y., Ma, H.-D., Sun, Y.-b., Li, Y., Sun, W.-M., Wu, D., et al. (2017). Hyperhalogen Properties of Early-Transition-Metal Borates. *RSC Adv.* 7, 47073–47082. doi:10.1039/C7RA10238K

Lundell, K. A., Olson, J. K., and Boldyrev, A. I. (2020). Exploring the Limits of Electronic Transmutation: Ab Initio Study of LinBen (N = 3-5). *Chem. Phys. Lett.* 739, 136994. doi:10.1016/j.cplett.2019.136994

Lüttschwager, N. O. B., Wassermann, T. N., Mata, R. A., and Suhm, M. A. (2013). The Last Globally Stable Extended Alkane. *Angew. Chem. Int. Ed.* 52, 463–466. doi:10.1002/anie.201202894

Marchaj, M., Freza, S., and Skurski, P. (2012). Why Are SiX5- and GeX5- (X = F, Cl) Stable but Not CF5- and CCl5-? *J. Phys. Chem. A.* 116, 1966–1973. doi:10.1021/jp300251t

McLean, A. D., and Chandler, G. S. (1980). Contracted Gaussian Basis Sets for Molecular Calculations. I Second Row Atoms, Z=11-18. *J. Chem. Phys.* 72, 5639–5648. doi:10.1063/1.438980

Metz, R. B., Kitsopoulos, T., Weaver, A., and Neumark, D. M. (1988). Study of the Transition State Region in the Cl+HCl Reaction by Photoelectron Spectroscopy of ClHCl−. *J. Chem. Phys.* 88, 1463–1465. doi:10.1063/1.454218

Olson, J. K., and Boldyrev, A. I. (2012). Electronic Transmutation: Boron Acquiring an Extra Electron Becomes 'carbon'. *Chem. Phys. Lett.* 523, 83–86. doi:10.1016/j.cplett.2011.11.079

Ortiz, J. V. (1988). Electron Binding Energies of Anionic Alkali Metal Atoms from Partial Fourth Order Electron Propagator Theory Calculations. *J. Chem. Phys.* 89, 6348–6352. doi:10.1063/1.455401

Osorio, E., Olson, J. K., Tiznado, W., and Boldyrev, A. I. (2012). Analysis of Why Boron Avoids Sp2 Hybridization and Classical Structures in the BnHn+2 Series. *Chem. Eur. J.* 18, 9677–9681. doi:10.1002/chem.201200506

Paduani, C. (2016). High-spin Multiplicities in Ferromagnetic Ground States of Supramolecular Halide Complexes Based on the Gadolinium Chloride. *Physica E: Low-dimensional Syst. Nanostructures* 77, 199–205. doi:10.1016/j.physe.2015.11.014

Paduani, C., and Jena, P. (2012). A Recipe for Designing Molecules with Ever-Increasing Electron Affinities. *J. Phys. Chem. A.* 116, 1469–1474. doi:10.1021/jp211736e

Paduani, C., and Jena, P. (2013). Structure, Stability and Superhalogen Properties of Sodium and Magnesium Borohydrides. *Chem. Phys. Lett.* 556, 173–177. doi:10.1016/j.cplett.2012.11.038

Pandey, S. K. (2021). Novel and Polynuclear K- and Na-Based Superalkali Hydroxides as Superbases Better Than Li-Related Species and Their Enhanced Properties: An Ab Initio Exploration. *ACS Omega* 6, 31077–31092. doi:10.1021/acsomega.1c04395

Popov, I. A., and Boldyrev, A. I. (2013). Computational Probing of All-boron Li2nB2nH2n+2 Polyenes. *Comput. Theor. Chem.* 1004, 5–11. doi:10.1016/j.comptc.2012.10.018

Popov, I. A., Zhang, X., Eichhorn, B. W., Boldyrev, A. I., and Bowen, K. H. (2015). Aluminum Chain in Li2Al3H8−as Suggested by Photoelectron Spectroscopy and Ab Initio Calculations. *Phys. Chem. Chem. Phys.* 17, 26079–26083. doi:10.1039/C5CP04148A

Rowe, D. J. (1968). Equations-of-Motion Method and the Extended Shell Model. *Rev. Mod. Phys.* 40, 153–166. doi:10.1103/RevModPhys.40.153

Schwabe, T., and Grimme, S. (2007). Double-hybrid Density Functionals with Long-Range Dispersion Corrections: Higher Accuracy and Extended Applicability. *Phys. Chem. Chem. Phys.* 9, 3397. doi:10.1039/b704725h

Shi, Y., Bian, S., Ma, Y., Wang, Y., Ren, J., and Kong, X. (2019). Structures and Superhalogen Properties of Pt2Cln ($2 \le N \le 10$) Clusters. *J. Phys. Chem. A.* 123, 187–193. doi:10.1021/acs.jpca.8b08349

Sikorska, C., and Skurski, P. (2012). The Saturation of the Excess Electron Binding Energy in $Al_nF_{(3n+1)}^-$ (N = 1–5) Anions. *Chem. Phys. Lett.* 536, 34–38. doi:10.1016/j.cplett.2012.03.089

Sikorska, C., Smuczyńska, S., Skurski, P., and Anusiewicz, I. (2008). BX4− and AlX4− Superhalogen Anions (X = F, Cl, Br): An Ab Initio Study. *Inorg. Chem.* 47, 7348–7354. doi:10.1021/ic800863z

Simons, J. (1971). Direct Calculation of First- and Second-Order Density Matrices. The Higher RPA Method. *J. Chem. Phys.* 55, 1218–1230. doi:10.1063/1.1676208

Skurski, P. (2021). "Superhalogens - Enormously Strong Electron Acceptors," in *Superatoms* (Wiley), 53–84. doi:10.1002/9781119619574.ch3

Smuczyńska, S., and Skurski, P. (2009). Halogenoids as Ligands in Superhalogen Anions. *Inorg. Chem.* 48, 10231–10238. doi:10.1021/ic901253r

Smuczyńska, S., and Skurski, P. (2008). Introducing Various Ligands into Superhalogen Anions Reduces Their Electronic Stabilities. *Chem. Phys. Lett.* 452, 44–48. doi:10.1016/j.cplett.2007.12.039

Sobczyk, M., Sawicka, A., and Skurski, P. (20032003). Theoretical Search for Anions Possessing Large Electron Binding Energies. *Eur. J. Inorg. Chem.* 2003, 3790–3797. doi:10.1002/ejic.200300180

Sun, W.-M., Li, X.-H., Li, Y., Wu, D., Li, C.-Y., Chen, J.-H., et al. (2016a). Can Fluorinated Molecular Cages Be Utilized as Building Blocks of Hyperhalogens? *ChemPhysChem* 17, 1468–1474. doi:10.1002/cphc.201600052

Sun, Y.-Y., Li, J.-F., Li, M.-M., Zhou, F.-Q., Li, J.-L., and Yin, B. (2016b). Could the Description on Polynuclear Superhalogens by DFT Be Comparable with High-Level Ab Initio Results? A Comparison between DFT and CCSD(T). *J. Chem. Phys.* 144, 054303. doi:10.1063/1.4941056

Sun, Y.-Y., Li, J.-F., Zhou, F.-Q., Li, J.-L., and Yin, B. (2016c). Probing the Potential of Halogen-free Superhalogen Anions as Effective Electrolytes of Li-Ion Batteries: a Theoretical prospect from Combined Ab Initio and DFT Studies. *Phys. Chem. Chem. Phys.* 18, 28576–28584. doi:10.1039/C6CP05871J

Taylor, T. R., Xu, C., and Neumark, D. M. (1998). Photoelectron Spectra of the C2nH− (N=1-4) and C2nD− (N=1-3) Anions. *J. Chem. Phys.* 108, 10018–10026. doi:10.1063/1.476462

Thomas, L. L., Christakis, T. J., and Jorgensen, W. L. (2006). Conformation of Alkanes in the Gas Phase and Pure Liquids. *J. Phys. Chem. B* 110, 21198–21204. doi:10.1021/jp064811m

Tian, W.-J., Xu, H.-G., Kong, X.-Y., Chen, Q., Zheng, W.-J., Zhai, H.-J., et al. (2014). Photoelectron Spectroscopy of Lithium and Gold Alloyed boron Oxide Clusters: Charge Transfer Complexes, Covalent Gold, Hyperhalogen, and Dual Three-center Four-Electron Hyperbonds. *Phys. Chem. Chem. Phys.* 16, 5129–5136. doi:10.1039/c3cp55362k

Wang, Q., Sun, Q., and Jena, P. (2009). Superhalogen Properties of CuFn Clusters. *J. Chem. Phys.* 131, 124301. doi:10.1063/1.3236576

Wang, X.-B., Ding, C.-F., Wang, L.-S., Boldyrev, A. I., and Simons, J. (1999). First Experimental Photoelectron Spectra of Superhalogens and Their Theoretical Interpretations. *J. Chem. Phys.* 110, 4763–4771. doi:10.1063/1.478386

Weaver, A., Metz, R. B., Bradforth, S. E., and Neumark, D. M. (1988). Spectroscopy of the Iodine Atom + Hydrogen Iodide Transition-State Region by Photodetachment of IHI-. *J. Phys. Chem.* 92, 5558–5560. doi:10.1021/j100331a004

Weigend, F., and Ahlrichs, R. (2005). Balanced Basis Sets of Split Valence, Triple Zeta Valence and Quadruple Zeta Valence Quality for H to Rn: Design and Assessment of Accuracy. *Phys. Chem. Chem. Phys.* 7, 3297. doi:10.1039/b508541a

Wileńska, D., Skurski, P., and Anusiewicz, I. (2014). High-symmetry Compact Structures Are Preferred Equilibrium Configurations of Li N F N+1 − ( N = 2-5) Superhalogen Anions. *J. Fluorine Chem.* 168, 99–104. doi:10.1016/j.jfluchem.2014.09.015

Willis, M., Götz, M., Kandalam, A. K., Ganteför, G. F., and Jena, P. (2010). Hyperhalogens: Discovery of a New Class of Highly Electronegative Species. *Angew. Chem. Int. Edition* 49, 8966–8970. doi:10.1002/anie.201002212

Wu, H., Desai, S. R., and Wang, L.-S. (1996). Observation and Photoelectron Spectroscopic Study of Novel Mono- and Diiron Oxide Molecules: FeOy- (Y = 1–4) and Fe2Oy- (Y = 1–5) J Am Chem. Soc 1996, 118, 5296–5301. *J. Am. Chem. Soc. .J. Am. Chem. Soc.* 118118, 52967434–53017434. doi:10.1021/ja9654140

Yang, Y.-f., Cui, Z.-h., and Ding, Y.-h. (2014). Bottom-up Substitution Assembly of AuF4−n0,−+nPO3 (N = 1-4): a Theoretical Study of Novel Oxyfluoride Hyperhalogen Molecules and Anions AuF4−n(PO3)n0,−. *Mol. Phys.* 112, 1589–1599. doi:10.1080/00268976.2013.845702

Yin, B., Li, T., Li, J.-F., Yu, Y., Li, J.-L., Wen, Z.-Y., et al. (2014). Are Polynuclear Superhalogens without Halogen Atoms Probable? A High-Level Ab Initio Case Study on Triple-Bridged Binuclear Anions with Cyanide Ligands. *J. Chem. Phys.* 140, 094301. doi:10.1063/1.4867009

Zakrzewski, V. G., Dolgounitcheva, O., and Ortiz, J. V. (1996a). Ionization Energies of Anthracene, Phenanthrene, and Naphthacene. *J. Chem. Phys.* 105, 8748–8753. doi:10.1063/1.472654

Zakrzewski, V. G., Ortiz, J. V., Nichols, J. A., Heryadi, D., Yeager, D. L., and Golab, J. T. (1996b). Comparison of Perturbative and Multiconfigurational Electron Propagator Methods. *Int. J. Quan. Chem.* 60, 29–36. doi:10.1002/(sici)1097-461x(1996)60:1<29::aid-qua3>3.0.co;2-7

Zakrzewski, V. G., and Ortiz, J. V. (1994). Semidirect Algorithms in Electron Propagator Calculations. *Int. J. Quan. Chem.* 52, 23–27. doi:10.1002/qua.560520806

Zhang, X., Lundell, K. A., Olson, J. K., Bowen, K. H., and Boldyrev, A. I. (2018a). Electronic Transmutation (ET): Chemically Turning One Element into Another. *Chem. Eur. J.* 24, 9200–9210. doi:10.1002/chem.201800517

Zhang, X., Popov, I. A., Lundell, K. A., Wang, H., Mu, C., Wang, W., et al. (2018b). Realization of an Al≡Al Triple Bond in the Gas-Phase Na 3 Al 2 − Cluster *via* Double Electronic Transmutation. *Angew. Chem. Int. Ed.* 57, 14060–14064. doi:10.1002/anie.201806917

Zhao, R.-F., Yu, L., Zhou, F.-Q., Li, J.-F., and Yin, B. (2017). Could the Increased Structural Versatility Imposed by Non-halogen Ligands Bring Something New for Polynuclear Superhalogens? A Case Study on Binuclear [Mg2L5]− (L = -OH, -OOH and -OF) Anions. *Phys. Chem. Chem. Phys.* 19, 26986–26995. doi:10.1039/C7CP05037B

**Conflict of Interest:** The authors declare that the research was conducted in the absence of any commercial or financial relationships that could be construed as a potential conflict of interest.

**Publisher's Note:** All claims expressed in this article are solely those of the authors and do not necessarily represent those of their affiliated organizations, or those of the publisher, the editors and the reviewers. Any product that may be evaluated in this article, or claim that may be made by its manufacturer, is not guaranteed or endorsed by the publisher.

frontiers | Frontiers in Chemistry

ORIGINAL RESEARCH
published: 21 June 2022
doi: 10.3389/fchem.2022.918704

# Theoretical Study of Alkaline-Earth Metal (Be, Mg, and Ca)-Substituted Aluminum Nitride Nanocages With High Stability and Large Nonlinear Optical Responses

*Hui-Min He*[1], *Hui Yang*[2]*, *Ying Li*[3] *and Zhi-Ru Li*[3]

[1]Department of Physics, Institute of Computational and Applied Physics, Taiyuan Normal University, Jinzhong, China, [2]School of Chemistry and Chemical Engineering, Shanxi Datong University, Datong, China, [3]Laboratory of Theoretical and Computational Chemistry, Jilin University, Changchun, China

By replacing one Al or N atom of aluminum nitride nanocage $Al_{12}N_{12}$ with an alkaline-earth metal atom, two series of compounds, namely, $M@Al_{12}N_{11}$ and $M@Al_{11}N_{12}$ (M = Be, Mg, and Ca), were constructed and investigated in theory. The substituted effect of alkaline-earth metal on the geometric structure and electronic properties of $Al_{12}N_{12}$ is studied in detail by density functional theory (DFT) methods. The calculated binding energies, HOMO–LUMO gaps, and VIE values of these compounds reveal that they possess high stability, though the NBO and HOMO analyses show that they are also excess electron compounds. Due to the existence of diffuse excess electrons, these alkaline-earth metal-substituted compounds exhibit larger first hyperpolarizabilities ($\beta_0$) than pure $Al_{12}N_{12}$ nanocage. In particular, these considered compounds exhibit satisfactory infrared (IR) (>1800 nm) and ultraviolet (UV) (< 250 nm) transparency. Therefore, these proposed excess electron compounds with high stability may be regarded as potential candidates for new UV and IR NLO molecules.

**Keywords: nonlinear optical response (NLO), excess electron compound, aluminum nitride nanocage, first hyperpolarizabilities, density functional theory**

OPEN ACCESS

***Edited by:***
*Ambrish Kumar Srivastava, Deen Dayal Upadhyay Gorakhpur University, India*

***Reviewed by:***
*Sarvesh Kumar Pandey, Indian Institute of Science (IISc), India*
*Ruby Srivastava, Centre for Cellular and Molecular Biology (CCMB), India*

***Correspondence:**
*Hui Yang*
*yanghui091900@126.com*

***Specialty section:***
*This article was submitted to Physical Chemistry and Chemical Physics, a section of the journal Frontiers in Chemistry*

***Received:*** *12 April 2022*
***Accepted:*** *16 May 2022*
***Published:*** *21 June 2022*

***Citation:***
*He H-M, Yang H, Li Y and Li Z-R (2022) Theoretical Study of Alkaline-Earth Metal (Be, Mg, and Ca)-Substituted Aluminum Nitride Nanocages With High Stability and Large Nonlinear Optical Responses. Front. Chem. 10:918704. doi: 10.3389/fchem.2022.918704*

## INTRODUCTION

Over the past few decades, the design and synthesis of nonlinear optical (NLO) materials with excellent performance have exerted a tremendous fascination on researchers in consideration of their widespread applications in optics and optoelectronics (Marder Seth et al., 1994; Priyadarshy et al., 1996; Nakano et al., 2002; Zhang et al., 2005; Xiao et al., 2008; Xu et al., 2013). Up to now, abundant strategies have been proposed to acquire high-performance NLO materials of the new type, for instance, designing donor–π-conjugated-bridge-acceptor (D–π-A) models (Kanis et al., 1994), decorating or modifying $sp^2$-hybridized carbon nanomaterials (Bai et al., 2013; Muhammad et al., 2013; Yu et al., 2013; Karamanis et al., 2014; Zhou et al., 2014), synthesizing octupolar molecules (Ja Lee et al., 2003), utilizing a multideck sandwich cluster as the building block (Wang et al., 2015), applying the bond length alternation (BLA) theory (Meyers et al., 1994), enhancing push–pull effects (Liu et al., 2010), and doping metal atoms (Di Bella, 2001; Zhong et al., 2012b; Wu et al., 2014), etc. In particular, Chen et al. (2004) and Li et al. (2004) have revealed that the

introduction of loosely bound excess electrons into a molecule is an effective measure to dramatically enhance its NLO response. Therein, the diffuse excess electron is responsible for improved NLO response. Subsequently, a lot of compounds with dispersed excess electrons, namely, excess electron compounds, are designed in theory, and as expected, they exhibit considerable large NLO responses (Zhong et al., 2015).

In previous studies, it has been found that alkali-metal-doped organic complexants exhibit large first hyperpolarizabilities (Chen et al., 2005; Xu et al., 2007; Wang et al., 2012). In these systems, excess electrons are formed when organic complexants push/pull valence electrons of alkali metal atoms. Therefore, such systems were classified as excess electron compounds, where the alkali metal atom acts as the excess electron source. However, the introduction of active alkali metal atoms reduces stability of these compounds. Therefore, selecting the proper excess electron source to achieve new excess electron compounds will be an efficient way to obtain NLO materials with high stability. To achieve this aim, we have used alkaline-earth metal atoms as an electron source to design several types of excess electron compounds (He et al., 2017a; He et al., 2017b; He et al., 2019) with large first hyperpolarizabilities and satisfying stability.

On the other word, fullerene-like hollow nanocages with noncarbon have attracted great attention owing to their special optoelectronic properties in recent years (Golberg et al., 1998; Strout, 2000; Fu et al., 2001; Stafström et al., 2001; Bertolus et al., 2004; Wang et al., 2005; Beheshtian et al., 2011; Ahmadi Peyghan et al., 2012; Beheshtian et al., 2012c). In particular, Group III–V nitrides are the most promising nanoscale materials in various fields. Therefore, a lot of theoretical and experimental studies have been carried out on the Group III-V fullerene-like nanostructures, especially the most significant AlN nanocages because of their high thermal conductivity and chemical stability (Silaghi-Dumitrescu et al., 1996; Oku et al., 2004; Koi et al., 2005; Yang et al., 2005; Zhang and Zhang, 2005; Zope and Dunlap, 2005; Li et al., 2007; Beheshtian et al., 2012a; Liu et al., 2013; Saeedi et al., 2013). *Ab initio* calculations revealed that the $Al_{12}N_{12}$ nanocage is the most stable AlN nanostructure and thereby can be regarded as an ideal inorganic fullerene-like candidate (Wu et al., 2003). Considering the unique structural and electronic structure of this cage, it has been used as an excellent starting material to design NLO molecules. For instance, two inorganic electrides, $M@Al_{12}N_{12}$(M = Li, Na, and K) (Niu et al., 2014) and $M_3O@Al_{12}N_{12}$ (M = Li, Na, and K) (Sun et al., 2016), were achieved by doping alkali metal atoms and superalkali clusters on the $Al_{12}N_{12}$ nanocage, while the $M@Al_{12}N_{11}$ and $M@Al_{11}N_{12}$ compounds were designed by substituting one atom of $Al_{12}N_{12}$ with an alkali-metal atom (Maria et al., 2016). All these $Al_{12}N_{12}$-based excess electron compounds exhibit considerably high NLO responses.

In order to enhance the NLO responses and stability of such $Al_{12}N_{12}$-based compounds, two series of inorganic compounds, $M@Al_{12}N_{11}$ and $M@Al_{11}N_{12}$ (M = Be, Mg, and Ca), were obtained by substituting Al or N atom in the $Al_{12}N_{12}$ with alkaline-earth metal in the current work. We mainly focus on the following issues: 1) Can loosely bound excess electrons that can dramatically enhance molecular NLO response be generated in these proposed inorganic compounds with alkaline-earth substituted? 2) Do these novel compounds possess larger stability and first hyperpolarizability ($\beta_0$) than those of previously reported alkali-metal-substituted systems $M@Al_{12}N_{11}$ and $M@Al_{11}N_{12}$ (M = Li, Na, and K)? Our results revealed that these inorganic compounds $M@Al_{12}N_{11}$ and $M@Al_{11}N_{12}$ (M = Be, Mg, and Ca) indeed contain diffuse excess electrons and thus exhibit larger $\beta_0$ values than alkali-metal-substituted systems. In particular, These excess electron compounds exhibit excellent infrared (IR) (>1800 nm) and ultraviolet (UV) (˂ 250 nm) transparency for their potential applications with modern laser frequency conversion technology and optical parameter oscillator processes (Zhang et al., 2009; Luo et al., 2014).

## COMPUTATIONAL DETAILS

The geometric structures with all real frequencies are obtained by using a combination of Becke's hybrid 3-parameter exchange functional (Becke, 1993a) and Lee–Yang–Parr's correlation function (Lee et al., 1988) (B3LYP). In a previous study, the Pople-type (Bilbrey et al., 2013) basis set 6-31+G(d) was selected because it has been proved to be reliable for the geometry optimization of similar systems (Niu et al., 2014). Natural bond orbital (NBO) analyses, vertical ionization energies (VIE), and binding energy ($E_b$) calculations were also performed at the B3LYP/6-31+G(d) level. The binding energy of the alkaline-earth metal atom M was calculated using the counterpoise procedure (Alkorta and Elguero, 1999) and is defined as follows: For $M@Al_{12}N_{11}$,

$$E_b = \left(E_{Al_{12}N_{11}} + E_M\right) - E_{M@Al_{12}N_{11.}} \quad (1)$$

For $M@Al_{12}N_{11}$,

$$E_b = \left(E_{Al_{11}N_{12}} + E_M\right) - E_{M@Al_{11}N_{12.}} \quad (2)$$

The VIE is the energy difference between neutral molecule and cation systems at the neutral optimization geometry (Wang et al., 2012; Bai et al., 2013; Sun et al., 2015; He et al., 2019).

Polarizability and first hyperpolarizability calculations are carried out on long-range correlated methods CAM-B3LYP (Tawada et al., 2004; Yanai et al., 2004) and BHandHLYP (Becke, 1993b) in conjunction with the 6-31+G(d) basis set. As all the systems are in the doublet states, values of spin eigenvalue $\langle S^2 \rangle$ involved in the structural optimization and NLO computations are in the range of 0.760–0.789, which shows an error range of 1.3%–4.9%, indicating that the spin contamination is negligible in the current calculations.

The static polarizability ($\alpha_0$) and the first hyperpolarizability ($\beta_0$) are defined as follows:

$$\alpha_0 = \frac{1}{3}\left(a_{xx} + a_{yy} + a_{zz}\right), \quad (3)$$

$$\beta_0 = \sqrt{\beta_x^2 + \beta_y^2 + \beta_z^2}, \quad (4)$$

where $\beta_i = \frac{3}{5}\left(\beta_{iii} + \beta_{ijj} + \beta_{ikk}\right)$, $i, j, k = x, y, z$.

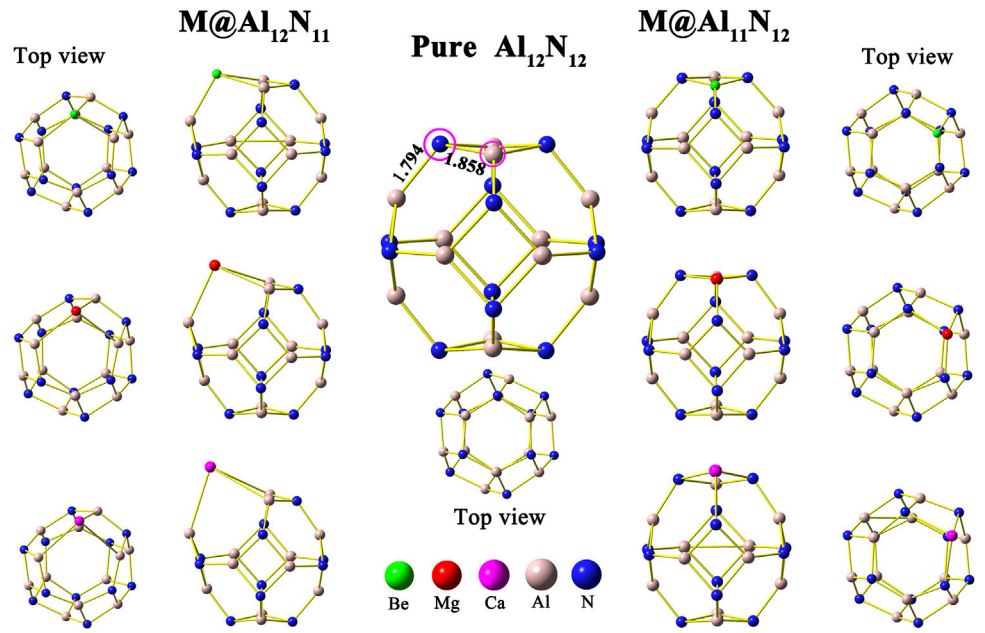


**FIGURE 1 |** Optimized geometric structure of undoped $Al_{12}N_{12}$ and alkaline-earth metal-doped $M@Al_{12}N_{11}$ and $M@Al_{11}N_{12}$ (M = Be, Mg, and Ca).

For electronic transition properties, the transition energy $\Delta E$, oscillator strength $f_0$, and the difference of dipole moment $\Delta\mu$ between the ground and the crucial excited state are estimated by the time-dependent density functional theory, TD-CAM-B3LYP, with the 6-31+G(d) basis set. Simultaneously, ultraviolet-visible–infrared (UV-VIS-IR) absorption spectra of all the systems were also obtained at the same level. All the UV-VIS-IR spectra were reflected with Gaussian curves under a full-width at half-maximum (FWHM) of 0.10 eV.

All of the calculations were carried out by using the Gaussian 16 program package (Frisch et al., 2016). Molecular configurations and molecular orbital (MO) plots were generated with the GaussView program (Dennington et al., 2016).

## RESULTS AND DISCUSSION

First, the isolated aluminum nitride nanocage $Al_{12}N_{12}$ was optimized, and its structure is shown in **Figure 1**. In this study, the pure $Al_{12}N_{12}$ nanocage is found to be a $T_h$-symmetric fullerene-like cage consisting of six 4-membered rings and eight 6-membered rings, in which the Al–N bond lengths are 1.794 and 1.858 Å, respectively, in consistent with earlier reports (Beheshtian et al., 2012a; Beheshtian et al., 2012b; Niu et al., 2014). Then, the initial geometry structures of $M@Al_{12}N_{11}$ and $M@Al_{11}N_{12}$ (M = Be, Mg, and Ca) were constructed by replacing one atom (Al or N) in the $Al_{12}N_{12}$ nanocage with an alkaline-earth metal atom M. In the $M@Al_{12}N_{11}$ series, one alkaline-earth metal atom is substituted for one nitrogen atom, whereas one aluminum atom is replaced with one alkaline-earth metal atom in $M@Al_{11}N_{12}$. After optimization, six equilibrium conformations of $M@Al_{12}N_{11}$ and $M@Al_{11}N_{12}$ have been obtained and are shown in **Figure 1**. The selected geometrical parameters, VIE values, and HOMO–LUMO gap values of these resulting compounds as well as the binding energies and NBO charges of alkaline-earth metal atoms in them are listed in **Table 1**.

**TABLE 1 |** Symmetry, average M–Al bond length (in Å), average M–N bond length (in Å), HOMO–LUMO gap (H-L Gap, in eV), and vertical ionization energies (VIE, in eV) as well as the binding energy ($E_b$, in kcal/mol) and NBO charge of alkaline-earth metal atom for $M@Al_{12}N_{11}$ and $M@Al_{11}N_{12}$ (M = Be, Mg, and Ca).

| Property | $Al_{12}N_{12}$ | $M@Al_{12}N_{11}$ | | | $M@Al_{11}N_{12}$ | | |
|---|---|---|---|---|---|---|---|
| | | Be | Mg | Ca | Be | Mg | Ca |
| Symmetry | $T_h$ | $C_s$ | $C_s$ | $C_1$ | $C_s$ | $C_s$ | $C_1$ |
| Bond length | 1.794/1.858 | 2.374 | 2.787 | 3.206 | 1.685 | 2.051 | 2.385 |
| $q^M$ | | -0.358 | 0.394 | 0.938 | 1.101 | 1.591 | 1.798 |
| VIE | 19.75 | 6.66 | 6.22 | 5.93 | 8.95 | 8.80 | 7.78 |
| $E_b$ | | 62 | 33 | 37 | 244 | 163 | 173 |
| H-L gap | 3.84 | 2.32 | 2.11 | 1.73 | 1.19 | 1.22 | 1.19 |

As shown in **Table 1**, when one nitrogen or aluminum atom is replaced, the original Al-N bond is elongated. That is to say, the bond lengths of M–Al and M–N in the displaced systems are longer than those of the original Al-N in the pure $Al_{12}N_{12}$ nanocage. Nevertheless, the Be-N bond is a special case in $Be@Al_{11}N_{12}$. The Be-N bond in the $Be@Al_{11}N_{12}$ decreases by ca. 0.175 Å as compared with the Al-N bond in the isolated $Al_{12}N_{12}$ nanocage, which may be attributed to the fact that the nitrogen atom possesses larger electronegativity and the Be atom has smaller atomic radii. It is also found that the bond lengths of M–Al and M–N show a monotonous increase with the increasing atomic number of M. In addition, the M–Al bond length of $M@Al_{12}N_{11}$ series exhibits a larger increment than the M-N bond

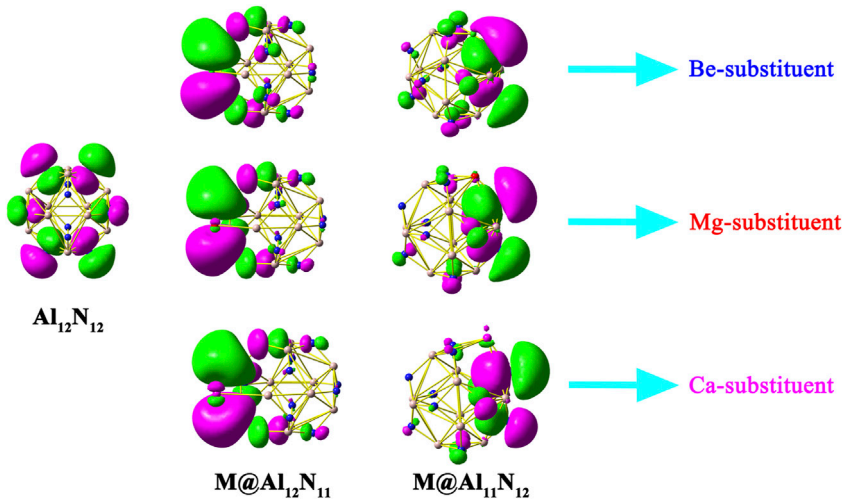


**FIGURE 2 |** HOMOs of $Al_{12}N_{12}$, $M@Al_{12}N_{11}$, and $M@Al_{11}N_{12}$ (M = Be, Mg, and Ca) systems.

length of the $M@Al_{11}N_{12}$ series as compared with the Al-N bond length of pure $Al_{12}N_{12}$ nanocage.

**Figure 2** displays HOMOs of $Al_{12}N_{12}$ nanocage, $M@Al_{12}N_{11}$, and $M@Al_{11}N_{12}$ (M = Be, Mg, and Ca). It can be seen that the HOMO of a pure $Al_{12}N_{12}$ nanocage consists of p atomic orbitals of N atoms. Differently, all the HOMOs of $M@Al_{12}N_{11}$ and $M@Al_{11}N_{12}$ systems possess diffuse excess electrons, reflecting the unique electric characteristics of these studied compounds. Therefore, these proposed $M@Al_{12}N_{11}$ and $M@Al_{11}N_{12}$ (M = Be, Mg, and Ca) systems can be regarded as a new type of inorganic excess electron compounds. Interestingly, it is found that these systems exhibit almost the same HOMOs.

NBO analysis was carried out to analyze charge transfer in nanocages and electronic structures of these systems. The computed NBO charges on alkaline-earth metal atoms in these studied compounds are given in **Table 1**. From **Table 1**, it can be seen that the NBO charges of alkaline-earth metal atoms in $M@Al_{11}N_{12}$ (M = Be, Mg, and Ca) are in the range of (1.101–1.798) |e|, which is much larger than the charges (0.496–0.788) |e| (Maria et al., 2016) on alkali metal atoms in $M@Al_{11}N_{12}$ (M = Li, Na, and K) and the charges of (0.32-0.60) |e| (Ullah et al., 2020) on alkaline-earth metal atoms in $AEM@Al_{12}N_{12}$ (M = Be, Mg, and Ca), indicating that more charges are transferred from alkaline-earth metal atoms to the nanocages in these compounds. In addition, it is also found that the charges on M atoms in the $M@Al_{11}N_{12}$ series are more electropositive than those of the $M@Al_{12}N_{11}$ series, which may be attributed to the fact that the electronegativity of the nitrogen atom is larger than that of the aluminum atom. When an alkaline-earth metal atom is substituted for an Al atom or N atom, the nitrogen atom has a stronger ability to absorb electrons than the Al atom. Therefore, introducing M atoms in the $M@Al_{11}N_{12}$ series loses more electrons and displays more electropositivity. Additionally, it is found that the charges on M atoms increase along with the increasing M atomic number in both series because of the increasing electropositivity of M. Moreover, the NBO analysis also reveals that the alkaline-earth metal atoms can serve as the source of diffuse excess electrons for these excess electron compounds.

It is known that the stability of molecules is of great significance for their synthesis in the laboratory and further application in practice. Moreover, the kinetic stability, chemical reactivity, and optical polarizability of any molecule can be described from the energy gap between the highest occupied molecular orbital (HOMO) and the lowest unoccupied molecular orbital (LUMO). HOMO–LUMO gaps of all the studied excess electron compounds are calculated and are summarized in **Table 1**. As can be seen from **Table 1**, pure $Al_{12}N_{12}$ has a large band gap of 3.84 eV, which is a barrier in the way of its applications in electronic devices. As compared with $Al_{12}N_{12}$, a crucial decrease in the HOMO–LUMO gap was noticed for all replaced systems. That is to say, the HOMO–LUMO gaps of $M@Al_{12}N_{11}$ and $M@Al_{11}N_{12}$ are reduced to (1.19–2.32) eV. Even so, the gap values of $M@Al_{12}N_{11}$ (M = Be, Mg, and Ca) compounds are much larger than those (1.39–1.78) eV (Maria et al., 2016) of $M@Al_{12}N_{11}$ (M = Li, Na, and K) compounds, comparable to that (1.57 eV) (Wang et al., 1999) of the kinetically stable $C_{60}$, and those (1.59–3.79) eV (Ullah et al., 2020) of $AEM@Al_{12}N_{12}$ (M = Be, Mg, and Ca), suggesting the large chemical stability of the studied $M@Al_{12}N_{11}$ (M = Be, Mg, and Ca) species. From **Figure 3**, it is also found that the gap values decrease along with the decreasing M atomic number for the $M@Al_{12}N_{11}$ series, whereas they are hardly equal for the $M@Al_{11}N_{12}$ series.

Furthermore, the large electronic stability of these excess electron compounds can also be characterized by their higher vertical ionized energies (VIEs) of (5.93–8.95) eV, which are slightly higher than the reported values of inorganic and organic excess electron compounds (Chen et al., 2005; Zhong et al., 2012a; He et al., 2017a; He et al., 2017b; Ullah et al., 2020), indicating that these proposed nanocage compounds exhibit high electronic stability. **Figure 3** demonstrates the alkaline-earth metal

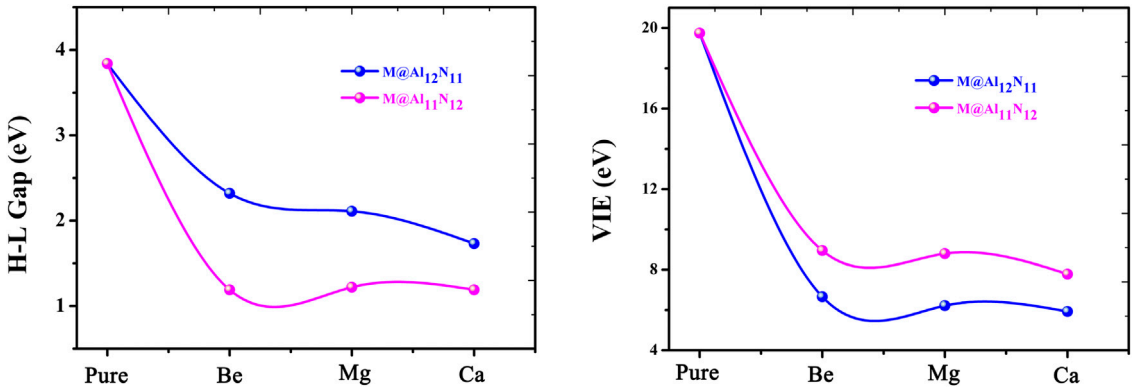


**FIGURE 3 |** Relationship between H-L Gaps and VIE values with the atomic number of alkaline-earth metals.

**TABLE 2 |** Static polarizability ($\alpha_o$), static first hyperpolarizability $\beta_o$, oscillator strength ($f_o$), transition energy ($\Delta E$, in eV), and difference of dipole moment ($\Delta\mu$ in D) between the ground and the crucial excited states and crucial transition for M@$Al_{12}N_{11}$ and M@$Al_{11}N_{12}$ (M = Be, Mg and Ca).

| | | $\alpha_o$ | $\beta_o$[a] | $\beta_o$[b] | $f_o$ | $\Delta E$ | $\Delta\mu$ | Crucial transition |
|---|---|---|---|---|---|---|---|---|
| $Al_{12}N_{12}$ | - | 286 | 0 | 0 | 0.0176 | 4.759 | 0 | - |
| M@$Al_{12}N_{11}$ | Be | 331 | 861 | 875 | 0.0434 | 3.32 | 2.53 | $\alpha$H→$\alpha$L+3 (23.8%) |
| | | | | - | | | | $\alpha$H→$\alpha$L+5 (19.1%) |
| | | | | - | | | | $\beta$H-1→$\beta$L (17.2%) |
| | Mg | 369 | 1979 | 2006 | 0.1034 | 2.93 | 2.27 | $\alpha$H-1→$\alpha$L+1 (37.1%) |
| | | | | - | | | | $\beta$H→$\beta$L+2 (41.2%) |
| | Ca | 410 | 6,140 | 6,473 | 0.0783 | 2.83 | 2.19 | $\alpha$H-1→$\alpha$L+2 (18.9%) |
| | | | | - | | | | $\alpha$H-1→$\alpha$L+1 (15.7%) |
| | | | | - | | | | $\beta$H→$\beta$L+2 (39.7%) |
| M@$Al_{11}N_{12}$ | Be | 312 | 1,079 | 1796 | 0.0181 | 0.77 | 3.40 | $\beta$H→$\beta$L (87.1%) |
| | Mg | 326 | 969 | 1,628 | 0.0354 | 0.97 | 2.53 | $\beta$H→$\beta$L (64.5%) |
| | | | | - | | | | $\beta$H-2→$\beta$L (19%) |
| | Ca | 345 | 1,683 | 3,687 | 0.0420 | 0.92 | 2.09 | $\beta$H→$\beta$L (49.6%) |
| | | | | - | | | | $\beta$H-1→$\beta$L (32.7%) |

[a]*for CAM-B3LYP level.*
[b]*for BHandHLYP level.*

atomic number effect on VIE values, namely, the larger the atomic number, the smaller the VIE value.

Additionally, the binding energies ($E_b$) of these designed M@$Al_{12}N_{11}$ and M@$Al_{11}N_{12}$ compounds are also calculated and given in **Table 1**. The $E_b$ values are defined as the negative of the intramolecular interaction energies between the alkaline-earth metal M and the remaining $Al_{12}N_{11}$ or $Al_{11}N_{12}$ moieties. Thus, the larger the $E_b$ value is, the stronger the interaction between two subunits. From **Table 1**, it can be seen that all the proposed excess electron compounds exhibit much larger $E_b$ values of (33.0-244.0) kcal/mol than those (31-89 kcal/mol) (Maria et al., 2016) of previously reported alkali-metal substituted compounds, indicating that alkaline-earth metal atoms are more tightly bound to the remaining $Al_{12}N_{11}$ or $Al_{11}N_{12}$ units than the alkali metal atoms in M@$Al_{12}N_{11}$ and M@$Al_{11}N_{12}$ (M = Li, Na, and K). More importantly, the M@$Al_{11}N_{12}$ (M = Be, Mg, and Ca) series exhibit extremely large $E_b$ values up to (173-244) kcal/mol, which are far more than those of (64-89) kcal/mol for M@$Al_{11}N_{12}$ (M = Li, Na, and K) (Maria et al., 2016). Thus, as compared with alkali metal atoms, the introduction of alkaline-earth metal atoms into the $Al_{12}N_{12}$ nanocage can produce more stable species with excess electrons. In addition, the $E_b$ values of proposed alkaline-earth metal substituted excess electron compounds are also comparable to those (59-106) kcal/mol of small clusters with alkaline-earth metal atoms (Srivastava et al., 2018).

To evaluate nonlinear optical response, the dipole moments ($\mu_0$), polarizabilities ($\alpha_0$), and first hyperpolarizabilities ($\beta_0$) of pure $Al_{12}N_{12}$ and the proposed M@$Al_{12}N_{11}$ and M@$Al_{11}N_{12}$ compounds were calculated and are summarized in **Table 2**. To better visualize the results, the dependences of the polarizability ($\alpha_0$) and first hyperpolarizability ($\beta_0$) values on the alkaline-earth metal atomic number are exhibited in **Figure 4**. Our results revealed that the $\alpha_0$ (286 au) of the $Al_{12}N_{12}$ nanocage is increased to 319-410 au for replaced compounds, indicating that the substitution of alkaline-earth metal atoms virtually affects the $\alpha_0$ value of the $Al_{12}N_{12}$ molecule. As shown in **Table 2** and **Figure 4**, the $\alpha_0$ changes in the order of 331 au (Be) < 369 au (Mg)

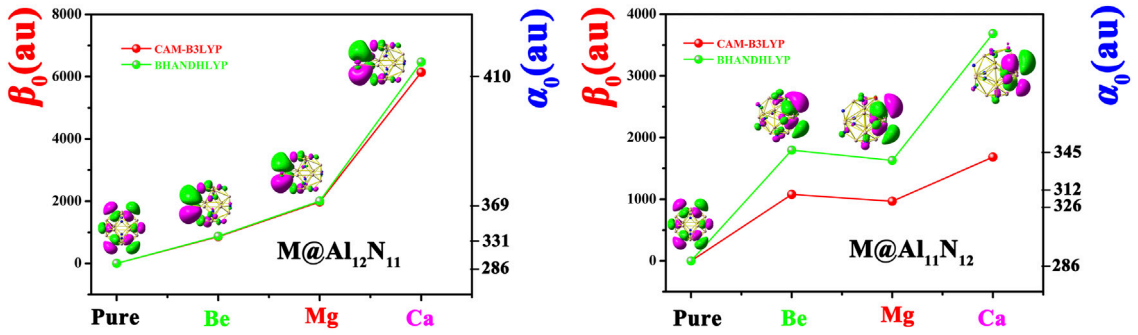


**FIGURE 4 |** Dependences of $\alpha_0$ and $\beta_0$ values on the M atomic number for $Al_{12}N_{12}$, $M@Al_{12}N_{11}$, and $M@Al_{11}N_{12}$ and the first hyperpolarizability comparison of two different methods.

< 410 au (Ca) in the $M@Al_{12}N_{11}$ series and similarly, varies in the order of 312 au (Be) < 326au (Mg) < 345au (Ca) in the $M@Al_{11}N_{12}$ series. In short, $\alpha_0$ increases along with the increasing M atomic number. Also, it is observed that the $M@Al_{12}N_{11}$ exhibits a relatively larger $\alpha_0$ value than the corresponding $M@Al_{11}N_{12}$, indicating that the excess electrons in the HOMOs of the former are more diffuse than the latter because static polarizability is sensitive to electronic delocalization.

Due to the pure $Al_{12}N_{12}$ nanocage being centrosymmetric, its $\beta_0$ values are zero. Thus, different from $\alpha_0$, the substitution of M for Al or N atom in $Al_{12}N_{12}$ brings a prominent improvement of first hyperpolarizability ($\beta_0$) of the $Al_{12}N_{12}$ nanocage, which is because that M-substitution not only destroys the centrosymmetry of $Al_{12}N_{12}$ but also makes two kinds of replaced systems possessing the dispersed excess electrons. Two different long-range corrected methods were used to calculate the hyperpolarizability $\beta_0$ values, which have been listed in **Table 2**. **Figure 4** manifests the first hyperpolarizability at CAM-B3LYP for $M@Al_{12}N_{11}$ and $M@Al_{11}N_{12}$ follows the same trend as for BHandHLYP. However, the calculated values at CAM-B3LYP are slightly lower than BHandHLYP.

Additionally, it can be distinctly seen from **Table 2** and **Figure 4** that the $\beta_0$ values of Ca-substitution compounds are greatly larger than those of Be-substitution and Mg-substitution compounds, signifying an evident effect of the M atomic number on the NLO responses of $M@Al_{12}N_{11}$ and $M@Al_{11}N_{12}$. To be specific, the varying order for $\beta_0$ is 861au (Be) < 1979au (Mg) < 6140au (Ca) in the $M@Al_{12}N_{11}$ series, which is consistent with the change sequence of $\alpha_0$ values. That is, the compounds with higher polarizabilities also present relatively higher NLO responses because of the more diffuse excess electrons in them.

The comparison of $\beta_0$ values between our proposed excess electron compounds and previously reported alkali-metal substituted compounds is meaningful. In the $M@Al_{12}N_{11}$ series, it can be seen that reported alkali-metal substituted compounds exhibit much larger $\beta_0$ values of (2,500-9,100) au (in CAM-B3LYP/6-311 + g* level) (Maria et al., 2016) than those (861-6,140) au of our proposed alkaline-earth metal substituted excess electron compounds. However, the resultant comparison of $\beta_0$ values is inverse in the $M@Al_{11}N_{12}$ series, namely, $\beta_0$ values (1,628–3,687) au of alkaline-earth metal-substituted compounds are larger than those (420–770) kcal/mol of alkali-metal-substituted compounds. Thus, when a N atom is substituted by alkaline-earth metal atoms in an $Al_{12}N_{12}$ nanocage, excess electron compounds $M@Al_{11}N_{12}$ (M = Be, Mg, and Ca) can exhibit larger NLO responses than $M@Al_{11}N_{12}$ (M = Li, Na, and K).

For intensive discernment of this significant increase in first hyperpolarizability due to substitution of alkaline-earth metal in the $Al_{12}N_{12}$ nanocage, let us consider the simplest two-level model (Maroulis, 1996; Xu et al., 2009), which is derived from the sum-over states method:

$$\beta_0 \approx \frac{\Delta\mu f_0}{\Delta E^3}, \tag{5}$$

where involved $\Delta E$, $f_0$, and $\Delta\mu$ are the transition energy, oscillator strength, and difference of the dipole moment between the ground state and the crucial excited state, respectively. The expression distinctly displays that $\beta_0$ is inversely proportional to the third power of $\Delta E$. Therefore, crucial transition energy plays an important role in the evaluation of $\beta_0$. In the current work, the TD-CAM-B3LYP calculations are performed to obtain the dominated excited states of these studied compounds. The crucial transitions and the corresponding $\Delta E$, $f_0$, and $\Delta\mu$ values are presented in **Table 2** and **Figure 5**, respectively. It is noted that the electrons involved in the crucial excited states of these considered species primarily come from their HOMO, HOMO-1, and HOMO-2 orbitals. Meanwhile, from **Figure 5**, it can be seen that crucial transitions make the electrons more diffuse, which may lead to the large $\beta_0$.H

Moreover, compared to the large $\Delta E$ value (4.759 eV) in pure $Al_{12}N_{12}$, the $M@Al_{12}N_{11}$ and $M@Al_{11}N_{12}$ compounds exhibit much smaller $\Delta E$ values of (0.77-3.32) eV, which are comparable to those of (1.295–1.982) eV for the alkali metal-based electrides, including Li@(calix [4]pyrrole) (Chen et al., 2005), $Li_n$-H-$(CF_2\text{-}CH_2)_3$-H ($n$ = 1, 2) (Xu et al., 2007), $H_4C_4N_2\cdots Na_2$ (Ma et al., 2008), and $Li@B_{10}H_{14}$ (Muhammad et al., 2009), and far less than (4.6–6.7) eV of $M@Al_{12}N_{11}$ and $M@Al_{11}N_{12}$(M = Li, Na, and K) (Maria et al., 2016), as well as (1.80–4.76) eV of $AEM@Al_{12}N_{12}$ (Ullah et al., 2020). Hence, these small $\Delta E$ values bring forth the large $\beta_0$ values of these proposed alkaline-earth metal-based excess electron compounds.

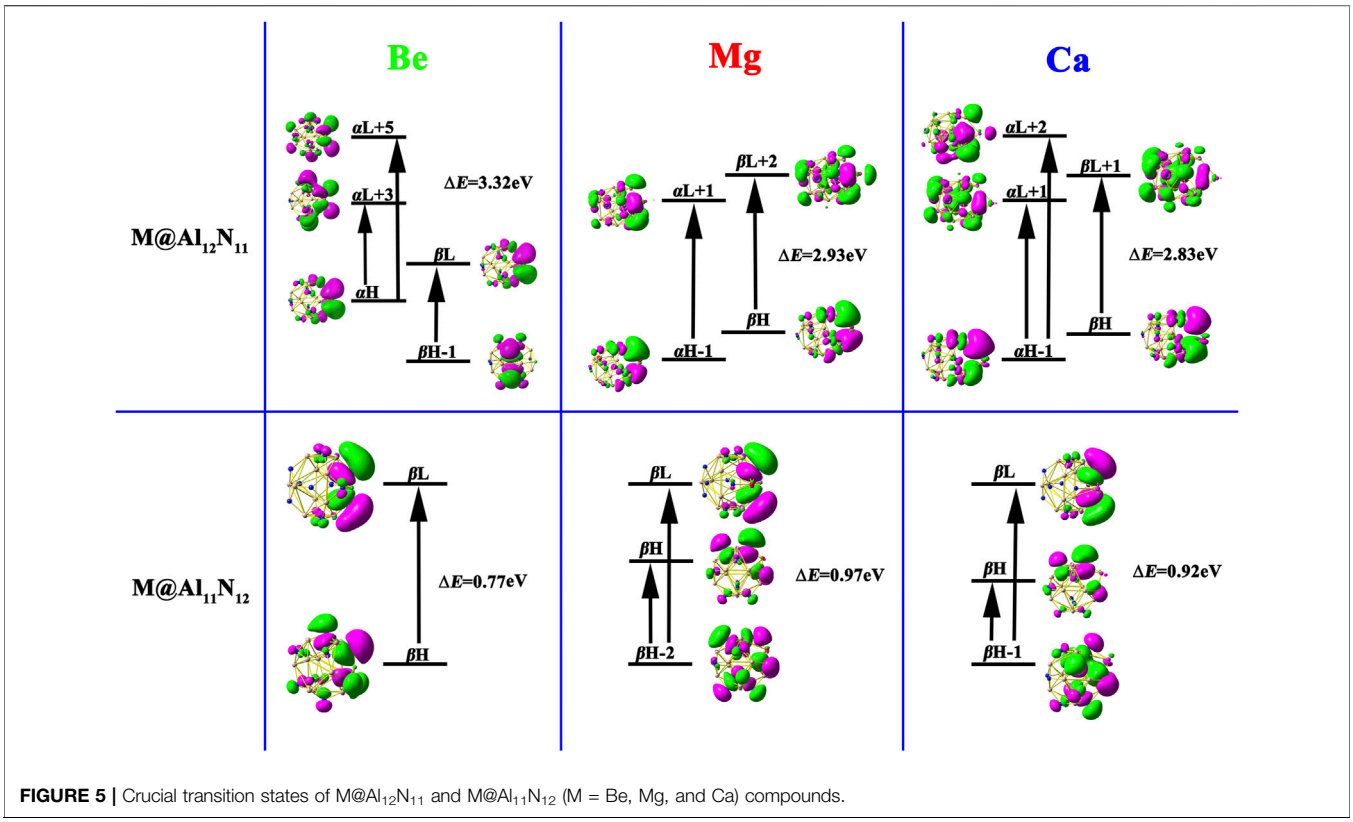


**FIGURE 5 |** Crucial transition states of $M@Al_{12}N_{11}$ and $M@Al_{11}N_{12}$ (M = Be, Mg, and Ca) compounds.

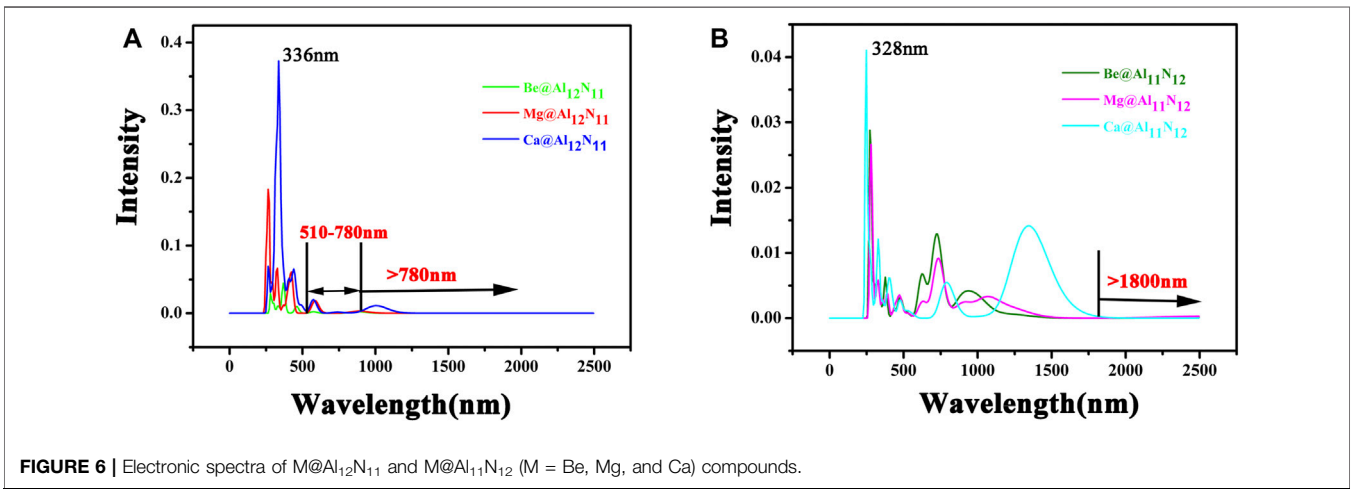


**FIGURE 6 |** Electronic spectra of $M@Al_{12}N_{11}$ and $M@Al_{11}N_{12}$ (M = Be, Mg, and Ca) compounds.

It is well-known that the main applications for NLO materials are in doubling frequency and second harmonic generation (SHG). Accordingly, the superior NLO materials not only need large NLO response but also must be transparent under the applied laser region. Therefore, the ultraviolet-visible–infrared (UV-VIS-NIR) absorption spectra of these $M@Al_{12}N_{11}$ and $M@Al_{11}N_{12}$ compounds are gained and shown in **Figure 6**. From **Figure 6A**, it can be seen that the main absorption region of $M@Al_{12}N_{11}$ compounds is from 300 to 500 nm. The absorption of these compounds in the infrared spectral region is weak, especially for $Be@Al_{12}N_{11}$, there is no absorption in the visible region of (510–780) nm and the infrared spectral region, which suggests that $Be@Al_{12}N_{11}$ has satisfying transparency in both the visible region of (510–780) nm and infrared spectral region. In addition, **Figure 6B** shows that the $M@Al_{11}N_{12}$ series have an infrared (IR) transparent region at wavelength >1800 nm. Thus, it is hoped that these six excess electron compounds could be used as new IR NLO materials. Simultaneously, it is observed that they also have an ultraviolet (UV) transparent region at wavelength ˂ 250 nm. Then, they may be taken as a new candidate for UV NLO materials.

## CONCLUSIONS

Using the density functional theory (DFT), two new series of excess electron compounds, i.e., $M@Al_{12}N_{11}$ and $M@Al_{11}N_{12}$ (M = Be, Mg, and Ca), have been obtained and studied theoretically in this work. The substituted effect of alkaline-earth metal on the geometric structures and electronic properties of aluminum nitride ($Al_{12}N_{12}$) nanocage has been investigated in detail. Binding energy calculations display that these proposed compounds, particularly the Al-replaced nanocages have high structural stability. In addition, the substitution of alkaline-earth metal for Al and N in $Al_{12}N_{12}$ significantly reduces its HOMO–LUMO gap and VIE value, which may bring forth large optical polarizability. More importantly, these studied compounds contain diffuse excess electrons and thus show high NLO responses. Particularly, our results reveal that all these considered compounds show satisfying infrared (IR) transparent region (>1800 nm) and ultraviolet (UV) region (< 250 nm). Thus, we hope that this study could not only provide new candidates of potential NLO molecules but also promote future applications of Al-N fullerene-like nanocages in the field of nonlinear optics.

## DATA AVAILABILITY STATEMENT

The raw data supporting the conclusion of this article will be made available by the authors, without undue reservation.

## AUTHOR CONTRIBUTIONS

All authors listed have made a substantial, direct, and intellectual contribution to the work and approved it for publication.

## FUNDING

This work was supported by the Science and Technology Innovation Project of Higher Education in Shanxi Province (2020L0507, 2020L0516, and 2021L370).

## ACKNOWLEDGMENTS

We thank the National Supercomputing Center in Shenzhen for providing computational resources.

## REFERENCES

Ahmadi Peyghan, A., Pashangpour, M., Bagheri, Z., and Kamfiroozi, M. (2012). Energetic, Structural, and Electronic Properties of Hydrogenated $Al_{12}P_{12}$ Nanocluster. *Phys. E Low-dimensional Syst. Nanostructures* 44 (7), 1436–1440. doi:10.1016/j.physe.2012.03.007

Alkorta, I., and Elguero, J. (1999). Theoretical Study of Strong Hydrogen Bonds between Neutral Molecules: The Case of Amine Oxides and Phosphine Oxides as Hydrogen Bond Acceptors. *J. Phys. Chem. A* 103 (2), 272–279. doi:10.1021/jp982644n

Bai, Y., Zhou, Z.-J., Wang, J.-J., Li, Y., Wu, D., Chen, W., et al. (2013). New Acceptor-Bridge-Donor Strategy for Enhancing NLO Response with Long-Range Excess Electron Transfer from the $NH_2$.M/$M_3O$ Donor (M = Li, Na, K) to inside the Electron Hole Cage C20F19 Acceptor through the Unusual σ Chain Bridge $(CH_2)_4$. *J. Phys. Chem. A* 117 (13), 2835–2843. doi:10.1021/jp3120594

Becke, A. D. (1993b). A New Mixing of Hartree-Fock and Local Density-functional Theories. *J. Chem. Phys.* 98 (2), 1372–1377. doi:10.1063/1.464304

Becke, A. D. (1993a). Density-functional Thermochemistry. III. The Role of Exact Exchange. *J. Chem. Phys.* 98 (7), 5648–5652. doi:10.1063/1.464913

Beheshtian, J., Bagheri, Z., Kamfiroozi, M., and Ahmadi, A. (2012a). A Comparative Study on the $B_{12}N_{12}$, $Al_{12}N_{12}$, $B_{12}P_{12}$ and $Al_{12}P_{12}$ Fullerene-like Cages. *J. Mol. Model.* 18 (6), 2653–2658. doi:10.1007/s00894-011-1286-y

Beheshtian, J., Bagheri, Z., Kamfiroozi, M., and Ahmadi, A. (2011). Toxic CO Detection by $B_{12}N_{12}$ Nanocluster. *Microelectron. J.* 42 (12), 1400–1403. doi:10.1016/j.mejo.2011.10.010

Beheshtian, J., Peyghan, A. A., Bagheri, Z., and Kamfiroozi, M. (2012c). Interaction of Small Molecules (NO, $H_2$, $N_2$, and $CH_4$) with BN Nanocluster Surface. *Struct. Chem.* 23 (5), 1567–1572. doi:10.1007/s11224-012-9970-9

Beheshtian, J., Peyghan, A. A., and Bagheri, Z. (2012b). Selective Function of $Al_{12}N_{12}$ Nano-Cage towards NO and CO Molecules. *Comput. Mater. Sci.* 62, 71–74. doi:10.1016/j.commatsci.2012.05.041

Bertolus, M., Finocchi, F., and Millié, P. (2004). Investigating Bonding in Small Silicon-Carbon Clusters: Exploration of the Potential Energy Surfaces of $Si_3C_4$, $Si_4C_3$, and $Si_4C_4$ Using Ab Initio Molecular Dynamics. *J. Chem. Phys.* 120 (9), 4333–4343. doi:10.1063/1.1636717

Bilbrey, J. A., Kazez, A. H., Locklin, J., and Allen, W. D. (2013). Exact Ligand Cone Angles. *J. Comput. Chem.* 34 (14), 1189–1197. doi:10.1002/jcc.23217

Chen, W., Li, Z.-R., Wu, D., Gu, F.-L., Hao, X.-Y., Wang, B.-Q., et al. (2004). The Static Polarizability and First Hyperpolarizability of the Water Trimer anion:Ab Initiostudy. *J. Chem. Phys.* 121 (21), 10489–10494. doi:10.1063/1.1811609

Chen, W., Li, Z.-R., Wu, D., Li, Y., Sun, C.-C., and Gu, F. L. (2005). The Structure and the Large Nonlinear Optical Properties of Li@Calix[4]pyrrole. *J. Am. Chem. Soc.* 127 (31), 10977–10981. doi:10.1021/ja050601w

Dennington, R. D., Keith, T. A., and Millam, J. M. (2016). *GaussView, Version6. Shawnee Mission*. KS: Semichem Inc.

Di Bella, S. (2001). Second-order Nonlinear Optical Properties of Transition Metal Complexes. *Chem. Soc. Rev.* 30 (6), 355–366. doi:10.1039/B100820J

Frisch, M. J., Trucks, G. W., Schlegel, H. B., Scuseria, G. E., Robb, M. A., Cheeseman, J. R., et al. (2016). *Gaussian 16, Revision A.03*. Wallingford CT, USA: Gaussian, Inc.

Fu, C.-C., Weissmann, M., Machado, M., and Ordejón, P. (2001). Ab Initiostudy of Silicon-Multisubstituted Neutral and Charged Fullerenes. *Phys. Rev. B* 63 (8), 085411. doi:10.1103/PhysRevB.63.085411

Golberg, D., Bando, Y., Stéphan, O., and Kurashima, K. (1998). Octahedral Boron Nitride Fullerenes Formed by Electron Beam Irradiation. *Appl. Phys. Lett.* 73 (17), 2441–2443. doi:10.1063/1.122475

He, H.-M., Li, Y., Yang, H., Yu, D., Li, S.-Y., Wu, D., et al. (2017a). Efficient External Electric Field Manipulated Nonlinear Optical Switches of All-Metal Electride Molecules with Infrared Transparency: Nonbonding Electron Transfer Forms an Excess Electron Lone Pair. *J. Phys. Chem. C* 121 (1), 958–968. doi:10.1021/acs.jpcc.6b11919

He, H.-M., Li, Y., Yang, H., Yu, D., Wu, D., Zhong, R.-L., et al. (2017b). Effects of the Cage Number and Excess Electron Number on the Second Order Nonlinear Optical Response in Molecular All-Metal Electride Multicage Chains. *J. Phys. Chem. C* 121 (45), 25531–25540. doi:10.1021/acs.jpcc.7b06464

He, H.-M., Luis, J. M., Chen, W.-H., Yu, D., Li, Y., Wu, D., et al. (2019). Nonlinear optical response of endohedral all-metal electride cages $2e^-Mg^{2+}(M@E^{12})^{2-}Ca^{2+}$ (M = Ni, Pd, and Pt; E = Ge, Sn, and Pb). *J. Mat. Chem. C* 7 (3), 645–653. doi:10.1039/C8TC05647A

Ja Lee, M., Piao, M., Jeong, M.-Y., Hae Lee, S., Min Kang, K., Jeon, S.-J., et al. (2003). Novel azo octupoles with large first hyperpolarizabilities. *J. Mat. Chem.* 13 (5), 1030–1037. Electronic supplementary information (ESI) is available: molar absorptivity spectra of 1a,d,e, P1 and P2 in THF and plots of I2ω vs. number

density for 1a,d,e and 2a,c,e in THF at 1064 nm. See http://www.rsc.org/suppdata/jm/b3/b300777d/. doi:10.1039/b300777d

Kanis, D. R., Ratner, M. A., and Marks, T. J. (1994). Design and Construction of Molecular Assemblies with Large Second-Order Optical Nonlinearities. Quantum Chemical Aspects. *Chem. Rev.* 94 (1), 195–242. doi:10.1021/cr00025a007

Karamanis, P., Otero, N., and Pouchan, C. (2014). Unleashing the Quadratic Nonlinear Optical Responses of Graphene by Confining White-Graphene (*H*-BN) Sections in its Framework. *J. Am. Chem. Soc.* 136 (20), 7464–7473. doi:10.1021/ja502631w

Koi, N., Oku, T., Narita, I., and Suganuma, K. (2005). Synthesis of Huge Boron Nitride Cages. *Diam. Relat. Mater.* 14 (3), 1190–1192. doi:10.1016/j.diamond.2004.12.018

Lee, C., Yang, W., and Parr, R. G. (1988). Development of the Colle-Salvetti Correlation-Energy Formula into a Functional of the Electron Density. *Phys. Rev. B* 37 (2), 785–789. doi:10.1103/PhysRevB.37.785

Li, J., Xia, Y., Zhao, M., Liu, X., Song, C., Li, L., et al. (2007). Theoretical Prediction for the $(AlN)_{12}$ Fullerene-like Cage-Based Nanomaterials. *J. Phys. Condens. Matter* 19 (34), 346228. doi:10.1088/0953-8984/19/34/346228

Li, Y., Li, Z.-R., Wu, D., Li, R.-Y., Hao, X.-Y., and Sun, C.-C. (2004). An Ab Initio Prediction of the Extraordinary Static First Hyperpolarizability for the Electron-Solvated Cluster $(FH)_2\{e\}(HF)$. *J. Phys. Chem. B* 108 (10), 3145–3148. doi:10.1021/jp036808y

Liu, Z.-B., Zhou, Z.-J., Li, Y., Li, Z.-R., Wang, R., Li, Q.-Z., et al. (2010). Push-pull Electron Effects of the Complexant in a Li Atom Doped Molecule with Electride Character: a New Strategy to Enhance the First Hyperpolarizability. *Phys. Chem. Chem. Phys.* 12 (35), 10562–10568. doi:10.1039/c004262e

Liu, Z., Wang, X., Liu, G., Zhou, P., Sui, J., Wang, X., et al. (2013). Low-density Nanoporous Phases of Group-III Nitrides Built from Sodalite Cage Clusters. *Phys. Chem. Chem. Phys.* 15 (21), 8186–8198. doi:10.1039/C3CP50814E

Luo, Z.-Z., Lin, C.-S., Zhang, W.-L., Zhang, H., He, Z.-Z., and Cheng, W.-D. (2014). $Ba_8Sn_4S_{15}$: A Strong Second Harmonic Generation Sulfide with Zero-Dimensional Crystal Structure. *Chem. Mat.* 26 (2), 1093–1099. doi:10.1021/cm403369m

Ma, F., Li, Z.-R., Xu, H.-L., Li, Z.-J., Li, Z.-S., Aoki, Y., et al. (2008). Lithium Salt Electride with an Excess Electron Pair-A Class of Nonlinear Optical Molecules for Extraordinary First Hyperpolarizability. *J. Phys. Chem. A* 112 (45), 11462–11467. doi:10.1021/jp8040023

Marder, S. R., Gorman, C. B., Meyers, F., Perry, J. W., Bourhill, G., Brédas, J.-L., et al. (1994). A Unified Description of Linear and Nonlinear Polarization in Organic Polymethine Dyes. *Science* 265 (5172), 632–635. doi:10.1126/science.265.5172.632

Maria, M., Iqbal, J., and Ayub, K. (2016). Theoretical Study of the Non Linear Optical Properties of Alkali Metal (Li, Na, K) Doped Aluminum Nitride Nanocages. *RSC Adv.* 6 (96), 94228–94235. doi:10.1039/C6RA21797D

Maroulis, G. (1996). Electric Properties of Carbon Tetrafluoride. *Chem. Phys. Lett.* 259 (5), 654–660. doi:10.1016/0009-2614(96)00728-2

Meyers, F., Marder, S. R., Pierce, B. M., and Bredas, J. L. (1994). Electric Field Modulated Nonlinear Optical Properties of Donor-Acceptor Polyenes: Sum-Over-States Investigation of the Relationship between Molecular Polarizabilities (.alpha., .beta., and .gamma.) and Bond Length Alternation. *J. Am. Chem. Soc.* 116 (23), 10703–10714. doi:10.1021/ja00102a040

Muhammad, S., Xu, H.-L., Zhong, R.-L., Su, Z.-M., Al-Sehemi, A. G., and Irfan, A. (2013). Quantum Chemical Design of Nonlinear Optical Materials by Sp2-Hybridized Carbon Nanomaterials: Issues and Opportunities. *J. Mat. Chem. C* 1 (35), 5439–5449. doi:10.1039/c3tc31183j

Muhammad, S., Xu, H., Liao, Y., Kan, Y., and Su, Z. (2009). Quantum Mechanical Design and Structure of the $Li@B_{10}H_{14}$ Basket with a Remarkably Enhanced Electro-Optical Response. *J. Am. Chem. Soc.* 131 (33), 11833–11840. doi:10.1021/ja9032023

Nakano, M., Fujita, H., Takahata, M., and Yamaguchi, K. (2002). Theoretical Study on Second Hyperpolarizabilities of Phenylacetylene Dendrimer: Toward an Understanding of Structure−Property Relation in NLO Responses of Fractal Antenna Dendrimers. *J. Am. Chem. Soc.* 124 (32), 9648–9655. doi:10.1021/ja0115969

Niu, M., Yu, G., Yang, G., Chen, W., Zhao, X., and Huang, X. (2014). Doping the Alkali Atom: An Effective Strategy to Improve the Electronic and Nonlinear Optical Properties of the Inorganic $Al_{12}N_{12}$ Nanocage. *Inorg. Chem.* 53 (1), 349–358. doi:10.1021/ic4022917

Oku, T., Nishiwaki, A., and Narita, I. (2004). Formation and Atomic Structure of $B_{12}N_{12}$ Nanocage Clusters Studied by Mass Spectrometry and Cluster Calculation. *Sci. Technol. Adv. Mater.* 5 (5), 635–638. doi:10.1016/j.stam.2004.03.017

Priyadarshy, S., Therien, M. J., and Beratan, D. N. (1996). Acetylenyl-Linked, Porphyrin-Bridged, Donor−Acceptor Molecules: A Theoretical Analysis of the Molecular First Hyperpolarizability in Highly Conjugated Push−Pull Chromophore Structures. *J. Am. Chem. Soc.* 118 (6), 1504–1510. doi:10.1021/ja952690q

Saeedi, M., Anafcheh, M., Ghafouri, R., and Hadipour, N. L. (2013). A Computational Investigation of the Electronic Properties of Octahedral Al n N n and Al n P N Cages (n = 12, 16, 28, 36, and 48). *Struct. Chem.* 24 (2), 681–689. doi:10.1007/s11224-012-0119-7

Silaghi-Dumitrescu, I., Lara-Ochoa, F., and Haiduc, I. (1996). $A_{12}B_{12}$ (A = B,Al; B = N,P) Fullerene-like Cages and Their Hydrogenated Forms Stabilized by Exohedral Bonds. An AM1 Molecular Orbital Study. *J. Mol. Struct. THEOCHEM* 370 (1), 17–23. doi:10.1016/s0166-1280(96)04677-5

Srivastava, A. K., Misra, N., and Pandey, S. K. (2018). DFT Study on Planar $(CaO)_n$ Rings (N = 1-5) and Their Hydrogen Storage Behavior: Ca-O versus Mg-O Clusters. *J. Clust. Sci.* 29 (1), 57–65. doi:10.1007/s10876-017-1306-x

Stafström, S., Hultman, L., and Hellgren, N. (2001). Predicted Stability of A New aza[60]Fullerene Molecule, $C_{48}N_{12}$. *Chem. Phys. Lett.* 340 (3), 227–231. doi:10.1016/S0009-2614(01)00418-3

Strout, D. L. (2000). Structure and Stability of Boron Nitrides: Isomers of $B_{12}N_{12}$. *J. Phys. Chem. A* 104 (15), 3364–3366. doi:10.1021/jp994129a

Sun, W.-M., Li, X.-H., Wu, D., Li, Y., He, H.-M., Li, Z.-R., et al. (2016). A Theoretical Study on Superalkali-Doped Nanocages: Unique Inorganic Electrides with High Stability, Deep-Ultraviolet Transparency, and a Considerable Nonlinear Optical Response. *Dalton Trans.* 45 (17), 7500–7509. doi:10.1039/C6DT00342G

Sun, W.-M., Wu, D., Li, Y., Liu, J.-Y., He, H.-M., and Li, Z.-R. (2015). A Theoretical Study on Novel Alkaline Earth-Based Excess Electron Compounds: Unique Alkalides with Considerable Nonlinear Optical Responses. *Phys. Chem. Chem. Phys.* 17 (6), 4524–4532. doi:10.1039/C4CP04951A

Tawada, Y., Tsuneda, T., Yanagisawa, S., Yanai, T., and Hirao, K. (2004). A Long-Range-Corrected Time-dependent Density Functional Theory. *J. Chem. Phys.* 120 (18), 8425–8433. doi:10.1063/1.1688752

Ullah, F., Kosar, N., Ali, A., MariaMahmood, T., Mahmood, T., and Ayub, K. (2020). Design of Novel Inorganic Alkaline Earth Metal Doped Aluminum Nitride Complexes $(AEM@Al_{12}N_{12})$ with High Chemical Stability, Improved Electronic Properties and Large Nonlinear Optical Response. *Optik* 207, 163792. doi:10.1016/j.ijleo.2019.163792

Wang, J.-J., Zhou, Z.-J., Bai, Y., Liu, Z.-B., Li, Y., Wu, D., et al. (2012). The Interaction between Superalkalis ($M_3O$, M = Na, K) and a $C_{20}F_{20}$ Cage Forming Superalkali Electride Salt Molecules with Excess Electrons inside the $C_{20}F_{20}$ Cage: Dramatic Superalkali Effect on the Nonlinear Optical Property. *J. Mat. Chem.* 22 (19), 9652–9657. doi:10.1039/C2JM15405F

Wang, R., Zhang, D., and Liu, C. (2005). Theoretical Prediction of a Novel Inorganic Fullerene-like Family of Silicon-Carbon Materials. *Chem. Phys. Lett.* 411 (4), 333–338. doi:10.1016/j.cplett.2005.06.055

Wang, S.-J., Wang, Y.-F., and Cai, C. (2015). Multidecker Sandwich Cluster $V_nBen_{n+1}$(n= 1, 2, 3, 4) as a Polarizable Bridge for Designing 1D Second-Order NLO Chromophore: Metal−π Sandwich Multilayer Structure as a Particular Charge-Transfer Axis for Constructing Multidimensional NLO Molecules. *J. Phys. Chem. C* 119 (28), 16256–16262. doi:10.1021/acs.jpcc.5b04656

Wang, X.-B., Ding, C.-F., and Wang, L.-S. (1999). High Resolution Photoelectron Spectroscopy of $C_{60}^-$Anions and Accurate Determination of the Electron Affinity of $C_{60}$. *J. Chem. Phys.* 110 (17), 8217–8220. doi:10.1063/1.478732

Wu, H.-Q., Xu, H.-L., Sun, S.-L., and Su, Z.-M. (2014). Li Doped Effect of through Novel Noncovalent Charge Transfer on Nonlinear Optical Properties. *Dyes Pigments* 106, 7–13. doi:10.1016/j.dyepig.2014.01.031

Wu, H.-S., Zhang, F.-Q., Xu, X.-H., Zhang, C.-J., and Jiao, H. (2003). Geometric and Energetic Aspects of Aluminum Nitride Cages. *J. Phys. Chem. A* 107 (1), 204–209. doi:10.1021/jp027300i

Xiao, D., Bulat, F. A., Yang, W., and Beratan, D. N. (2008). A Donor−Nanotube Paradigm for Nonlinear Optical Materials. *Nano Lett.* 8 (9), 2814–2818. doi:10.1021/nl801388z

Xu, H.-L., Li, Z.-R., Wu, D., Ma, F., Li, Z.-J., and Gu, F. L. (2009). Lithiation and Li-Doped Effects of [5]Cyclacene on the Static First Hyperpolarizability. *J. Phys. Chem. C* 113 (12), 4984–4986. doi:10.1021/jp806864w

Xu, H.-L., Li, Z.-R., Wu, D., Wang, B.-Q., Li, Y., Gu, F. L., et al. (2007). Structures and Large NLO Responses of New Electrides: Li-Doped Fluorocarbon Chain. *J. Am. Chem. Soc.* 129 (10), 2967–2970. doi:10.1021/ja068038k

Xu, X., Hu, C.-L., Kong, F., Zhang, J.-H., Mao, J.-G., and Sun, J. (2013). $Cs2GeB_4O_9$: a New Second-Order Nonlinear-Optical Crystal. *Inorg. Chem.* 52 (10), 5831–5837. doi:10.1021/ic302774h

Yanai, T., Tew, D. P., and Handy, N. C. (2004). A New Hybrid Exchange-Correlation Functional Using the Coulomb-Attenuating Method (CAM-B3lyp). *Chem. Phys. Lett.* 393 (1), 51–57. doi:10.1016/j.cplett.2004.06.011

Yang, Z., Shi, L., Chen, L., Gu, Y., Cai, P., Zhao, A., et al. (2005). Synthesis, Characterization and Properties of Novel BN Nanocages from a Single-Source Precursor. *Chem. Phys. Lett.* 405 (1), 229–233. doi:10.1016/j.cplett.2005.02.041

Yu, G., Zhao, X., Niu, M., Huang, X., Zhang, H., and Chen, W. (2013). Constructing a Mixed π-conjugated Bridge: a Simple and Effective Approach to Realize a Large First Hyperpolarizability in Carbon Nanotube-Based Systems. *J. Mat. Chem. C* 1 (24), 3833–3841. doi:10.1039/c3tc00022b

Zhang, D., and Zhang, R. Q. (2005). Geometrical Structures and Electronic Properties of AlN Fullerenes: A Comparative Theoretical Study of AlN Fullerenes with BN and C Fullerenes. *J. Mat. Chem.* 15 (29), 3034–3038. doi:10.1039/B503724G

Zhang, Q., Chung, I., Jang, J. I., Ketterson, J. B., and Kanatzidis, M. G. (2009). Chalcogenide Chemistry in Ionic Liquids: Nonlinear Optical Wave-Mixing Properties of the Double-Cubane Compound $[Sb7S8Br_2](AlCl_4)_3$. *J. Am. Chem. Soc.* 131 (29), 9896–9897. doi:10.1021/ja903881m

Zhang, T.-G., Zhao, Y., Asselberghs, I., Persoons, A., Clays, K., and Therien, M. J. (2005). Design, Synthesis, Linear, and Nonlinear Optical Properties of Conjugated (Porphinato)Zinc(II)-Based Donor−Acceptor Chromophores Featuring Nitrothiophenyl and Nitrooligothiophenyl Electron-Accepting Moieties. *J. Am. Chem. Soc.* 127 (27), 9710–9720. doi:10.1021/ja0402553

Zhong, R.-L., Xu, H.-L., Li, Z.-R., and Su, Z.-M. (2015). Role of Excess Electrons in Nonlinear Optical Response. *J. Phys. Chem. Lett.* 6 (4), 612–619. doi:10.1021/jz502588x

Zhong, R.-L., Xu, H.-L., Muhammad, S., Zhang, J., and Su, Z.-M. (2012a). The Stability and Nonlinear Optical Properties: Encapsulation of an Excess Electron Compound LiCN···Li within Boron Nitride Nanotubes. *J. Mat. Chem.* 22 (5), 2196–2202. doi:10.1039/C1JM14358A

Zhong, R.-L., Xu, H.-L., Sun, S.-L., Qiu, Y.-Q., and Su, Z.-M. (2012b). The Excess Electron in a Boron Nitride Nanotube: Pyramidal NBO Charge Distribution and Remarkable First Hyperpolarizability. *Chem. Eur. J.* 18 (36), 11350–11355. doi:10.1002/chem.201201570

Zhou, Z.-J., Yu, G.-T., Ma, F., Huang, X.-R., Wu, Z.-J., and Li, Z.-R. (2014). Theoretical Investigation on Nonlinear Optical Properties of Carbon Nanotubes with Stone-Wales Defect Rings. *J. Mat. Chem. C* 2 (2), 306–311. doi:10.1039/c3tc31904k

Zope, R. R., and Dunlap, B. I. (2005). Electronic Structure of Fullerenelike Cages and Finite Nanotubes of Aluminum Nitride. *Phys. Rev. B* 72 (4), 045439. doi:10.1103/PhysRevB.72.045439

**Conflict of Interest:** The authors declare that the research was conducted in the absence of any commercial or financial relationships that could be construed as a potential conflict of interest.

**Publisher's Note:** All claims expressed in this article are solely those of the authors and do not necessarily represent those of their affiliated organizations, or those of the publisher, the editors, and the reviewers. Any product that may be evaluated in this article, or claim that may be made by its manufacturer, is not guaranteed or endorsed by the publisher.

frontiers | Frontiers in Chemistry

ORIGINAL RESEARCH
published: 01 July 2022
doi: 10.3389/fchem.2022.936936

# Design of a Novel Series of Hetero-Binuclear Superhalogen Anions $MM'X_4^-$ (M = Li, Na; M′ = Be, Mg, Ca; X = Cl, Br)

*Hui Yang[1], Hui-Min He[2], Ning Li[1]*, Shang Jiang[1], Min-Jun Pang[1], Ying Li[3] and Jian-Guo Zhao[1]**

[1]Institute of Carbon Materials Science, Shanxi Datong University, Datong, China, [2]Physics Department, Taiyuan Normal University, Taiyuan, China, [3]Institute of Theoretical Chemistry, College of Chemistry, Jilin University, Changchun, China

A series of hetero-binuclear superatom motifs involving chloride/bromide ligands, that is, $MM'X_4^-$ (M = Li, Na; M′ = Be, Mg, Ca; X = Cl, Br) anions, have been characterized by using many-body perturbation theory calculations. Large vertical electron detachment energies (VDEs, 5.470–6.799 eV) confirm the superhalogen identity of these anions. A larger VDE value can be obtained by introducing small M or large M′ central atoms and small halogen ligand atoms. Thus, one isomer of $LiCaCl_4^-$ possesses the largest VDE value. Besides, when the extra electron is shared by all ligand atoms or three bridging ligand atoms, the isomers have relatively larger VDE values.

**Keywords: superhalogen, chloride or bromine ligands, binuclear, vertical electron detachment energy, theoretical calculation**

OPEN ACCESS

***Edited by:***
*Iwona Anusiewicz,*
*University of Gdansk, Poland*

***Reviewed by:***
*Jakub Brzeski,*
*University of Pittsburgh, United States*
*Shi-Bo Cheng,*
*Shandong University, China*

****Correspondence:***
*Ning Li*
*lin224@nenu.edu.cn*
*Jian-Guo Zhao*
*jgzhaoshi@163.com*

***Specialty section:***
*This article was submitted to Physical Chemistry and Chemical Physics, a section of the journal Frontiers in Chemistry*

***Received:*** *05 May 2022*
***Accepted:*** *07 June 2022*
***Published:*** *01 July 2022*

***Citation:***
*Yang H, He H-M, Li N, Jiang S, Pang M-J, Li Y and Zhao J-G (2022) Design of a Novel Series of Hetero-Binuclear Superhalogen Anions $MM'X_4^-$ (M = Li, Na; M′ = Be, Mg, Ca; X = Cl, Br). Front. Chem. 10:936936. doi: 10.3389/fchem.2022.936936*

## INTRODUCTION

Superhalogens are unusual molecules possessing higher electron affinity (EA) than those of any halogen atom (Gutsev and Boldyrev, 1981). They were first proposed by Gutsev and Boldyrev in 1981 and verified by a variety of theoretical chemical methods (Gutsev and Boldyrev, 1981). Meanwhile, a new class of highly stable anions (superhalogen anions) were also reported. Now, superhalogen anions have been proved to possess very large vertical electron detachment energies (VDEs) (Anusiewicz et al., 2003; Koirala et al., 2010; Yang et al., 2017; Li et al., 2019; Li et al., 2020; Zhao et al., 2020), even approaching 14 eV in certain systems (Freza and Skurski, 2010). Moreover, it is found that the superhalogen anions have much high stability, such as $BF_4^-$, $AlCl_4^-$, and $AsF_6^-$, and other superhalogen anions have been confirmed to be stable in crystalline solids or gaseous molecules.

In 1981, Gutsev and Boldyrev proposed the representative formula $MX_{k+1}$ for a class of superhalogens, in which M represents the central main group atom, K is the highest valence of M atom, and X is the halogen atom (Gutsev and Boldyrev, 1981). In 1999, the superhalogen anions $MX_2^-$ (M = Li, Na; X = Cl, Br, and I) were reported by Wang et al., and their VDE values were experimentally measured for the first time and theoretically calculated applying the outer valence Green function (OVGF) method, which are consistent with each other well (Wang et al., 1999). Shortly afterward, the EA value of the $BO_2$ superhalogen (Zhai et al., 2007) and the VDE value of the $MX_3^-$ (M = Be, Mg, Ca; X = Cl, Br) superhalogen anion (Elliott et al., 2005) were determined by the same experimental means. During subsequent studies on superhalogens and their corresponding anions, the central atom M of $MX_{k+1}$ formula was no longer limited to the main group metal atoms

(Anusiewicz et al., 2003; Elliott et al., 2005), and the transition metal atoms (Gutsev et al., 1999; Gutsev et al., 2001; Yang et al., 2003), coinage metal atoms (Feng et al., 2011; Lu et al., 2019), and nonmetal atoms (Arnold et al., 2002) could act as central atoms to construct superhalogens. In addition, the researchers found that increasing the number of central atoms benefits the dispersion of extra negative charges without increasing the repulsion between ligands. Therefore, some binuclear/multinuclear superhalogen anions have been proposed by experimental synthesis or theoretical prediction (Anusiewicz and Skurski, 2007; Anusiewicz, 2008; Czapla, 2017; Yang et al., 2017; Yang et al., 2018).

Besides, it is realized that halogen atoms are not the necessary units for the construction of superhalogens. In recent years, the ligands of superhalogens have been extended from halogen atoms to oxygen atoms (Gutsev et al., 1999; Zhai et al., 2007), acid functional groups (Anusiewicz, 2009b), various monovalent groups (Smuczynska and Skurski, 2009), nine-electron ligands (Sikorska et al., 2011), hydroxyl groups (Świerszcz and Anusiewicz, 2011), and electrophilic substituents (Anusiewicz, 2009a). In addition, M@Nk-type superhalogens with inclusion complexes of metal (Zhai et al., 2004) and carborane cage superhalogens (Pathak et al., 2011) have also been proposed. Recently, a new class of cluster was designed in which the central atom was modified by superhalogen ligands replacing the halogen ligands. These clusters have higher EAs than their superhalogen ligands; thus, they are termed "hyperhalogen" (Willis et al., 2010). Subsequently, many hyperhalogens with various geometries of superhalogen ligands have been proposed (Paduani et al., 2011; Gutsev et al., 2012; Sun et al., 2015; Sun et al., 2016; Yang et al., 2021; Dong et al., 2022).

Superhalogens play an important role in chemistry given the strong oxidation capability. For example, they can be used as capable oxidants to oxidize substances that have relatively high ionization potentials (e.g., $O_2$ (Bartlett and Lohmann, 1962), noble gas atom (Bartlett, 1962), and $(H_2O)n$ clusters (Marchaj et al., 2013)). They can also be used to synthesize and prepare noble gas compounds (Saha et al., 2018; Chang et al., 2019), supersalts (Giri et al., 2014a), ion battery electrolytes (Giri et al., 2014b), ionic liquids (Srivastava et al., 2021), liquid crystalline molecules (Srivastava, 2021), solar cells (Kim et al., 2022), and so on. Therefore, exploring various new species classified as superhalogens and studying their structures, stability, and properties has become a significant and attractive research topic in recent years.

To the best of our knowledge, most hitherto proposed superhalogens are mono- or homo-nuclear. The hetero-nuclear superhalogens involving different central atoms, however, have received very little attention. The investigation on the influence of different ligands on hetero-nuclear superhalogen properties, however, has not been reported yet. In this research, we aim to design a new class of superhalogen anions with two different central atoms using chloride or bromine atoms as ligands. Consequently, the $MM'X_4^-$ (M = Li, Na; M′ = Be, Mg, Ca; X = Cl, Br) anions have been proposed and systematically investigated. The considerable VDE values of these anions confirm their superhalogen identity. The geometric features and relative stability of these anions were analyzed. Meanwhile, the correlations between their VDEs and structural features, ligand and central atoms, and extra electron distribution are also revealed. The present investigation predicts a new member of superhalogens and conduces to the development of new strong oxidizing agents.

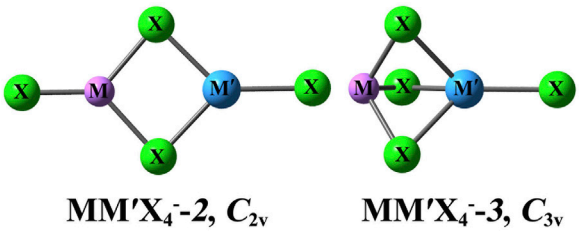


**FIGURE 1 |** Optimized structures of the $MM'X_4^-$ anions at the MP2/6–311+G (3df) level. Color legend: green for X atom, light purple for M atom, and blue for M′ atom.

## COMPUTATIONAL DETAILS

Initially, the structures of the $MM'X_4^-$ (M = Li, Na; M′ = Be, Mg, Ca; X = Cl, Br) anions were built by considering all the possible connection between M, M′, and X atoms. Then, all the constructed structures of anions were optimized using the Møller–Plesset perturbation method (MP2) (Møller and Plesset, 1934) together with the 6–311+G (3df) basis set (Yang et al., 2017; Yang et al., 2018). Meanwhile, frequency analysis was performed at the same computational level to ensure that the obtained structures are stable on potential energy surfaces without imaginary frequency. Natural bond orbital (NBO) (Reed et al., 1985) and single-point energy calculations were carried out at the same level.

The vertical electron detachment energies (VDEs) of the $MM'X_4^-$ anions were calculated applying the outer valence Green function (OVGF) approximation (Cederbaum, 1975) with the 6–311+G (3df) basis set. The smallest pole strength (PS) in our study is 0.90, justifying the validity of the OVGF method (Zakrzewski et al., 1996).

The above-mentioned calculations were performed using the GAUSSIAN 16 program package (Frisch et al., 2016). The plots of molecular structures and orbitals were generated with the GaussView program (Dennington et al., 2016).

## RESULTS AND DISCUSSION

### Geometrical Structures and Relative Stability

The optimized geometries of $MM'X_4^-$anions are depicted schematically in **Figure 1**. The relative energies, the lowest vibrational frequencies, bond lengths, and angles are listed in **Tables 1**, **2**. As shown in the figure, each $MM'X_4^-$ anion has two types of structures, that is, central atoms M and M′ are connected

**TABLE 1 |** Relative energies $E_{rel}$ (kcal/mol), the lowest vibrational frequencies $\upsilon$ ($cm^{-1}$), total NBO charges on the MCl subunit (|e|), vertical detachment energies VDE (eV), bond lengths (Å), and select bond angles (degree) of the $MM'Cl_4^-$ (M = Li, Na; M′ = Be, Mg, Ca) anions.

| *Isomer* | Symmetry | $E_{rel}$ | $\upsilon$ | Q[a] | VDE | $Cl_t$-M | M-$Cl_b$ | $Cl_b$-M′ | M′-$Cl_t$' | ∠$Cl_b$M'$Cl_t$' |
|---|---|---|---|---|---|---|---|---|---|---|
| $LiBeCl_4^-$-***2*** | $C_{2v}$ | 0.00 | 24 | –0.073 | 6.240 | 2.146 | 2.427 | 1.940 | 1.888 | 123.6 |
| $LiBeCl_4^-$-***3*** | $C_{3v}$ | 9.09 | 127 | 0.049 | 6.275 | | 2.292 | 2.197 | 1.923 | 117.6 |
| $LiMgCl_4^-$-***3*** | $C_{3v}$ | 0.00 | 86 | –0.017 | 6.700 | | 2.325 | 2.425 | 2.266 | 124.5 |
| $LiMgCl_4^-$-***2*** | $C_{2v}$ | 4.48 | 21 | –0.075 | 6.180 | 2.150 | 2.459 | 2.289 | 2.242 | 129.3 |
| $LiCaCl_4^-$-***3*** | $C_{3v}$ | 0.00 | 65 | –0.066 | 6.799 | | 2.327 | 2.691 | 2.559 | 129.7 |
| $LiCaCl_4^-$-***2*** | $C_{2v}$ | 10.92 | 20 | –0.080 | 6.042 | 2.156 | 2.447 | 2.566 | 2.536 | 134.4 |
| $NaBeCl_4^-$-***2*** | $C_{2v}$ | 0.00 | 22 | –0.039 | 6.116 | 2.503 | 2.772 | 1.940 | 1.891 | 122.4 |
| $NaBeCl_4^-$-***3*** | $C_{3v}$ | 10.36 | 113 | 0.088 | 5.946 | | 2.620 | 2.103 | 1.940 | 115.0 |
| $NaMgCl_4^-$-***3*** | $C_{3v}$ | 0.00 | 79 | 0.025 | 6.573 | | 2.657 | 2.420 | 2.277 | 121.0 |
| $NaMgCl_4^-$-***2*** | $C_{2v}$ | 4.42 | 21 | –0.038 | 6.081 | 2.504 | 2.805 | 2.291 | 2.242 | 127.4 |
| $NaCaCl_4^-$-***3*** | $C_{3v}$ | 0.00 | 63 | 0.003 | 6.786 | | 2.664 | 2.688 | 2.565 | 125.8 |
| $NaCaCl_4^-$-***2*** | $C_{2v}$ | 11.12 | 19 | –0.040 | 5.998 | 2.509 | 2.804 | 2.570 | 2.534 | 131.8 |

[a]*$Cl_tM$ for isomer $MM'Cl_4^-$-**2** and $MCl_b$, for $MM'Cl_4^-$-**3**.*
*Italics values represents that the number of bridging X atoms.*

**TABLE 2 |** Relative energies $E_{rel}$ (kcal/mol), the lowest vibrational frequencies $\upsilon$ ($cm^{-1}$), total NBO charges on MBr subunit (|e|), vertical detachment energies VDE (eV), bond lengths (Å), and select bond angles (degree) of the $MM'Br_4^-$ (M = Li, Na; M′ = Be, Mg, Ca) anions.

| *Isomer* | Symmetry | $E_{rel}$ | $\upsilon$ | Q[a] | VDE | $Br_t$-M | M-$Br_b$ | $Br_b$-M′ | M′-$br_t$' | ∠$Br_b$M'$Br_t$' |
|---|---|---|---|---|---|---|---|---|---|---|
| $LiBeBr_4^-$-***2*** | $C_{2v}$ | 0.00 | 14 | –0.087 | 5.792 | 2.312 | 2.584 | 2.103 | 2.051 | 123.2 |
| $LiBeBr_4^-$-***3*** | $C_{3v}$ | 7.93 | 77 | 0.060 | 5.795 | | 2.452 | 2.275 | 2.089 | 116.8 |
| $LiMgBr_4^-$-***3*** | $C_{3v}$ | 0.00 | 53 | –0.020 | 6.174 | | 2.491 | 2.592 | 2.423 | 123.5 |
| $LiMgBr_4^-$-***2*** | $C_{2v}$ | 3.88 | 13 | –0.089 | 5.750 | 2.313 | 2.616 | 2.448 | 2.398 | 128.5 |
| $LiCaBr_4^-$-***3*** | $C_{3v}$ | 0.00 | 42 | –0.002 | 6.296 | | 2.492 | 2.852 | 2.713 | 128.5 |
| $LiCaBr_4^-$-***2*** | $C_{2v}$ | 10.36 | 12 | –0.100 | 5.650 | 2.317 | 2.609 | 2.721 | 2.690 | 133.1 |
| $NaBeBr_4^-$-***2*** | $C_{2v}$ | 0.00 | 13 | –0.046 | 5.730 | 2.658 | 2.930 | 2.103 | 2.054 | 122.1 |
| $NaBeBr_4^-$-***3*** | $C_{3v}$ | 9.50 | 73 | 0.106 | 5.470 | | 2.777 | 2.272 | 2.105 | 114.4 |
| $NaMgBr_4^-$-***3*** | $C_{3v}$ | 0.00 | 50 | 0.032 | 6.080 | | 2.817 | 2.587 | 2.434 | 120.1 |
| $NaMgBr_4^-$-***2*** | $C_{2v}$ | 3.77 | 13 | –0.048 | 5.707 | 2.658 | 2.962 | 2.449 | 2.399 | 126.5 |
| $NaCaBr_4^-$-***3*** | $C_{3v}$ | 0.00 | 40 | 0.001 | 6.322 | | 2.822 | 2.850 | 2.718 | 124.8 |
| $NaCaBr_4^-$-***2*** | $C_{2v}$ | 10.27 | 12 | –0.051 | 5.640 | 2.662 | 2.961 | 2.726 | 2.687 | 130.8 |

[a]*$Br_tM$ for isomer $MM'Br_4^-$-**2** and $MBr_b$, for $MM'Br_4^-$-**3**.*
*Italics values represents that the number of bridging X atoms.*

by two or three bridging X atoms. Notably, these two structures are also presented in the superhalogen anions with F ligands (Yang et al., 2017). Unlike $MM'F_4^-$ anions (Yang et al., 2017), the structures involving one bridging ligand atom are not stable, which turn to the above two types of structures after optimization. In terms of the number of bridging X atoms, the isomers of $MM'X_4^-$ are termed $MM'X_4^-$-***2*** and $MM'X_4^-$-***3***, respectively. For the sake of convenience, the terminal X atoms that bind with M and M′ atoms are named $X_t$ and $X_t$', respectively, and the bridging X atom that connects M and M′ atoms is named $X_b$.

It can be seen in **Figure 1** that the $MM'Cl_4^-$-***2*** and $MM'Cl_4^-$-***3*** isomers possess planar and three-dimensional structures with $C_{2v}$ and $C_{3v}$ symmetries, respectively. From the data in **Table 1**, it is found that for $MM'Cl_4^-$-***2*** and $MM'Cl_4^-$-***3*** isomers, when M′ atom varies from Be to Ca, the $Cl_t$-M and M-$Cl_b$ bond lengths change very little, while the ∠$Cl_b$M'$Cl_t$ angle showed a tendency of increasing; for example, the orders of ∠$Cl_b$M'$Cl_t$ angle in $NaM'Cl_4^-$-***2*** and $NaM'Cl_4^-$-***3*** are 122.4° < 127.4° < 131.8° and 115.0° < 121.0° < 125.8° with varying M′ atoms, respectively. Thus, the $MM'Cl_4^-$-***2*** and $MM'Cl_4^-$-***3*** structures tend to elongate along the M-M′ axis with the increasing radius of M′ atoms. Besides, the $Cl_t$-M bond is shorter than the M-$Cl_b$ bond in $MM'Cl_4^-$-***2*** isomers. For instance, the $Cl_t$-Na bonds are about 2.80 Å, while the Na-$Cl_b$ bonds are 2.50 Å in $NaM'Cl_4^-$-***2*** isomers. On the other hand, when the M atom goes from Li to Na, the $Cl_b$-M′ and M′-$Cl_t$' bond lengths also show minor difference in $MM'Cl_4^-$ anions, but the ∠$Cl_b$M'$Cl_t$' angles show a decrease, e.g., the ∠$Cl_b$M'$Cl_t$' angles of $LiBeCl_4^-$-***2*** and $LiBeCl_4^-$-***3*** are 1.4 and 1.6° larger than that of the corresponding $NaBeCl_4^-$-***2*** and $NaBeCl_4^-$-***3***, respectively. In addition, the total NBO charges of $Cl_tM$ subunits are in the range of -0.080–0.088|e|, which are close to zero (see **Table 1**); consequently, the total NBO charges of $M'Cl_3$ subunits approximate -1. In this sense, the $MM'Cl_4^-$ structures can be regarded as a combination of an MCl molecule and a superhalogen anion $M'Cl_3^-$.

$MM'Br_4^-$ series show similar structural characteristics with $MM'Cl_4^-$ anions. From the data in **Tables 1**, **2**, it is noticed that ∠$X_b$M'$X_t$' angles of $MM'Cl_4^-$ anions are always larger than that of the corresponding $MM'Br_4^-$ anions; for example, the ∠$Cl_b$M'$Cl_t$' angles of $NaMgCl_4^-$-***3*** and $NaMgCl_4^-$-***2*** are 121.0° and 127.4°, respectively, which are larger than the

**TABLE 3 |** The largest vertical detachment energies VDE (eV) of superhalogen anions $MM'X_4^-$ (M = Li, Na; M′ = Be, Mg, Ca, X = Cl, Br) and $M'X_3^-$ (M′ = Be, Mg, Ca, X = Cl, Br).

| *anion* | VDE | *anion* | VDE | *anion* | VDE |
|---|---|---|---|---|---|
| $LiBeCl_4^-$ | 6.275 | $NaBeCl_4^-$ | 6.116 | $BeCl_3^-$ | 6.184 |
| $LiMgCl_4^-$ | 6.700 | $NaMgCl_4^-$ | 6.573 | $MgCl_3^-$ | 6.685 |
| $LiCaCl_4^-$ | 6.799 | $NaCaCl_4^-$ | 6.786 | $CaCl_3^-$ | 6.741 |
| $LiBeBr_4^-$ | 5.795 | $NaBeBr_4^-$ | 5.730 | $BeBr_3^-$ | 5.643 |
| $LiMgBr_4^-$ | 6.174 | $NaMgBr_4^-$ | 6.080 | $MgBr_3^-$ | 6.140 |
| $LiCaBr_4^-$ | 6.296 | $NaCaBr_4^-$ | 6.322 | $CaBr_3^-$ | 6.243 |

$\angle Br_bM'Br_t$' angles of $NaMgBr_4^-$-***3*** (120.1°) and $NaMgBr_4^-$-***2*** (126.5°), respectively.

It is reported that the isomers could exhibit higher stability with more bridging ligands in the previous studies on the dual-nuclear superhalogen anions with F ligands, such as homonuclear $Mg_2F_5^-$(Anusiewicz and Skurski, 2007) and heteronuclear ones $NaM'F_4^-$(M' = Mg, Ca) (Yang et al., 2017). $MM'X_4^-$ anions also follow this rule except the $MBeX_4^-$ series. However, $MBeX_4^-$ anions show a reverse trend; that is, structure 2 is more stable than structure *3*. In other words, Be atoms are more likely to bond with three ligands than four ligands. This may be due to the smaller atomic radius of the central Be atom, the three bridging ligands are more crowded in structure 3 of $MBeX_4^-$ anions than in structure 3 of $MMgX_4^-$ and $MCaX_4^-$. This can be confirmed by the shorter $Cl_b$-$Cl_b$ and $Br_b$-$Br_b$ distance in structures 3 of $MBeX_4^-$ than $MMgX_4^-$ and $MCaX_4^-$; for example, the $Cl_b$-$Cl_b$ and $Br_b$-$Br_b$ distances in $LiBeCl_4^-$-*3* and $LiBeBr_4^-$-*3* are 0.226 Å and 0.229 Å shorter than that in $LiMgCl_4^-$-***3*** and $LiMgBr_4^-$-***3***, respectively. Thereby, $MBeX_4^-$-***3*** is less stable than the $MBeX_4^-$-***2***.

## Vertical Electron Detachment Energies (VDEs)

The VDE values of $MM'X_4^-$ anions are gathered in **Tables 1**, **2**. As one can notice, all anions have considerable VDE values (5.470–6.799 eV) exceeding the electron affinity of the Cl atom; thus undoubtedly, these anions can be identified as superhalogen anions. In addition, it is found that the factors affecting the VDE values of these studied anions were as follows:

(1) When the M atom varies from the Li atom to Na atom, the VDE values of the studied anions show a tendency of decreasing in similar structures. For example, the VDE values of the isomers $LiMgCl_4^-$-***3*** and $LiMgCl_4^-$-***2*** are greater than those of $NaMgCl_4^-$-***3*** and $NaMgCl_4^-$-***2***, respectively. However, the only one exception is the VDE values of isomers $LiCaBr_4^-$-***3*** and $NaCaBr_4^-$-***3.*** This is probably due to the different extra electron distribution of these two isomers, which will be discussed in the following. Therefore, the hetero-binuclear superhalogen anions with large VDE values could be constructed by introducing small alkali metal atoms into the system. It is worth noting that the same trend was found for the other hetero-binuclear anions with the F atom, cyanide, and isocyanide as ligands (Yang et al., 2017; Yang et al., 2018).

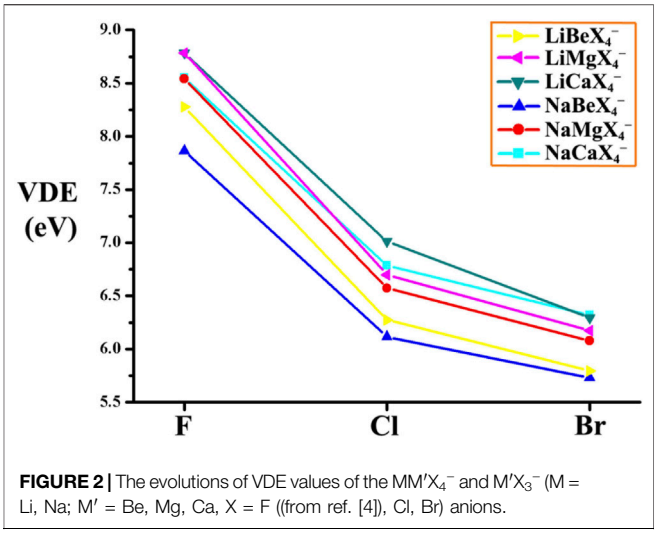


**FIGURE 2 |** The evolutions of VDE values of the $MM'X_4^-$ and $M'X_3^-$ (M = Li, Na; M′ = Be, Mg, Ca, X = F ((from ref. [4]), Cl, Br) anions.

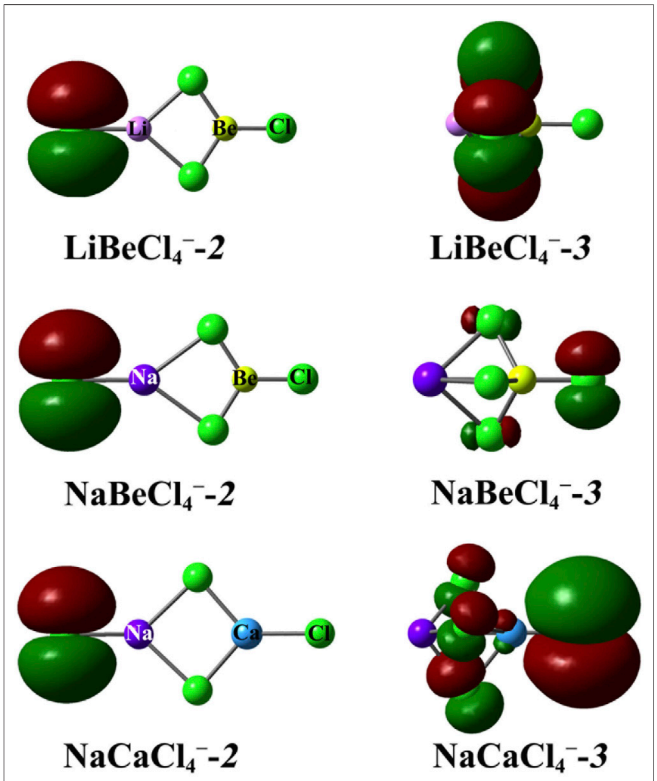


**FIGURE 3 |** HOMO orbitals of superhalogen anions $LiBeCl_4^-$, $NaBeCl_4^-$, and $NaCaCl_4^-$.Color legend: green for Cl atom, light purple for Li atom, dark purple for Na atom, and blue for Ca atom.

(2) The largest VDE values for each $MM'X_4^-$ anions are presented in **Table 3**. From the table, the VDE values increase in the order: $MBeX_4^-$→$MMgX_4^-$→$MCaX_4^-$. Hence, the hetero-binuclear superhalogen anion $MM'X_4^-$ could possess a larger VDE value by involving larger alkaline earth metal atoms. Note that it also holds true for

the superhalogen anions with other ligands (Yang et al., 2017; Yang et al., 2018).

As pointed out earlier, the $MM'X_4^-$ anions can be regarded as $MX\ (M'X_3)^-$; thus, the comparison between $MM'X_4^-$ anions and their corresponding mononuclear superhalogen anions $M'X_3^-$ is also necessary. For this reason, the VDE values of $M'X_3^-$ (X = Cl, Br) anions were also calculated at the same level and are listed in **Table 3** as well. From the table, the VDE values of mononuclear anions $M'X_3^-$ also increase from $BeX_3^-$ to $CaX_3^-$. Besides, the mononuclear anions $M'X_3^-$ possess lower VDE values than their corresponding hetero-nuclear anions $MM'X_4^-$ (except for $NaBeCl_4^-$ and $NaMgX_4^-$ series). So again, the superhalogen anions could gain larger VDE values by increasing the number of central atoms.

(3) The relationship between the VDE values and the ligand atoms is plotted in **Figure 2**. The six curves show similar varying trends, that is, the largest VDE values of each $MM'X_4^-$ (X = F (Yang et al., 2017), Cl, Br) species show a decreasing order: $MM'F_4^- > MM'Cl_4^- > MM'Br_4^-$. This may be attributed to the different electronegativity of X atoms. To be specific, the F atom possesses larger electronegativity and stronger electron-accepting ability than Cl and Br atoms, which is more beneficial for the anions to bind with the extra electron. Thereby, the larger electronegativity the ligand atom possesses, the higher VDE value the $MM'X_4^-$ anion has.

(4) For the two isomers of $LiM'X_4^-$, the VDE values of $LiM'X_4^-$-***3*** are always larger than those of $LiM'X_4^-$-*2*. This is probably due to the fact that the extra electron distribution in two isomers is different. To analyze this clearly, the highest occupied molecular orbitals (HOMOs) of some representative $MM'X_4^-$ isomers are depicted in **Figure 3**. As can be seen from the figure, the extra electron is confined to a single $X_t$ atom in $LiBeCl_4^-$-***2***, while localized on the three bridging $X_b$ atoms in $LiBeCl_4^-$-***3,*** which is a benefit for the extra negative charge dispersion, and thus, $LiBeCl_4^-$-***3*** possesses a larger VDE value. For $NaBeX_4^-$ anions, the extra electrons of two isomers are all distributed on the terminal X atom. Interestingly, the isomer $NaBeX_4^-$-***2*** in which the extra electron goes on $X_t$ atom has a higher VDE value than isomer $NaBeX_4^-$***3***, which goes on the $X_t$' atom (see **Figure 3**). As to $NaMgX_4^-$ and $NaCaX_4^-$ species, the situation is similar to that of the $LiM'X_4^-$ anions. However, unlike $LiM'X_4^-$-***3*** and $NaMgX_4^-$-***3***, the extra electron is shared by all X ligand atoms instead of three $X_b$ ligands in $NaCaX_4^-$-***3***, which leads to the extra negative charge being more evenly distributed (see **Figure 3**), and, hence, a relatively larger VDE values for these isomers. This may also explain why $NaCaBr_4^-$-***3*** exhibits larger VDE values than $LiCaBr_4^-$-***3.*** Therefore, the extra electron distribution is an important factor affecting the VDE values of the hetero-binuclear superhalogen anions.

## CONCLUSION

Our systematic investigation of the $MM'X_4^-$ (M = Li, Na; M′ = Be, Mg, Ca; X = Cl, Br) species has theoretically proposed a series of hetero-binuclear superhalogen anions. The results show that these heteronuclear superhalogen anions could gain larger VDE values by involving a smaller alkali metal atom M, a larger alkaline earth metal atom M′, and a higher electronegative ligand atom X. Thereby, of all the anions studied, an isomer of $LiCaCl_4^-$ anions possesses the largest VDE value (6.799 eV). Moreover, the extra electron distribution is a very influential factor in the VDE values of structural isomers. For the $NaBeX_4^-$ anions, the isomers have larger VDE values when the extra electron is distributed on the terminal $X_t$ ligand atom instead of the $X_t$' ligand atom. For the other anions, the isomers possess larger VDE values when the extra electron is shared by all ligand atoms or three bridging ligand atoms.

## DATA AVAILABILITY STATEMENT

The original contributions presented in the study are included in the article/supplementary material; further inquiries can be directed to the corresponding authors.

## AUTHOR CONTRIBUTIONS

All authors listed have made a substantial, direct, and intellectual contribution to the work and approved it for publication.

## FUNDING

This work was supported by the Scientific and Technological Innovation Programs of Higher Education Institutions in Shanxi (2021L370, 2020L0507, and 2020L0516), the National Natural Science Foundation of China (Grant Nos. 21573089 and 51872057), the Doctoral Scientific Foundation Research Foundation of Shanxi Datong University (Grant Nos. 2019-B-11 and 2017-B-04), and the Basic Research Project Fund of Shanxi Province (20210302124491 and 20210302123341).

## REFERENCES

Anusiewicz, I., and Skurski, P. (2007). Unusual Structures of $Mg_2F_5^-$ Superhalogen Anion. *Chem. Phys. Lett.* 440, 41–44. doi:10.1016/j.cplett.2007.04.016

Anusiewicz, I., Sobczyk, M., Dąbkowska, I., and Skurski, P. (2003). An Ab Initio Study on MgX3− and CaX3− Superhalogen Anions (X=F, Cl, Br). *Chem. Phys.* 291, 171–180. doi:10.1016/s0301-0104(03)00208-8

Anusiewicz, I. (2008). Mg2Cl5 - and Mg3Cl7 - Superhalogen Anions. *Aust. J. Chem.* 61, 712–717. doi:10.1071/ch08212

Anusiewicz, I. (2009a). Electrophilic Substituents as Ligands in Superhalogen Anions. *J. Phys. Chem. A* 113, 6511–6516. doi:10.1021/jp901910q

Anusiewicz, I. (2009b). Superhalogen Anions Utilizing Acidic Functional Groups as Ligands. *J. Phys. Chem. A* 113, 11429–11434. doi:10.1021/jp907246w

Arnold, S. T., Miller, T. M., and Viggiano, A. A. (2002). A Theoretical Study of High Electron Affinity Sulfur Oxyfluorides: SO3F, SO2F3, and SOF5.

*Int. J. Mass Spectrom.* 218, 207–215. doi:10.1016/s1387-3806(02)00713-3

Bartlett, N., and Lohmann, D. H. (1962). Fluorides of the Noble Metals. Part II. Dioxygenyl Hexafluoroplatinate(V), O2 +[PtF6]? *J. Chem. Soc.* 0, 5253–5261. doi:10.1039/jr9620005253

Bartlett, N. (1962). Xenon Hexafluoroplatinate (V) $Xe^{+}[PtF_6]^{-}$. *Chem. Soc.* 218.

Cederbaum, L. S. (1975). One-body Green's Function for Atoms and Molecules: Theory and Application. *J. Phys. B* 8, 290–303. doi:10.1088/0022-3700/8/2/018

Chang, X.-T., Li, Y., Liu, J.-Y., Ma, H.-D., and Wu, D. (2019). Noble Gas Insertion Compounds of Hydrogenated and Lithiated Hyperhalogens. *Phys. Chem. Chem. Phys.* 21, 20156–20165. doi:10.1039/c9cp01284b

Czapla, M. (2017). Dinuclear Superhalogen Anions Containing Two Different Central Atoms. *J. Fluor. Chem.* 199, 97–102. doi:10.1016/j.jfluchem.2017.05.003

Dennington, R., Keith, T., and Millam, J. (2016). *GaussView. version 6*. Shawnee Mission, KS: Semichem Inc.

Dong, X.-X., Zhao, Y., Li, J., Wang, H., Bu, Y., and Cheng, S.-B. (2022). Dual External Field-Engineered Hyperhalogen. *J. Phys. Chem. Lett.* 13, 3942–3948. doi:10.1021/acs.jpclett.2c00916

Elliott, B. M., Koyle, E., Boldyrev, A. I., Wang, X.-B., and Wang, L.-S. (2005). MX3- Superhalogens (M = Be, Mg, Ca; X = Cl, Br): A Photoelectron Spectroscopic and Ab Initio Theoretical Study. *J. Phys. Chem. A* 109, 11560–11567. doi:10.1021/jp054036v

Feng, Y., Xu, H.-G., Zheng, W., Zhao, H., Kandalam, A. K., and Jena, P. (2011). Structures and Photoelectron Spectroscopy of Cun(BO2)m− (N, M = 1, 2) Clusters: Observation of Hyperhalogen Behavior. *J. Chem. Phys.* 134, 094309. doi:10.1063/1.3556818

Freza, S., and Skurski, P. (2010). Enormously Large (Approaching 14 eV!) Electron Binding Energies of [HnFn+1]- (N= 1-5, 7, 9, 12) Anions. *Chem. Phys. Lett.* 487, 19–23. doi:10.1016/j.cplett.2010.01.022

Frisch, M. J., Trucks, G. W., Schlegel, H. B., Scuseria, G. E., Robb, M. A., Cheeseman, J. R., et al. (2016). *GAUSSIAN 16*. Wallingford CT: Gaussian, Inc.

Giri, S., Behera, S., and Jena, P. (2014a). Superalkalis and Superhalogens as Building Blocks of Supersalts. *J. Phys. Chem. A* 118, 638–645. doi:10.1021/jp4115095

Giri, S., Behera, S., and Jena, P. (2014b). Superhalogens as Building Blocks of Halogen-free Electrolytes in Lithium-Ion Batteries. *Angew. Chem. Int. Ed.* 53, 13916–13919. doi:10.1002/anie.201408648

Gutsev, G. L., and Boldyrev, A. I. (1981). DVM-xα Calculations on the Ionization Potentials of MXk+1− Complex Anions and the Electron Affinities of MXk+1 "superhalogens". *Chem. Phys.* 56, 277–283. doi:10.1016/0301-0104(81)80150-4

Gutsev, G. L., Rao, B. K., Jena, P., Wang, X.-B., and Wang, L.-S. (1999). Origin of the Unusual Stability of MnO4−. *Chem. Phys. Lett.* 312, 598–605. doi:10.1016/s0009-2614(99)00976-8

Gutsev, G. L., Jena, P., Zhai, H.-J., and Wang, L.-S. (2001). Electronic Structure of Chromium Oxides, CrOn− and CrOn (N=1-5) from Photoelectron Spectroscopy and Density Functional Theory Calculations. *J. Chem. Phys.* 115, 7935–7944. doi:10.1063/1.1405438

Gutsev, G. L., Weatherford, C. A., Johnson, L. E., and Jena, P. (2012). Structure and Properties of the Aluminum Borates Al(BO2)n and Al(BO2)n−, (N = 1-4). *J. Comput. Chem.* 33, 416–424. doi:10.1002/jcc.21984

Kim, H., Lim, J., Sohail, M., and Nazeeruddin, M. K. (2022). Superhalogen Passivation for Efficient and Stable Perovskite Solar Cells. *Sol. RRL*, 2200013. doi:10.1002/solr.202200013

Koirala, P., Willis, M., Kiran, B., Kandalam, A. K., and Jena, P. (2010). Superhalogen Properties of Fluorinated Coinage Metal Clusters. *J. Phys. Chem. C* 114, 16018–16024. doi:10.1021/jp101807s

Li, J., Huang, H.-C., Wang, J., Zhao, Y., Chen, J., Bu, Y.-X., et al. (2019). Polymeric Tungsten Carbide Nanoclusters: Structural Evolution, Ligand Modulation, and Assembled Nanomaterials. *Nanoscale* 11, 19903–19911. doi:10.1039/c9nr05613k

Li, J., Zhao, Y., Bu, Y.-F., Chen, J., Wei, Q., and Cheng, S.-B. (2020). On the Theoretical Construction of Nb2N2-Based Superatoms by External Field Strategies. *Chem. Phys. Lett.* 754, 137709. doi:10.1016/j.cplett.2020.137709

Lu, S.-J., Wu, L.-S., and Lin, F. (2019). Structural, Bonding, and Superhalogen Properties of Au4X 4 −/0 (X = F, Cl, Br, and I) Clusters. *Theor. Chem. Acc.* 138, 51. doi:10.1007/s00214-019-2442-1

Marchaj, M., Freza, S., Rybacka, O., and Skurski, P. (2013). Superhalogen Oxidizers Capable of Ionizing Water Molecules. *Chem. Phys. Lett.* 574, 13–17. doi:10.1016/j.cplett.2013.05.009

Møller, C., and Plesset, M. S. (1934). Note on an Approximation Treatment for Many-Electron Systems. *Phys. Rev.* 46, 618. doi:10.1103/PhysRev.46.618

Paduani, C., Wu, M. M., Willis, M., and Jena, P. (2011). Theoretical Study of the Stability and Electronic Structure of Al(BH4)n=1→4 and Al(BF4)n=1→4 and Their Hyperhalogen Behavior. *J. Phys. Chem. A* 115, 10237–10243. doi:10.1021/jp206330d

Pathak, B., Samanta, D., Ahuja, R., and Jena, P. (2011). Borane Derivatives: A New Class of Super- and Hyperhalogens. *ChemPhysChem* 12, 2423–2428. doi:10.1002/cphc.201100320

Reed, A. E., Weinstock, R. B., and Weinhold, F. (1985). Natural Population Analysis. *J. Chem. Phys.* 83, 735–746. doi:10.1063/1.449486

Saha, R., Mandal, B., and Chattaraj, P. K. (2018). HNgBeF3 (Ng = Ar-Rn): Superhalogen-Supported Noble Gas Insertion Compounds. *Int. J. Quantum Chem.* 118, e25499. doi:10.1002/qua.25499

Sikorska, C., Freza, S., Skurski, P., and Anusiewicz, I. (2011). Theoretical Search for Alternative Nine-Electron Ligands Suitable for Superhalogen Anions. *J. Phys. Chem. A* 115, 2077–2085. doi:10.1021/jp2000392

Smuczynska, S., and Skurski, P. (2009). Halogenoids as Ligands in Superhalogen Anions. *Inorg. Chem.* 48, 10231–10238. doi:10.1021/ic901253r

Srivastava, A. K., Kumar, A., and Misra, N. (2021). Superhalogens as Building Blocks of Ionic Liquids. *J. Phys. Chem. A* 125, 2146–2153. doi:10.1021/acs.jpca.1c00599

Srivastava, A. K. (2021). Prediction of Novel Liquid Crystalline Molecule Based on BO2 Superhalogen. *J. Mol. Liq.* 344, 117968. doi:10.1016/j.molliq.2021.117968

Sun, W.-M., Hou, D., Wu, D., Li, X.-H., Li, Y., Chen, J.-H., et al. (2015). Theoretical Characterization of a Series of N5-Based Aromatic Hyperhalogen Anions. *Dalton Trans.* 44, 19901–19908. doi:10.1039/c5dt03575a

Sun, W.-M., Li, X.-H., Li, Y., Wu, D., Li, C.-Y., Chen, J.-H., et al. (2016). Can Fluorinated Molecular Cages Be Utilized as Building Blocks of Hyperhalogens? *ChemPhysChem* 17, 1468–1474. doi:10.1002/cphc.201600052

Świerszcz, I., and Anusiewicz, I. (2011). Neutral and Anionic Superhalogen Hydroxides. *Chem. Phys.* 383, 93–100. doi:10.1016/j.chemphys.2011.04.018

Wang, X.-B., Ding, C.-F., Wang, L.-S., Boldyrev, A. I., and Simons, J. (1999). First Experimental Photoelectron Spectra of Superhalogens and Their Theoretical Interpretations. *J. Chem. Phys.* 110, 4763–4771. doi:10.1063/1.478386

Willis, M., Götz, M., Kandalam, A. K., Ganteför, G. F., and Jena, P. (2010). Hyperhalogens: Discovery of a New Class of Highly Electronegative Species. *Angew. Chem. Int. Ed.* 49, 8966–8970. doi:10.1002/anie.201002212

Yang, X., Wang, X.-B., Wang, L.-S., Niu, S., and Ichiye, T. (2003). On the Electronic Structures of Gaseous Transition Metal Halide Complexes, FeX4− and MX3− (M=Mn, Fe, Co, Ni, X=Cl, Br), Using Photoelectron Spectroscopy and Density Functional Calculations. *J. Chem. Phys.* 119, 8311–8320. doi:10.1063/1.1610431

Yang, H., Li, Y., He, H.-M., Tong, J., Wu, D., and Li, Z.-R. (2017). Superhalogen Properties of Hetero-Binuclear Anions MM′F4− and MM″F5− (M = Li, Na, M′ = Be, Mg, Ca; M″ = B, Al, Ga). *Chem. Phys. Lett.* 684, 273–278. doi:10.1016/j.cplett.2017.07.010

Yang, H., Li, Y., He, H.-M., Yu, D., Wu, D., and Li, Z.-R. (2018). Hetero-binuclear Superhalogen Anions with Cyanide And/or Isocyanide as Ligands. *Chem. Phys. Lett.* 713, 203–209. doi:10.1016/j.cplett.2018.10.039

Yang, H., Li, Y., Zhao, J.-G., Xing, B.-Y., He, H.-M., Jiang, S., et al. (2021). On Structure and Hyperhalogen Properties of Hetero-Binuclear Superatoms MM′(BO2)− (M = Na, Mg; M′ = Mg, Al; N = 4-6). *Polyhedron* 209, 115456. doi:10.1016/j.poly.2021.115456

Zakrzewski, V. G., Dolgounitcheva, O., and Ortiz, J. V. (1996). Ionization Energies of Anthracene, Phenanthrene, and Naphthacene. *J. Chem. Phys.* 105, 8748–8753. doi:10.1063/1.472654

Zhai, H.-J., Li, J., and Wang, L.-S. (2004). Icosahedral Gold Cage Clusters: $M@Au_{12}^-$(M = V, Nb, and Ta). *J. Chem. Phys.* 121, 8369–8374. doi:10.1063/1.1799574

Zhai, H.-J., Wang, L.-M., Li, S.-D., and Wang, L.-S. (2007). Vibrationally Resolved Photoelectron Spectroscopy of BO- and BO2-: A Joint Experimental and Theoretical Study. *J. Phys. Chem. A* 111, 1030–1035. doi:10.1021/jp0666939

Zhao, Y., Wang, J., Huang, H.-C., Li, J., Dong, X.-X., Chen, J., et al. (2020). Tuning the Electronic Properties and Performance of Low-Temperature CO Oxidation of the Gold Cluster by Oriented External Electronic Field. *J. Phys. Chem. Lett.* 11, 1093–1099. doi:10.1021/acs.jpclett.9b03794

**Conflict of Interest:** The authors declare that the research was conducted in the absence of any commercial or financial relationships that could be construed as a potential conflict of interest.

**Publisher's Note:** All claims expressed in this article are solely those of the authors and do not necessarily represent those of their affiliated organizations, or those of the publisher, the editors, and the reviewers. Any product that may be evaluated in this article, or claim that may be made by its manufacturer, is not guaranteed or endorsed by the publisher.

frontiers | Frontiers in Chemistry

TYPE Review
PUBLISHED 07 November 2022
DOI 10.3389/fchem.2022.1019166



OPEN ACCESS

EDITED BY
Ambrish Kumar Srivastava,
Deen Dayal Upadhyay Gorakhpur University, India

REVIEWED BY
Wei-Ming Sun,
Fujian Medical University, China
Abhishek Kumar,
University of Lucknow, India

*CORRESPONDENCE
Sarvesh Kumar Pandey,
sarveshp@iisc.ac.in

SPECIALTY SECTION
This article was submitted to Physical Chemistry and Chemical Physics, a section of the journal Frontiers in Chemistry

RECEIVED 14 August 2022
ACCEPTED 13 October 2022
PUBLISHED 07 November 2022

CITATION
Pandey SK, Arunan E, Das R, Roy A and Mishra AK (2022), Recent advances in in silico design and characterization of superalkali-based materials and their potential applications: A review. *Front. Chem.* 10:1019166. doi: 10.3389/fchem.2022.1019166



# Recent advances in *in silico* design and characterization of superalkali-based materials and their potential applications: A review

Sarvesh Kumar Pandey[1]*, Elangannan Arunan[1], Ratnesh Das[2], Atish Roy[2] and Arunesh Kumar Mishra[2]

[1]Department of Inorganic and Physical Chemistry, Indian Institute of Science Bengaluru, Bengaluru, Karnataka, India, [2]Department of Chemistry, Dr. Harisingh Gour University (A Central University), Sagar, Madhya Pradesh, India

In the advancement of novel materials, chemistry plays a vital role in developing the realm where we survive. Superalkalis are a group of clusters/molecules having lower ionization potentials (IPs) than that of the cesium atom (3.89 eV) and thus, show excellent reducing properties. However, the chemical industry and material science both heavily rely on such reducing substances; an *in silico* approach-based design and characterization of superalkalis have been the focus of ongoing studies in this area along with their potential applications. However, although superalkalis have been substantially sophisticated materials over the past couple of decades, there is still room for enumeration of the recent progress going on in various interesting species using computational experiments. In this review, the recent developments in designing/modeling and characterization (theoretically) of a variety of superalkali-based materials have been summarized along with their potential applications. Theoretically acquired properties of some novel superalkali cations ($Li_3^+$) and $C_6Li_6$ species, etc. for capturing and storing $CO_2/N_2$ molecules have been unveiled in this report. Additionally, this report unravels the first-order polarizability-based nonlinear optical (NLO) response features of numerous computationally designed novel superalkali-based materials, for instance, fullerene-like mixed-superalkali-doped $B_{12}N_{12}$ and $B_{12}P_{12}$ nanoclusters with good UV transparency and mixed-valent superalkali-based $CaN_3Ca$ (a high-sensitivity alkali-earth-based aromatic multi-state NLO molecular switch, and lead-founded halide perovskites designed by incorporating superalkalis, supersalts, and so on) which can indeed be used as a new kind of electronic nanodevice used in designing hi-tech NLO materials. Understanding the mere interactions of alkalides in the gas and liquid phases and the potential to influence how such systems can be extended and applied in the future are also highlighted in this survey. In addition to offering an overview of this research area, it is expected that this review will also provide new insights into the possibility of expanding both the experimental synthesis and the practical use of superalkalis and their related species. Superalkalis present the intriguing possibility of acting as cutting-edge construction blocks of

nanomaterials with highly modifiable features that may be utilized for a wide-ranging prospective application.

KEYWORDS

binding energy (BE), HOMO-LUMO (highest occupied molecular orbital-lowest unoccupied molecular orbital), ionization potential (IP), NLO (nonlinear optical), superalkali

## Introduction

Superalkalis are one distinct class of superatoms that consist of characteristics similar to those of alkali metals but have a substantially lower ionization potential (IP) than them (Wang et al., 1999). As a result, due to their low IPs, superalkalis quickly lose their valence electrons (Gutsev and Boldyrev, 1982; Khanna and Jena, 1995, Khanna and Jena, 2011). Gutsev and Boldyrev were the first to make use of the term "superalkali" in 1982 to refer to the distinct electronic structures of numerous radical forms of lithium and sodium-related species (Gutsev and Boldyrev, 1981). Recent research has proven that superalkalis are the superior supplier of extra electrons for creating novel materials with high initial hyperpolarizabilities than other materials that drop electrons rapidly from their outermost shell (Wang et al., 2012; Sun et al., 2014b, Sun et al., 2014a, Sun et al., 2016a). These species can give one electron to other molecules and survive as cations due to their IPs being lower than those of the alkali metal atoms (5.39–3.89 eV) in the periodic table of all elements (Lias et al., 1988) which means that they are more reactive even though they do not always resemble other elements (Wang et al., 2007). Researchers are constantly executing appropriate research work on the designing and characterization (experimentally or theoretically) of the superalkalis along with their potential applications. Nowadays, scientists have put significant effort into creating and describing diverse comical superalkali-based species.

The standard formula for superalkalis is $M_{k+1}L$, where k is 1 for L (F, Cl, Br, and I) and 2 for L (O) atoms; $Li_nX$ (Velickovic et al., 2006; Velickovic et al., 2007; Velickovic et al., 2012) extended to $K_2X$ (X = F, Cl, Br, and I) (Velickovic et al., 2011) and $Li_3O$ (Zintl and Morawietz, 1938; Kudo et al., 1978; Wu et al., 1979) are two instances that come up frequently in this series. $Li_2F$ has been the subject of extensive theoretical (Gutsev and Boldyrev, 1982; Honea et al., 1989, Honea et al., 1993; Rehm et al., 1992; Koput, 2008; Wright et al., 2009) and experimental (Yokoyama et al., 2000; Neskovic et al., 2003; Fernandez-Lima et al., 2009) research. Well-known superalkalis, $M_3O$ (M = Li, Na, and K), have a greater propensity than their equivalent alkali atoms to lose an outer electron (Gutsev and Boldyrev, 1987; Rehm et al., 1992). Comprehensive experiments on the superalkalis having one nonmetal acting as the central atom (B, N, and O) connected by the alkali metal atoms can be seen in the literature, for instance, $OM_3$ (M = Li, Na, and K) (Wang et al., 2011; Zein and Ortiz, 2011), $NLi_4$ (Rehm et al., 1992), $CLi_5$, $SiLi_n$ ($n$ = 1–5), $CLi_6$ (Schleyer et al., 1983; Otten and Meloni, 2018), and $BLi_6$ (Li et al., 2007). Next, a comprehensive work based on the *in silico* approach for binuclear superalkali cations having the formula $M_2Li_{2k+1}$ (M = F, O, N, C, and B for $k$ = 1, 2, 3, 4, and 5, correspondingly) was reported by Tong et al. (2009). Furthermore, using the *ab initio*-based inspections, a series of binuclear superalkali cations $M_2Li_{2k+1}^+$ ($F_2Li_3^+$, $O_2Li_5^+$, $N_2Li_7^+$, and $C_2Li_9^+$) was proposed by the same group (Tong et al., 2011). Then, focusing on the expansion from mono to binuclear superalkali cations, attempts have been made by Tong et al. (2012) in describing polynuclear superalkali cations $YLi_3^+$ (Y = $CO_3$, $SO_3$, $SO_4$, $O_4$, and $O_5$) (Tong et al., 2013). The aforementioned remarkable cations/compounds offer a great deal of potential for use in the production of novel charge-transfer (CT) salts and cluster-assembled nanomaterials with customized characteristics, the reduction of carbon dioxide ($CO_2$), and activation of very stable nitrogen molecules ($N_2$), nitrogen oxides (NO), or as hydrogen (energy) storage materials as well as noble-gas trapping agents, ferroelectrics, catalysts, and nonlinear optical (NLO) response, among other things (Zhang et al., 2021b; Zhang et al., 2021a). These molecular species have the capability to reduce substances and can be employed to produce various cutting-edge building blocks of nanoscale materials having highly tunable features, particularly the CT salts. The superalkali cations can produce the CT salts such as a crystal salt $Li_3O^+NO_2^-$ consisting of a single singly charged superalkali cation ($Li_3O^+$) (introduced by Zintl and Morawietz, 1938) that alkali elements cannot because of the unfavorable energetics, the metal atom's relatively high IP, or steric hindrance (Li et al., 2008; Tong et al., 2009). Subsequently, the real nature of sodium nitrate ($NaNO_3$) was revealed to be sodium oxide nitrite, $Na_3O^+(NO_2)^-$ (Jansen, 1977). They can be utilized to create uncommon CT salts whose counterparts have a low electron affinity (EA). *In silico* design and characterization of superalkalis based on Zintl ions and the superatom compounds with an NLO response have been reported by some research groups along with Zintl clusters as a new class of superhalogens which can be seen in the literature (Reddy et al., 2018b, Reddy et al., 2018a; Sun et al., 2018; Sinha et al., 2022).

Design, synthesis, and potential applications of new materials consisting of large second-order NLO responses (involving optical data storage, optical computing, telecommunications, optical information processing, etc.) have gained increasing attention (Chemla and Zyss, 1987; Prasad and Williams, 1991; Bredas et al., 1994; Geskin et al., 2003). Several reports on organic

molecules consisting of donor–acceptor- (D-A) or donor–π-conjugated bridge-acceptor (D-π-A) skeletons can be seen in the literature which demonstrate considerably large first hyperpolarizabilities and show high photovoltaic performance in developing new non-fullerene small-molecule acceptors (Marder, 2006; Wei et al., 2022). Such frameworks found with larger CT in the systems can establish substantial differences between the dipole moments of the ground state and the excited state as well as low-energy CT transitions (Xu et al., 2007). For example, a sequence of formal D-A chromophores is expected to show a significant NLO response and high stability when $M_3O$ (electron donor) interacts with its counterpart, $BC_{59}$ (electron acceptor), and creates the CT dyads as $M_3O$-$BC_{59}$ (Tu et al., 2014).

Moreover, superalkali cations may interact with superhalogen anions, just like alkali metal cations, and this interaction is predicted to be stronger than the former due to the even lower IPs of the superalkalis. The ability of the superalkali clusters to replicate the chemical behavior of alkali metals makes them potentially useful as building blocks in the construction of innovative nanostructured materials, which is one of their most intriguing discoveries. In some situations, they can combine to form assemblies or super-atom compounds while retaining their identity, much like regular atoms, and thus can demonstrate unique chemical or tunable electronic characteristics. Examples include $BF_4$-M (M = Li, $FLi_2$, $OLi_3$, and $NLi_4$) (Yang et al., 2012), $BLi_6$-X (X = F, $LiF_2$, $BeF_3$, and $BF_4$) (Li et al., 2008), $Na_2XY$ (X = SCN, OCN, and CN; Y = $MgCl_3$, Cl, and $NO_2$) (Anusiewicz, 2010), and $Al_{13}(K_3O)$ as well as $Al_{13}(Na_3O)$ (Reber et al., 2007). As a result, it makes sense to study the characterization and prediction of the superalkali-based clusters. Recent investigations have attempted to suggest various unique superalkali species (Sun et al., 2016b, Sun et al., 2019; Tkachenko et al., 2019; Ye et al., 2022; Sun et al., 2022), including organic heterocyclic superalkalis [$C_3N_2(CH_3)_5$ acquired from a familiar aromatic heterocycle, pyrrole] (Reddy and Giri, 2016), organo-Zintl superalkalis (P7R4) (Giri et al., 2016), non-metallic superalkali cations [$F_2H_3^+$, $O_2H_5^+$, $N_2H_7^+$, and $C_2H_9^+$] (Hou et al., 2013), and aromatic superalkali species [$MLi_{n+1}^+$ aromatic superatom cations and $Au_3$ core connected with pyridine (Py) and imidazole (IMD) ligands] (Sun et al., 2013; Parida et al., 2018) (33a, 33b).

As was earlier mentioned, the superalkali clusters are a common type of super-atoms that can function as alkali metal atoms, so they can construct an extended nanostructure when put together (Reber et al., 2007; Reber and Khanna, 2017). Additionally, it has been suggested that superalkali cations could act as hydrogen storage materials (Barbatti et al., 2002; Giri et al., 2011; Pan et al., 2012) and noble gas-trapping agents (Chakraborty et al., 2010; Pan et al., 2013a; Pan et al., 2013b). For instance, Giri et al. (2011) investigated the potential of the cationic superalkalis $Li_3^+$ and $Na_3^+$ for $H_2$-binding. Additionally, it has been noted that the superalkali cation $O_2Li_5^+$ can bind up to seven noble gas (Ng) atoms (Ng = He, Ne, Ar, and Kr) (Pan et al., 2013a) and up to 12 Xe atoms (Pan et al., 2013b).

The trinuclear $Au_3(IMD)_3$ [IMD = imidazole] combination turns aromatic, according to a recent work on the construction of a novel family of organometallic superalkali compounds (Gutsev and Boldyrev, 1982; Gutsev and Boldyrev, 1985; Parida et al., 2018; Tkachenko et al., 2019). Examining large systems such as fullerenes, the prediction of superalkali@C60 endofullerenes, their enhanced stability, and interesting properties have been reported comprehensively by Misra et al. in 2016 along with an understanding of the nanoconfinement effect on halogen bonding in $(CH_3Br\cdots NH_3)@C_{60}$ (Srivastava et al., 2016b; Srivastava et al., 2016a).

Even though superalkalis have advanced significantly over the past several decades, an overview of the recent advances in a variety of remarkable species appears to be missing in the literature (Sun and Wu, 2019; Pal et al., 2021). The most advanced developments in recent years, design/modeling, characterization in the framework of *in silico* approaches, and first-time use of superalkali-based novel materials are outlined in this review along with their potential applications. We attempted to share the predictions for their future growth in the hopes of pointing designers in the right direction as they continue to create and use such special species. We believe that this report can open new directions in the organized interpretation of the superalkali-based materials.

## Results and discussion

In this section, the authors have attempted to provide snippets on the structure, stability, and electronic features of various superalkali-based species such as $NM_4$ (M = Li, Na, and K) superalkalis; *ab initio* exploration of the polynuclear K- and Na-based superalkali hydroxides as superbases; theoretical studies on the hydration effect on the superalkali cations, $Li_3^+$; and the role of the size and composition on the design of superalkalis. Moreover, in terms of the applications of a range of superalkali-based materials (i.e., high-performance NLO material/molecular switch), design and characterization (theoretically) of a novel series of D-A frameworks through superalkali–superhalogen assemblage, superalkalis doped with $B_{12}N_{12}$ nanocages, boron phosphide nanocages doped with superalkalis as novel electrides, and innovative inorganic aromatic mixed-valent superalkali electride, $CaN_3Ca$, have been highlighted in this report. This report unravels a brief overview of the capturing of nitrogen by unveiling the potential of superalkali cation $Li_3^+$ and the reduction/activation of carbon dioxide with a superalkali. A short description of the modeling of aromatic organometallic superalkali complexes and superalkali ligands as the building blocks for aromatic

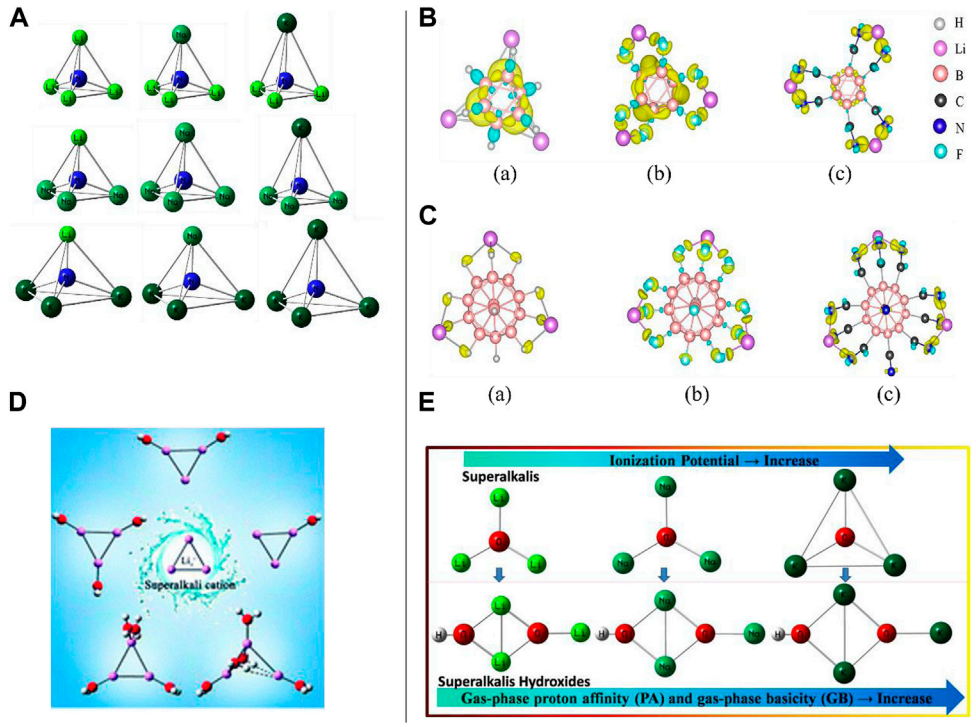


FIGURE 1
**(A)** Geometric structures of $NM_4$ (M = Li, Na, and K) clusters reproduced from Zhang and Chen (2019); **(B)** charge density difference in **(A)** $Li_3B_6H_6$, **(B)** $Li_3B_6F_6$, and **(C)** $Li_3B_6(CN)_6$ clusters reproduced from Banjade et al. (2021). **(C)** Charge density difference in **(A)** $Li_3B_{12}H_{12}$, **(B)** $Li_3B_{12}F_{12}$, and **(C)** $Li_3B_{12}(CN)_{12}$ clusters (Banjade et al., 2021); **(D)** superalkali cation $Li_3^+$ with water molecules, $Li_3^+(H_2O)_n$ ($n$ = 1–5), reproduced from Hou et al. (2018) with permission from the Royal Society of Chemistry; **(E)** a small series of hydroxides ($XM_{n+1}OH$) where ($XM_{n+1}$): superalkali; M (K and Na): alkali metal atom; n, maximal formal valence of the central atom X (F, O, and N), and $n \geq 1$.

trinuclear Cu(I)-NHC complexes, the nature of the aluminum trimer combined with different superatom clusters, superalkali–alkalide interactions, ion pairing in low-polarity solvents, and lead-based halide perovskites associated with superalkali species have been reported.

## Structural and electronic features of superalkali-based species

Superalkalis are known as super-atoms which can imitate the chemistry of atoms and can be used in the synthesis of novel materials with diverse interesting features. Using high theoretical-level Gaussian 3 (G3) calculations, Zhang and Chen proposed models of a small series of superalkali $NM_4$ (where M = Li, Na, and K) (see Figure 1A) clusters consisting of homo- and hetero-alkalis, and studied their stability and electronic structures (Zhang and Chen, 2019). The calculated vertical IPs (3.22–3.74 eV) have been found to be smaller than that of the Cs atom having an IP value of 3.89 eV, and binding energies (BEs) and positive energies of the dissociation channel such as ($NM_3$ + M') confirmed the stabilities (thermodynamically) of all probed species where $NLi_4$ was found to be the most stable among all the homo- and hetero-superalkalis. The order of the calculated BEs for the $NM_4$ clusters was found to be $NLi_4$ (−9.25 eV) > $NNa_4$ (−5.88 eV) > $NK_4$ (−1.92 eV), separately, where the size of the alkaline atoms has a substantial impact on the overall stability of the clusters when such atoms are combined, followed by ionic bond formation. Encouraged by the reports highlighted in this study, novel materials can be constructed by the previously designed and characterized (theoretically) species having high stability along with tetrahedral geometry. It is important to note that the structures of the $NM_4$ species with homogeneous alkali atoms (like $NLi_4$, $NNa_4$, and $NK_4$) have Jahn–Teller distortion-resistant $T_d$ symmetry, while the clusters constructed from the heterogeneous alkali atoms have $C_{3v}$ symmetry. Furthermore, the Frontier molecular orbital (FMO) approach appeared to show that the highest occupied molecular orbitals (HOMOs) of all such species are mainly spread over the complete clusters shown to diminish the repulsion among the electrons repelling each other. Their *ab initio* modeling approaches (MP2/MP4) described the highly symmetric structural parameters and the low IP values of the $NM_4$ clusters from the electronic origin point of view.

It is to be noted that although significant signs of progress have been made in designing, synthesis, and characterization of superhalogens, there is still room for related studies on superalkalis. With the combination of superalkalis having low IPs and superhalogens having high EA, super-ions may be used as construction blocks of a novel series of supersalts having uses in multiferroic materials, metal-ion batteries, solar cells, and so on. Jena et al. thoroughly described the role of size and composition in the design of supersalts consisting of two dissimilar classes of clusters belonging to the *closo*-borane family, $Li_mB_nX_n$ ($m$ = 1–3; $n$ = 6, 12; X = H, F, and CN) and Zintl ion family, $Li_mBe@Ge_9$, in the framework of the density functional theory (DFT) with hybrid exchange-correlation functional (ωB97xd) as well as Gaussian basis sets [6-311+G (d, p)] (Banjade et al., 2021). In this work, the stabilities of such a composition of clusters were regulated by the Wade–Mingos polyhedral skeleton electron pair theory (i.e., shell closure rule), and additionally, the jellium shell closure rule was deployed to understand the stability of the $Be@Ge_9$ cluster. The analyzed IP values were well-connected to the EAs of the X ligands (the higher the EA, the larger the IP). They found that like the lowest IP value (2.84 eV) for $Li_3B_6H_6$ among $Li_3B_nX_n$ clusters, both the *closo*-borane family and Zintl ion-related clusters followed the same IP patterns; however, conversely and beyond the hope, the IP values were not reduced ($n$ = 6–12) with enhancing the cluster volume followed by being weakly bounded. It should be noted that EAs of the $B_nX_n$ enhanced proceeding from $n$ = 6 to $n$ = 12, since the association of the Li atoms with the $B_{12}X_{12}$ cluster is stronger than that with the $B_6X_6$ cluster. Likewise, as the substitution of the X travels from the H atom to the F atom to the CN group in the $Li_3B_{12}X_{12}$ clusters (X = H, F, and CN), the IP values are enhanced. The charge density difference (CDD) plots were visualized for all six species (three *closo*-borane and three Zyntl ion families). For example, in the case of $Li_3B_6H_6$, the CDD showed that the electrons have been amassed in the area sandwiched between the three successive Li–B bonds and uniform diffusion of the electron near the Li–B bonding region (see Figure 1B), whereas a much larger charge accumulation between the Li and F atoms can be seen for the $Li_3B_6F_6$ cluster. These findings were consistent with the structural features. Furthermore, electron accumulation along the Li–C bonds for the $Li_3B_{12}X_{12}$ clusters demonstrated that the Li atoms were bonded to mostly the X atoms (see Figure 1C) which agreed with their geometries. Very importantly, however, there was an increment in the cluster volume and the F atom, as well as the CN group consisting of more electronegativity than the H atom, and stronger interactions between the cluster and the Li atoms have been observed. The IPs of the Zintl-ion family clusters were found to be higher than those in the *closo*-borane-family clusters since these behave like superalkalis. Very interestingly, it is noteworthy to mention that despite having the same electron count in both the $Li_5Ge_9$ and $Li_3Be@Ge_9$ clusters, the IP of the former is found to be smaller than that of the latter, implying that, indeed, composition matters therein.

Using the *ab initio* modeling approach, Li *et al.* reported an extensive study on the influence of hydration on the structure, stability (through energy decomposition analyses), and electronic features of the superalkali cation $Li_3^+$ in the framework of the MP2/6-311++(d, p) level of theory (Hou et al., 2018). Assuming all possible arrangements of $H_2O$ molecules around the $Li_3^+$ cation, a series of $Li_3^+(H_2O)_n$ ($n$ = 1–5) structures (see Figure 1D) have been obtained where the $Li_3^+$ cation is observed to have a maximum of four coordination numbers. Interacting with five molecules of water, the CT of the $Li_3^+$ cation appeared to be critically irregular which was shown by natural population analysis (NPA), and as a result, the $Li_3^+$ cation lacks the ring conjugation and comes apart into the isomer of $Li_3^+(H_2O)_5$ having the lowest energy. Using the NPA tool, water ligands appeared to have a dominant role in the charge distribution of $Li_3^+$ along with the CT from the $H_2O$ ligand to the $Li_3^+$ skeleton. With the deployment of the polarization continuum model (PCM) tool in calculating the Gibbs free energies ($\Delta G_r^{298}$) at 298.15 K, the lowest-energy isomers of $Li_3^+(H_2O)_n$ ($n$ = 1–5) are not appropriate for detaching spontaneously. It is important to mention that a coordination number of 12 has been vaticinated for the $Li_3^+$ cation associated with hydrogen clusters. The outcomes of the *in silico* approach revealed that structural and electronic integrity was maintained by the $Li_3^+$ cation followed by low-lying isomers of the $Li_3^+(H_2O)_{1-4}$ complexes, while in the lowest-energy structure of $Li_3^+(H_2O)_5$, it destroyed and left its superalkali individuality. Based on such findings, like $Li^+$ in water clusters, the superalkali $Li_3^+$ cation contributes to the same maximum coordination number. Like the case of the lithium-ion hydrates, the localized molecular orbital energy decomposition approach showed that the electrostatic interactions play a prime role in the binding of the water molecules with the $Li_3^+$ cation. A sharp increase in the contribution of the exchange-repulsion energy can be seen when the number of water ligands arrives at five and even this exchange-repulsion energy surpasses that of the electrostatic term.

Very recently, computational designing and characterization of Na- and K-based superalkali hydroxides acting as superbases have been reported by S. K. Pandey for the first time (Pandey, 2021b). A new kind of hydroxide of the superalkalis ($XM_{n+1}OH$) [where the fragment $XM_{n+1}$ refers to the superalkali moieties, X (F, O, and N), and $n \geq 1$] has been modeled, and inclusive computational experiments on such fascinating species have been performed using the framework of the *ab initio* method (see Figure 1E). To inspect the relative basic nature of such polynuclear superalkali hydroxides (SAHs) against the representative alkali metal hydroxide (KOH, NaOH, and LiOH) along with the Li-related SAHs, the *ab initio* findings demonstrated that both the Na- and K-based SAHs are stronger bases than the LiOH and Li-related SAHs which is due to the larger gas-phase proton affinity (**PA**) and gas-phase basicity

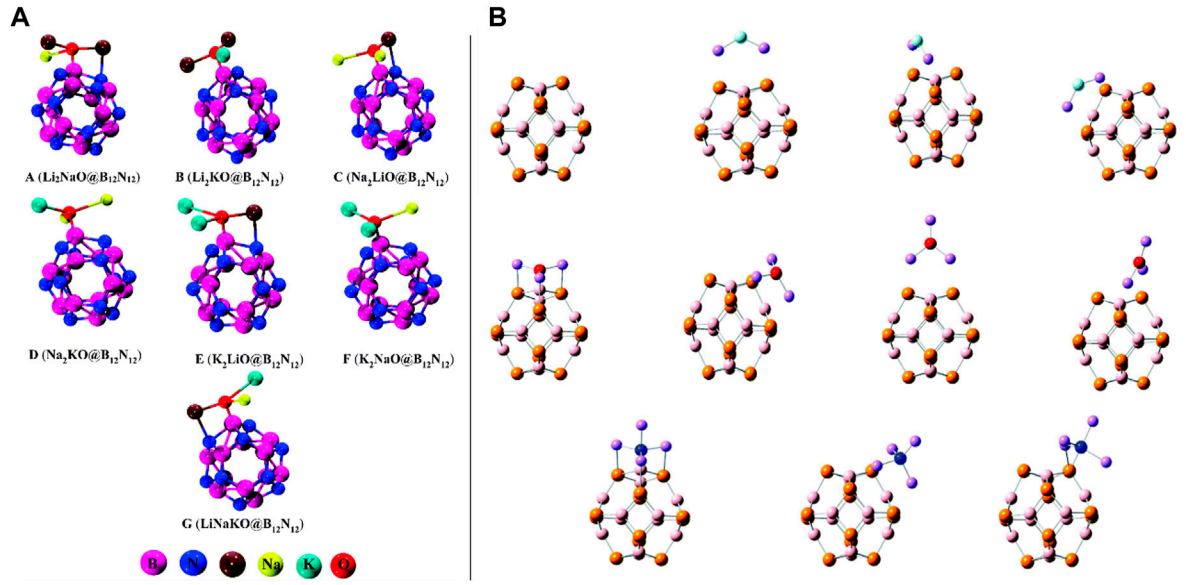


FIGURE 2
**(A)** Optimized geometries of the most stable complexes of mixed-superalkali-doped $B_{12}N_{12}$ adapted from Bano et al. (2022) with permission from the Royal Society of Chemistry; **(B)** optimized structures of $C_6Li_6$-$nCO_2$ complexes (front and side views) for $n$ = 1–6 adopted from Srivastava (2019b) with the permission of Wiley.

(**GB**) values of the Na- and K-related SAHs. Noticeably, the highest **PA** (1168.4 kJ/mol) and **GB** (1146.9 kJ/mol) of the $OK_3OH$ base revealed its strongest basicity nature among all the existing strong bases and superbases along with the proposed K- and Na-based SAHs. The values adequately surpassed the **ΔPA** (142.1 kJ/mol) and **ΔGB** (146.9 kJ/mol) values of the threshold values (PA: 1026.3 kJ/mol and GB: 1000 kJ/mol) of a very popular IUPAC-defined superbase (DMAN).

To probe the structure, stability (bonding features), and electronic properties of the SAHs, the popular noncovalent interaction (NCI)-plot and quantum theory of atoms in molecules (QTAIM) tools were used for a variety of chemical to biochemical species to materials along with exploration of the computational studies on the HAP biomaterials including the first-principle DFT, *ab initio* modeling, and molecular dynamics simulations (Awasthi et al., 2021a; Awasthi et al., 2021b; Pandey, 2021a; Pandey and Arunan, 2021). In this report, new insights into the basicity features were facilitated by an *ab initio* modeling approach. Design, fabrication, and synthesis of the theoretically explored SAHs may lead to providing an alternative pathway for the experimentally availing applications.

## High-performance NLO response material/molecular switch

Very recently, Bano et al. presented theoretical work where they showed that the mixed superalkalis ($Li_2NaO$, $Li_2KO$, $Na_2LiO$, $Na_2KO$, $K_2LiO$, $K_2NaO$, and $LiNaKO$) could be a better alternative than the pure superalkalis for $B_{12}N_{12}$ nanocages in designing hi-tech NLO materials (Bano et al., 2022). The optimized structures of the mixed-superalkali-doped $B_{12}N_{12}$ complexes can be seen in Figure 2A. Throughout the computational experiments, the structure, stability, electronic, and NLO response features of superalkali cluster-mixed $B_{12}N_{12}$ nanocages were examined. They have chosen a total of seven (**A–G**) thermodynamically stable designed complexes consisting of very high interaction energies ranging from −98.02 kcal/mol to −123.13 kcal/mol, which were compared with the previously reported $Li_3O@B_{12}N_{12}$ having an interaction energy ($E_{int}$) as −92.71 kcal/mol along with the narrow variation of the HOMO-LUMO energy gaps (from 3.36 eV to 4.27 eV) compared against the pristine $B_{12}N_{12}$ (11.13 eV) species. This group confirmed the CT phenomenon occurring in such probed complexes which were acquired from the NPA technique, non-bonding interactions between the doped superalkalis and nanocages followed by the QTAIM, as well as NCI-plot tools. The maximum absorbance was found in the near-infrared (IR) region ranging from 1,076–1,486 nm which appeared to be transparent in the ultraviolet (UV) region. The computed first hyperpolarizability ($\beta_{tot}$) of complex C was analyzed as $1.7 \times 10^4$ au which was much greater than that of the pure $Li_3O$ superalkali-doped $B_{12}N_{12}$ complex ($3.7 \times 10^4$ au) perceived from the same theoretical level of approach (by Sun *et al.* in 2016). As in nanoelectronics, designing and synthesizing stable and high-performance NLO

materials is the foremost precedence for the scientists and researchers; an increased NLO response was detected in this work by a large second hyperpolarizability. To gain more insights into such complexes, they also computed hyper-Rayleigh scattering ($6.71 \times 10^{10}$ au), second harmonic generation ($1.17 \times 10^{10}$ au), and electro-optical Pockels ($3.29 \times 10^{10}$ au) effect along with the maximum obtained values of the electric field-induced second harmonic generation ($3.46 \times 10^{10}$ au) and electro-optic-dc-Kerr effect ($3.96 \times 10^{11}$ au) at 1,064 nm wavelength. At the same wavelength for all A-G complexes, significant increments in quadratic nonlinear refractive index ($n_2$) values were seen along with the largest value of $3.35 \times 10^{-8}$ $cm^2 \cdot W^{-1}$. The theoretical findings based on the ωB97XD/6-31G (d, p) level of approach indicated that such mixed superalkali-doped nanoclusters could have broad applications in designing, fabrication, and characterization of hi-tech optoelectronics (i.e., high-performance NLO materials).

However, various procedures can be seen in the literature in designing high-performance NLO materials; the NLO response of three series (a total of 10 isomers, **I**–**X**) of theoretically designed compounds $Li_2F@B_{12}P_{12}$, $Li_3O@B_{12}P_{12}$, and $Li_4N@B_{12}P_{12}$ having three (**I**–**III**), four (**IV**–**VII**), and three (**VIII**–**X**) isomers, correspondingly, was inspected thoroughly using the DFT approach (see Figure 2B) (Ullah et al., 2019). This research work explored the effects of superalkali ($Li_2F$, $Li_3O$, and $Li_4N$) when these were doped on the $B_{12}P_{12}$ nanocage. The computational outcomes showed that most of the complexes [all isomers of the $Li_2F@B_{12}P_{12}$ and $Li_3O@B_{12}P_{12}$ model compounds (**I**–**III** and **IV**–**VII**) along with one isomer of the $Li_4N@B_{12}P_{12}$ complex (**IX**)] possessed excess electrons, whereas only two isomers of the $Li_4N@B_{12}P_{12}$ (**VIII** and **X**) compound were found to be inorganic electrides. It was computationally inspected that the superalkalis were chemisorbed on the boron phosphide nanocage and all such formed nanocage complexes were found to be quite stable which was confirmed by their calculated BEs. There was substantial enrichment in the first hyperpolarizability values of the system when doping a $B_{12}P_{12}$ nanocage with the superalkali. Isomer **III** of the $Li_2F@B_{12}P_{12}$ system showed the largest first hyperpolarizability ($3.48 \times 10^5$ au) and lowest the HOMO-LUMO gap (1.46 eV) among the three isomers (**I**–**III**) along with good transparency in the UV region, showing that the superalkali $Li_2F$ provided better hyperpolarizability increment than the $Li_3O$ and $Li_4N$ superalkalis when associated with the $B_{12}P_{12}$ nanocage. In addition, the influences of several superalkalis and various doping locations on the NLO response were comprehensively examined for all three variants of model systems in the framework of the quantum chemical calculations using the DFT approach. This work will promote prospective uses of the $C_{60}$-like $B_{12}P_{12}$-based nanostructures doped with the superalkali and novel electronic nanodevices, and hi-tech NLO materials consisting of good UV transparency could be designed by the employment of new excess electron systems and electrides (**VIII** and **X**).

As several research groups have focused on designing novel superatoms with high NLO responses, A. Omidvar reported a range of representative D-A model skeleton species having elevated NLO responses through bonding the superalkali-like $M_3O$ ($K_3O$, $Na_3O$, $Li_3O$, $Li_2KO$, $Li_2NaO$, $Na_2KO$, $Na_2LiO$, $K_2LiO$, $K_2NaO$, and LiNaKO) blended with the superhalogens ($Al_{13}$ cluster) (see Figure 3A) (Omidvar, 2018). These superalkalis consist of a low IP to the superhalogen $Al_{13}$ having a larger EA. Additionally, the electric field gradient tensors of the $^{17}O$ nuclei and the natural bond orbital (NBO) analysis-based charges of the $M_3O$ superalkalis were also computed. In this study, he represented the theoretical signatures for the feasibility of employing the super-atoms $Al_{13}$ and $M_3O$ as construction blocks to construct nanomaterials with strong NLO responses. He observed that the IP and $^{17}O$ nuclear quadrupole resonance parameters of the $M_3O$ superalkalis have been efficiently affected by the M ligands. The electron transfer phenomenon in such types of super-atoms in the bonding superalkalis is responsible for the competent narrow HOMO-LUMO gap as well as increasing the first hyperpolarizability remarkably in the pristine $Al_{13}$ cluster. Significant CT takes place from the $M_3O$ component to the $Al_{13}$ assembly. It was observed that the data based on the $\eta_Q$ parameters of the $^{17}O$ nuclei significantly increase when the pure ligands were substituted with the doped ligands in the $M_3O$ superalkali species. The Q value (an asymmetry parameter) provides evidence of the chemical bonds taking part therein. Importantly, according to the findings of this investigation, the electropositivity of the alkali ligands was shown to play an important role in the determination of the IPs of the superalkalis. Moreover, a comprehensive exploration of the NLO response of the super-atoms $M_3O$-$Al_{13}$ can be seen that is altered by the oriented external electric fields. When the imposed oriented external electric field is enhanced along the CT direction ($M_3O \rightarrow Al_{13}$) ranging from zero to a critical external electric field, a gradual increment in the first hyperpolarizability can be seen for the superatom compounds which appears to be used as an effective approach based on the theoretical findings.

Using quantum mechanical approaches, a total of three configurations [two $C_{3v}$ point groups (**1** and **3**) and one $D_{3h}$ point group (**2**)] of trigonal bipyramidal (TBP) $CaN_3Ca$ structures were chosen as models, and the role of the NLO response was analyzed by aiming at pioneering hi-tech single-pole double-throw (SPDT) NLO molecular switches (Wang et al., 2020). One marginally longer and one shorter vertical Ca-$N_3^{3-}$ length was found in the case of both $C_{3v}$ configurations (**1** and **3**), whereas there were two identical bond lengths of Ca-$N_3^{3-}$ in configuration **2**. The *ab initio* (MP2/6-311+G (3df) method-based equilibrium structures of the chosen $CaN_3Ca$ species can be seen in Figure 3B where the Ca atoms are located over and

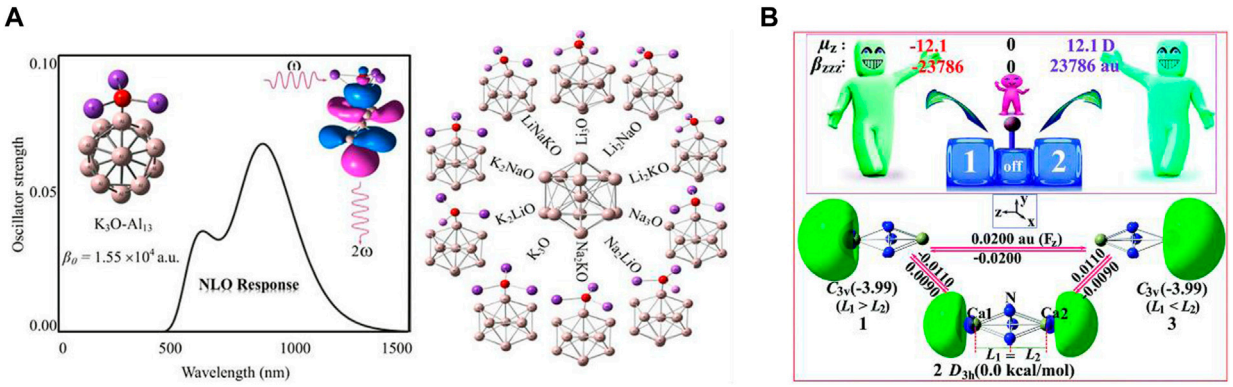


FIGURE 3
**(A)** Structures of superalkalis, $M_3O$ (where M = Li, Na, and K) associated with the $Al_{13}$ nanocluster reproduced with permission from Omidvar (2018); **(B)** different configurations (1, 2, and 3) of the $CaN_3Ca$ molecule adopted from Wang et al. (2020) with permission from the Royal Society of Chemistry.

under the usual triangular $N_3$ ring. It should be noted that energy configurations **1** and **3** are 3.99 kcal/mol smaller than that of configuration **2** at the CCSD(T)/6-311+G (3df) level of theory which illustrates that the former two configurations (**1** and **3**) have a larger thermal stability than configuration **2**. Moreover, in the case of the configuration **2**, the excess electrons equally occupied the two hemispherical orbital lobes (HOMOs) positioned over the two extremes of the $CaN_3Ca$ molecule, while in the case of the other two configurations (**1** and **3**), the excess electrons mainly occupied one hemispherical orbital lobe (HOMO) (located on the left side for **1** and right side for **2**) of the $CaN_3Ca$ species. Importantly, Figure 3B also confirms that a uniform external electric field (EEF) triggered a reversible configuration conversion between **1** (L1 > L2) and **3** (L1 < L2). Hence, by deploying an appropriate external homogeneous electric field, interconversion between **1**, **2**, and **3** can be realized easily. All these species belonged to the novel alkaline-earth-based aromatic mixed-valent superalkalis along with acting as fascinating electrides. Very importantly, the electronic structure of the salt-like species containing configuration **2** showed a delocalized structure in the form of $e^{0.5-}\cdots Ca^{2+}N_3^{3-}Ca^{2+}\cdots e^{0.5-}$ demonstrating class III-type mixed-valent superalkali electrides, whereas the other two configurations **1** and **3** were confirmed as the rare inorganic Robin–Day class II-type structure consisting of localized redox centers. Moreover, comparison outcomes of remarkable static and dynamic first hyperpolarizabilities of all three configurations have been reported since all three were excellent candidates for SPDT NLO molecular switches.

Finally, using the *ab initio* modeling approach, Zhang *et al.* showed that the phenalenyl radical and $M_3$ ring ($M_3$–PHY, M = Li, Na, and K) stacked with parallel and vertical geometries are potential applicants for molecular switches which can exist in both superalkali electrides and superalkalides (Yi et al., 2022). A range of similar kinds of interesting research studies can be seen in the aforementioned literature. In this work, they have shown that $M^{\delta-}$-$M_2^{(1-\delta)+}$-PHY$^-$ acts as a superalkalide, whereas the $e^-\cdots M_3^+$-PHY acts as a superalkali electride where the former may isomerize to the latter using suitable long-wavelength irradiation and the latter may isomerize to the former with appropriate short-wavelength irradiation. In this report, the researchers have combined both electride and alkalide characteristics in one molecular switch and concluded that both forms demonstrated an excellent functioning NLO response.

## Capturing carbon dioxide/nitrogen/hydrogen

Reduction (*via* electron transfer i.e. CT phenomenon) of carbon dioxide ($CO_2$) by the capability of the superalkali $Li_3F_2$ has been shown by Park and Meloni (2017). The equilibrium structure of neutral planar and non-planar clusters trapping the $CO_2$ and $N_2$ molecules can be seen in Figure 4A. To attain trustworthy outcomes on the structural and energetics/stability of the species, a composite CBS-QB3 model was deployed. The association of $CO_2$ with the $Li_3F_2$ superalkali was examined by scanning the potential energy surface (PES) which led to the formation of their transition states (TSs) and minima. Structural alterations were exposed in the terms of spin density and charge flow. The large BE (ionic interactions between the $Li_3F_2$ and $CO_2$ having the largest BE (163 kJ/mol) among the three optimized structural isomers), CT phenomenon, and the HOMO-LUMO gap explained the energetics and stability of the $Li_3F_2/CO_2$-associated species. It is worth mentioning that the largest determined BE (163 kJ/mol) was found to be significantly larger than that of the superhalogen cluster $Sb_3F_{16}/CO_2$ reported by Czapla and Skurski (2017). The choice of the

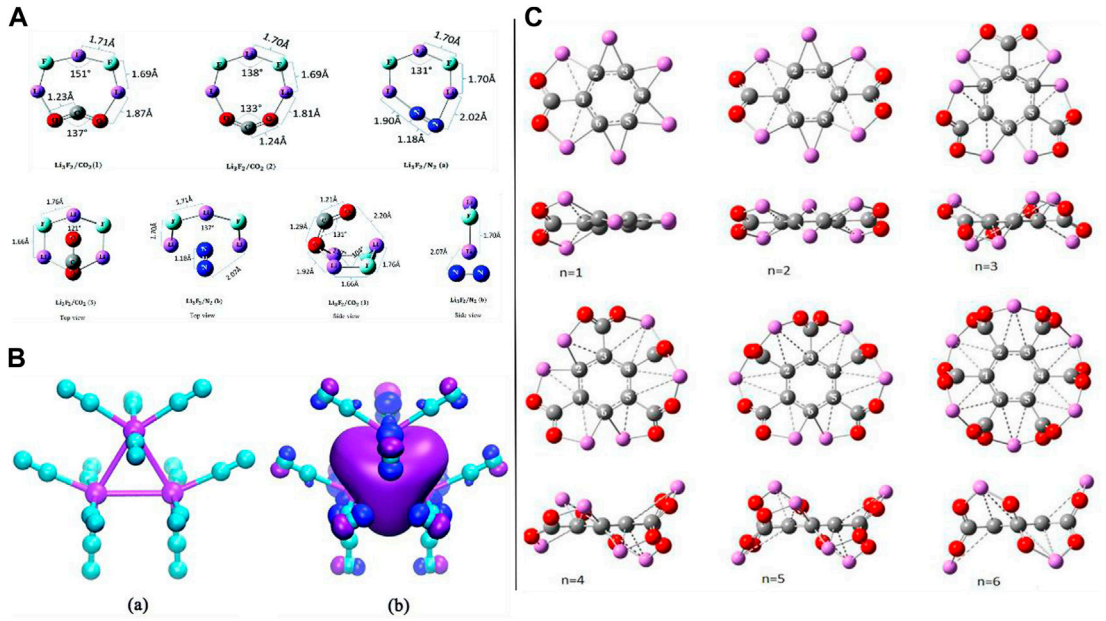


FIGURE 4
**(A)** Optimized geometries of neutral planar clusters (top) and neutral non-planar clusters (bottom) adapted from Park and Meloni (2017) with permission from the Royal Society of Chemistry; **(B) (a)** optimized structure of the $Li_3^+(N_2)_{12}$ complex and **(b)** its HOMO 3D isosurface map adapted from Yu et al. (2020) with permission from the Royal Society of Chemistry; **(C)** optimized structures of $C_6Li_6$–$nCO_2$ complexes (front and side views) for $n$ = 1–6 adopted from Srivastava (2019b) with the permission of Wiley.

$Li_3F_2$ toward the $CO_2$ has been taken using the same level of approach by which computational experiments on the association of the most copious atmospheric $N_2$ gaseous molecule have been conducted (a very small chemical affinity of the $Li_3F_2$ for $N_2$). In the case of the $N_2$ association with the superalkali $Li_3F_2$, the calculated BE value was only 51 kJ/mol, which reveals that the capability of the superalkali $Li_3F_2$ for $CO_2$ reduction has high selectivity over the $N_2$ molecule. $CO_2$ is actively reduced by the superalkali $Li_3F_2$ followed by transferring an electron as well as geometric change which brings up the $CO_2$ molecule in a bent shape, and it can be probably used in transforming $CO_2$ into fuel.

With the deployment of the MP2/6-311+G(d) level of approach, an investigation was conducted by Yu et al. (2020) to obtain new insights into the capability of the superalkali cation $Li_3^+$ for capturing $N_2$ gas as well as its behavior in gaseous nitrogen. To reduce inter-ligand Coulombic repulsion, the $N_2$ molecules (i.e., a maximum coordination number of 12 was envisaged for the trinuclear $Li_3^+$ because every vertex Li can capture four $N_2$ molecules) approached to attach at various apexes of the trinuclear $Li_3^+$ core of the $Li_3^+(N_2)_n$ ($n$ = 1–7) complexes which were confirmed by the structure, stability, and electronic feature analyses. It is worth to mention that only in the case of the lowest-lying series of the $Li_3^+(N_2)_n$ complexes (where the number "n" ranges from 1 to 4) complexes, the trinuclear $Li_3^+$ core retains its superatom dignity using the NPA and FMO approaches. Importantly, the interaction between the $Li_3^+$ with $N_2$ [for example, it reached up to −24.5 kcal/mol for the $Li_3^+(N_2)_4$ complex] is stronger than that with $H_2$ but weaker than that with $H_2O$ molecules. The difference in the Gibbs free energies for the same series of model complexes (through possible fragmentation channels) specified the thermodynamic stability of the $Li_3^+$ in the $(N_2)_n$ clusters. As electrostatic interaction plays a dominant role over the polarization component in the case of the $Li_3^+(H_2O)_n$ complexes, a different case was found in the construction of the $Li_3^+(N_2)_n$ complex having a non-covalent nature where the electrostatic and polarization components contributed almost equally. Furthermore, they concluded that the superalkali trinuclear $Li_3^+$ cation is a much better candidate than its other heavy alkali metal cations ($Na_3^+$ and $K_3^+$) in terms of capturing $N_2$ molecules which is due to a larger BE and favorable structural features for the $Li_3^+(N_2)_n$ complexes as compared to the $N_2$ associated with the $Na^+$ and $K^+$ cations. Moreover, by resemblance, the $Li_3^+$ superalkali cation (along with retaining its identity) has been predicted to have 12 maximum coordination numbers in the nitrogen clusters whose structure (see Figure 4Ba) was assured by the *ab initio* molecular modeling approach with the deployment of the MP2/6-311+G(d) level of theory and the local minima was confirmed by the frequency calculations. Analogous to the isolated $Li_3^+$ alkali metal cation, a delocalized s-type bonding HOMO was detected in the case of $Li_3^+(N_2)_{12}$ which can be seen in Figure 4Bb. The computed NMR

parameters (chemical shifts ranging from −95.5 to −94.1 ppm and −66.8 to −64.0 ppm for the $^{15}$N1 and $^{15}$N1′ nuclei, correspondingly) can indeed provide significant information for the experimental classification of the complexes. Of course, this work provided an in-depth understanding of the mechanism of binding interactions in the $Li_3^+(N_2)_n$ complexes and explored the superalkali-based nitrogen-gas-trapping agents by spurring more computational and experimental attempts.

As $CO_2$, with the property of trapping greenhouse gases, has a crucial role in the global carbon balance purpose along with its conversion into fuel, a very recent *in silico*-based report by H. Srivastava and A. K. Srivastava on the activation of $CO_2$ by various types of superalkalis can be seen in the literature where they showed comprehensive and interesting theoretical outcomes (see Figure 4C) (Srivastava and Srivastava, 2022). Some studies on the superbases which were designed with the help of superalkalis can be seen in the literature (Srivastava and Misra, 2015, Srivastava and Misra, 2016). Because of the superalkalis, for example, typical superalkalis ($FLi_2$, $OLi_3$, and $NLi_4$), special superalkalis [$Al_3$, $Mn(B_3N_3H_6)_2$, $B_9C_3H_{12}$, and $C_5NH_6$], binuclear superalkalis ($Li_3F_2$), non-metallic superalkalis ($O_2H_5$ and $N_2H_7$), and polynuclear superalkalis ($Al_{12}P$, $N_4Mg_6M$) having lower IP than those of the alkali atoms and can easily transfer an electron (due to its hypervalent nature) to the $CO_2$ molecule, these species possess strong reducing power and play an imperative role in altering the geometry of $CO_2$ (bent shape) from its linear structure by donating an electron to it, which have been reported based on the quantum chemical methods. Examining different theory-based reports, it was observed that the extent of the CT (electron transfer) is mainly dependent on the size, geometrical, and electronic features as well as the (IPs) of the superalkali species. *In silico*-based investigations and discussions on the activation of $CO_2$ by a small $Li_3F_2$ cluster inside the Buckminsterfullerene can also be seen in the literature. It was also found that the $CO_2$ molecule is not only activated by the $C_6Li_6$ molecule but also a total of six $CO_2$ molecules can be trapped by the same species. From this report, Srivastava et al. came up with concluding remarks that the reported theoretical findings imply that superalkalis could be utilized as an economical catalyst for the activation of a $CO_2$ molecule, and since the fuel can be formed by the activated $CO_2$ ion like methanol ($CH_3OH$) followed by the hydrogenation reaction. Moreover, Srivastava et al. (2022) have reported various computational experiments using the DFT as well as *ab initio* modeling approaches on the superalkali cations (X = F, O, and N) with methyl ligands, superalkali behavior of ammonium and hydronium cations, and many more studies (Srivastava, 2019b). Moreover, introducing the superalkalis, an *ab initio* study on single- and double-electron reductions of $CO_2$ was reported in 2018 (Srivastava, 2018).

## Complex formations and interactions involved therein

To begin with the idea of superalkalis, complexes are superalkalis with a lower IP than the corresponding alkali and alkaline earth metals; Parida et al. reported work on the computational designing of aromatic organometallic superalkali complexes using the first principle calculations (see Figure 5A) (Parida et al., 2018). A trigonal all-metal core coupled with imidazole (IMD) and pyridine (Py) has been proposed which facilitate the probable existence of a superalkali complex. Low IEs (as compared to the Cesium atom) were found for the organometallic complexes, $Au_3(IMD)_3$ and $Au_3(Py)_3$, which imitated the general features of a superalkali very well. All the superalkali clusters revealed $sp^2$ hybridization, and therefore, a planar geometry all along with the $Au_3^+$ ring showed a "doubly aromatic" character. The HOMO-LUMO gap value of the $Au_3(Py)^+$ species (4.11 eV) was found to be greater than that of the $Au_3(IMD)^+$ (3.84 eV). As some of the organometallic complexes were capable of showing good NLO features using the static first-order hyper-polarizability calculations, it also appeared that the characteristics of such Au-based complexes are like the features of a superalkali. Such outcomes concluded that various coinage metal-based superalkali complexes having broad applications can be synthesized in the laboratory.

Combinations of aluminum trimer and two distinct forms of the representative superatom clusters [(super) alkalis: M = F, $FLi_2$, $OLi_3$, and $NLi_4$; and (super) halogens: X = $LiF_2$, $BeF_3$, and $BF_4$)] were chosen, and the diverse structural, stability (interactions involved in the $Al_3$-M and $Al_3$-X superatom compounds), and electronic features were theoretically explored by Yang et al. (2018) at the MP2/6-311+(3df) level of theory. The $Al_3$-M and $Al_3$-X compounds (see Figure 5B) showed different structures where point-to-side interactions were seen between the $Al_3$ and X components of the $Al_3$-X compound, providing the most favorable bonding pattern while the least preferable was face-to-face. In the case of $Al_3$-M systems, $Al_3$ favored interacting with the $FLi_2$ and Li (super) alkalis *via* its ring plane, whereas it favored binding with $NLi_4$ and $OLi_3$ superalkalis over the Al–Al edge. Interestingly, the $Al_3$ moiety of the $Al_3$-X species acts as the cation (electron donor), whereas it acts as an anion (electron acceptor) in the $Al_3$-M compound assured by the NPA approach. Enhanced CT was detected between the $Al_3$ component and the super-atoms (M and X) in both polar and nonpolar solvents. The HOMO-LUMO gap values, BEs, and bond energies were calculated to be large which confirmed the stability of such blended species ($Al_3$-M and $Al_3$-X compounds) supported by strong interactions taking part between the $Al_3$ and super-atoms (M/X). Importantly, the solvent effect has an important role in the case of the $Al_3$-M (especially, the $Al_3$-$NLi_4$) compounds where it was found that such species were better stabilized in the presence of the solvent molecules, whereas the outcomes were not significant for the

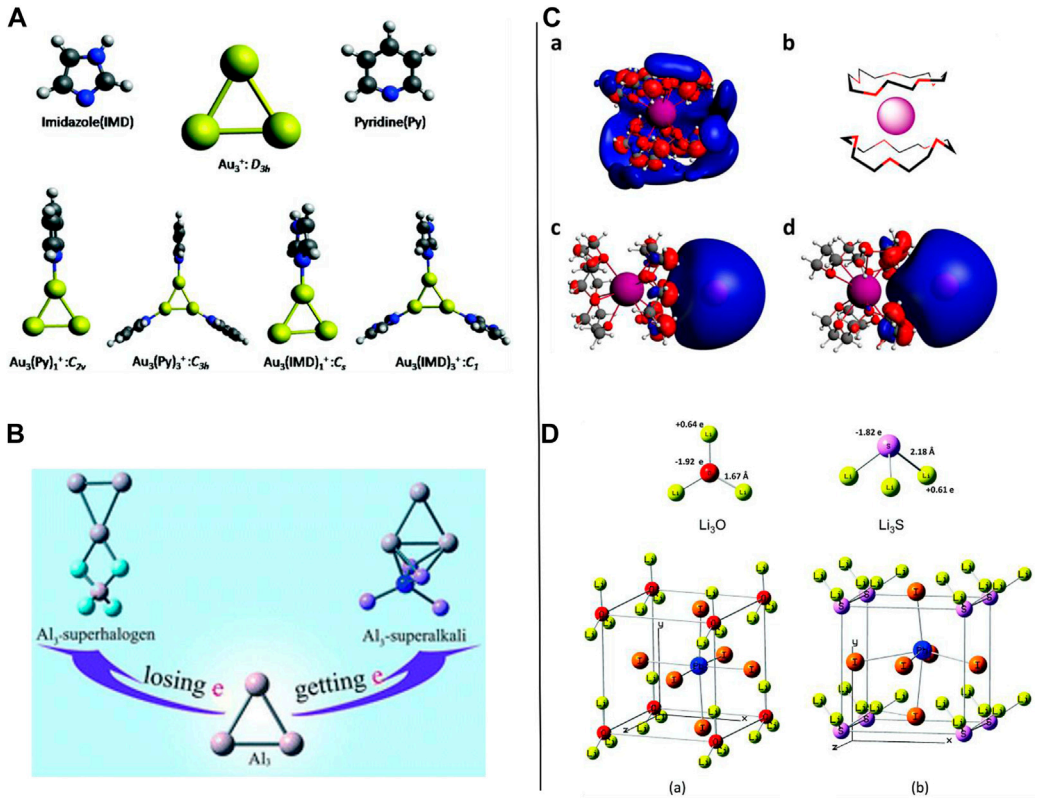


FIGURE 5
**(A)** Optimized geometries of the ligands and the $Au_3$-coupled complexes reproduced with permission from Parida et al. (2018); **(B)** representative $Al_3$-M and $Al_3$-X superatom compounds where M is a (super)alkali (M = Li, $FLi_2$, $OLi_3$, and $NLi_4$) and X is a superhalogen (X = F, $LiF_2$, $BeF_3$, and $BF_4$) reproduced from Yang et al. (2018) with permission from the Royal Society of Chemistry; **(C)** computed SOMO/HOMO 3D isosurfaces of the superalkali K-15-crown-$5_2$ model **(a)** and superalkali–alkalide $(K\text{-}15\text{-}crown\text{-}5_2)^{\delta+}(Na)^{\delta-}$ with the alkalide in the axial reproduced from Riedel et al. (2021) **(c)** and equatorial **(d)** positions with respect to the sandwich complex [as illustrated in the form of a cartoon **(b)**]; **(D)** optimized geometries for **(a)** $Li_3O$ and **(b)** $Li_3S$ (top); cubic $ABX_3$ perovskite structures with superalkali clusters occupying the A sites, Pb atoms occupying the B sites, and I atoms occupying the X sites (bottom) adapted from Paduani and Rappe (2017) with permission from the Royal Society of Chemistry.

stability of the $Al_3$-X compounds. Moreover, the $Al_3^+$ ring exhibited different aromatic characters ($\sigma$ and $\pi$ aromaticity) when associated with diverse superhalogen anions either in the gas or in liquid phases.

As it has been conventionally considered that the anionic alkali metals in the solution possess a gas-like and unperturbed nature recently, Barrett *et al.* reported experimental and theoretical findings on superalkali–akalide interaction-related studies which assisted ion pairing in alkalide solutions in solvents having low polarity (Riedel et al., 2021). The experimental evidence (based on coherent neutron scattering, dielectric spectroscopy, and concentration-dependent macroscopic ionic conductivity) of the observation and influence of ion pairing of alkalides in the solution agreed with each other. Furthermore, to understand the structural, stability, and electronic features, the DFT studies for a range of possible superalkali–alkalide complexes chosen as models were carried out in the framework of *ab initio* simulations, including the superalkalis and superalkali dimers where such species were revealed to play the dominant role in the solution. The visualized singly occupied molecular orbital (SOMO)/HOMO 3D isosurface maps of the superalkali K-15-crown-$5_2$ model (a), superalkali–alkalide $(K\text{-}15\text{-}crown\text{-}5_2)^{\delta+}(Na)^{\delta-}$ associated with the alkalide in the axial (c), and equatorial (d) sites concerning the sandwich complex are exemplified in the form of a cartoon (b) as shown in Figure 5C. The conformational flexibility of the alkalide systems measured by the temperature-dependent alkali metal NMR spectra appeared to show both reversible perturbation and thermally triggered demonstrating a complex replacement mechanism for the ion-paired moieties. The outcomes of their research work facilitated a picture of alkalide moieties acting as a gas-like ion in the solution and attached a great significance to the interactions of the alkalide with its complex counteraction (superalkali) which could be chemically regulated and established by contemplating the interactions between the superalkali and alkalides.

Recently (in 2021), to synthesize aromatic trinuclear Cu(I)-NHC complexes constructed from superalkali ligands as a building block, a variety of NHC (N-heterocyclic carbene) ligands based on imidazole and benz-imidazole have been computationally designed by Giri *et al.* Six different ligands were chosen based on the pyridazine, pyrimidine, and pyrazine acting as the skeletons (Parida et al., 2019). According to the outcomes of the calculated vertical electron affinity, all of the ligands chosen in this work seem to be of the superalkali kind of molecule which has excellent NLO properties. The Cu(I)@NHC complexes were formed by the NHC ligands consisting of trinuclear $Cu_3$ as the central moiety. From the contribution of canonical molecular orbitals toward the computed nucleus independent chemical shift (NICS) values, the trinuclear $Cu_3$ ring appeared to show high σ- and low π-aromaticity. Depending on the various ligand environments, the aromatic features were altered along with other reactivity parameters such as electrophilicity and hardness. According to their theoretical findings, a more reactive and less aromatic complex can be produced by the pyrazine-based NHC ligand as opposed to pyridazine and pyrimidine-based NHCs. Like the $BH_3$ molecule, the inspected super-atomic clusters exhibit $sp^2$ hybridization based on the natural localized molecular orbitals (LMOs). Very interestingly, the UV-Vis spectrum calculations using the first principle study in the acetonitrile solvent showed a blue shift. It is believed that such modeled and theoretically explored complexes can be simply synthesized and utilized as catalysts in advanced synthetic chemistry.

The influence of variations in the ionicity of CT and bonding mechanism on the geometrical and electronic features of novel lead-based halide perovskites formed by introducing the superalkali species was reported by Paduani and Rappe in 2017 with the employment of the scalar relativistic DFT approach (Paduani and Rappe, 2017). In this work, the authors used two superalkalis such as $Li_3O$ [see Figure 5Da] and $Li_3S$ [see Figure 5Db] which were replaced by the Cs atoms in the $CsPbI_3$ having a cubic structure which were detected to be slightly tetragonally distorted, and the band gap values of both superalkali-based species were much lower than that of the cubic $CsPbI_3$. The *in silico*-based outcomes facilitated encouraging performance which can have applications in optoelectronics, for instance, as long-wave infrared (IR) sensors and thermoelectrics. They found that the incorporation of suitable superalkali species at the cationic A-positions in the $ABX_3$-type ($CsPbI_3$) structure can have the capability to tune the band gap of such species. Smaller band gaps (mainly occurring from the effective hybridization between the Pb and Li s-states at the top of the valence band) for the minimum-energy (i.e., equilibrium) crystal structures of both the $[Li_3S]PbI_3$ and $[Li_3O]PbI_3$ compounds were analyzed as 0.41 eV (indirect) and 0.36 eV (direct), correspondingly, where the latter is slightly larger than the former. The $[Li_3O]PbI_3$ compound was hoped to be more resistant to water exposure which was confirmed by the cluster calculations. In comparison to the CsPbI3 species, harsh alterations can be seen in the shape of both valance and conduction bands when the chemical environment was changed in the case of the Pb-halide perovskite structure. Because of the construction of the delocalized energy states, additional electronic states near the Fermi level were formed by introducing the superalkali cations. Such studies have the capability to crease the excitation diffusion length at a longer wavelength and promote hole mobility. Berry-phase simulations demonstrate considerable spontaneous polarization in both novel materials $[Li_3O]PbI_3$ and $[Li_3S]PbI_3$ having non-centrosymmetric structures (lacking inversion symmetry) and thus, allow this material to be used in communications, ferroelectrics, and remote sensing in a prolonged spectrum region.

Taking a quick glimpse at a different type of superalkali cation, a series of interesting computational experiments on the structural, stability/energetics, and electronic feature analyses of some new series of interesting non-metallic superalkali cations such as chain-shaped $F_nH_{n+1}^+$ species, $O_xH_{2x+1}^+$ clusters, and $N_nH_{3n+1}^+$ species were reported by Srivastava (2019a), Srivastava (2019d), and Srivastava (2019c).

## Concluding remarks and future perspectives

The recent advances in the theoretical development, characterization, and first-time use of superalkalis are outlined in this review. In this report, we have made an effort to provide a general overview of modeling/design and characterization (theoretically) of superalkalis and their applications including sharing predictions for their future growth in the hopes of pointing designers in the right direction as they continue to create and use these special species. Efforts have been made to unveil the potential of some novel superalkali cations ($Li_3^+$) and $C_6Li_6$ type species for capturing and storing $CO_2/N_2$ molecules. The first-order hyperpolarizability-based NLO response properties of many new computationally designed superalkali-based materials (for example, fullerenes such as mixed-superalkali-doped $B_{12}N_{12}$ and $B_{12}P_{12}$ nanoclusters having good UV transparency and novel inorganic aromatic mixed-valent superalkali $CaN_3Ca$ as an alkali-earth-based high sensitivity multi-state NLO molecular switch, and novel lead-based halide perovskites formed by introducing the superalkali species) which can, indeed, be used as a new kind of electronic nanodevice for designing hi-tech NLO materials have been unraveled in this review. Understanding the mere interactions of alkalides in a solution, as well as in the gas phase where the potential to influence how such systems can be extended and applied in the future, is also highlighted in this survey. Understanding earned from this report will, indeed, assist in the discovery of novel superalkalis and will enrich the library's arsenal of supersalts.

Although, based on this review, we can predict the forthcoming directions at the industrial level, there are still tasks to better understand the fascinating features of superalkalis and their characteristics to be measured precisely in the fields of inorganic, organic, and material chemistry. We are hopeful that further experiments, as well as theoretical investigations, will be capable of developing the present strategies and contributing to our future sights in better understanding the attention-grabbing features of a variety of already synthesized and designed/modeled novel superalkalis or related species. Moreover, the reported model complexes (as building new materials) in this report will be advantageous, and these may pave alternative pathways for experimentally rewarding applications and can have potential uses in advanced synthetic chemistry as catalysts.

## Author contributions

SP contributed mainly to this report (selection of the topic, its conception, and design). Material preparation, data collection, and figure implementation were mainly performed by SP. All version of the drafts of the manuscript were written and edited by SP, and all other co-authors commented on all drafts of the manuscript. All the authors read and approved the final manuscript.

## Acknowledgments

SKP is thankful to the University Grant Commission (UGC), New Delhi, India, for providing D. S. Kothari - Postdoctoral Fellowship (CH/19-20/0028).

## Conflict of interest

The authors declare that the research was conducted in the absence of any commercial or financial relationships that could be construed as a potential conflict of interest.

## Publisher's note

All claims expressed in this article are solely those of the authors and do not necessarily represent those of their affiliated organizations, or those of the publisher, the editors, and the reviewers. Any product that may be evaluated in this article, or claim that may be made by its manufacturer, is not guaranteed or endorsed by the publisher.

## References

Anusiewicz, I. (2010). The Na2X superalkali species (X=SH , SCH3 , OCH3 , CN , N3 ) as building blocks in the Na2XY salts ( Y = MgCl3 , Cl , NO2 ). An ab initio study of the electric properties of the Na2XY salts. *Aust. J. Chem.* 63, 1573–1581. doi:10.1071/CH10160

Awasthi, S., Gaur, J. K., Pandey, S. K., Bobji, M. S., and Srivastava, C. (2021a). High-strength , strongly bonded nanocomposite hydrogels for cartilage repair. *ACS Appl. Mat. Interfaces* 13, 24505–24523. doi:10.1021/acsami.1c05394

Awasthi, S., Pandey, S. K., Arunan, E., and Srivastava, C. (2021b). A review on hydroxyapatite coatings for the biomedical applications: Experimental and theoretical perspectives. *J. Mat. Chem. B* 9, 228–249. doi:10.1039/d0tb02407d

Banjade, H. R., DeepikaGiri, S., Sinha, S., Fang, H., and Jena, P. (2021). Role of size and composition on the design of superalkalis. *J. Phys. Chem. A* 125, 5886–5894. doi:10.1021/acs.jpca.1c02817

Bano, R., Ayub, K., Mahmood, T., Arshad, M., Sharif, A., Tabassum, S., et al. (2022). Mixed superalkalis are a better choice than pure superalkalis for B12N12 nanocages to design high-performance nonlinear optical materials. *Dalton Trans.* 51, 8437–8453. doi:10.1039/d2dt00321j

Barbatti, M., Jalbert, G., Antonio, M., and Nascimento, C. (2002). Clustering of hydrogen molecules around a molecular Cation: the $Li_3^+(H_2)$ <sub>n</sub> clusters (n = 1 − 6). *J. Phys. Chem. A* 106, 551–555. doi:10.1021/jp013159m

Brédas, J. L., Adant, C., Tackx, P., Persoons, A., and Pierce, B. M. (1994). Third-order nonlinear optical response in organic materials: Theoretical and experimental aspects. *Chem. Rev.* 94, 243–278. doi:10.1021/cr00025a008

Chakraborty, A., Giri, S., and Chattaraj, P. K. (2010). Trapping of noble gases (He-Kr) by the aromatic H3+ and Li3+ species: A conceptual DFT approach. *New J. Chem.* 34, 1936–1945. doi:10.1039/c0nj00040j

Chemla, D. S., and Zyss, J. (1987). *Nonlinear optical properties of organic molecules and crystals*. New York: Elsevier Inc. doi:10.1016/B978-0-12-170612-8.X5001-9

Czapla, M., and Skurski, P. (2017). Oxidizing CO2 with superhalogens. *Phys. Chem. Chem. Phys.* 19, 5435–5440. doi:10.1039/c6cp08043j

Fernandez-Lima, F. A., Vilela-Neto, O. P., Pimentel, A. S., Ponciano, C. R., Caher-Nascimento, M. A., Silveira, E. F. d., et al. (2009). Theoretical and experimental study of negative LiF clusters produced by fast ion impact on a polycrystalline $^7$LiF target. *J. Phys. Chem. A* 113, 15031–15040. doi:10.1021/jp905138d

Geskin, V. M., Lambert, C., and Brédas, J. L. (2003). Origin of high second- and third-order nonlinear optical response in ammonio/borato diphenylpolyene zwitterions: The remarkable role of polarized aromatic groups. *J. Am. Chem. Soc.* 125, 15651–15658. doi:10.1021/ja035862p

Giri, S., Chakraborty, A., and Chattaraj, P. K. (2011). Potential use of some metal clusters as hydrogen storage materials-a conceptual DFT approach. *J. Mol. Model.* 17, 777–784. doi:10.1007/s00894-010-0761-1

Giri, S., Reddy, G. N., and Jena, P. (2016). Organo-zintl clusters [P7R4]: A new class of superalkalis. *J. Phys. Chem. Lett.* 7, 800–805. doi:10.1021/acs.jpclett.5b02892

Gutsev, G. L., and Boldyrev, A. I. (1982). DVM xα calculations on the electronic structure of "superalkali" cations. *Chem. Phys. Lett.* 92, 262–266. doi:10.1016/0009-2614(82)80272-8

Gutsev, G. L., and Boldyrev, A. I. (1981). DVM-Xα calculations on the ionization potentials of MXk+1- complex anions and the electron affinities of MXk+1 "superhalogens. *Chem. Phys.* 56, 277–283. doi:10.1016/0301-0104(81)80150-4

Gutsev, G. L., and Boldyrev, A. I. (1987). The electronic structure of superhalogens and superalkalies. *Russ. Chem. Rev.* 56, 519–531. doi:10.1070/RC1987v056n06ABEH003287

Gutsev, G. L., and Boldyrev, A. I. (1985). The theoretical investigation of the electron affinity of chemical compounds. *Adv. Chem. Phys.* 61, 169–221. doi:10.1002/9780470142851.ch3

Honea, E. C., Homer, M. L., Labastie, P., and Whetten, R. L. (1989). Localization of an excess electron in sodium halide clusters. *Phys. Rev. Lett.* 63, 394–397. doi:10.1103/physrevlett.63.394

Honea, E. C., Homer, M. L., and Whetten, R. L. (1993). Electron binding and stability of excess-electron alkali halide clusters: Localization and surface states. *Phys. Rev. B* 47, 7480–7493. doi:10.1103/PhysRevB.47.7480

Hou, J. H., Wu, D., Liu, J. Y., Li, S. Y., Yu, D., and Li, Y. (2018). The effect of hydration on the electronic structure and stability of the superalkali cation Li3+. *Phys. Chem. Chem. Phys.* 20, 15174–15182. doi:10.1039/c8cp00862k

Hou, N., Li, Y., Wu, D., and Li, Z. R. (2013). Do nonmetallic superalkali cations exist? *Chem. Phys. Lett.* 575, 32–35. doi:10.1016/j.cplett.2013.05.014

Jansen, M. Z. (1977). Meue untersuchungen an Na3N03. *Z. Anorg. Allg. Chem.* 435, 13–20. doi:10.1002/zaac.19774350102

Khanna, S., and Jena, P. (1995). Atomic clusters: Building blocks for a class of solids. *Phys. Rev. B* 51, 13705–13716. doi:10.1103/PhysRevB.51.13705

Khanna, S. N., and Jena, P. (2011). Assembling crystals from clusters. *Phys. Rev. Lett.* 69, 1664–1667. doi:10.1103/PhysRevLett.69.1664

Koput, J. (2008). *Ab initio* study on the structure and vibration-rotation energy levels of dilithium monofluoride. *J. Chem. Phys.* 129, 154306. doi:10.1063/1.2996108

Kudo, H., Wu, C. H., and Ihle, H. R. (1978). Mass-spectrometric study of the vaporization of Li2O(s) and thermochemistry of gaseous LiO, Li2O, Li3O, and Li2O2. *J. Nucl. Mater.* 78, 380–389. doi:10.1016/0022-3115(78)90460-9

Li, Y., Wu, D., and Li, Z. R. (2008). Compounds of superatom clusters: Preferred structures and significant nonlinear optical properties of the BLi6-X (X = F, LiF2, BeF3, BF4) motifs. *Inorg. Chem.* 47, 9773–9778. doi:10.1021/ic800184z

Li, Y., Wu, D., Li, Z. R., and Sun, C. C. (2007). Structural and electronic properties of boron-doped lithium clusters: *Ab initio* and DFT studies. *J. Comput. Chem.* 28, 1677–1684. doi:10.1002/jcc.20637

Lias, S. G., Bartmess, J. E., Liebman, J. F., Homes, J. L., Levin, R. D., and Mallard, W. G. (1988). Gas-phase ion and neutral thermochemistry. *J. Phys. Chem. Ref. Data* 17, 872.

Marder, S. R. (2006). Organic nonlinear optical materials: Where we have been and where we are going. *Chem. Commun.* 2006, 131–134. doi:10.1039/b512646k

Nešković, O. M., Veljković, M. V., Veličković, S. R., Petkovska, L. T., and Perić-Grujić, A. A. (2003). Ionization energies of hypervalent Li2F, Li2Cl and Na2Cl molecules obtained by surface ionization electron impact neutralization mass spectrometry. *Rapid Commun. Mass Spectrom.* 17, 212–214. doi:10.1002/rcm.896

Omidvar, A. (2018). Design of a novel series of donor-acceptor frameworks via superalkali-superhalogen assemblage to improve the nonlinear optical responses. *Inorg. Chem.* 57, 9335–9347. doi:10.1021/acs.inorgchem.8b01322

Otten, A., and Meloni, G. (2018). Stability of lithium substituted silyls superalkali species. *Chem. Phys. Lett.* 692, 214–223. doi:10.1016/j.cplett.2017.12.044

Paduani, C., and Rappe, A. M. (2017). Tuning the gap of lead-based halide perovskites by introducing superalkali species at the cationic sites of ABX3-type structure. *Phys. Chem. Chem. Phys.* 19, 20619–20626. doi:10.1039/c7cp02091k

Pal, R., Poddar, A., and Chattaraj, P. K. (2021). Atomic clusters: Structure, reactivity, bonding, and dynamics. *Front. Chem.* 9, 730548–730624. doi:10.3389/fchem.2021.730548

Pan, S., Contreras, M., Romero, J., Reyes, A., Chattaraj, P. K., and Merino, G. (2013a). C5Li7+ and O2Li 5+ as noble-gas-trapping agents. *Chem. Eur. J.* 19, 2322–2329. doi:10.1002/chem.201203245

Pan, S., Jalife, S., Romero, J., Reyes, A., Merino, G., and Chattaraj, P. K. (2013b). Attractive Xe-Li interaction in Li-decorated clusters. *Comput. Theor. Chem.* 1021, 62–69. doi:10.1016/j.comptc.2013.06.026

Pan, S., Merino, G., and Chattaraj, P. K. (2012). The hydrogen trapping potential of some Li-doped star-like clusters and super-alkali systems. *Phys. Chem. Chem. Phys.* 14, 10345–10350. doi:10.1039/c2cp40794a

Pandey, S. K., and Arunan, E. (2021). Effects of multiple OH/SH substitution on the H-Bonding/Stability versus aromaticity of benzene rings: From computational insights. *ChemistrySelect* 6, 5120–5139. doi:10.1002/slct.202100689

Pandey, S. K. (2021a). Computational study on the structure, stability, and electronic feature analyses of trapped halocarbons inside a novel bispyrazole organic molecular cage. *ACS Omega* 6, 11711–11728. doi:10.1021/acsomega.1c01019

Pandey, S. K. (2021b). Novel and polynuclear K- and Na-based superalkali hydroxides as superbases better than Li-related species and their enhanced properties: An ab initio exploration. *ACS Omega* 6, 31077–31092. doi:10.1021/acsomega.1c04395

Parida, R., Das, S., Karas, L. J., Wu, J. I. C., Roymahapatra, G., and Giri, S. (2019). Superalkali ligands as a building block for aromatic trinuclear Cu(i)-NHC complexes. *Inorg. Chem. Front.* 6, 3336–3344. doi:10.1039/c9qi00873j

Parida, R., Reddy, G. N., Ganguly, A., Roymahapatra, G., Chakraborty, A., and Giri, S. (2018). On the making of aromatic organometallic superalkali complexes. *Chem. Commun.* 54, 3903–3906. doi:10.1039/c8cc01170b

Park, H., and Meloni, G. (2017). Reduction of carbon dioxide with a superalkali. *Dalton Trans.* 46, 11942–11949. doi:10.1039/c7dt02331f

Prasad, P. N., and Williams, D. J. (1991). *Introduction to nonlinear optical effects in molecules and polymers*. New York: John Wiley & Sons.

Reber, A. C., Khanna, S. N., and Castleman, A. W. (2007). Superatom compounds, clusters, and assemblies: Ultra alkali motifs and architectures. *J. Am. Chem. Soc.* 129, 10189–10194. doi:10.1021/ja071647n

Reber, A. C., and Khanna, S. N. (2017). Superatoms: Electronic and geometric effects on reactivity. *Acc. Chem. Res.* 50, 255–263. doi:10.1021/acs.accounts.6b00464

Reddy, G. N., and Giri, S. (2016). Organic heterocyclic molecules become superalkalis. *Phys. Chem. Chem. Phys.* 18, 24356–24360. doi:10.1039/c6cp04430a

Reddy, G. N., Kumar, A. V., Parida, R., Chakraborty, A., and Giri, S. (2018a). Zintl superalkalis as building blocks of supersalts. *J. Mol. Model.* 24, 306. doi:10.1007/s00894-018-3806-5

Reddy, G. N., Parida, R., Chakraborty, A., and Giri, S. (2018b). Deltahedral organo-zintl superhalogens. *Chem. Eur. J.* 24, 13654–13658. doi:10.1002/chem.201802713

Rehm, E., Schleyer, P. v. R., and Boldyrev, A. I. (1992). *Ab initio* study of superalkalis. First ionization potentials and thermodynamic stability. *Inorg. Chem.* 31, 4834–4842. doi:10.1021/ic00049a022

Riedel, R., Seel, A. G., Malko, D., Miller, D. P., Sperling, B. T., Choi, H., et al. (2021). Superalkali-alkalide interactions and ion pairing in low-polarity solvents. *J. Am. Chem. Soc.* 143, 3934–3943. doi:10.1021/jacs.1c00115

Schleyer, P. v. R., Würthwein, E. U., Kaufmann, E., Clark, T., and Pople, J. A. (1983). Effectively hypervalent molecules. 2. Lithium carbide (CLi5), lithium carbide (CLi6), and the related effectively hypervalent first row molecules, CLi5-nHn and CLi6-nHn. *J. Am. Chem. Soc.* 105, 5930–5932. doi:10.1021/ja00356a045

Sinha, S., Jena, P., and Giri, S. (2022). Functionalized nona-silicide [Si9R3] zintl clusters: A new class of superhalogens. *Phys. Chem. Chem. Phys.* 24, 21105–21111. doi:10.1039/d2cp02619h

Srivastava, A. K. (2019a). *Ab initio* investigations on non-metallic chain-shaped F H+1+ series of superalkali cations. *Chem. Phys. Lett.* 721, 7–11. doi:10.1016/j.cplett.2019.02.021

Srivastava, A. K. (2019b). CO2-activation and enhanced capture by C6Li6: A density functional approach. *Int. J. Quantum Chem.* 119, 1–8. doi:10.1002/qua.25904

Srivastava, A. K. (2019c). Design of the N: NH3 n+1+ series of "non-metallic" superalkali cations. *New J. Chem.* 43, 4959–4964. doi:10.1039/c8nj06126b

Srivastava, A. K., and Misra, N. (2015). *Ab initio* investigations on the gas phase basicity and nonlinear optical properties of FLinOH species (n = 2-5). *RSC Adv.* 5, 74206–74211. doi:10.1039/c5ra14735b

Srivastava, A. K., and Misra, N. (2016). OLi3O- anion: Designing the strongest base to date using OLi3 superalkali. *Chem. Phys. Lett.* 648, 152–155. doi:10.1016/j.cplett.2016.02.010

Srivastava, A. K. (2019d). O H2+1+ clusters: A new series of non-metallic superalkali cations by trapping H3O+ into water. *J. Mol. Graph. Model.* 88, 292–298. doi:10.1016/j.jmgm.2019.02.010

Srivastava, A. K., Pandey, S. K., and Misra, N. (2016a). (CH3Br···NH3)@C60: The effect of nanoconfinement on halogen bonding. *Chem. Phys. Lett.* 662, 240–243. doi:10.1016/j.cplett.2016.09.036

Srivastava, A. K., Pandey, S. K., and Misra, N. (2016b). Prediction of superalkali@C60 endofullerenes, their enhanced stability and interesting properties. *Chem. Phys. Lett.* 655–656, 71–75. doi:10.1016/j.cplett.2016.05.039

Srivastava, A. K. (2018). Single- and double-electron reductions of CO2 by using superalkalis: An *ab initio* study. *Int. J. Quantum Chem.* 118, 255988–e25606. doi:10.1002/qua.25598

Srivastava, A. K., Srivastava, H., Tiwari, A., and Misra, N. (2022). X(CH3)+1+ superalkali cations (X = F, O and N) with methyl ligands. *Chem. Phys. Lett.* 790, 139352. doi:10.1016/j.cplett.2022.139352

Srivastava, H., and Srivastava, A. K. (2022). Superalkalis for the activation of carbon dioxide: A review. *Front. Phys.* 10, 870205. doi:10.3389/fphy.2022.870205

Sun, W. M., Cheng, X., Ye, Y. L., Li, X. H., and Ni, B. L. (2022). On the possibility of using aza-cryptands to design superalkalis. *Organometallics* 41, 412–417. doi:10.1021/acs.organomet.1c00674

Sun, W. M., Fan, L. T., Li, Y., Liu, J. Y., Wu, D., and Li, Z. R. (2014a). On the potential application of superalkali clusters in designing novel alkalides with large nonlinear optical properties. *Inorg. Chem.* 53, 6170–6178. doi:10.1021/ic500655s

Sun, W. M., Li, Y., Li, X. H., Wu, D., He, H. M., Li, C. Y., et al. (2016a). Stability and nonlinear optical response of alkalides that contain a completely encapsulated superalkali cluster. *ChemPhysChem* 17, 2672–2678. doi:10.1002/cphc.201600389

Sun, W. M., Li, Y., Wu, D., and Li, Z. R. (2013). Designing aromatic superatoms. *J. Phys. Chem. C* 117, 24618–24624. doi:10.1021/jp408810e

Sun, W. M., Wu, D., Kang, J., Li, C. Y., Chen, J. H., Li, Y., et al. (2018). Decorating zintl polyanions with alkali metal cations: A novel strategy to design superatom cations with low electron affinity. *J. Alloys Compd.* 740, 400–405. doi:10.1016/j.jallcom.2017.12.075

Sun, W. M., Wu, D., Li, X. H., Li, Y., Chen, J. H., Li, C. Y., et al. (2016b). Quasi-chalcogen characteristics of Al12Be: A new member of the three-dimensional periodic table. *J. Phys. Chem. C* 120, 2464–2471. doi:10.1021/acs.jpcc.5b11917

Sun, W. M., Wu, D., Li, Y., and Li, Z. R. (2014b). Theoretical study on superalkali (Li3) in ammonia: Novel alkalides with considerably large first hyperpolarizabilities. *Dalton Trans.* 43, 486–494. doi:10.1039/c3dt51559a

Sun, W. M., and Wu, D. (2019). Recent progress on the design, characterization, and application of superalkalis. *Chem. Eur. J.* 25, 9568–9579. doi:10.1002/chem.201901460

Sun, W. M., Zhang, X. L., Pan, K. Y., Chen, J. H., Wu, D., Li, C. Y., et al. (2019). On the possibility of using the jellium model as a guide to design bimetallic superalkali cations. *Chem. Eur. J.* 25, 4358–4366. doi:10.1002/chem.201806194

Tkachenko, N. V., Sun, Z. M., and Boldyrev, A. I. (2019). Record low ionization potentials of alkali metal complexes with crown ethers and cryptands. *ChemPhysChem* 20, 2060–2062. doi:10.1002/cphc.201900422

Tong, J., Li, Y., Wu, D., Li, Z. R., and Huang, X. R. (2011). *Ab initio* investigation on a new class of binuclear superalkali cations $M_2Li_{2<i>k</i>+1}^+$ ($F_2Li_3^+$, $O_2Li_5^+$, $N_2Li_7^+$, and $C_2Li_9^+$). *J. Phys. Chem. A* 115, 2041–2046. doi:10.1021/jp110417z

Tong, J., Li, Y., Wu, D., Li, Z. R., and Huang, X. R. (2009). Low ionization potentials of binuclear superalkali B2Li 11. *J. Chem. Phys.* 131, 164307. doi:10.1063/1.3254835

Tong, J., Li, Y., Wu, D., and Wu, Z. J. (2012). Theoretical study on polynuclear superalkali cations with various functional groups as the central core. *Inorg. Chem.* 51, 6081–6088. doi:10.1021/ic202675j

Tong, J., Wu, Z., Li, Y., and Wu, D. (2013). Prediction and characterization of novel polynuclear superalkali cations. *Dalton Trans.* 42, 577–584. doi:10.1039/c2dt31429k

Tu, C., Yu, G., Yang, G., Zhao, X., Chen, W., Li, S., et al. (2014). Constructing (super)alkali-boron-heterofullerene dyads: An effective approach to achieve large first hyperpolarizabilities and high stabilities in M3O-BC59 (M = Li, Na and K) and K@n-BC59 (n = 5 and 6). *Phys. Chem. Chem. Phys.* 16, 1597–1606. doi:10.1039/c3cp53639d

Ullah, F., Kosar, N., Ayub, K., Gilani, M. A., and Mahmood, T. (2019). Theoretical study on a boron phosphide nanocage doped with superalkalis: Novel electrides having significant nonlinear optical response. *New J. Chem.* 43, 5727–5736. doi:10.1039/C9NJ00225A

Velickovic, S., Djordjevic, V., Cveticanin, J., Djustebek, J., Veljkovic, M., and Neskovic, O. (2006). Ionization energies of LinX(n=2, 3; X=Cl, Br, I) molecules. *Rapid Commun. Mass Spectrom.* 20, 3151–3153. doi:10.1002/rcm.2712

Veličković, S. R., Djustebek, J. B., Veljković, F. M., Radak, B. B., and Veljković, M. V. (2012). Formation and ionization energies of small chlorine-doped lithium clusters by thermal ionization mass spectrometry. *Rapid Commun. Mass Spectrom.* 26, 443–448. doi:10.1002/rcm.6122

Veličković, S. R., Koteski, V. J., Čavor, J. N. B., Djordjević, V. R., Cvetićanin, J. M., Djustebek, J. B., et al. (2007). Experimental and theoretical investigation of new hypervalent molecules LinF (n = 2-4). *Chem. Phys. Lett.* 448, 151–155. doi:10.1016/j.cplett.2007.09.082

Veličković, S. R., Veljković, F. M., Perić-Grujić, A. A., Radak, B. B., and Veljković, M. V. (2011). Ionization energies of K2X (X=F, Cl, Br, I) clusters. *Rapid Commun. Mass Spectrom.* 25, 2327–2332. doi:10.1002/rcm.5128

Wang, B. Q., Li, Z. R., Wu, D., and Wang, F. F. (2007). Structures and static electric properties of novel alkalide anions F -Li+Li- and F-Li3+Li3-. *J. Phys. Chem. A* 111, 6378–6382. doi:10.1021/jp071218b

Wang, D., Graham, J. D., Buytendyk, A. M., and Bowen, K. H. (2011). Photoelectron spectroscopy of the molecular anions, Li3O - and Na3O-. *J. Chem. Phys.* 135, 164308. doi:10.1063/1.3657854

Wang, J. J., Zhou, Z. J., Bai, Y., Liu, Z. B., Li, Y., Wu, D., et al. (2012). The interaction between superalkalis (M3O, M = Na, K) and a C20F20 cage forming superalkali electride salt molecules with excess electrons inside the C20F20 cage: Dramatic superalkali effect on the nonlinear optical property. *J. Mat. Chem.* 22, 9652–9657. doi:10.1039/c2jm15405f

Wang, X. B., Ding, C. F., Wang, L. S., Boldyrev, A. I., and Simons, J. (1999). First experimental photoelectron spectra of superhalogens and their theoretical interpretations. *J. Chem. Phys.* 110, 4763–4771. doi:10.1063/1.478386

Wang, Y. F., Qin, T., Tang, J. M., Liu, Y. J., Xie, M., Li, J., et al. (2020). Novel inorganic aromatic mixed-valent superalkali electride CaN3Ca: An alkaline-earth-based high-sensitivity multi-state nonlinear optical molecular switch. *Phys. Chem. Chem. Phys.* 22, 5985–5994. doi:10.1039/c9cp06848a

Wei, T., Dahiya, H., Liang, X., Zhu, W., Pandey, S. K., Singh, M. K., et al. (2022). Bulk heterojunction organic photovoltaic cells based on D–A type BODIPY small molecules as non-fullerene acceptors. *J. Mat. Chem. C Mat.* 10, 12776–12788. doi:10.1039/d2tc02497g

Wright, K. W. A., Rogers, D. E., and Lane, I. C. (2009). Geometric bonding effects in the X [sup 2]A[sub 1], A [sup 2]Σ[sub u] [sup +], and B [sup 2]Π[sub g] states of Li[sub 2]F. *J. Chem. Phys.* 131, 104306. doi:10.1063/1.3216373

Wu, C. H., Kudo, H., and Ihle, H. R. (1979). Thermochemical properties of gaseous Li3O and Li2O2. *J. Chem. Phys.* 70, 1815–1820. doi:10.1063/1.437656

Xu, H. L., Li, Z. R., Wu, D., Wang, B. Q., Li, Y., Gu, F. L., et al. (2007). Structures and large NLO responses of new electrides: Li-Doped fluorocarbon chain. *J. Am. Chem. Soc.* 129, 2967–2970. doi:10.1021/ja068038k

Yang, H., Li, Y., Wu, D., and Li, Z. R. (2012). Structural properties and nonlinear optical responses of superatom compounds BF4-M (M = Li, FLi2, OLi3, NLi4). *Int. J. Quantum Chem.* 112, 770–778. doi:10.1002/qua.23053

Yang, H., Wu, D., He, H. M., Yu, D., Li, Y., and Li, Z. R. (2018). The behavior of the aluminum trimer when combining with different superatom clusters. *RSC Adv.* 8, 6667–6674. doi:10.1039/c7ra12852e

Ye, Y. L., Pan, K. Y., Ni, B. L., and Sun, W. M. (2022). Designing special nonmetallic superalkalis based on a cage-like adamanzane complexant. *Front. Chem.* 10, 853160–853167. doi:10.3389/fchem.2022.853160

Yi, X. G., Wang, Y. F., Zhang, H. R., Cai, J. H., Liu, X. X., Li, J., et al. (2022). Can a molecular switch exist in both superalkali electride and superalkalide forms? *Phys. Chem. Chem. Phys.* 24, 5690–5699. doi:10.1039/d1cp05657c

Yokoyama, K., Haketa, N., Tanaka, H., Furukawa, K., and Kudo, H. (2000). Ionization energies of hyperlithiated Li2F molecule and Li F−1 (n=3, 4) clusters. *Chem. Phys. Lett.* 330, 339–346. doi:10.1016/S0009-2614(00)01109-X

Yu, D., Wu, D., Liu, J. Y., Li, Y., and Sun, W. M. (2020). Unveiling the potential of superalkali cation Li3+for capturing nitrogen. *Phys. Chem. Chem. Phys.* 22, 26536–26543. doi:10.1039/d0cp03769a

Zein, S., and Ortiz, J. V. (2011). Interpretation of the photoelectron spectra of superalkali species: Li 3O and Li3O-. *J. Chem. Phys.* 135, 164307. doi:10.1063/1.3636082

Zhang, X. L., Ye, Y. L., Zhang, L., Li, X. H., Yu, D., Chen, J. H., et al. (2021a). Designing an alkali-metal-like superatom Ca3B for ambient nitrogen reduction to ammonia. *Phys. Chem. Chem. Phys.* 23, 18908–18915. doi:10.1039/d1cp01533h

Zhang, X. L., Zhang, L., Ye, Y. L., Li, X. H., Ni, B. L., Li, Y., et al. (2021b). On the role of alkali-metal-like superatom Al12P in reduction and conversion of carbon dioxide. *Chem. Eur. J.* 27, 1039–1045. doi:10.1002/chem.202003733

Zhang, Z., and Chen, H. (2019). Superalkali NM4 (M = Li, Na, K): Stabilities and electronic structures. *Phys. Lett. A* 383, 125952. doi:10.1016/j.physleta.2019.125952

Zintl, E., and Morawietz, W. (1938). Orthosalze von Sauerstoffsäuren. *Z. Anorg. Allg. Chem.* 236, 372–410. doi:10.1002/zaac.19382360134

# Advantages of publishing in Frontiers

**OPEN ACCESS**
Articles are free to read for greatest visibility and readership

**FAST PUBLICATION**
Around 90 days from submission to decision

**HIGH QUALITY PEER-REVIEW**
Rigorous, collaborative, and constructive peer-review

**TRANSPARENT PEER-REVIEW**
Editors and reviewers acknowledged by name on published articles

**Frontiers**
Avenue du Tribunal-Fédéral 34
1005 Lausanne | Switzerland

**Visit us:** www.frontiersin.org
**Contact us:** frontiersin.org/about/contact

**REPRODUCIBILITY OF RESEARCH**
Support open data and methods to enhance research reproducibility

**DIGITAL PUBLISHING**
Articles designed for optimal readership across devices

**FOLLOW US**
@frontiersin

**IMPACT METRICS**
Advanced article metrics track visibility across digital media

**EXTENSIVE PROMOTION**
Marketing and promotion of impactful research

**LOOP RESEARCH NETWORK**
Our network increases your article's readership